

AD-A190 964

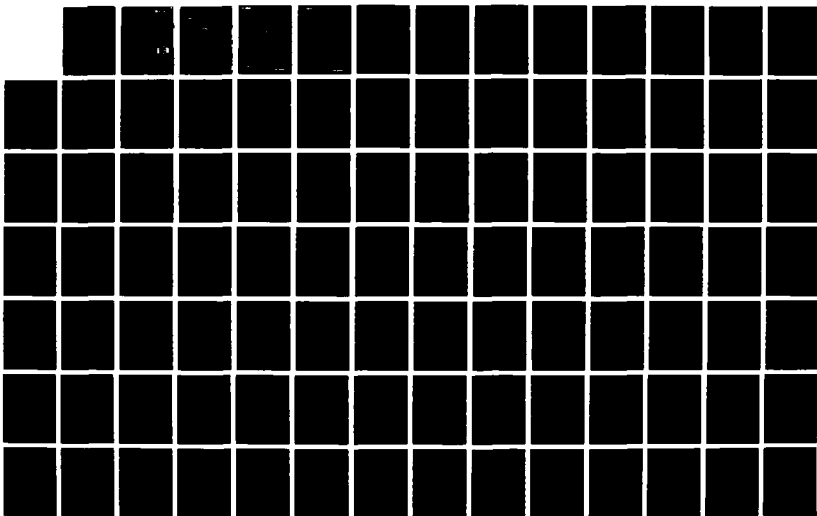
STUDY OF POLYATOMIC DYNAMICS IN THE ATMOSPHERE(U)
SPECTRAL SCIENCES INC BURLINGTON MA F BIEN ET AL.
25 MAR 87 5551-TR-116 AFGL-TR-87-0223 F19628-84-C-0029

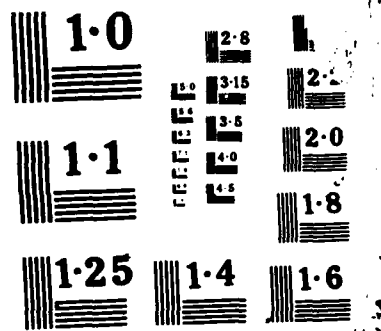
1/3

UNCLASSIFIED

F/G 4/1

NL





AFGL-TR-87-0223

DTIC FILE COPY

4

**STUDY OF POLYATOMIC DYNAMICS
IN THE ATMOSPHERE**

F. Bien, S. M. Adler-Golden and N. M. Goldstein
Spectral Sciences, Inc.
111 South Bedford Street
Burlington, MA 01803

25 March 1987

Final Report for period 30 December 1983 - 30 January 1987

Approved for public release; distribution unlimited.

Air Force Geophysics Laboratory
Air Force Systems Command
United States Air Force
Hanscom Air Force Base, MA 01731

DTIC
ELEMENT
FEB 03 1988
S H D

88 1 26 05 1

AD-A190 964

"This technical report has been reviewed and is approved for publication"


ARTHUR CORMAN
Contract Manager


ROBERT R. O'NEIL, Chief
Infrared Dynamics Branch

FOR THE COMMANDER


RANDALL E. MURPHY, Director
Infrared Technology Division

This report has been reviewed by the ESD Public Affairs Office (PA) and is releasable to the National Technical Information Service (NTIS).

Qualified requestors may obtain additional copies from the Defense Technical Information Center. All others should apply to the National Technical Information Service.

If your address has changed, or if you wish to be removed from the mailing list, or if the addressee is no longer employed by your organization, please notify AFGL/DAA, Hanscom AFB, MA 01731. This will assist us in maintaining a current mailing list.

Do not return copies of this report unless contractual obligations or notices on a specific document requires that it be returned.

UNCLASSIFIED

SECURITY CLASSIFICATION OF THIS PAGE

REPORT DOCUMENTATION PAGE

1a. REPORT SECURITY CLASSIFICATION UNCLASSIFIED			1b. RESTRICTIVE MARKINGS N/A	
2a. SECURITY CLASSIFICATION AUTHORITY			3. DISTRIBUTION/AVAILABILITY OF REPORT Approved for public release; Distribution Unlimited	
2b. DECLASSIFICATION/DOWNGRADING SCHEDULE N/A				
4. PERFORMING ORGANIZATION REPORT NUMBER(S) SSI-TR-116			5. MONITORING ORGANIZATION REPORT NUMBER(S) AFGL-TR-87-0223	
6a. NAME OF PERFORMING ORGANIZATION Spectral Sciences, Inc.		6b. OFFICE SYMBOL (If applicable) N/A	7a. NAME OF MONITORING ORGANIZATION Air Force Geophysics Laboratory	
6c. ADDRESS (City, State, and ZIP Code) 111 S. Bedford Street Burlington, MA 01803			7b. ADDRESS (City, State, and ZIP Code) Hanscom Air Force Base, MA 01731	
8a. NAME OF FUNDING/SPONSORING ORGANIZATION Air Force, Geophysics Lab.		8b. OFFICE SYMBOL (If applicable) LSI	9. PROCUREMENT INSTRUMENT IDENTIFICATION NUMBER F19628-84-C-0029	
8c. ADDRESS (City, State, and ZIP Code) Hanscom Air Force Base, MA 01731			10. SOURCE OF FUNDING NUMBERS	
			PROGRAM ELEMENT NO. 61102F	PROJECT NO. 2310
11. TITLE (Include Security Classification) Study of Polyatomic Dynamics in the Atmosphere				
12. PERSONAL AUTHOR(S) F. Bion, S. M. Adler-Golden and N. M. Goldstein				
13a. TYPE OF REPORT FINAL		13b. TIME COVERED FROM 12/30/83 TO 1/30/87	14. DATE OF REPORT (Year, Month, Day) 87-March-25	15. PAGE COUNT 214
16. SUPPLEMENTARY NOTATION				
17. COSATI CODES			18. SUBJECT TERMS (Continue on reverse if necessary and identify by block number) Infrared Radiation NO O ₃ Einstein Coefficients NO ₂ Vibrational Band Strengths	
FIELD	GROUP	SUB-GROUP		
19. ABSTRACT (Continue on reverse if necessary and identify by block number) This report describes research efforts in support of the LABCEDE and COCHISE programs at the Air Force Geophysics Laboratory. Chapter I contains the analytical effort in support of the COCHISE program where the vibrational bands of O ₃ and NO ₂ are studied. Vibrational band strengths for high v levels of O ₃ were calculated. Dipole matrix elements were determined for the O ₃ v ₃ bands. NO ₂ chemiluminescence was modeled and related to both the normal atmosphere and the Shuttle ram glow. Chapter II of this report describes work carried out in the LABCEDE facility. The production of NO due to electron beam irradiation of N ₂ O ₂ mixtures was studied. NO produced in the vibrational ground state was measured by absorption of light from a tunable diode laser. The measured				
20. DISTRIBUTION/AVAILABILITY OF ABSTRACT <input checked="" type="checkbox"/> UNCLASSIFIED/UNLIMITED <input type="checkbox"/> SAME AS RPT. <input type="checkbox"/> DTIC USERS			21. ABSTRACT SECURITY CLASSIFICATION UNCLASSIFIED	
22a. NAME OF RESPONSIBLE INDIVIDUAL A. Corman			22b. TELEPHONE (Include Area Code) (617) 377-3694	22c. OFFICE SYMBOL AFGL/LSI

UNCLASSIFIED

UNCLASSIFIED

SECURITY CLASSIFICATION OF THIS PAGE

Block No. 18 Continued (Subject Terms)

Electron Irradiation

Absorption

Diode Lasers

Block No. 19 Continued (Abstract)

concentrations of NO was modeled. These concentrations were found to be very sensitive to atomic nitrogen formation from the electron dissociation of N_2 , particularly to the branching ratio $N(^2D)/N(^4S)$. A branching ratio of .55-.45 to .6/.4 was found to fit the observations. Sensitivity of this ratio to other possible reactions are assessed.

UNCLASSIFIED

SECURITY CLASSIFICATION OF THIS PAGE

TABLE OF CONTENTS

<u>Chapter</u>		<u>Page</u>
	PREFACE	v
I	ANALYTICAL PROGRAM	I-1
II	LARCEDE	II-1
 <u>Appendix</u>		
A	FORMULAS FOR TRANSFORMING FROM INTERNAL COORDINATES TO ECKART FRAME COORDINATES OF A SYMMETRIC TRIATOMIC MOLECULE	A-1
B	THEORETICAL CALCULATION OF OZONE VIBRATIONAL INFRARED INTENSITIES	B-1
C	A COMPARISON OF FORCE FIELDS AND CALCULATION METHODS FOR VIBRATION INTERVALS OF ISOTOPIC H_3^+ MOLECULES	C-1
D	THE $NO + O$ AND $NO + O_3$ REACTIONS: I. ANALYSIS OF NO_2 VIBRATIONAL CHEMILUMINESCENCE	D-1
E	THE $NO + O$ AND $NO + O_3$ REACTIONS: II. ANALYSIS OF NO_2 CONTINUUM CHEMILUMINESCENCE	E-1



Accession For	
NTIS GRA&I	<input checked="" type="checkbox"/>
DTIC TAB	<input type="checkbox"/>
Unannounced	<input type="checkbox"/>
Justification	
By	
Distribution/	
Availability Codes	
Dist	Avail and/or Special
A-1	

(THIS PAGE INTENTIONALLY LEFT BLANK)

PREFACE

Program Goals

"Study of Polyatomic Dynamics of the Atmosphere" is a three year program encompassing both experimental and analytical tasks. The aim of the experimental portion, is to conduct experiments on and to interpret the spatial and temporal dependence of the rate of formation of ground vibrational state populations which are important in the disturbed upper atmosphere, with a specific focus on NO (nitric oxide) formation in AFGL's LABCEDE experiment. The aim of the analytical portion of the study is to "determine theoretically the properties of triatomic molecules important to dynamics of the atmosphere", with a specific focus on the infrared properties of O_3 (ozone) and NO_2 (nitrogen dioxide). These goals were fully achieved during the contract period.

Program Motivation

The purpose of this work has been to study a number of infrared-active species, produced in the disturbed atmosphere, both experimentally and theoretically. These comprehensive studies will aid the interpretation of existing laboratory and field data. These studies are especially valuable because the existing data base and models have been deficient in their ability to predict the highly non-thermal chemical, physical and radiative properties of the upper atmosphere, particularly under disturbed conditions. The analytical portion of this report is presented in Chapter I. The experimental program is presented in Chapter II.

CHAPTER I

ANALYTICAL PROGRAM

TABLE OF CONTENTS

<u>Section</u>	<u>Page</u>
1. INTRODUCTION	I-1
2. ANALYTICAL PROGRAM OVERVIEW	I-3
3. CALCULATION OF VIBRATIONAL BAND STRENGTHS FOR OZONE HIGH VIBRATIONAL LEVELS	I-5
3.1 Introduction	I-5
3.2 Algorithm Development	I-6
3.3 Recommended Einstein Coefficients for Ozone 9.6 μm Chemiluminescence	I-9
3.3.1 Introduction	I-9
3.3.2 Procedure	I-10
3.3.3 Results	I-12
3.3.4 Discussion	I-13
4. NO ₂ CHEMILUMINESCENCE MODELING	I-14
4.1 Introduction	I-14
4.2 Predicted NO ₂ IR Chemiluminescence in the Normal Atmosphere	I-17
4.2.1 Introduction	I-17
4.2.2 The NO ₂ Chemiluminescence Mechanism	I-18
4.2.3 Model Description	I-20
4.2.4 Results	I-22
4.2.5 Discussion	I-24
4.3 NO ₂ * Emission Model for Shuttle Ram Glow	I-25
4.3.1 Introduction	I-25
4.3.2 Spectral Modeling	I-26
4.3.3 Field-of-View Effects	I-29
4.3.4 Radiative Lifetimes	I-29
4.3.5 Continuum and Vibrational Band Intensities	I-31
4.3.6 Discussion	I-31
5. CONCLUSIONS	I-33
6. REFERENCES	I-34

LIST OF ILLUSTRATIONS

<u>Figure</u>	<u>Page</u>
1. NO ₂ Continuum Spectral Intensity as a Function of Excitation Energy, E	I-27
2. Calculated and Observed (Reference 25) Tile Surface Spectrum	I-28
3. Comparison of Tile Surface Spectrum and Volume- Integrated Spectrum	I-30

LIST OF TABLES

<u>Table</u>		
1. Wavefunction Coefficients for Darling-Dennison Resonance		I-11
2. Calculated Values of the Ratio of Dipole Moment Matrix Elements Squared, (R/R_{001}) , ⁽²⁾ for Ozone ν_3 Transitions		I-12
3. Atmospheric Input Data		I-22
4. Calculated IR Band Radiance (photons/cm ³ -sec)		I-23
5. Calculated Column-Integrated Radiance (w/km ² -sr)		I-23
6. Effective Radiative Lifetimes $\tau(\lambda)$ (msec)		I-31
7. Absolute Intensities (Photons/Molec per sec) of Continuum and IR Band Emission		I-32

1. INTRODUCTION

This portion of the program deals with the theoretical calculation of infrared properties of triatomic molecules, focusing on O_3 and NO_2 . These molecules are present in the normal atmosphere as well as in disturbed atmospheres. O_3 emission at 9.6μ is found to be greatly enhanced in auroras, as seen in HIRIS.⁽¹⁾ NO_2 has been proposed by Archer⁽²⁾ as an important emitter.

The analytical program is subdivided into two main areas:

1. The calculation of vibrational band strengths for high v levels of O_3 . This work is directly relevant to the interpretation of field observations of ozone 9.6μ emission⁽¹⁾ as well as the COCHISE laboratory studies at AFGL.⁽³⁻⁵⁾

2. The development of a model for upper atmospheric NO_2 infrared chemiluminescence. This work is directly relevant to the prediction of NO_2 background radiance in a nuclear scenario.

The analytical program was highly successful, resulting in two published papers related to ozone vibrational intensities,^(6,7) two manuscripts (to be submitted) on NO_2 chemiluminescence (SSI-TR-111 and

-
1. W. T. Rawlins, G. E. Caledonia, J. J. Gibson, and A. T. Stair, Jr., J. Geophys. Res., **90**, 2896 (1985).
 2. D. H. Archer, "Requirements for Improved Infrared Prediction Capability: LWIR," Mission Research Corporation, Rpt. No. MRC-R-583, DN5471F (1980).
 3. W. T. Rawlins and R. A. Armstrong, "COCHISE Observations of O_3 Formed by Three Body Recombination of O and O_2 ," Rpt. No. AFGL-TR-82-0273, Air Force Geophysics Laboratory, Hanscom AFB, MA (1982). ADA123653
 4. W. T. Rawlins and R. A. Armstrong, "Dynamics of Vibrationally Excited Ozone Formed by Three-Body Recombination. I: Spectroscopy," to be submitted.
 5. W. T. Rawlins, G. E. Caledonia, and R. A. Armstrong, "Dynamics of Vibrationally Excited Ozone Formed by Three-Body Recombination. II: Kinetics and Mechanism," to be submitted.
 6. S. M. Adler-Golden and G. D. Carney, Chem. Phys. Lett., **113**, 582 (1985).
 7. S. M. Adler-Golden, S. R. Langhoff, C. W. Bauschlicher, Jr., and G. D. Carney, J. Chem. Phys., **83**, 255 (1985).

SSI-TR-112), and an AFGL Technical Report⁽⁸⁾ on atmospheric radiance from NO₂ vibrational bands. Additional results and applications include recommended ozone Einstein coefficients for 9.6 μ emission, and a model for NO₂ visible and IR emission in the ram glow off the Space Shuttle and other low earth-orbiting satellites. Two other publications related to this program also appeared during the contract period. The first paper,⁽⁹⁾ based on work of the previous contract period, was a study of the variational method for calculating vibrational energy levels. The second paper,⁽¹⁰⁾ authored by G. Carney, is an application of the variational method to the H₃⁺ molecule, an important test case, and grew out of our collaboration in developing the computer code for ozone.

The organization of the analytical portion of this Report is as follows. Section 2 provides an overview of the role of vibrationally excited molecules, particularly O₃ and NO₂, in atmospheric IR backgrounds, and presents in greater detail the motivation for the current analytical studies. Section 3 describes the calculation of the ozone vibrational band strengths, and Section 4 describes the NO₂ modeling studies. For further technical details the reader is referred to our papers (References 6, 7 and 10) and manuscripts (SSI-TR-111 and -112), which for convenience have been reproduced in Appendices A-E.

-
8. S. M. Adler-Golden, "Predicted NO₂ IR Chemiluminescence in the Natural Atmosphere," AFGL-TR-86-0099, Air Force Geophysics Laboratory, Hanscom AFB, MA (1986). ADA173812
 9. S. M. Adler-Golden, J. Phys. Chem., **89**, 964 (1985).
 10. G. D. Carney, S. M. Adler-Golden, and D. C. Leseski, J. Chem. Phys., **84**, 3921 (1986).

2. ANALYTICAL PROGRAM OVERVIEW

In the upper atmosphere a number of chemical and physical processes occur which populate high-lying molecular vibrational levels. Due to the very low upper atmospheric density these levels have the opportunity to emit infrared radiation before they are removed by collisions. The resulting non-thermal, hot band emission has a different spectrum than the thermal emission seen under ordinary laboratory conditions of higher density. Hot bands occur to the red of the cold emission, and have higher band strengths (i.e., larger Einstein coefficients) than the corresponding cold bands. In addition, new intercombination bands are possible at high vibrational energies. The result is that emission from highly excited upper atmospheric molecules tends to fill in the infrared "window" regions associated with ambient temperature molecules.

In disturbed atmospheres new processes occur which enhance the concentrations of infrared-active molecules. Ozone emission at $9.6\ \mu$ has been found to be greatly enhanced in auroras, possibly due to ozone formation via a 2-body reaction between O_2 and O_2^* (electronically excited oxygen). The normal atmospheric $9.6\ \mu$ limb radiance is $10^{-8}\ W\ cm^{-2}\ sr^{-1}$ at 110 km according to SPIRE,⁽¹¹⁾ whereas HIRIS⁽¹⁾ measured radiances of around $10^{-7}\ W\ cm^{-2}\ sr^{-1}$ at 110-120 km in an aurora. Similarly, NO_2 , ordinarily a weak emitter in the upper atmosphere (as evidenced by its absence in SPIRE spectra above 35 km) may be greatly enhanced in a nuclear scenario due to increased NO formation, followed by the reaction $NO + O (+M) \rightarrow NO_2 (+M)$. These are both examples of chemiluminescence mechanisms, in which vibrationally excited molecules are directly formed. Another mechanism for enhancement of infrared radiance is the pumping of vibrational modes by thermally excited air molecules. NO and CO_2 emissions are excited in this way in the normal atmosphere,⁽¹²⁾ and would be even more strongly excited at the high temperatures anticipated in a nuclear

11. A. T. Stair, Jr., R. D. Sharma, R. M. Nadile, D. J. Baker, and W. F. Grieder, J. Geophys. Res., **90** (1985) 9763.
12. B. F. Gordiets, Yu. N. Kulikov, M. N. Markov, and M. Ya. Marov, J. Geophys. Res., **87** (1982) 4504.

scenario. In addition, electronically excited species, such as metastable O atoms and O₂ molecules, as well as vibrationally excited species such as N₂, are capable of pumping infrared-active molecules.

The ability to reliably model this upper atmospheric infrared emission requires detailed knowledge of the excitation and quenching processes and the radiative properties of these molecules. Laboratory data, such as ozone chemiluminescence spectra obtained in the COCHISE facility at AFGL,⁽³⁾ are very useful, but require modeling for their analysis, since laboratories do not duplicate the conditions of low density and long optical paths found in the upper atmosphere. In the case of the ozone chemiluminescence, accurate modeling requires reliable Einstein coefficients for high vibrational levels, as discussed by Rawlins.⁽¹³⁾ Without this information, it is impossible to properly analyze laboratory or atmospheric data, determine the vibrational level populations, and ultimately predict the atmospheric background radiance at all wavelengths, altitudes, and degrees of auroral excitation. |

The main purpose of the current analytical program was to provide detailed spectroscopic and/or mechanistic information for two specific molecules, O₃ and NO₂, which are important disturbed atmosphere radiators. The ozone work in particular supports the COCHISE experimental program at AFGL. A subsidiary goal was to develop both conceptual models and computer codes useful for similar calculations of radiance from other small molecules in the atmosphere.

13. W. T. Rawlins, J. Geophys. Res., 90, 12283 (1985).

3. CALCULATION OF VIBRATIONAL BAND STRENGTHS FOR OZONE HIGH VIBRATIONAL LEVELS

3.1 Introduction

As discussed in Section 2, Einstein coefficients for high v levels of ozone are critical for the proper interpretation of upper atmospheric ozone radiance as well as the analysis of the COCHISE results. Accurate ab initio variational calculations of these quantities, begun during the previous contract period, were completed and published during this program, and are one of the main accomplishments of the analytical effort.

The calculation was a collaborative effort between Spectral Sciences, G. Carney (NIT) and S. Langhoff and C. Bauschlicher (NASA Ames). One of the key ingredients was the ab initio dipole moment calculated by Langhoff using the CASSCF method. This method has yielded the most accurate results available for the notoriously difficult ozone molecule. The second important ingredient was the variational algorithm, developed by Cropek and Carney⁽¹⁴⁾ and modified by us. A brief description of the algorithm and the modifications, which corrected an error in the original code and extended the code to handle ozone and improve its convergence properties, is found in Subsection 3.2 below. A test of the new algorithm was provided by calculations on H_3^+ , which gave excellent agreement with independent methods (see Reference 10, reproduced in Appendix C). A third ingredient required was the transformation of the ab initio dipole moment to the Eckart frame, which we accomplished using a new, exact method (see Reference 6, reproduced in Appendix A). The final ozone results are described in Reference 7 (also in Appendix B).

In a follow-up calculation, the variational results for 9.6 μ emission, which cover all vibrational levels having up to 3 quanta, were extrapolated semi-empirically to the highest vibrational levels seen in COCHISE. This resulted in a set of recommended Einstein coefficients for

14. D. Cropek and G. D. Carney, J. Chem. Phys., **80**, 4280 (1984).

9.6 μ emission, described in Subsection 3.3. We estimate that these Einstein coefficients are accurate to ~20% or better. A detailed comparison of the recommended Einstein coefficients with earlier, less accurate estimates is given by Rawlins and Armstrong.⁽⁴⁾ In brief, the recommended values are smaller than harmonic oscillator scaling predictions, but the differences do not exceed a factor of 2 for the bands observed in COCHISE.

3.2 Algorithm Development

The core of the current calculations is a variational algorithm developed by G. Carney and D. Cropek while at Allegheny College. This algorithm uses an exact, internal coordinate formulation of the quantum mechanical Hamiltonian for a bent, symmetric triatomic molecule. We have extended the original code as described below for application to the problem of ozone infrared intensities.

The Carney-Cropek variational algorithm is described in detail elsewhere.⁽¹⁵⁾ In brief, it utilizes an internal coordinate Hamiltonian developed by Lai and Hagstrom,⁽¹⁶⁾ with basis functions which are numerical solutions to 1-dimensional bond stretching and angle bending Schrodinger equations. The off-diagonal matrix elements arise from both kinetic energy and potential energy coupling terms, and are evaluated using either numerical quadrature or Simpson's rule. The potential energy surface is expressed as a polynomial in a set of expansion variables, such as $(\theta - \theta_{eq})$, ρ_1 , ρ_2 , as defined by Simons, Parr and Finlan,^(16,17) or, in alternative code versions, the radial variables $(R - R_{eq})$ or Morse

15. G. D. Carney, "Vibration Energies and Wavefunctions for Bent Triatomic Molecules," and D. Cropek, "A Numerical Variational Method for Calculating Vibrational Energies of Bent Triatomic Molecules," Allegheny College, Meadville, PA (1983).
16. G. D. Carney, L. L. Sprandel, and C. W. Kern, "Variational Approaches to Vibration-Rotation Spectroscopy for Polyatomic Molecules," Adv. Chem. Phys., **37** (1978).
17. G. Simons, R. G. Parr and J. M. Finlan, J. Chem. Phys., **59**, 3229 (1973).

oscillator (exponential) variables. Diagonalization is accomplished using the efficient GIVENS routine available from the Quantum Chemistry Program Exchange, Indiana University.

The code developed by Spectral Sciences extends the capabilities of the original algorithm in the following ways:

1. The number of potential energy surface coefficients is increased to an arbitrary number which is currently set at 50.
2. Matrix elements of powers of the expansion variables (up to the sixth power) are output, as are the eigenfunctions. This feature permits the calculation of dipole moment matrix elements.
3. Configuration lists can be automatically generated if desired using quantum number cutoff criteria.
4. Auxiliary programs have been developed for generating input files of force constants and dipole moment coefficients, and for generating dipole moment matrix elements using the variational eigenstates.

These codes have been run on both the PRIME 750 at Abt Associates, Inc., used by Spectral Sciences, and on the VAX 780 at AFGL. The VAX was used for running the codes with large basis sets, and the PRIME has been used for program development.

In addition, it should be noted that the current variational code corrects an error in the original Carney-Cropek program. Verification of the accuracy of the new code is provided by a calculation of the eigenvalues of the Barbe quartic potential function;⁽¹⁸⁾ they are found to agree with a previous, converged calculation⁽¹⁹⁾ (which used the Watson Hamiltonian in "t" coordinates) to within 0.1 cm^{-1} .

18. A. Barbe, C. Secroun, and P. Jouve, J. Molec. Spectrosc., 49, 171 (1974).

19. G. D. Carney, L. A. Curtiss, and S. R. Langhoff, J. Molec. Spectrosc., 61, 371 (1976).

Having in hand accurate vibrational wavefunctions from the variational code, we can begin the dipole moment matrix element calculation. Ab initio dipole moment vectors at a number of geometries were provided to us by Langhoff; they were calculated on a CRAY 1 at NASA/Ames using the CASSCF method with a large DZP basis set. Further details are given in Reference 7, along with a comparison of various ab initio methods. After transformation to the Eckart frame (see the following paragraph), the dipole moment vectors were fit to polynomial functions (one for each vector component) in the vibrational expansion variables using a least-squares routine. This reduced the dipole moment matrix elements to a linear combination of matrix elements of the expansion variable powers, which as mentioned earlier are part of the variational code output.

The ab initio dipole moment vector is initially expressed in the valence angle bisector (VAB) coordinate system, whose unit vectors are parallel and perpendicular to the bisector of the instantaneous angle. For asymmetric geometries these unit vectors are not fixed in the laboratory frame, so that the valence angle bisector dipole moment components cannot directly be used for the dipole moment matrix element calculation. As described by Carney et al.,⁽¹⁶⁾ one must first transform the dipole moment vector to the Eckart frame by multiplying by a rotation matrix. The angle of the rotation, β , is derived by expressing the instantaneous geometry in terms of Eckart coordinates such as normal, "t", or symmetry coordinates. We developed a new, exact method for calculating β , which is described in detail in Reference 6. The effect of this coordinate rotation on the ozone band intensities has been discussed by Carney et al.;⁽²⁰⁾ for most bands it is found to be minor.

Upon closer investigation, it appears that the above procedure for correcting for the motion of the VAB coordinates is not exact. Specifically, for large amplitude motions the vibrational angular momentum term causes a relative angular velocity between the Eckart frame and the instantaneous geometry that is not accounted for in the above treatment;

20. G. D. Carney, S. Giorgianni, and K. N. Rao, J. Molec. Spectrosc., 80, 158 (1980).

this angular velocity depends on linear momenta as well as coordinates. Thus, the Eckart frame components do not exactly correspond to the fixed laboratory frame components. Furthermore, evidence of the approximate nature of the above treatment is provided by our observation that the rotation angle β is found to depend slightly on the definition of the equilibrium geometry, a physically unreasonable result. A more exact treatment would be an interesting theoretical problem, but was beyond the scope of the current investigation.

The detailed ozone results and comparison with experimental vibrational intensities appear in Reference 7. An additional application of our variational algorithm was the calculation of vibrational levels of H_3^+ , a molecule of astrophysical significance which has attracted considerable experimental and theoretical interest. The potential surfaces were provided by Carney and the vibrational level calculations were performed by Spectral Sciences. The H_3^+ molecule proved to be a severe test for our algorithm, and required us to squarely face the issues of basis set selection and computational speed. Details are provided in Reference 10. The experience acquired in handling H_3^+ will prove useful in future, more ambitious calculations on ozone and other molecules.

3.3 Recommended Einstein Coefficients for Ozone 9.6 μ Chemiluminescence

3.3.1 Introduction

The theoretical calculation described in Reference 7 resulted in dipole moment matrix elements R for all transitions involving ozone vibrational levels having up to three quanta. Since the Einstein A coefficient is related to the dipole moment matrix element via the equation

$$A \text{ (sec}^{-1}\text{)} = 2.026 \times 10^{-6} \nu^3 R^2 \quad (1)$$

(where R is in a. u.), it is a simple matter to convert the theoretical R values into Einstein coefficients for use in ozone chemiluminescence modeling. As shown in Reference 7, our theoretical dipole moment matrix elements for the cold bands show good overall consistency with experimental

data. We feel that the calculations for the hot bands are comparably reliable. Furthermore, we believe that the relative accuracy of the predicted ν_3 hot band dipole moment matrix elements is superior to their absolute accuracy, so that improved values can be obtained by scaling relative to the known value for the ν_3 fundamental.

In the COCHISE experiment ν_3 emission is observed from levels having as many as four or five vibrational quanta. Unfortunately, our variational calculation was unable to access these highest energy states. In addition to the problem of convergence of the calculation, an even more severe limitation is the fact that these states probe regions of the potential energy and dipole moment surfaces which are essentially unknown. The purpose of this Section is to present a plausible extrapolation of the variationally calculated matrix elements to these high vibrational levels. These new values represent our current best guess and are probably accurate to within about 20%. There is one cautionary note, however. The possibility exists for these very high lying levels to be involved in accidental resonances with nearby levels containing additional bending excitation. In that case the transition strength calculated here would be divided among the resonating states. On the other hand, there seems to be no direct evidence of this effect in COCHISE.

3.3.2 Procedure

The matrix element extrapolation was accomplished using a suitable functional form. We focus on the ν_3 transitions emanating from states $(0 \nu_2 \nu_3)$ and $(1 \nu_2 \nu_3)$, which may be described using the function

$$R = d''dg(\nu_1, \nu_2, \nu_3) + e''eg(\nu_1 + 2, \nu_2, \nu_3 - 2) \\ + f''fg(\nu_1 + 4, \nu_2, \nu_3 - 4) \quad (2)$$

where

$$g(\nu_1, \nu_2, \nu_3) = \sqrt{\nu_3}(c_0 - c_1\nu_1 - c_2\nu_2 - c_3\nu_3) \quad (3)$$

The quantities d, e, and f are wavefunction coefficients found from diagonalizing the Darling-Dennison perturbation matrix,⁽²¹⁾ and are listed in Table 1. (d, e, and f are the weights of the v_1, v_2, v_3 state in the unperturbed basis functions $[v_1 v_2 v_3]$, $[v_1 + 2 v_2 v_3 - 2]$ and $[v_1 + 4 v_2 v_3 - 4]$, respectively; the " superscript indicates that v_3 is to be replaced by $v_3 - 1$.) The quantities c_0 through c_3 are adjustable parameters. We fixed R for the v_3 fundamental to the variationally calculated value, leaving three independently adjustable parameters.

Equation (2) is theoretically rigorous for a model which includes electrical anharmonicity of up to third degree, and Darling-Dennison coupling of the vibrational wavefunctions. Inclusion of mechanical anharmonicity effects into the uncoupled wavefunctions would result in a more complicated function involving terms of higher degree in the vibrational quantum numbers. These complications are overcome for the most

TABLE 1. WAVEFUNCTION COEFFICIENTS FOR
DARLING-DENNISON RESONANCE

(v_1, v_2, v_3)	d	e	f
(0 0 5)	0.714	0.663	0.225
(1 0 4)	0.846	0.525	0.093
(0 0 4)	0.847	0.522	0.098
(1 0 3)	0.920	0.391	
(0 0 3)	0.935	0.353	
(1 0 2)	0.972	0.234	
(0 0 2)	0.982	0.191	
(1 0 1)	1.000		
(0 0 1)	1.000		
(0 1 4)	0.872	0.482	0.084
(1 1 3)	0.929	0.369	
(0 1 3)	0.947	0.321	
(1 1 2)	0.976	0.218	
(0 1 2)	0.985	0.173	
(1 1 1)	1.000		
(0 1 1)	1.000		

21. R. T. Darling and D. M. Dennison, Phys. Rev., 57, 128 (1940).

part by using Equation (2) in an empirical manner, fitting it directly to the variationally calculated matrix elements in Reference 7. (The Reference 7 calculation employed accurate, anharmonic vibrational wavefunctions.)

3.3.3 Results

The dipole moment matrix element R was calculated using Equation (2) with the values $c_0 = 0.06932$, $c_1 = 0.003$, $c_2 = 0.0006$, $c_3 = 0.0012$, which were chosen to give a good overall fit to the variationally calculated ν_3 transitions of interest. The calculated R values were then squared and ratioed to the ν_3 fundamental. The resulting ratios are presented in Table 2 for transitions from vibrational levels of potential relevance to the COCHISE experiment. Agreement of the Equation (2) values with the variational calculation is excellent. We are therefore confident that the Equation (2) values for the four and five quantum states closely

TABLE 2. CALCULATED VALUES OF THE RATIO OF
DIPOLE MOMENT MATRIX ELEMENTS SQUARED,
 $(R/R_{001})^2$, FOR OZONE ν_3 TRANSITIONS.

Upper State ($\nu_1 \nu_2 \nu_3$)	Harmonic Model	Variational (from Ref. 7)	Eq. (2)
(0 0 5)	5		3.24
(1 0 4)	4		2.73
(0 0 4)	4		3.00
(1 0 3)	3	2.15	2.27
(0 0 3)	3	2.51	2.55
(1 0 2)	2	1.66	1.66
(0 0 2)	2	1.88	1.86
(1 0 1)	1	0.92	0.91
(0 1 4)	4		3.04
(1 1 3)	3		2.25
(0 1 3)	3	2.50	2.54
(1 1 2)	2		1.65
(0 1 2)	2	1.85	1.84
(1 1 1)	1	0.91	0.90
(0 1 1)	1	0.98	0.98

approximate the results which would be obtained by extending the variational treatment to higher energies. Given the good accuracy of the variational treatment, especially for fundamental bands, we estimate an accuracy of around 20% or better for all of the Table 2 ratios.

3.3.4 Discussion

If one adopts an electrically and mechanically harmonic model for the ozone ν_3 bands the dipole moment ratios $(R/R_{001})^2$ are predicted to be directly proportional to ν_3 , as given in the second column of Table 2. Comparison with the Equation (2) ratios shows significant deviation from this harmonic model starting at around $\nu_3 = 3$. Approximately half of this deviation is caused by the Darling-Dennison resonance, the remainder being due to other sources of anharmonicity accounted for by the coefficients c_1 through c_3 .

While these differences are not large enough to alter the essential conclusions of the COCHISE data analysis, they are still significant differences, especially given our confidence in the Equation (2) values. Therefore, we highly recommend that the Equation (2) or variational dipole moment ratios be used instead of the harmonic approximation for the analysis of both COCHISE and atmospheric data.

4. NO₂ CHEMILUMINESCENCE MODELING

4.1 Introduction

In a survey on infrared radiators in a nuclear scenario Archer⁽²⁾ identifies NO₂ as a potentially important emitter throughout the LWIR. Vibrationally excited NO₂ would be produced via the chemiluminescent reactions



These reactions are known to produce visible and near-infrared continuum chemiluminescence as well as NO₂ vibrational band emission at 3.7 μ and 6.3 μ. In a nuclear scenario the NO could be considerably enhanced (by one or two orders of magnitude) over ambient concentrations, so the radiation from these reactions could be much more important than in the ambient atmosphere. Archer's NO₂ chemiluminescence model, which incorporates the WOE code⁽²²⁾ and a few basic kinetic and spectroscopic parameters, was found to predict very strong NO₂ emission ($> 10^{-9} \text{ W cm}^{-2} \text{ sr}^{-1} \mu^{-1}$ in the 3 - 5 μ and 7 - 9 μ regions below 110 km), resulting in virtual elimination of the "window" regions in the upper atmosphere, as the result of these nuclear-enhanced reactions.

More recently, Kofsky and co-workers^(23,24) have considered this problem and a related one, NO₂ chemiluminescence from the Space Shuttle. They developed an NO₂ chemiluminescence model using a different set of assumptions from Archer, predicting much less emission (by 1 or 2 orders of magnitude) over a much narrower spectral range.

22. T. L. Stephens, General Electric-TEMPO (1979), cited in Reference 2.

23. I. L. Kofsky, J. L. Barrett, and L. McVay, "Infrared Radiance Structure of the Aurora and Airglow," AFGL-TR-82-0220, Air Force Geophysics Laboratory, Hanscom AFB, MA (1982). ADA130468

24. I. L. Kofsky and J. L. Barrett, Journal of Spacecraft and Rockets, 24, 2, 133 (1987).

A major goal of our analytical program was to resolve these differences by developing an accurate, theoretically grounded model for the NO₂ infrared chemiluminescence expected in the atmosphere. This goal was successfully accomplished using input from a wide range of NO₂ chemiluminescence, fluorescence, and kinetic data published over the last ~20 years.

The NO₂ chemiluminescence model we developed has a number of unique features which account for its reliability. Firstly, the model takes into full account the dependence of spectroscopic and kinetic parameters of NO₂ upon internal energy through the use of a "stepladder" formulation. Secondly, the model incorporates the visible-near infrared continuum emission mechanism, which is essential to a correct description of the infrared band (as well as continuum) radiation. Thirdly, the model was designed for consistency with all available data on these reactions, including continuum spectra, infrared band spectra, reaction rates, and quenching rates, as well as NO₂ spectral data such as vibrational intensities and continuum radiative lifetimes. When compared with observed spectra, the model is found to be accurate to better than a factor of 2 in absolute intensity and 3% in wavelength over the entire visible and infrared regions.

The infrared band portion of the model, which treats the two most intense bands, ν_3 and $\nu_1 + \nu_3$, is described in SSI-TR-112 (Appendix D), where comparison with experimental results is also made. Further validation is provided by a comparison between the full model and experimental visible and near-infrared continuum spectra, found in SSI-TR-111 (Appendix E). This model also provides a new interpretation of the NO + O₃ reaction mechanism. To our knowledge, the current NO₂ infrared model is the first which has been validated by these extensive comparisons. In addition to providing support for the infrared band model, the continuum predictions may be useful in their own right for analysis of the nightglow.

The model detailed in SSI-TR-112 and SSI-TR-111 provides a good description of NO₂ chemiluminescence observed in the laboratory. However, it has two drawbacks for atmospheric modeling: it is fairly complicated, and it may be less accurate at the very low densities found in the upper atmosphere. To correct these deficiencies, a second, much simpler infrared

band model was developed, described in Subsection 4.2 below. This model, although less detailed, is more versatile than the first in several respects: it treats not only the strong bands mentioned above but also the weaker bands ν_1 and ν_2 , it takes into account the temperature variation of the formation and relaxation rate constants, and it behaves reasonably in the limit of low number density. Its mathematical form is similar to Archer's model, and thus it is well-suited to existing atmospheric radiance codes. Using this second model, calculations of upper atmospheric radiance were performed for normal atmospheric conditions, as described in Subsection 4.2. The atmospheric conditions correspond to those of Kofsky et al⁽²³⁾ for the sake of comparison.

The normal atmosphere radiance predictions from the current model are found to be even smaller than Kofsky's (by a factor of 3 to 4). For a 95 km limb view the predictions for the ν_2 , ν_3 and $\nu_1 + \nu_3$ band radiances are 0.008, 0.2, and 0.03 W km⁻² sr⁻¹ respectively. Assuming band widths of 0.7 μ for ν_3 (6.3 μ) and 0.5 μ for $\nu_1 + \nu_3$ (3.7 μ), these translate into peak radiances of 3×10^{-11} W cm⁻² sr⁻¹ μ^{-1} for ν_3 and 6×10^{-12} W cm⁻² sr⁻¹ μ^{-1} for $\nu_1 + \nu_3$. For comparison, in the normal atmosphere Archer's predicted radiances are $> 10^{-10}$ W cm⁻² sr⁻¹ μ^{-1} over the entire 3 - 9 μ region, and an order of magnitude larger at 3.7 μ in the 85 - 105 km altitude range.

The results for the normal atmosphere may be roughly scaled to the disturbed atmosphere using the appropriate NO concentration. Unfortunately, Archer did not report the NO concentration used in his model. However, the comparison of results for the normal atmosphere implies that Archer's nuclear scenario radiance estimates are too high by at least two orders of magnitude at most wavelengths, with the exception of 6.3 μ where the discrepancy is about one order of magnitude. Whereas Archer predicted substantial radiance throughout the infrared, the current model (as well as Kofsky's) predicts significant emission in only two bands, ν_3 (6.3 μ) and $\nu_1 + \nu_3$ (3.7 μ). In conclusion, NO₂ chemiluminescence in a nuclear environment is not nearly as important as has been suggested. However, given sufficient NO density and a limb view, emission at 6.3 μ may still provide a non-negligible nuclear background source.

Finally, having in hand an accurate model for NO_2 emission, we decided that a brief look at the Shuttle ram glow problem was worthwhile, inasmuch as Mende and co-workers⁽²⁵⁾ have proposed NO_2 as the source of this radiation and similar glows from other low earth-orbiting satellites. The goal of this investigation was to use the glow spectrum observed in the visible region together with our NO_2 continuum model to derive an NO_2 vibrational temperature, and then predict the continuum and band spectrum in the infrared. The Shuttle glow model, results and comparison with predictions by Kofsky and Barrett⁽²⁴⁾ are described in Subsection 4.3 below. In brief, the Shuttle glow was found to be consistent with NO_2 continuum emission at a vibrational temperature of around 3500 K, and a desorption velocity of around 1.7 km/sec.

4.2 Predicted NO_2 IR Chemiluminescence in the Normal Atmosphere

4.2.1 Introduction

Archer⁽²⁾ has proposed that NO_2 chemiluminescence from the $\text{NO} + \text{O}$ and $\text{NO} + \text{O}_3$ reactions would be a significant source of atmospheric background IR radiance in a disturbed atmosphere. Predicting this radiance requires a reliable model of NO_2 IR emission in addition to knowledge of the species concentrations. Several NO_2 radiance models have been developed, each of which uses different assumptions and gives significantly different results. Archer's model assumes the WOE code⁽²²⁾ spectral distribution, which is based on "theoretical considerations of energy conservation." This spectrum gives all three fundamental bands a comparable intensity, and also includes numerous overtone and combination bands, resulting in substantial radiance throughout the LWIR. A second model, due to Kofsky and co-workers,^(23,24) is based on experimental data which observes roughly a 10:1 ratio of ν_3 to

25. G. R. Swenson, S. B. Mende, and K. S. Clifton, J. Geophys. Res., 12, 97 (1984).

$\nu_1 + \nu_3$ intensity, with no other bands included. Finally, an elaborate room temperature model for ν_3 and $\nu_1 + \nu_3$ chemiluminescence has recently been developed by Adler-Golden,⁽²⁶⁾ and gives excellent agreement with laboratory data at pressures in the 0.02 - 2 torr range.

In this section a simple NO_2 IR chemiluminescence model is presented for use at the pressures and temperatures found in the upper atmosphere. The model is used to calculate radiance in the normal atmosphere in the 80 - 135 km range, where comparison can be made with the predictions of both Kofsky⁽²³⁾ and Archer. Since the radiance is proportional to the NO density (all else being equal), the calculation may be extrapolated to the conditions of elevated NO expected in a disturbed atmosphere.

The current model, which utilizes the results of Reference 26, gives essentially the same infrared band emission at laboratory pressures. However, at very low pressures there are factor-of-3 differences for the ν_3 and $\nu_1 + \nu_3$ bands, and furthermore the current model includes new bands (ν_1 and ν_2) not treated previously.

4.2.2 The NO_2 Chemiluminescence Mechanism

The previous modeling efforts⁽²⁶⁾ have shed considerable light on the detailed molecular mechanism of NO_2 chemiluminescence. We summarize below key points relevant to the current upper atmospheric problem.

1. The $\text{NO} + \text{O}$ reaction (either 2-body or 3-body) initially yields an activated complex that possesses approximate energy equipartition between its electronic and vibrational modes. This complex relaxes either radiatively (via continuum emission) or collisionally, with vibrational equipartition maintained in either case as a consequence of chaotic dynamics in the excited electronic ($^2\text{B}_2$) state. In the low pressure (2-body) limit the vibrational distribution immediately following continuum emission is characterized by an average energy of about 5000 cm^{-1} .

26. S. M. Adler-Golden, "The $\text{NO} + \text{O}$ and $\text{NO} + \text{O}_3$ Reactions: I. Analysis of NO_2 Vibrational Chemiluminescence," SSI-TR-112, Spectral Sciences, Inc., under AFGL Contract No. F19628-84-C-0029 (July, 1986) (reproduced in Appendix D). Air Force Geophysics Laboratory Rpt. No. AFGL-TR-87-0223.

2. The $\text{NO} + \text{O}_3$ reaction directly yields NO_2 in vibrational equipartition. The nascent state distribution is close to statistical, with an average energy of about 6000 cm^{-1} . These conclusions are consistent with trajectory calculations⁽²⁷⁾ as well as the shapes and absolute intensities of the continuum and IR band spectra.
3. During collisional relaxation of vibrationally excited NO_2 , equipartition between the ν_1 and ν_3 modes is approximately maintained, resulting in a $\sim 10:1$ ratio of ν_3 to $\nu_1 + \nu_3$ emission. This indicates that ν_1 and ν_3 quanta are collisionally removed with comparable rates. This behavior is consistent with either rapid intermode V-V coupling, or similar V-R,T rates for ν_1 and ν_3 , or, as suggested by studies of vibrational deactivation in other triatomics,⁽²⁸⁻³⁰⁾ a blend of the two mechanisms. No information is available on the relaxation of ν_2 . In triatomics such as O_3 ,⁽²⁸⁾ CO_2 ,⁽²⁹⁾ and OCS ,⁽³⁰⁾ the rate of intermode coupling is roughly comparable to the rate of relaxation of the ν_2 mode, leading to similar effective quenching rates for all 3 vibrational modes. Similar behavior would be expected for NO_2 .
4. $\text{NO}_2(\nu)$ is removed by atomic oxygen at a rate which is close to the $\text{NO}_2 + \text{O}$ reaction rate of $9 \times 10^{-12} \text{ cm}^3 \text{ molec}^{-1} \text{ sec}^{-1}$. Using typical N_2 , O_2 and O atom densities above 100 km altitude, where NO_2 vibrational emission should peak, and assuming NO_2 vibrational relaxation rates measured in the laboratory for N_2 and O_2 ,^(31,32) it is seen that most of the collisional removal of $\text{NO}_2(\nu)$ proceeds via reaction with O atoms rather than relaxation. This means that even if the relaxation assumptions in the previous paragraph are inaccurate, the impact on calculated radiances will not be large.
5. The Einstein A coefficients for emission appear to be consistent with harmonic oscillator scaling rules; i.e., $A \sim \nu$ for fundamental bands. In this approximation, and neglecting overtone and combination bands, the rate constant for radiative removal of energy from a given mode is simply the Einstein coefficient of the $\nu=1$ fundamental. Breakdown in this model may occur with a very weakly emitting mode

-
27. R. Viswanathan and L. Raff, J. Phys. Chem., **87**, 3251 (1983).
 28. S. M. Adler-Golden and J. I. Steinfeld, Chem. Phys. Lett., **76**, 479 (1980).
 29. D. C. Clary, Chem. Phys., **65**, 247 (1982).
 30. M. L. Mandich and G. W. Flynn, J. Chem. Phys., **73**, 1265 (1980).
 31. K. K. Hui and T. A. Cool, J. Chem. Phys., **68**, 1022 (1978).
 32. M. F. Golde and F. Kaufman, Chem. Phys. Lett., **29**, 480 (1974).

such as ν_1 , which may prefer to lose its quanta via the stronger $\nu_1 + \nu_3$ combination band. Fortunately, the effects of this breakdown would be seen only at the very highest altitudes, where even weak bands are collisionally unquenched.

4.2.3. Model Description

The current model employs equations similar to Archer's Eq. (B 4).⁽²⁾

$$I(j) = [NO][O](k_2 + \sum_i k_{3i}[M_i])\phi(j)Q(j) \quad (6)$$

for the NO + O reaction, and

$$I(j) = [NO][O_3]k_1\phi(j)Q(j) \quad (7)$$

for the NO + O reaction, where $I(j)$ is the radiance of band j in photons/cm³ sec, k_1 is the NO + O₃ rate constant, k_2 and k_3 are the 2 body and 3-body NO + O rate constants, $\phi(j)$ is the quantum yield, and $Q(j)$ is the quenching factor, given by

$$Q(j) = A_j / (\sum_i q_i[M_i] + k_0[O] + A_j) \quad (8)$$

where A_j is the Einstein coefficient of band j , q_i is the vibrational quenching rate constant for species M_i , and k_0 is the rate of reaction with O atoms, taken as 1×10^{-11} cm³ molec⁻¹ sec⁻¹.

The rate constants k_1 , k_2 and k_3 have room temperature values given previously.⁽²⁶⁾ The temperature dependences are taken from Sharp⁽³³⁾ for the NO + O reaction, and Borders and Birks⁽³⁴⁾ for the NO + O₃ reaction.

33. W. E. Sharp, Planet. Space Sci., **32**, 257 (1984).

34. R. A. Borders and J. W. Birks, J. Phys. Chem., **86**, 3295 (1982).

Assuming that about 5000 cm^{-1} of vibrational energy is deposited in NO_2 in both reactions, and assuming equipartition among the three vibrational modes, the quantum yields are 1.1, 2.2, and 1.0 for ν_1 , ν_2 , and ν_3 , respectively. q_1 is taken as $5 \times 10^{-13}\text{ cm}^3\text{ molec}^{-1}\text{ sec}^{-1}$ for $M = \text{O}_2$ and 2×10^{-13} for $M = \text{N}_2$.^(31,32) The Einstein coefficients are taken as 110 sec^{-1} for ν_3 , as in Reference 26, and 0.02 sec^{-1} for ν_2 , based on the measured band strength.⁽³⁵⁾ The Einstein coefficient for the very weak ν_1 band is unknown, since a reliable band strength is not available. For the sake of argument we take the value 0.01 sec^{-1} , which probably is an upper limit.

Unfortunately, this model does not provide a simple way to derive effective quantum yields for overtone or combination bands. For the present we shall take the $\nu_1 + \nu_3$ band intensity as 0.1 of the ν_3 intensity, consistent with both experiments and modeling at laboratory pressures. This ratio might change slightly under upper atmospheric conditions, however. We assume that emission from other 2-quantum bands is much smaller than $\nu_1 + \nu_3$ emission, and can be neglected.

The current formulation is fully consistent with the Reference 26 model at laboratory pressures. However, it yields factor-of-3 smaller ν_3 and $\nu_1 + \nu_3$ radiances in the low pressure limit. This is because the Reference 26 model assumes essentially instantaneous intermode vibrational mixing, causing virtually all of the vibrational energy emitted by unquenched molecules to appear in the strong ν_3 band. The present model takes the opposite point of view, and assumes that the energy initially apportioned to each mode (i.e., $1/3$ of the average vibrational energy) cannot be radiated by another mode. This also appears to be the point of view of the WOE spectrum used by Archer. Put another way, the Reference 26 model assumes an effective ν_3 quantum yield 3 times as large, and an effective Einstein coefficient $1/3$ as large. The neglect of intermode mixing in the present model means that the ν_3 radiance may be underestimated and that the predicted ν_1 and ν_2 radiances may be

35. V. M. Devi et al., *J. Mol. Spectrosc.*, **88**, 251 (1981).

overestimated in the low pressure, low O atom limit. However, as explained in paragraph 4 of Subsection 4.2.2, the NO_2 radiance should be fairly insensitive to details of vibrational relaxation at most altitudes.

4.2.4 Results

ν_1 , ν_2 , ν_3 and $\nu_1 + \nu_3$ band radiances were calculated using the altitudes and nighttime O, NO and O_3 densities shown in Table 3 of Kofsky et al. (23) The N_2 and O_2 densities and temperature were taken from the U. S. Standard Atmosphere. (36) The input data are given in Table 3, and the computed radiances are given in Table 4. Integrated zenith and 95 km limb radiances were computed for the ν_3 , $\nu_1 + \nu_3$, and ν_2 bands, and are given in Table 5 in Kofsky's units of $\text{W}/\text{km}^2\text{-sr}$. For the ν_3 and $\nu_1 + \nu_3$ bands these values turn out to be a factor of 3 to 5 lower than Kofsky's. We note that Kofsky assumed slightly different ν_3 and $\nu_1 + \nu_3$ quantum yields, and, more importantly, neglected $\text{NO}_2(\nu)$ quenching and reactive removal as well as temperature dependence of k_2 . Both studies find that the contribution from the $\text{NO} + \text{O}_3$ reaction is negligible at these altitudes.

TABLE 3. ATMOSPHERIC INPUT DATA

Altitude km	$\text{N}_2/\text{cm}^{-3}$	$\text{O}_2/\text{cm}^{-3}$	O/cm^{-3}	$\text{O}_3/\text{cm}^{-3}$	NO/cm^{-3}	T. °K
80	3.0E14	8.1E13	3.E10	2.E8	8.E6	199
90	5.5E13	1.5E13	2.E11	2.E8	1.E7	187
100	9.2E12	2.2E12	5.E11	3.E7	4.E7	195
110	1.6E12	2.6E11	2.E11	2.E6	5.E7	240
120	3.7E11	4.4E10	1.E11	2.E5	3.E7	360
135	8.7E10	8.6E9	4.E10	2.E4	8.E6	517

36. U. S. Standard Atmosphere, 1976, NOAA, Washington, D. C. (October 1976).

TABLE 4. CALCULATED IR BAND RADIANCE (photons/cm³-sec)

<u>NO - O Reaction</u>					<u>NO - O₃ Reaction</u>			
<u>Alt./km.</u>	<u>ν_1</u>	<u>ν_2</u>	<u>ν_3</u>	<u>$\nu_1 + \nu_3$</u>	<u>ν_1</u>	<u>ν_2</u>	<u>ν_3</u>	<u>$\nu_1 + \nu_3$</u>
80	0.0	0.1	12	1.2	0.0	0.0	2	0.2
90	0.3	0.9	37	3.7	0.0	0.1	2	0.2
100	1.6	5.3	92	9.2	0.0	0.1	3	0.3
110	1.6	5.3	31	3.1	0.0	0.1	1	0.1
120	1.9	5.9	17	1.7	0.0	0.1	0	0.0
135	0.7	2.0	3	0.3	0.0	0.0	0	0.0

TABLE 5. CALCULATED COLUMN-INTEGRATED RADIANCE (w/km²-sr)

	<u>ν_2</u>	<u>ν_3</u>	<u>$\nu_1 + \nu_3$</u>
zenith	0.00025	0.005	0.0008
Ref. 2		0.02	0.002
95 km limb	0.008	0.2	0.03
Ref. 2		1.0	0.1

4.2.5 Discussion

Although the present model uses equations similar to Archer's, a very important difference is the use of different Einstein coefficients (hence, different quenching factors) for each band. This results in spectra which are strongly dominated by ν_3 and $\nu_1 + \nu_3$, as predicted by Kofsky et al. The WOE type spectrum assumed by Archer, which shows comparable emission in all bands, is achieved only at the highest altitudes, where the intensity declines rapidly due to the falloff of NO and O densities.

A qualitative explanation for the altitude dependence of the vibrational band radiance in the 100-120 km range is as follows. Because of the large ν_3 Einstein coefficient, this band is essentially unquenched, hence it roughly tracks the $[O][NO]$ product, which peaks at 110 km. On the other hand, the weak ν_1 and ν_2 bands are efficiently removed by O atoms, hence these bands roughly track $[NO]$, which is nearly constant at these altitudes. At lower and higher altitudes different considerations apply. At 135 km all the bands are unquenched. Below 100 km all the bands are quenched, and in addition the 3-body contribution to the $NO + O$ reaction is important.

Since the model takes advantage of laboratory data on the strong ν_3 and $\nu_1 + \nu_3$ bands, the uncertainty in their radiances is low, probably no worse than a factor of 2 for most altitudes. The largest errors probably occur at the highest altitudes, where, for example, $\nu_1 + \nu_3$ may be enhanced by the reservoir of unquenched, unradiated ν_1 quanta, and where ν_3 may be enhanced by energy transfer from the other modes. However, at these altitudes the total chemiluminescence will be limited in any event because of the low densities of NO and O and the finite vibrational energy available from their reaction.

The uncertainty in the ν_2 radiance may be larger, since there is no chemiluminescence data for this band. The uncertainty arises mainly in our estimate of the ν_2 quantum yield, which may lead to an overall uncertainty of perhaps a factor of 4, the lower end of the range being more probable than the higher end because of the possibility of more rapid quenching of ν_2 compared to ν_1 and ν_3 . The calculated ν_1 band radiance is the most speculative of all, and represents an upper limit because of its extremely

small (and unknown) Einstein coefficient, combined with the possibilities of losing ν_1 quanta via alternative channels such as combination band radiation and intermode energy transfer.

In conclusion, while large uncertainties may exist for the radiances of bands other than ν_3 and $\nu_1 + \nu_3$, this is not a serious problem for atmospheric modelers given the extremely small radiances expected.

The ν_3 and $\nu_1 + \nu_3$ band radiances may be combined with typical chemiluminescence band shapes to yield radiances per micron. Since the bulk of the emission arises from high-lying vibrational levels, the bands are broadened and red shifted from the corresponding cold bands, as seen in laboratory data as well as the Reference 26 calculations. Because of the much lower pressures studied here, resulting in radiative cascade as opposed to collisional quenching, the band shapes may be somewhat different than in Reference 26. However, any reasonable guesses of band shapes will yield radiances at least two orders of magnitude weaker than predicted by Archer (who estimated 10^{-10} to 10^{-9} W sr $^{-1}$ μ^{-1} for a 95 km limb view), except perhaps at the peak of the ν_3 band at 6.3 μ , where according to the current model one may expect around 3×10^{-11} W sr $^{-1}$ μ^{-1} .

4.3 NO $_2^*$ Emission Model for Shuttle Ram Glow

4.3.1 Introduction

A number of explanations have been put forward for the visible ram glow off the Space Shuttle.⁽³⁷⁾ Recent measurements by Swenson et al.⁽²⁵⁾ indicate that the glow spectrum is structureless (at 34 Å resolution), suggesting that the emitting species is electronically excited NO $_2$ (NO $_2^*$) formed from NO + O surface recombination. Indeed, the Shuttle glow strongly resembles the spectral distribution obtained in laboratory measurements^(38,39) of NO + O recombination at moderate pressures, although it is shifted slightly to the red. The shape of the NO $_2^*$ spectrum depends

37. B. D. Green and G. E. Caledonia, J. Spacecraft, 22, 500 (1985).

38. A. Pontijn, C. B. Meyer, and H. I. Schiff, J. Chem. Phys., 40, 64 (1964).

39. M. Sutoh, Y. Morioka, and M. Nakamura, J. Chem. Phys., 72, 21 (1980).

on its state distribution, and therefore varies according to the mechanism by which it is produced, and the degree of relaxation present. The red shift of the Shuttle glow spectrum would imply that the NO_2^* energy distribution is colder in the Shuttle glow than it is in the laboratory, presumably due to rapid energy accommodation on the tile surface.

This section describes the results of a model calculation of the NO_2^* nascent distribution required to simulate the observed Shuttle glow spectrum. From the state distribution one can calculate additional quantities which have not yet been measured: 1. the effective lifetime of emission at a particular wavelength; 2. the shape of the near IR portion of the spectrum; and 3. the quantity of IR band radiation from vibrationally excited NO_2 . From the emission lifetime and the known spatial extent of the visible glow (around 20 cm⁽⁴⁰⁾) one can estimate the mean velocity of desorption from the surface, which may also be expressed as a translational temperature.

4.3.2 Spectral Modeling

The calculation makes use of an empirical expression for the NO_2^* continuum spectrum,*

$$I_\nu = \frac{5 \times 10^{-4} (E - 10000 - 3.2 \times 10^{-5} (\nu - 4000)^2)^{5/2} \nu^3}{(E - 10000)^3 (1 + 1.4 E^2 / (E - 9000)^2)} \quad (9)$$

where I_ν is the emission intensity in photons sec⁻¹ per cm⁻¹, ν is frequency in cm⁻¹, and E is the (vibrational) excitation energy in cm⁻¹. It is assumed that the states identified as NO_2^* are those having $E \geq 11000$ cm⁻¹; thus, lower energy states emit solely in IR vibrational bands. I_ν is converted to I_λ , intensity per Å⁰, by multiplying by $10^{-8} E^2$. This expression has been used successfully to simulate a wide range of

40. J. H. Yee and A. Dalgarno, AIAA-83-CP838, AIAA Shuttle Environment and Operations Meeting, 2660 (1983).

41. This expression is an earlier version of Eq. (3) in Ref. 42, but gives similar results.

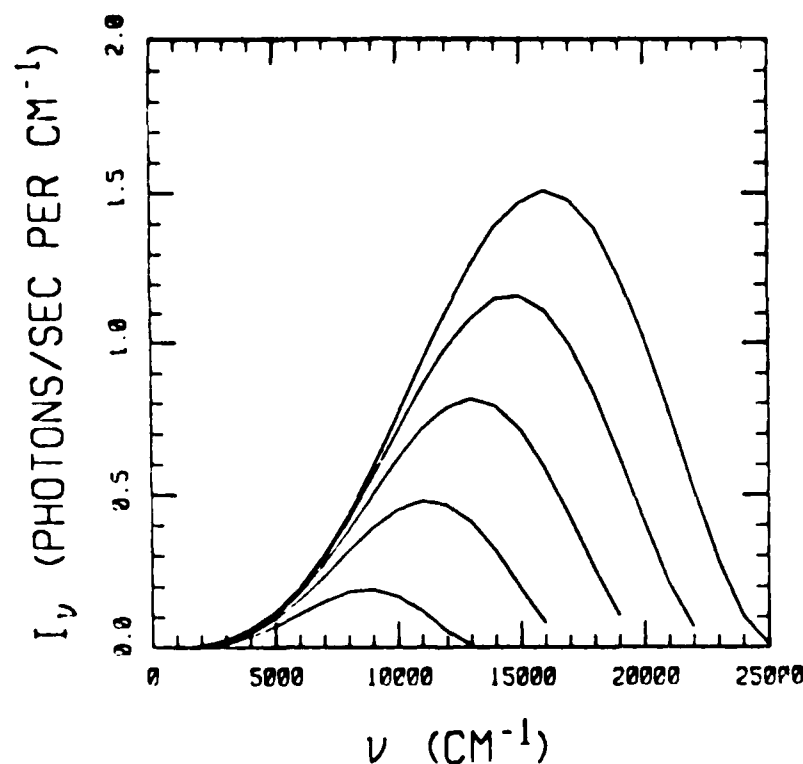


Figure 1. NO_2 Continuum Spectral Intensity as a Function of Excitation Energy, E . In Order of Increasing Intensity, $E = 13000, 16000, 19000, 22000$, and 25000 cm^{-1} .

laboratory NO_2^* spectra, including spectra of $\text{NO} + \text{O}$ chemiluminescence, NO_2^* laser-induced fluorescence, $\text{NO} + \text{O}_3$ chemiluminescence, and NO_2 thermal emission.⁽⁴¹⁾ The dependence of I_ν on energy E is shown in Figure 1, where it is seen that both the absolute intensity and the peak frequency are rapidly increasing functions of E .

For the sake of simplicity the nascent distribution $[\text{NO}_2(E)]$ was taken as a temperature distribution, and the classical harmonic oscillator density of states ($\sim E^2$) was used.

41. S. M. Adler-Golden, "The $\text{NO} + \text{O}$ and $\text{NO} + \text{O}_3$ Reactions: II. Analysis of NO_2 Continuum Chemiluminescence," SSI-TR-111, Spectral Sciences, Inc., under AFGL Contract No. F19628 84-C-0029 (July, 1986) (reproduced in Appendix E). Air Force Geophysics Laboratory Rpt. No. AFGL-TR-87-0223.

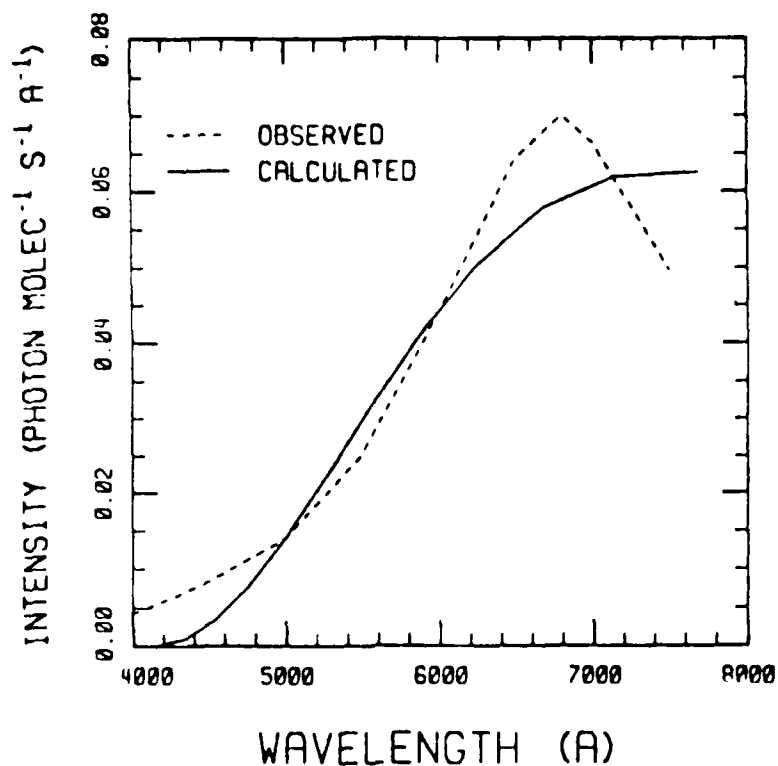


Figure 2. Calculated and Observed (Reference 25) Tile Surface Spectrum; The Observed Spectrum has been Scaled to Match the Calculation.

Overall agreement with the spectrum observed at the tile surface⁽³⁵⁾ was best for T-3500 K; the result is shown in Figure 2, where for the purpose of comparison the Shuttle spectrum has been scaled to match the units of the calculation. Judging from the sensitivity of the spectral shape to temperature, the temperature uncertainty is estimated to be 1000 K. The sharp falloff beyond ~7000 Å in the observed spectrum cannot be matched for any NO₂* state distribution, even if a non-thermal distribution is assumed. However, we note that the measured spectrum was not corrected for transmission of the window, which became fouled during the flight. A preliminary analysis of starlight spectra by Green⁽⁴²⁾ confirms a falloff in window transmission at long wavelengths.

42. B. D. Green, private communication.

4.3.3 Field-of-View Effects

As pointed out by Swenson et al., the ram glow spectrum will vary with viewing geometry if there is a wavelength variation in the radiative lifetime of the emitting species. To simulate the effects of different fields of view, we incorporated Equation (9) in a steady-state continuum model similar to that of Reference 42. In this model the NO_2^* is formed in the 3500 K nascent distribution and is removed with a first order rate constant k_1 corresponding to the rate of passage out of the field of view. The resulting spectral intensity $I(k_1)$ is given in units of photons/ cm^{-1} per molecule. The tile surface spectrum shown in Figure 1 is recovered by taking the product $I(k_1)k_1$ in the limit of large k_1 , i.e., where k_1 exceeds the fastest radiative rate.

In the $k_1 = 0$ limit, $I(k_1)$ may be interpreted as the spectrum seen from a distance when viewing the entire spacecraft, that is, the spectrum integrated over the full emitting volume. The resulting spectrum, denoted $I(0)$, is shown in Figure 3 along with the tile surface spectrum; the calculation displays the IR as well as visible wavelengths. $I(0)$ is red shifted from the tile surface spectrum because the large field of view gives the lower energy, longer lifetime states the full opportunity to emit. This red shift is especially pronounced in the NO_2 molecule because of the large variation in radiative lifetimes with excitation energy, although some shift is expected for any emitting species due to the ν^3 factor which enters into Einstein coefficients. While a spectral dependence on viewing geometry was indeed anticipated by Swenson et al., they incorrectly predicted a blue shift rather than a red shift.

4.3.4 Radiative Lifetimes

NO_2^* emission at a given wavelength can originate from many different states with a range of radiative lifetimes. However, it is shown here that one may derive a meaningful single "effective" lifetime, τ , for a given wavelength, resulting in a greatly simplified glow model.

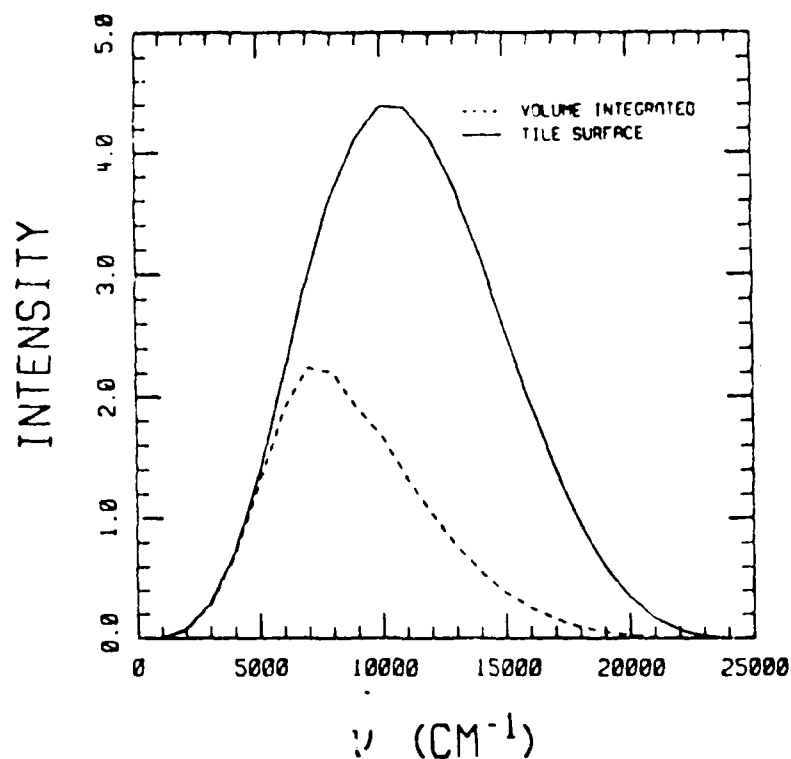


Figure 3. Comparison of Tile Surface Spectrum (in Units of 10^{-2} Photon Molec $^{-1}$ sec $^{-1}$ per cm^{-1}) and Volume-Integrated Spectrum (in Units of 10^{-5} Photon Molec $^{-1}$ per cm^{-1}).

Our approach is to apply a Stern-Volmer analysis to the kinetics, yielding

$$I(k_1)/I(0) = \frac{1/\tau}{1/\tau + k_1} \quad (10)$$

where $I(k_1)$ is the steady state intensity at a given wavelength and $I(0)$ is the volume integrated intensity at the same wavelength. Equation (10) allows τ to be defined for a given wavelength and k_1 value. We need to show that τ is only weakly dependent on the k_1 value chosen. For our first estimate of τ (Method 1) we choose k_1 as the value required to halve $I(0)$:

then $\tau = 1/k_1$. For our second estimate of τ we note that Equation (10) yields $I(k_1)k_1 = I(0)/\tau$ in the large k_1 limit. Thus, Method 2 is to define τ as the ratio of the volume integrated spectrum to the tile surface spectrum. Since the τ values computed by both methods (Table 6) are found to agree reasonably with each other, the effective lifetime is indeed a meaningful concept.

TABLE 6. EFFECTIVE RADIATIVE LIFETIMES $\tau(\lambda)$ (msec)

λ (μ)	Method 1	Method 2
2.00	1.1	0.94
1.43	1.1	0.75
1.00	0.49	0.38
0.77	0.25	0.21
0.63	0.14	0.13
0.50	0.084	0.084

4.3.5 Continuum and Vibrational Band Intensities

Predicted total continuum and IR vibrational band emission intensities (integrated over all wavelengths) were obtained from the steady-state model, and are given in Table 7 for the tile surface spectrum. It has been assumed that the 3500 K nascent distribution is valid for all NO_2 energies, and thus describes vibrationally excited NO_2 as well as NO_2^* . Since this assumption has not been proved, the IR band intensities should be taken with a grain of salt. However, if these results are qualitatively correct, the ν_3 band intensity should be of the same order as the total intensity of the visible portion of the surface glow.

The volume- and wavelength-integrated continuum intensity may be derived from Figure 3, which yields about 0.15 photon/molecule. This is close to the fractional NO_2 population at 3500 K having vibrational energy of at least $11,000 \text{ cm}^{-1}$, the approximate lower limit of excitation required for continuum emission. The volume integrated vibrational band intensities are difficult to calculate accurately, as they require a good model for radiative cascade of $\text{NO}_2(v)$ under nearly collision-free conditions.

TABLE 7. ABSOLUTE INTENSITIES (Photons/Molec per sec) OF CONTINUUM AND IR BAND EMISSION

Total continuum	430.
ν_3	120.
$\nu_1 + \nu_3$	14.

However, as discussed in Subsection 4.2, the strong ν_3 mode may be modeled reasonably well assuming stepladder radiative cascade with a radiative loss rate of 110 sec^{-1} . Combining this radiative rate with the tile surface intensity given in Table 7 yields 0.13 ν_3 photon/molecule.

4.3.6 Discussion

The Shuttle glow spectrum was previously analyzed in terms of NO_2 recombination by Swenson et al. (25) and Kofsky and Barrett. (24) Swenson et al. assumed an NO_2^* lifetime of 70 μsec , leading to a translational temperature of $\sim 10,000 \text{ K}$ from the known spatial extent of the glow in the visible region. The current calculation favors a longer lifetime; if we take the average lifetime in the visible region to be represented by $\lambda \sim 6000 \text{ \AA}$, then from Table 6 $\tau \sim 120 \mu\text{sec}$. This longer lifetime yields a desorption velocity of about 1.7 km/sec, corresponding to a translational temperature not very different from the vibrational temperature of 3500 K.

The current calculation predicts about one ν_3 photon per continuum photon, a factor of 3 smaller than predicted by Kofsky and Barrett. However, these predictions are rather uncertain and, furthermore, additional IR radiation in the vicinity of the Shuttle may be generated if unexcited NO_2 , which would make up the bulk of the NO_2 formed, is capable of collisional pumping by incoming O atom flux.

It is hoped that the current predictions of the emission lifetime, near IR spectrum, and IR band spectrum will be helpful in determining whether NO_2^* is indeed the true source of the Shuttle glow.

5. CONCLUSIONS

As described in greater detail in Section 2, the main results of the analytical program were the calculation of accurate Einstein coefficients for emission from vibrationally excited ozone, and the development of a quantitative model for NO_2 infrared chemiluminescence in the upper atmosphere. These results should have sufficient accuracy for current atmospheric modeling needs. We do not believe that significant improvements are possible using theoretical techniques alone, and would instead recommend experimental studies if better accuracy or increased confidence is required in the future. In addition, byproducts of this program, which include improved techniques and computer codes for vibrational states of small molecules, an NO_2 continuum model, and a model for the Shuttle ram glow, will be applicable to other upper atmospheric radiation problems.

6. REFERENCES

1. W. T. Rawlins, G. E. Caledonia, J. J. Gibson, and A. T. Stair, Jr., J. Geophys. Res., 90, 2896 (1985).
2. D. H. Archer, "Requirements for Improved Infrared Prediction Capability: LWIR," Mission Research Corporation, Rpt. No. MRC R-583, DN5471F (1980).
3. W. T. Rawlins and R. A. Armstrong, "COHISE Observations of O_3 Formed by Three Body Recombination of O and O_2 ," Rpt. No. AFGL-TR-82 0273, Air Force Geophysics Laboratory, Hanscom AFB, MA (1982). ADA123653
4. W. T. Rawlins and R. A. Armstrong, "Dynamics of Vibrationally Excited Ozone Formed by Three-Body Recombination. I: Spectroscopy," to be submitted.
5. W. T. Rawlins, G. E. Caledonia, and R. A. Armstrong, "Dynamics of Vibrationally Excited Ozone Formed by Three-Body Recombination. II: Kinetics and Mechanism," to be submitted.
6. S. M. Adler-Golden and G. D. Carney, Chem. Phys. Lett., 113, 582 (1985).
7. S. M. Adler-Golden, S. R. Langhoff, C. W. Bauschlicher, Jr., and G. D. Carney, J. Chem. Phys., 83, 255 (1985).
8. S. M. Adler-Golden, "Predicted NO_2 IR Chemiluminescence in the Natural Atmosphere," AFGL-TR-86-0099, Air Force Geophysics Laboratory, Hanscom AFB, MA (1986). ADA173812
9. S. M. Adler-Golden, J. Phys. Chem., 89, 964 (1985).
10. G. D. Carney, S. M. Adler-Golden, and D. C. Leseski, J. Chem. Phys., 84, 3921 (1986).
11. A. T. Stair, Jr., R. D. Sharma, R. M. Nadile, D. J. Baker, and W. F. Grieder, J. Geophys. Res., 90 (1985) 9763.
12. B. F. Gordiets, Yu. N. Kulikov, M. N. Markov, and M. Ya. Marov, J. Geophys. Res., 87 (1982) 4504.
13. W. T. Rawlins, J. Geophys. Res., 90, 12283 (1985).
14. D. Cropek and G. D. Carney, J. Chem. Phys., 80, 4280 (1984).
15. G. D. Carney, "Vibration Energies and Wavefunctions for Bent Triatomic Molecules," and D. Cropek, "A Numerical Variational Method for Calculating Vibrational Energies of Bent Triatomic Molecules," Allegheny College, Meadville, PA (1983).

16. G. D. Carney, L. L. Sprandel, and C. W. Kern, "Variational Approaches to Vibration-Rotation Spectroscopy for Polyatomic Molecules," Adv. Chem. Phys., 37 (1978).
17. G. Simons, R. G. Parr and J. M. Finlan, J. Chem. Phys., 59, 3229 (1973).
18. A. Barbe, C. Secroun, and P. Jouve, J. Molec. Spectrosc., 49, 171 (1974).
19. G. D. Carney, L. A. Curtiss, and S. R. Langhoff, J. Molec. Spectrosc., 61, 371 (1976).
20. G. D. Carney, S. Giorgianni, and K. N. Rao, J. Molec. Spectrosc., 80, 158 (1980).
21. B. T. Darling and D. M. Dennison, Phys. Rev., 57, 128 (1940).
22. T. L. Stephens, General Electric-TEMPO (1979), cited in Reference 2.
23. I. L. Kofsky, J. L. Barrett, and L. McVay, "Infrared Radiance Structure of the Aurora and Airglow," AFGL-TR-82-0220, Air Force Geophysics Laboratory, Hanscom AFB, MA (1982). ADA130468
24. I. L. Kofsky and J. L. Barrett, Journal of Spacecraft and Rockets, 24 2 (1987).
25. G. R. Swenson, S. B. Mende, and K. S. Clifton, J. Geophys. Res., 12, 97 (1984).
26. S. M. Adler-Golden, "The NO + O and NO + O₃ Reactions: I. Analysis of NO₂ Vibrational Chemiluminescence," SSI-TR-112, Spectral Sciences, Inc., under AFGL Contract No. F19628-84-C-0029 (July, 1986). Air Force Geophysics Laboratory Rpt. No. AFGL-TR-87-0223. (reproduced in Appendix D).
27. R. Viswanathan and L. Raff, J. Phys. Chem., 87, 3251 (1983).
28. S. M. Adler-Golden and J. I. Steinfeld, Chem. Phys. Lett., 76, 479 (1980).
29. D. C. Clary, Chem. Phys., 65, 247 (1982).
30. M. L. Mandich and G. W. Flynn, J. Chem. Phys., 73, 1265 (1980).
31. K. K. Hui and T. A. Cool, J. Chem. Phys., 68, 1022 (1978).
32. M. F. Golde and F. Kaufman, Chem. Phys. Lett., 29, 480 (1974).
33. W. E. Sharp, Planet. Space Sci., 32, 257 (1984).

34. R. A. Borders and J. W. Birks, J. Phys. Chem., 86, 3295 (1982).
35. V. M. Devi et al., J. Mol. Spectrosc., 88, 251 (1981).
36. U. S. Standard Atmosphere, 1976, NOAA, Washington, D. C. (October 1976).
37. B. D. Green and G. E. Caledonia, J. Spacecraft, 22, 500 (1985).
38. A. Fontijn, C. B. Meyer, and H. I. Schiff, J. Chem. Phys., 40, 64 (1964).
39. M. Sutoh, Y. Morioka, and M. Nakamura, J. Chem. Phys., 72, 21 (1980).
40. J. H. Yee and A. Dalgarno, AIAA-83-CP838, AIAA Shuttle Environment and Operations Meeting, 2660 (1983).
41. S. M. Adler-Golden, "The NO + O and NO + O₃ Reactions: II. Analysis of NO₂ Continuum Chemiluminescence," SSI-TR-111, Spectral Sciences, Inc., under AFGL Contract No. F19628-84-C-0029 (July, 1986) (reproduced in Appendix E). Air Force Geophysics Laboratory Rpt. No. AFGL-TR-87-0223.
42. B. D. Green, private communication.

CHAPTER II

LABCEDE

TABLE OF CONTENTS

<u>Section</u>	<u>Page</u>
1. INTRODUCTION	II-1
2. EXPERIMENTAL TECHNIQUE	II-3
2.1 Steady State Measurements	II-3
2.2 Transient Measurements	II-6
2.3 Absorption Signal Detection	II-7
3. EXPERIMENTAL MEASUREMENTS	II-12
3.1 Observed Steady State Signals	II-12
3.2 NO Removal by Beam Created Species	II-18
3.3 Transient Measurements	II-21
3.4 Signal to Noise	II-21
4. MODEL OF NO PRODUCTION	II-25
4.1 Ionization by Electron Beam	II-25
4.2 Effects of Diffusion and Flow	II-28
4.3 Chemistry in the LABCEDE Chamber	II-30
5. SIMULATION RESULTS AND DISCUSSION	II-41
5.1 Simulations of NO Formation	II-41
5.2 Simulations of NO Titration	II-48
5.3 Other Effects Not in the Model	II-49
6. SUMMARY AND CONCLUSIONS	II-56
7. REFERENCES	II-58

LIST OF ILLUSTRATIONS

<u>Figure</u>	<u>Page</u>
1. Schematic Design of LABCEDE Tunable Diode Laser Absorption Arrangement	II-4
2. Typical Chart Recording of Second Derivative Spectra Due to NO	II-13
3. Variation of NO Produced with O ₂ Pressure; Normalized to 1 mA Beam Current	II-14
4. Scaling of NO Column Density with Beam Current	II-15
5. Variation of NO Build Up with O ₂ Pressure Using .75 mA Beam Current	II-16
6. The Effect of Electron Beam Duty Cycle on the NO Produced	II-17
7. NO Absorption Signal When Electron Beam is Turned On and Off	II-18
8. Variation of NO Concentration with Beam Current, Normalized to 100 When Beam is Off	II-19
9. NO Reappearance After Beam Shut Off From 1 mA	II-20
10. Normalized Point Intensity Profile Versus r/L for Given Z/L from Cohn and Caledonia ⁽¹²⁾	II-27
11. Simulated Concentrations of Beam Coated Species after Steady State has been Established	II-42
12. Same as Figure 11 Except $\eta = .50$	II-43
13. Change in NO ($v = 0$) Concentration with Time Displayed with Expanded Density Scale of Figure 10	II-44
14. Change in NO ($v = 0$) Concentration with Time Expanded Scale from Figure 12	II-46
15. Comparison of NO Column Density Using $\eta = .50, .55$ and .60 to Data Points from Figure 5	II-47
16. Simulation of the NO Morphology for a .5 mA Electron Beams Irradiating 5.5 m torr NO in 55 torr N ₂	II-48

1. INTRODUCTION

Nitric oxide in the upper atmosphere both during quiescent and disturbed conditions form a major source of infrared radiation in the 2.7 to 3.3 μm and the 5.3 to 6 μm bands.^(1,2) When electrons interact with the natural atmosphere, ionization forms odd nitrogen in the form of $\text{N}(^2\text{P})$, $\text{N}(^2\text{D})$ and $\text{N}(^4\text{S})$ which in turn react with atmospheric oxygen to produce NO in vibrationally excited states. The emission of these chemiluminescent NO molecules provide a major source of infrared emission in the disturbed atmosphere. Once produced, the NO can either react with other species, or be pumped up into high vibrational levels by atomic O to provide more radiation. The amount of NO formed during the production reactions is of vital importance in the morphology of subsequent chemistry as even a small mixing ratio of NO would greatly change the ion composition during a nuclear disturbance. Since the chemiluminescent reaction could be a small fraction of the total formation of NO, the measurement of production NO in the vibrational ground state was attempted. This production rate is in turn found to be highly dependent on the imbalance of $\text{N}(^2\text{D})$ to $\text{N}(^4\text{S})$ formed in the interaction of electrons and N_2 .

The total NO formed due to continuous dosing of the atmosphere reaches a steady state concentration at which point the formation of NO just balances the removal. Since atomic nitrogen is both the main formation and the main removal channel for NO, the equilibrium NO concentration measures the ratio of the reaction rates times the relative production rate of doublet nitrogen to quartet nitrogen.

Measurements were carried out in the small LABCEDE facility to determine the amount of ground state NO formed by electron beam bombardment of N_2 and O_2 . Since the total production of NO in the $v = 1$ through 13

1. W. P. Reidy, T. C. Degges, A. G. Hurd, A. T. Stair, Jr., and J. C. Ulwick, "Auroral Nitric Oxide Concentration and Infrared Emission," J. Geophys. Res., **87**, 3591 (1982).
2. G. E. Caledonia and J. P. Kennealy, "NO Infrared Radiation in the Upper Atmosphere," Planet. Space Sci., **30**, 1043 (1982).

vibrational levels has been determined through emission.^(3 6) the corresponding fractional production of NO in the ground vibrational state would complete the picture of the interaction of electrons with the atmosphere. The amount of NO formed in the tank is measured in absorption by monitoring the the absorption of a single rotation line in the $v = 0$ level. This signal is proportional to all of the NO formed in the $v = 0$ level plus all of the NO cascading to this level. The steady state concentration of NO within the tank is a measure of the NO which can contribute to interpretation of the data during both transient absorption and emission measurements. Since the beam produced NO may participate in both the kinetics and the subsequent emission, its absolute concentration within the chamber must be determined. The transient build up of NO during the electron beam pulse is also of importance in determining the total branching ratio for NO formation mechanisms.

The following sections will describe the measurements carried out in LABCEDE. The experimental technique is described in Section 2. Section 3 describes the measurements made, Section 4 presents a model of the observations, and Section 5 presents a comparison of the model to the experimental results. Section 6 presents the summary and conclusions.

3. B. D. Green, G. E. Caledonia, and R. E. Murphy, "A Determination of the Nitric Oxide Einstein Coefficient Ratios," J. Quant. Spectrosc. Radiat. Transfer, 26, 215 (1981).
4. B. D. Green, G. E. Caledonia, L. G. Piper, J. S. Goela, A. Fairbairn, and R. E. Murphy, "LABCEDE Studies," Air Force Geophysics Laboratory Rpt. No. AFGL-TR-82-0060 (September 1981). ADA114389
5. B. D. Green, G. E. Caledonia, R. E. Murphy, and F. X. Robert, "The Vibrational Relaxation of NO($v=1,7$) by O_2 ," J. Chem. Phys., 76, 2441 (1982).
6. B. D. Green, L. G. Piper, G. E. Caledonia, P. F. Lewis, H. C. Murphy, and W. J. Marinelli, "Fluorescence from Electron Irradiated Gases in Refurbished Labcede," Air Force Geophysics Laboratory Rpt. No. AFGL TR 84 0218 (September 1985). ADA161674

2. EXPERIMENTAL TECHNIQUE

Measurements of NO absorption were made using a Spectra Physics PbSse diode laser in the small LABCEDE facility at the Air Force Geophysics Laboratory. These measurements were done in two phases; steady state measurements averaging over a pulsed electron beam excitation, and transient measurements attempting to see the build up of NO with time during a single electron beam pulse. While these measurements used essentially the same apparatus, different techniques were used to extract the information. Limits are placed on the total sensitivity of each measurement.

2.1 Steady State Measurements

The experimental arrangement for measuring the total steady state build-up of NO in the test chamber due to continuous operation of the electron beam is shown in Figure 1. The light from a lead salt tunable diode laser is directed through a monochromator to select a single laser frequency mode and then directed through the LABCEDE test chamber. The laser light is reflected off of a spherical mirror with 30 cm. radius of curvature in back of the chamber, directed back through the test chamber and brought to focus on a HgCdTe detector. A ZnSe flat is placed in the path between the monochromator and steering optics in order to introduce a visible laser beam for alignment. This flat allows approximately 60% of the light to reach the LABCEDE chamber, while redirecting 40% of the light into a reference cell filled with pure NO. This cell is used to identify the laser absorption feature to be measured in the test chamber. The actual line being studied was identified by comparing the monochromator position to positions of NO lines measured by Amiot et al.⁽⁷⁾ The HgCdTe detector could be moved to behind this reference cell to provide

7. C. Amiot, R. Bacis, and G. Guelachvili, "Infrared Study of the $X^2\Pi_v = 0, 1, 2$ Levels of $^{14}\text{N}^{16}\text{O}$. Preliminary Results on the $v = 0, 1$ Levels of $^{14}\text{N}^{17}\text{O}$, $^{14}\text{N}^{18}\text{O}$, and $^{15}\text{N}^{16}\text{O}$," Can. J. Phys., 56, 251 (1978).

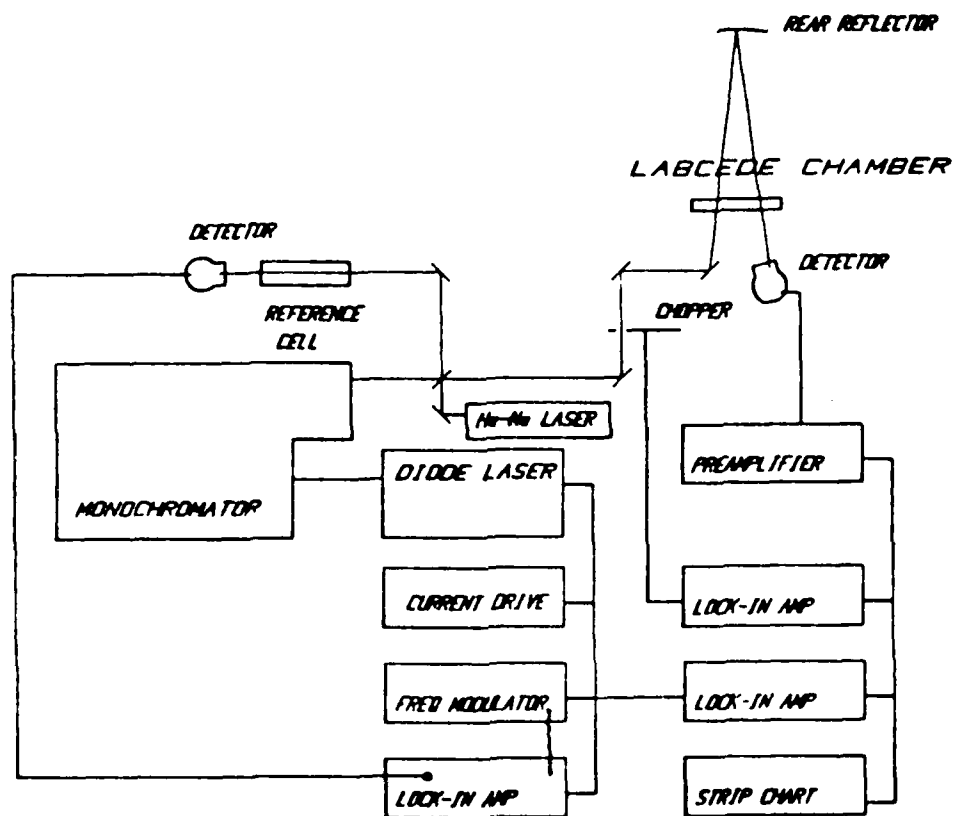


Figure 1. Schematic Design of LARCEDE Tunable Diode Laser Absorption Arrangement.

measurements of Doppler and collisional line widths of the NO line of interest under known steady state conditions. Provision was made to swing the ZnSe beam splitter out of the field of view to recover the 40% light lost during He-Ne laser alignment.

The double pass of the laser light formed a 40 cm absorption path within the test chamber. In order to gain sensitivity for detecting very weak transient signals within the chamber, a 40 pass White cell design was introduced into the chamber for some of the measurements. The added path allowed for the additional sensitivity necessary to measure the $v = 1$ to $v = 2$ transitions of NO in order to tie the absorption measurements to

emission measurements made previously in the same facility. Disturbances to the flow within the system, as well as etalons formed by the overlap of imaged laser light within the the White cell, however, limited the usefulness of this approach.

The output of this detector is amplified and fed into a lock in amplifier which is phase locked to the frequency scan rate of the laser. The signal from the detector is also fed into a storage oscilloscope. This allowed for sampling of the beam intensity during each run. Absorption measurements are made within the chamber by current tuning the diode laser through the absorption feature.

By modulating the laser at half the detection lock-in frequency, the curvature, or second derivative, of the absorption feature was determined. This second derivative signal is particularly sensitive to sharp spectral features, and forms a good rejection for wavelength dependent intensity variations as introduced by the monochromator slit function. Since the second derivative signal is directly proportional to the direct absorption signal when the absorption is small, the steady state NO concentration can be related to its absorption coefficient and determined by observing a single vibration-rotation line. The assumption being that the state is in rotational thermal equilibrium.

A gain factor is introduced because the lock-in amplifier does not actually take the second derivative, but instead compares the laser intensity at the detector at two relatively close frequency locations. The second harmonic signal from the lock-in is thus also a function of the modulation depth, a function of how much the signal changes between the in phase and out of phase components. Because the rate of change in intensity is large, it is impractical to measure the exact frequency change that the laser tunes through to determine the modulation depth. This problem is gotten around by introducing a known, calibrated, concentration of NO in a background of N_2 , to provide the proper collisional broadened line shape, into the absorption path and comparing the measured concentrations to this standard.

The absorption signal is also a function of the total light intensity when there is no absorption. Since the second derivative was used for the primary measurement, the determined concentration was not a function of the change in intensity, but only to the intensity itself. This absorption free laser intensity was gotten by measuring on the two sides of the absorption feature and interpolating to the line center. The intensity was measured simultaneously to the second derivative when there was less than

1% absorption by chopping the laser signal and feeding the resultant chopped signal into a second lock in amplifier. This signal, phase locked to the chopper frequency, provided an instantaneous monitor of the laser intensity. Since the laser intensity appeared to change only a few percent over a period of minutes, this chopper was often turned off in the open position during absorption measurements within the tank, in order to increase the duty cycle of the measurements.

2.2 Transient Measurements

The experimental arrangement for measuring the transient build-up of NO in the vicinity of the ionization region in LARCEDE was essentially the same as shown in Figure 1 except all three lock-in amplifiers are used simultaneously. The light passing through the reference cell is directed into a second HgCdTe detector whose signal is fed into a lock-in amplifier. For making transient measurements, this signal is used to wavelength lock the laser so that it scans only across the absorption feature. This is accomplished through a current feedback loop, based on taking the phase sensitive output from the lock-in amplifier and reintroducing it into the laser, thus modulating the laser into the peak of the absorption feature.

Since the phase sensitive detector compares the signal at zero phase with that at 180° , the voltage output from this detector is proportional to the mismatch of the absorption cross section at a wavelength shorter than the center of the absorption feature to the absorption cross-section at a wavelength longer than the center frequency, giving a first derivative signal. This resulting waveform goes to zero when the cross-sections on the two sides of the maximum absorption are exactly equal, corresponding to the zero slope at the line center. This phase sensitive output voltage is used as an error voltage and added to the current drive of the laser, such that that the laser tunes to a wavelength to exactly balance the cross-sections at either end of of the absorbing line. The resulting error voltage would then be identically zero, preventing further tuning the laser. By modulating the laser at a frequency which is much higher than most noise components, the laser is made to sit at the absorption maximum. In practice, the modulation frequency was limited to 2 kHz due to the

hysteresis in the diode frequency response. This is sufficient to compensate for all drifts in laser frequency on a 100 ms time scale or longer. The laser would remain phase locked to the NO absorption for periods of hours.

The laser light passing through the test chamber was modulated by changes in the absorption signal. This change is due to two effects; frequency modulation across the absorption feature and change in the total NO concentration within the tank. Thus, by modulating the electron beam, changes in absorption which are in phase with the electron beam would be due only to the transient increase in NO. The steady state concentration of NO in this chamber was measured by locking the absorption signal onto the laser modulation frequency. The fractional change in signal across the absorption line is then compared to the total throughput intensity of the electron beam. This absorption was then compared to the absorption signal seen when a reference amount of NO introduced into the test chamber. By locking into the phase of the pulsed electron beam, multiple transient measurements of NO production can be summed. If the laser modulation is also locked to the electron beam pulse, the transient NO concentration would be measured by comparing successive electron beam pulses on a transient recorder, thus increasing the signal to noise ratio.

There are several sources of noise which limit the signal to noise of this experimental arrangement, hence the ultimate sensitivity of measuring the instantaneous production of NO in the ground state. These are discussed below.

2.3 Absorption Signal Detection

The measurement of the absorption by a single vibration-rotation line of NO within the LABCEDE facility could be easily converted into a concentration of NO ($v = 0$) within the test chamber. The direct absorption signal is given by the Bouguer-Lambert law

$$\frac{I_v}{I^0_v} = \exp\left[-\int_0^L \alpha_v dx\right] \quad (1)$$

where I and I^0 are the transmitted and incident intensities, respectively, and α_ν is the absorption per unit path at frequency ν , x is the distance along the absorption path and L is the total path length. The absorption α_ν is equal to the absorption cross-section σ times a number density of absorbers N :

$$\alpha_\nu(x) = [N_l(x) - N_u(x)]\sigma_\nu \quad (2)$$

where N_l and N_u are the number densities of the absorbers in the the absorbing level and in the level that they move into, respectively. These densities are functions of distance along the absorption path x . The absorption cross section σ_ν for a vibration rotation line can be related to its integrated line strength and its line width.

The Doppler broadened absorption cross section is related to the integrated line strength by the expressions

$$\sigma = \sigma^0 \exp\left[-\frac{\Delta\omega^2 \ln 2}{b_D^2}\right] \quad (3)$$

and

$$\sigma^0 = \frac{S}{b_D} \sqrt{\ln 2 / \pi} \quad (4)$$

where σ^0 is the cross section at line center, S is the integrated line strength in cm , and b_D is the Doppler half width equal to

$$b_D = \sqrt{2 \ln 2 k T / m c^2} \omega_{ul} = 3.58 \times 10^{-7} \sqrt{T/M} \omega_{ul} \text{ (cm}^{-1}\text{)} \quad (5)$$

where T is the temperature in degrees Kelvin, ω_{ul} is the frequency of the transition, and M is the molecular weight of NO, equal to 30. For the $P_{22}(8.5)$ line the line strength at low pressure is calculated to be $.9 \times 10^{-17} \text{ cm}^2$ for each of the two lines in the A split doublet.⁽⁸⁾ The

8. P. K. Falcone, R. K. Hanson, and C. H. Kruger, "Tunable Diode Laser Measurements of the Band Strength and Collision Halfwidths of Nitric Oxide," J. Quant. Spectrosc. Radiat. Transfer, 29, 205 (1983).

observed line intensity is given by $\sigma = \sigma_1(\nu) + \sigma_2(\nu)$. Since these two lines are separated by only 30 MHz, the full Doppler broadened lines lie on top of each other, and would appear as a single line with the absorption cross section of $1.8 \times 10^{-17} \text{ cm}^{-1}$. At a total pressure of 1 torr, a 1% change in intensity at line center is equivalent to a partial pressure of 0.43 μtorr NO over the 40 cm absorption pathlength at 298 K.

The signal due to NO absorption is dependent on total pressure in the tank, as the line width changes from the Doppler limit to collisional limit in going from 1 torr to 50 torr total pressure. At 50 torr the absorption at line center is thus $\sigma^0 = S/\pi b_c$, where b_c is the collisional half width. The collisionally broadened absorption cross section is given by

$$\sigma_c = \frac{S b_c}{\pi(\Delta\omega^2 + b_c^2)} \quad (6)$$

where $\Delta\omega$ is the distance from line center. The collisional half width was experimentally measured by fitting the line shape in the reference cell at the appropriate pressure. Thus, at a cell pressure of 50 torr, this line width was measured to be $2b_c = 0.0072 \text{ cm}^{-1}$, corresponding to a collisional line width of $2b_c = 0.109 \text{ cm}^{-1} \text{ atm}^{-1}$. Combining Equations (4) and (6), the line center cross-section at 50 torr is

$$\sigma_c^0 = \sigma_D^0 \times \frac{b_D}{b_c(\pi \ln 2)} \quad (7)$$

This cross section is thus a factor of 4.5 lower at 50 torr than at one torr. Because the line width is larger at 50 torr, there is also an accompanying apparent line shift due to the fact that the absorption feature is actually a doublet. While the center position of each line in the doublet is constant, the adding of their absorption half-widths in the spectral region between the lines introduces some asymmetry to each line shape. This effect is particularly important in the ${}^2\Pi_{1/2} \rightarrow {}^2\Pi_{1/2}$ transitions where the A splitting is on the order of 300 MHz, or 0.01 cm^{-1} , comparable to twice the collisional line-width.⁽⁹⁾ Here, the contributions

9. A. S. Pine and K. W. Nill, "Molecular-Beam Tunable-Diode Laser Sub Doppler Spectroscopy of A-Doubling in Nitric Oxide," J. Mol. Spec., **74**, 43 (1979).

of both lines to the overall height in the region between the low lines create an additional added pedestal. Thus, the lines appear to shift towards each other.

The absorption, equal to the change in intensity in Equation (1), must be measured as a time varying signal due to the nature of the photoconductor detector. This AC signal can be measured by either modulating the laser on and off the absorption feature or by modulating the absorption feature into and out of the path. The ratio of I/I^0 can be rewritten as:

$$I/I^0 = \frac{I^0 - \Delta I}{I^0} = 1 - \Delta I/I^0 \quad (8)$$

and for small absorption signals

$$\Delta I \approx \sigma_{\nu} \int_0^L [N_l(x) - N_u(x)] dx. \quad (9)$$

Thus, by either changing ν , or changing N , ΔI becomes a varying signal.

The phase locked signal used in obtaining steady state NO concentrations were taken by modulating the laser frequency at 1/2 the reference frequency. Since a lock-in amplifier multiplies the incoming signal by either + 1 or - 1 depending on the reference phase, the resulting output compares the light absorption at nominally three frequencies. The output of this comparison is then low pass filtered. The second harmonic signal can be approximated by

$$I_{\text{detected}} = \langle I(\omega) - I(\omega + \Delta/2) + I(\omega + \Delta) - I(\omega + \Delta/2) \rangle \quad (10)$$

where Δ is the change in ω over the total excursion of the saw tooth laser current modulation. The intensity $I(\omega + \Delta/2)$ assumes a linear laser frequency tuning with current. Effects of non-linear frequency tuning with current modulation introduces a frequency bias to I_{detected} .

The signal detected in Equation (10) is seen to be a measure of the second derivative of the direct absorption signal times a constant. This measurement is directly proportional to the intensity at the three frequencies of interest and is in turn insensitive to small changes in intensity with time. This signal is also directly proportional to the number of absorbers in the path and provides a maximum signal at line center. Combining Equation (10) with Equation (6) we see that the total detected signal is also a function of the modulation depth Δ . These effects are discussed more in the signal to noise analysis.

From the above discussion it is seen that the detected signal is directly proportional to the difference in number densities between the lower and upper states of the absorbing transition. Because the signal is also a function of the modulation depth Δ , which must be determined with respect to the width of the collisionally broadened line, the final calibration was obtained by introducing a known column density of NO into the LABCEDE chamber. Thus, by introducing 1 torr of 0.11% NO in N_2 , together with 49 torr of pure N_2 , a signal equivalent to 1% absorption was observed. The second derivative signal was then maximized and compared to that measured in the chamber during electron beam operation.

3. EXPERIMENTAL MEASUREMENTS

Measurements were made in the LARCEDE facility using the technique described in the previous section. The operating conditions consisted of flowing N_2 with trace quantities of either O_2 for NO formation, or NO for calibration through the chamber. The total pressure within the chamber was maintained at a nominal 50 torr for the majority of the measurements. One set of measurements was also taken which systematically varied the total pressure. The flow rate of fresh gas was adjusted to provide 3.81 stand. l/min. to match the conditions used by Green et al.⁽³⁻⁶⁾ The O_2 pressure was varied from 0.1 to 10 torr, while decreasing the N_2 pressure to maintain the overall pressure and flow. The gases were introduced into the chamber at a point opposite the electron gun aperture and pumped out through both the beam aperture and through a valved port at the bottom of the chamber.

The electron beam was provided by a Pierce gun which produced a collimated beam of electrons at nominally 35 kV and 1 mA. Measurements were taken with a beam current ranging from 0.3 mA to 2.2 mA and a beam voltage varying from 25 to 40 Kv. This beam was pulsed on typically 1.5 ms and off for 23.5 ms. Both the repetition rate and the duty cycle of the electron beam were varied through the experimental set. The steady state measurement of NO was measured by slowly tuning through one rotational line in the $v = 0$ vibrational manifold while modulating the laser frequency to measure its second derivative. Once the peak of the derivative signal was established, the laser was allowed to sit on this peak while transient measurements were taken.

3.1 Observed Steady State Signals

The absorption signal by NO in steady state was taken using the second derivative, or 2f procedure outlined in the previous section. A typical signal during a frequency scan is shown in Figure 2. This trace, of the

TYPICAL SECOND DERIVATIVE SIGNAL

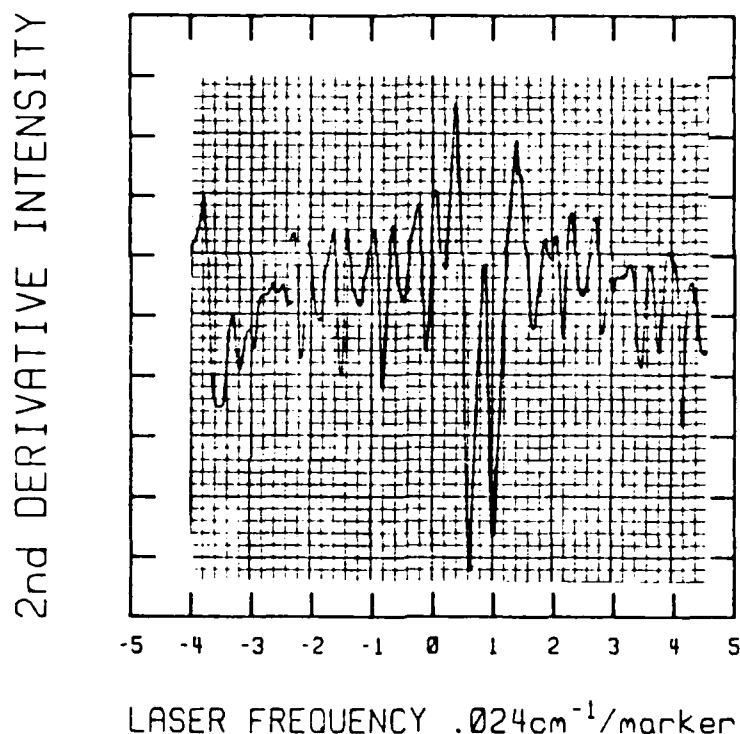


Figure 2. Typical Chart Recording of Second Derivative Spectra Due to NO. This Trace is of the NO ($v = 0$) $P_{11}(16.5)$ Doublet Taken at 1.5 torr O_2 in 49 torr N_2 . Secondary Peaks are Due to an Etalon Having 0.0167 cm^{-1} Spacing.

$P_{11}(16.5)$ doublet of the NO $v = 0$ shows a very slight negative curvature in the background, a slight overmodulation in the Δ and a very distinct etalon structure due to the White cell optics used in the particular measurement.

Typical steady state measurements of NO within the chamber for different O_2 pressures is shown in Figure 3. Here, one peak of the $P_{11}(16.5)$ NO $v = 0$ doublet was used in determining the absorption. Other operating conditions in this figure are 35 kV at 1.5 mA and 2.2 mA electron beam at a 1/20 duty cycle, 1.25 ms beam on, 23.5 ms beam off. The NO within the chamber is seen to increase with O_2 pressure, reaching an asymptotic limit of $5.16 \times 10^{13} \text{ cm}^{-3}$ mean density averaged over the 15 cm path in the chamber, or $3.5 \times 10^{14} \text{ cm}^{-2} \text{ mA}^{-1}$.

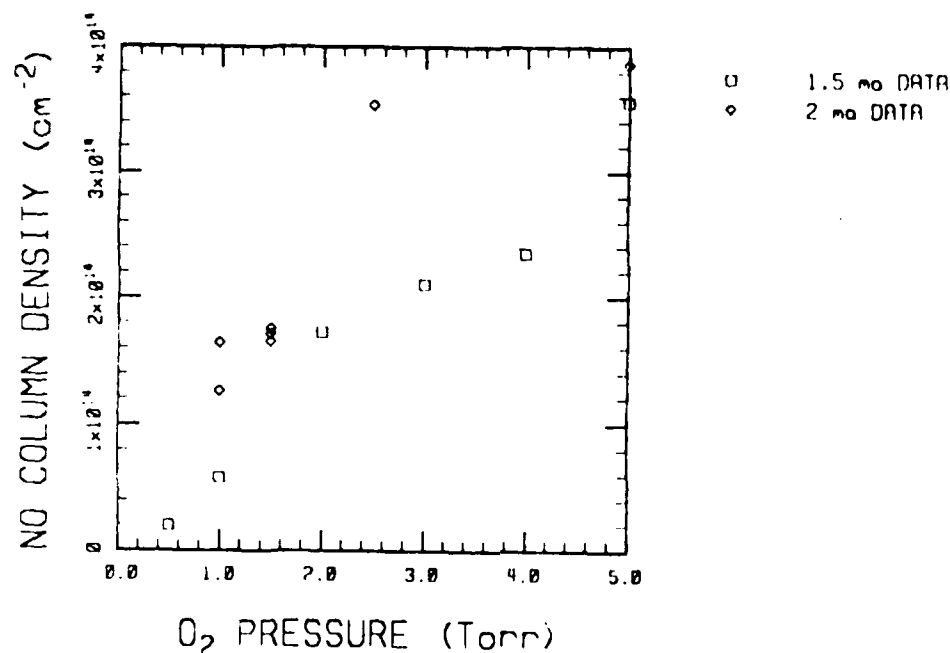


Figure 3. Variation of NO Produced with O₂ Pressure; Normalized to 1 mA Beam Current. The Squares Represent Data Set Taken with 1.5 mA Nominal Beam Current, Diamonds Represent 2 mA Nominal Current.

The dependence of NO on the O₂ concentration appeared to be linear between 1 and 2 torr, and increase slower with O₂ pressure above 2 torr. Measurements of NO when there was 1/2 torr of O₂ in the mixture was a factor of 3 to 4 less than for 1 torr of O₂. The resulting dependence of NO formation on O₂ thus formed an "S" shaped curve.

An entire matrix of runs, varying beam voltage, current, and duty cycle were made. The NO formed within the chamber appeared to be linear in electron current. Figure 4 shows the variation of the NO column density formed within the chamber as a function of electron beam current. The NO build up within the tank is seen to vary linearly with beam current. Figure 3 was thus also normalized to 1 mA.

The duty cycle was varied by both changing the pulse period and the total repetition rate of the beam. Figure 5 shows the same NO build up as show in Figure 3, except with the conditions of 2.7 ms beam on, followed by

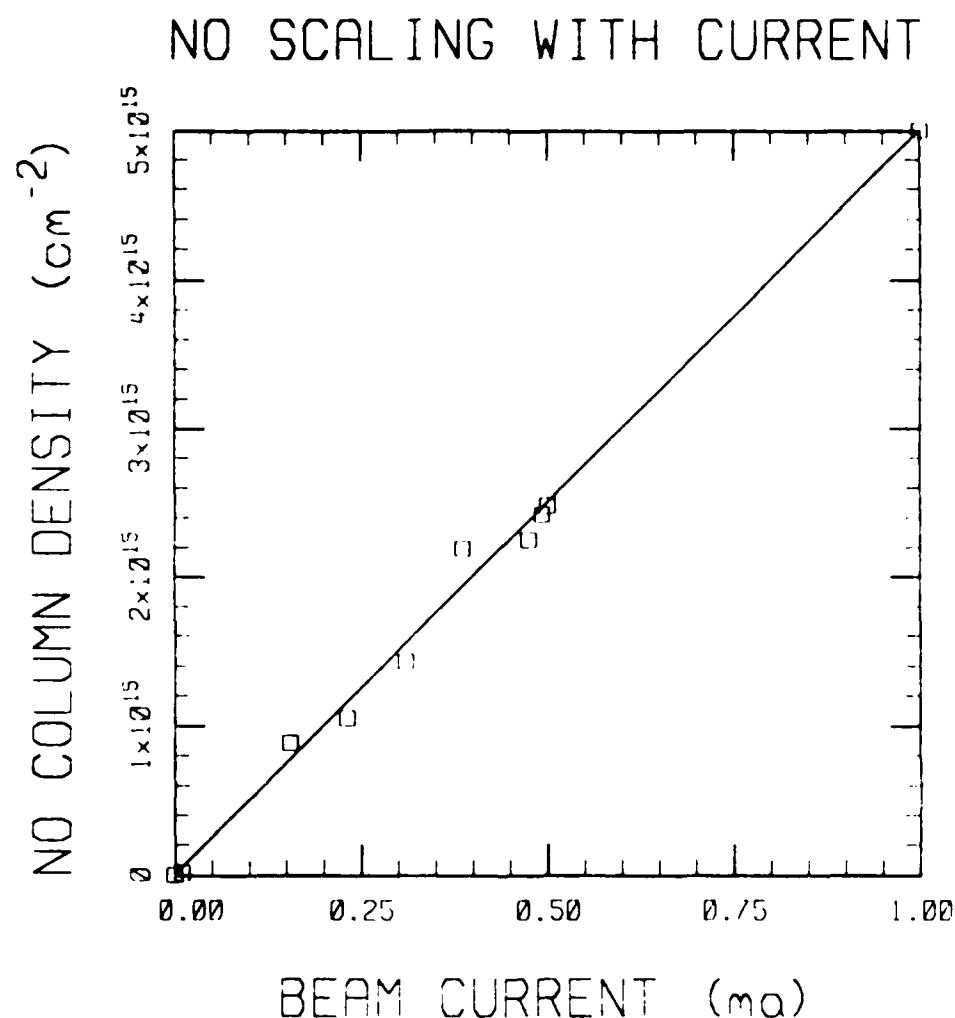


Figure 4. Scaling of NO Column Density with Beam Current.
Other Conditions: 5 torr O₂, 2 ms Beam on Vs. 22
ms Beam Off.

7.3 ms beam off, and 0.75 mA beam current. The path length in Figure 5 was also changed to 20 cm from the 15 cm used in Figures 3 and 4. The NO was monitored by observing the P₂₂ (8.5) line of the $v = 0$ level of NO. For these beam conditions, about $2 \times 10^{15} \text{ cm}^{-2}$ of NO was formed per torr O₂, and a limiting value of $7 \times 10^{15} \text{ cm}^{-2}$ NO was observed for the limiting case of 5 torr O₂ (0.10 mole fraction). The NO concentration was also seen to be a linear function of repetition rate. This relationship is illustrated in Figure 6.

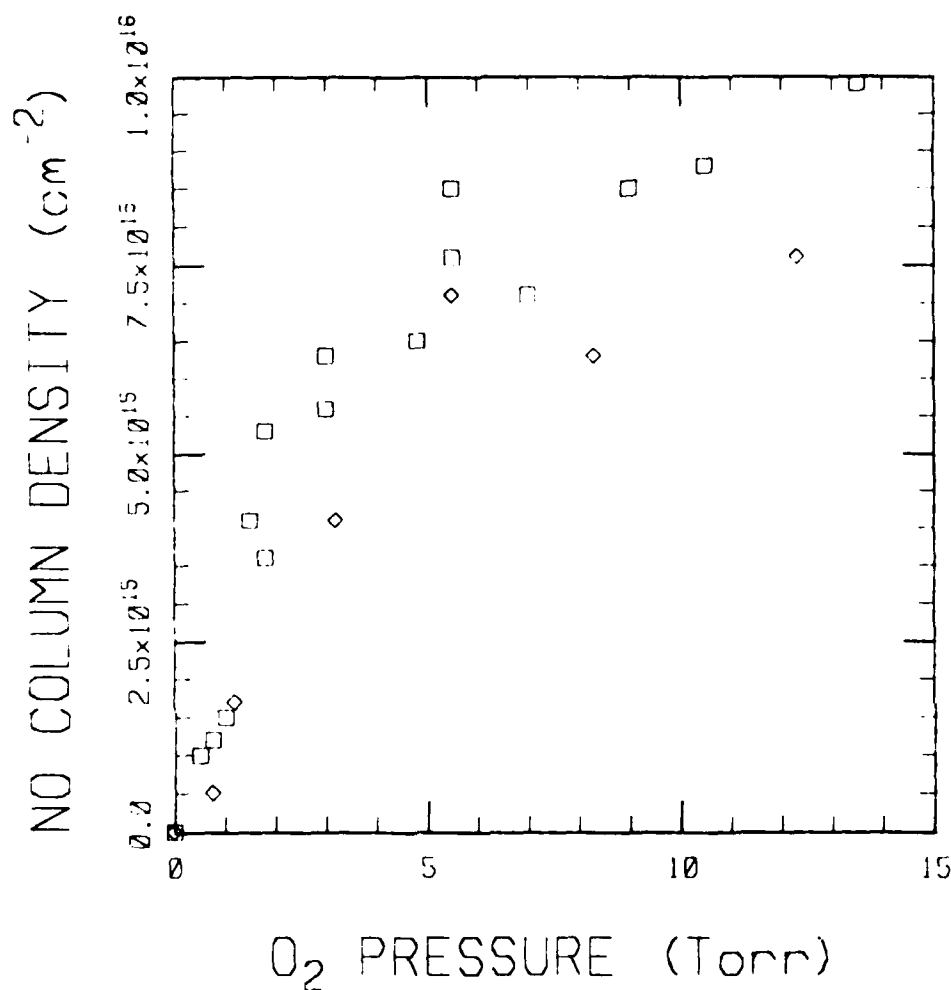


Figure 5. Variation of NO Build Up with O₂ Pressure Using .75 mA Beam Current. Total Pressure in Chamber was Kept at 50 torr. N₂ Comprising of the Remaining Pressure. The Squares and Diamonds Represent Two Separate Experiment Sets.

The flow time in the chamber for beam created NO to move out of the field of view was measured by waiting for steady state to be established then turning off the electron beam. This beam shut off was accompanied by NO disappearing from the field of view. The reaction times for both NO production by N(²D) plus O₂ and NO removal by N(⁴S) have time scales on the order of 0.1 ms. Thus, the disappearance and reappearance of NO was

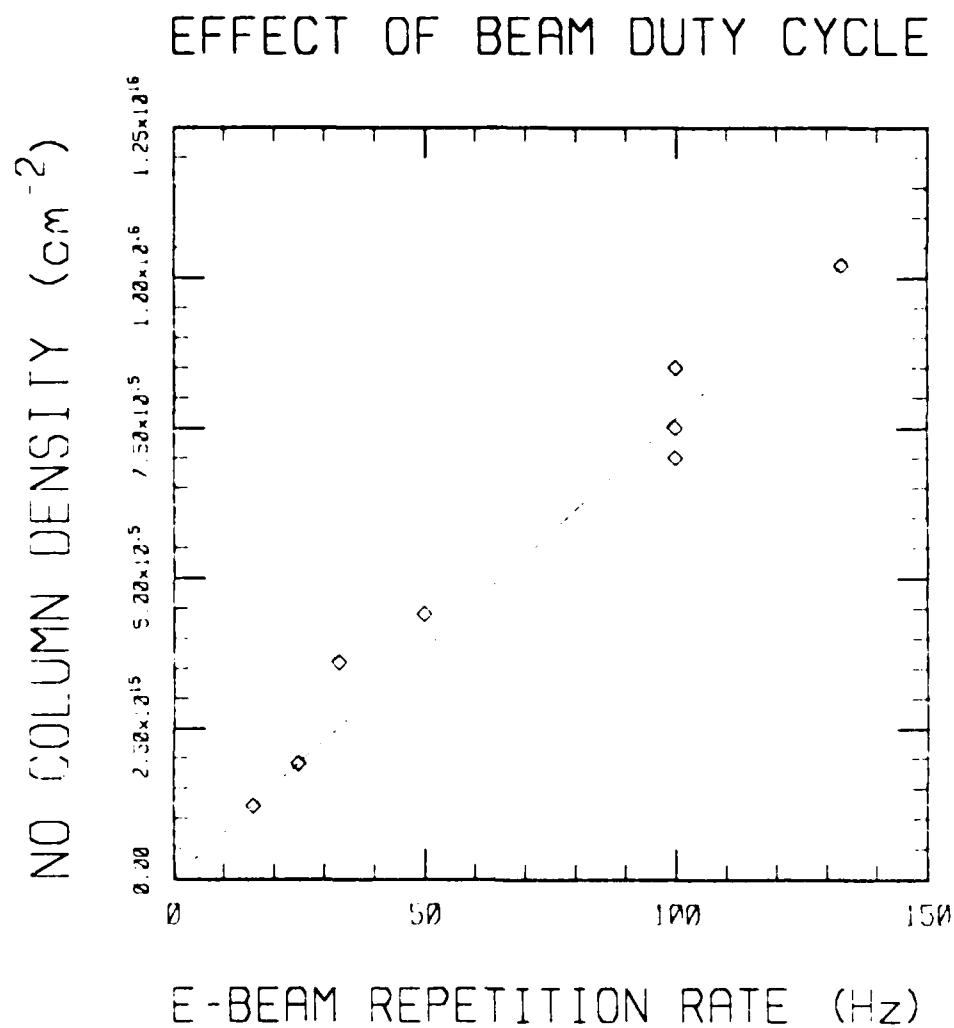


Figure 6. The Effect of Electron Beam Duty Cycle on the NO Produced. The Electron Beam Pulse Time was Kept Constant at 2.7 ms and the Beam Repetition Rate Varied. The Maximum Duty Cycle was thus 1/3.

controlled by diffusion and flow of the beam created NO into on out of the field of view. The approach to steady state population, either after turning on or off the electron beam, is characterized by a time $t(1/e)$ $5.4 \pm .8$ seconds under these conditions. This is shown in Figure 7.

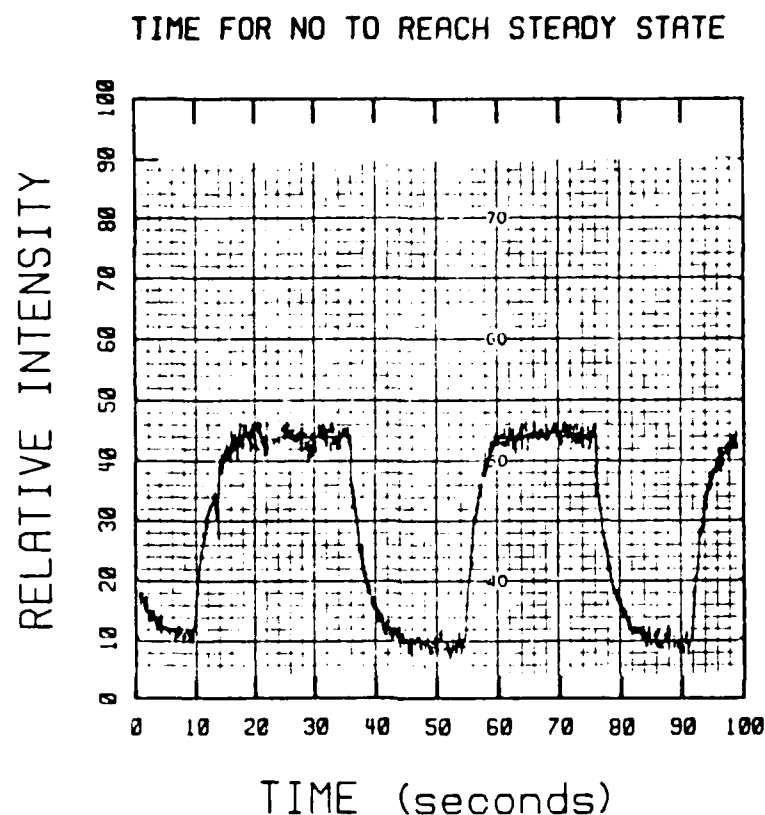


Figure 7. NO Absorption Signal when Electron Beam is Turned On and Off. The Mean Time to Reach Steady State is 5.4 ± 0.8 Seconds When no White Cell Flow Obstructions are in Place. Much Longer Times for NO Disappearance was Observed with White Cell in Place.

3.2 NO Removal by Beam Created Species

A second set of experiments were carried out where there was only N_2 and NO within the test chamber. Here, in the absence of O_2 , when the electron beam was turned on, the NO disappears. These measurements, where one atomic N produced destroys one NO molecule, give a measure of the total N formed by the direct electron beam. By titrating the NO to zero population, we can measure the net N atom production in the LABCEDE tank.

The amount of NO destroyed was a function of the the electron beam current and the total NO within the chamber. This is shown in Figure 8. In these measurements, the atomic nitrogen formed within the beam irradiated region destroys the NO introduced with the N_2 into the chamber. Once the NO within the beam core is destroyed, the additional N diffuses

NO REMOVAL BY BEAM SPECIES

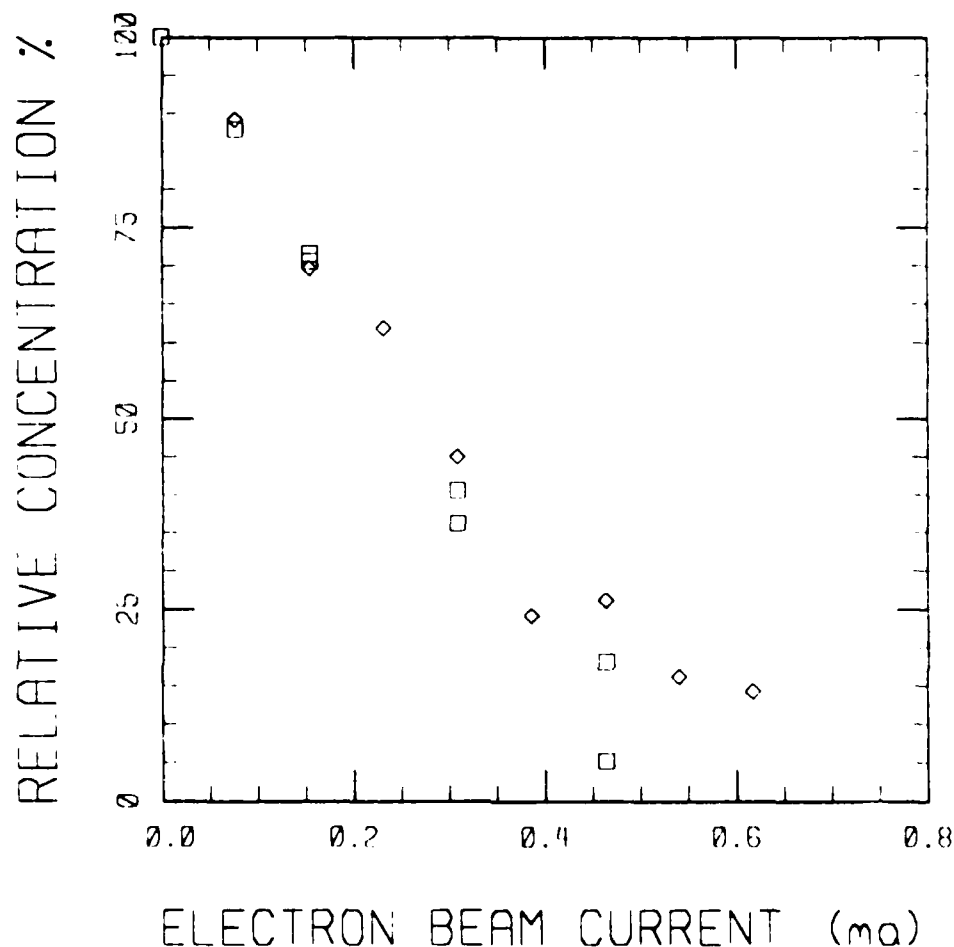


Figure 8. Variation of NO Concentration with Beam Current. Normalized to 100 When Beam is Off. Electron Beam Voltage was 35 kV, Beam on Time 1.6 ms, Beam Off 23.5 ms.

towards the walls of the chamber until NO is encountered. Since no O_2 is introduced into the chamber, $N(^2D)$ is quenched to $N(^4S)$ by N_2 . The NO titrated from the chamber in this manner is thus equal to all of the N formed by the beam plus all of the NO destroyed by reactions such as $NO + N_2^+ \rightarrow NO^+ + N_2$. Once again, the initial chemistry is much faster than the diffusion time. As the NO is destroyed, however, the $N(^4S)$ builds up

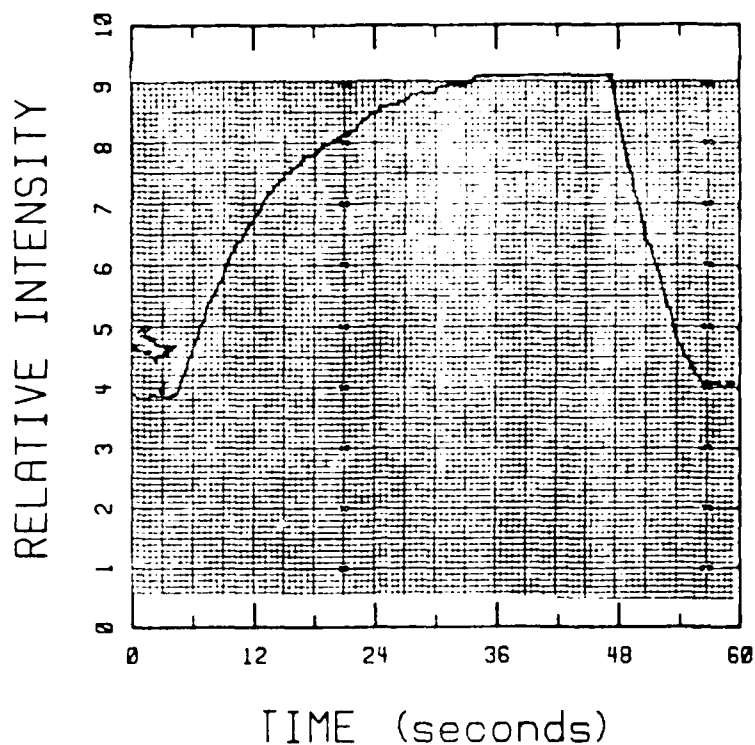


Figure 9. NO Reappearance After Beam Shut Off From 1 mA. Note 1.5 Second Lag Before Any NO Reappears. Very Long Build-Up Time is Indicative of Recirculation Around White Cell Optics. NO Disappearance with Activation of Electron Beam Comparable to NO Formation Experiments Shown in Figure 7.

within the chamber. The rate of removal of $N(^4S)$ by chemical means decreases to the point where this excess N must diffuse into other regions of the chamber before it can react with NO.

The rise time of NO within the absorption path when the electron beam is shut off and the disappearance of NO when the beam is turned on is shown in Figure 9. Note that these two times are greatly different and depend also on the total beam intensity. This is because the chemical time for NO removal is dependent on the total concentration of N within the chamber. As the $N(^4S)$ builds within the chamber, more and more NO upstream of the electron beam irradiated region is affected. The NO returning to the field of view after beam shut off is shown to lag beam off instant and is seen to take as long as 40 seconds before reaching steady state. This long time is

indicative of recirculation within the chamber caused by the White cell optics. The disappearance of the NO when the beam is turned on is a measure of the removal of NO upstream of the field of view by reaction. This time scale should be approximately equal to the measure of the reaction time for N to remove NO.

3.3 Transient Measurements

Transient measurements were attempted using the experimental technique described in the previous section. The maximum sensitivity to changes in NO column density on a millisecond time scale was $3 \times 10^{13} \text{ cm}^{-2}$ of NO in $v = 0$, for 1000 seconds of averaging. This corresponds to a mean concentration of $3 \times 10^{12} \text{ cm}^{-3}$ spread over the 20 cm path, establishing a minimum measurable density of $5 \times 10^{12} \text{ cm}^{-3}$ spread over the 5.5 cm diameter cloud. Transient signals within the field of view were not detectable at these levels, thus putting an upper bound on the change in NO $v = 0$ per electron beam pulse.

3.4 Signal to Noise

Noise Proportional to the Absorption Signal

The noise that is proportional to the absorption signal constitutes a fundamental limitation on the ability to detect time dependent concentration changes in the presence of a steady state NO population. The magnitude of this noise is determined by frequency instability in the laser. Even though the linewidth of the laser is on the order of 10^{-4} cm^{-1} , jitter in the absolute frequency of the laser due to both thermal and current variations limit the line width to 10^{-3} cm^{-1} . This wider jitter line width was found to be not random, but to carry both 120 Hz and 3 Hz components, corresponding to the line and cooling compressor frequencies, respectively.

The inherent laser frequency jitter, $\Delta\nu_j$, is responsible for most of the experimental limitations. The magnitude of this frequency jitter can be measured directly by introducing a known quantity of NO into the LARGEDE chamber and measuring the signal fluctuation. The intensity fluctuations

due to frequency jitter when the laser is tuned to the center of the absorption line can be estimated as follows:

$$I_J = I_0 e^{-\sigma_0 Nl} (1 - e^{-\Delta\sigma Nl}) \quad (11)$$

where

$$\Delta\sigma = \frac{\sigma_0 b_c^2}{\Delta_J^2 + b_c^2} \quad (12)$$

and where Δ_J represents the frequency jitter in cm^{-1} , σ_0 is the cross-section at line center, b_c is the collisional half-width at the chamber pressure where the measurements are taken, and Nl is the column density of the NO. At 50 torr N_2 , the collisional half-width is 0.0036 cm^{-1} . Thus, a 0.001 cm^{-1} jitter width would appear as a change in absorption of 5.6%, or, when the steady state NO concentration is 10^{15} cm^{-2} the minimum detectable change in NO would be on the order of $6 \times 10^{13} \text{ cm}^{-2}$. This changing signal can be enhanced somewhat by using phase locking techniques to reject changes not in phase with the electron beam. Multiples of the 120 Hz frequency which are nearly coincident with odd multiples of the electron beam repetition rate, however, are nearly impossible to reject.

The laser is somewhat stabilized by using a feedback circuit to lock the laser frequency to the peak of a Doppler broadened NO reference cell. By substituting b_D in Equation (3), for b_c in Equation (2), a smaller change in $\Delta\omega$ would result in comparable changes in ΔI or I_J . Thus, by locking the laser into a Doppler broadened NO cell, a 20 dB error voltage could narrow the jitter frequency to $2 \times 10^{-4} \text{ cm}^{-1}$. The requirement is that the feedback voltage must have a frequency response which is much higher than jitter frequency. Frequency locking using the present lock-in amplifiers thus easily rejected the 3 Hz temperature modulation on the laser, however, did not appear to effect the 120 Hz frequency ripple.

Noise Proportional to Laser Power

There is noise in the output signal from the signal channel which is proportional to the laser intensity, but independent of absorption. This

noise has frequency components which contain both 120 Hz, with an amplitude to approximately 2% of I_0 , and 3 Hz, with an amplitude of approximately 0.5% of I_0 .

These frequency components were seen within the second derivative scan. In addition to these noise signals, there was also a bias from zero in the second derivative scan, which indicated a curvature, or non linear change of intensity with frequency.

One possible explanation for the laser related noise is the frequency instability of the laser. All fluctuations of laser power at 1/2 the reference frequency or odd harmonics of that frequency result in a signal which is equivalent to the absorption signal. One such fluctuation is due to the variation of the detected laser power with wavelength. The laser power varies by 10% when the laser is tuned through 1011 cm^{-1} . This effect can be traced partly to the slit width of the monochromator which is used to separate the different laser modes. In order to reject laser modes which are 0.5 cm^{-1} from the mode of interest, the monochromator slit function must be set such that there is at least 5% change in signal over 1011 cm^{-1} . The other part of the variation of laser intensity with wavelength can be traced to the manner in which the wavelength is tuned. The current to the laser diode both heats the diode, tuning it to a higher frequency, and provides the number of transitions for the lasing, changing its intensity. The laser intensity thus increases when it is tuned to shorter wavelengths. By sitting on the right side of the monochromator slit, some of this effect can be canceled. Similarly, by using the second derivative signal, only the curvature of $I(\omega)$ is measured. However, this was not always possible, as the location of the monochromator slit depends on the spectral location of the competing modes. The slope of intensity vs current was different for different laser lines. While the intensity of the laser in all modes goes up with current, the actual intensity slope depends on the fraction of current driving the particular mode being used, which changes during the course of a day.

Note that a curvature is measured by the signal given in Equation (10) when the monochromator is centered on the laser frequency. The amount of curvature is infinite for a perfect triangular slit function. Therefore, the smaller the modulation depth, the larger the apparent curvature

becomes. When the Δ in Equation (10) is set to maximize the absorption line signal, the signal due to the monochromator produces a signal having the magnitudes of equal to 0.5% absorption by the line.

Other Noise Sources

Electronic noise primarily due to the noise induced by the preamplifiers also contribute to the intensity related noise. Since any intensity coming from the laser is multiplied, the amplifier noise always appears on top of the intensity which is being measured. For a laser power of $I_0 = 60 \mu\text{w}$, amplifier noise introduces an intensity fluctuation equivalent to 1% I_0 peak to peak. The component at $2f$ leads to an AC output noise, $\Delta S_p = .5\%$ S peak to peak, which is equivalent to an absorption due to .8 mtorr NO.

Limits of Sensitivity

Currently the fluctuations in laser intensity is approximately four times the electronic noise. After averaging the detection limits are as follows:

For time resolved detection with 1ms time resolution, the limiting noise is the 120 hz light noise, which is of a comparable frequency to the signal of interest. After 1000 repetitions of the experiment the noise level is equivalent to the absorption signal resulting from a change of NO column density, $3 \times 10^{13} \text{ cm}^{-2}$.

For steady state detection of NO, the limiting noise is from 3 hz laser light fluctuations caused by the cryocooler pump cycle. After 30 seconds of averaging the noise is equivalent to a NO column density of $2 \times 10^{13} \text{ cm}^{-2}$. Both of these limits are below the absorption signal limit for observing transients in the presence of a background concentration of NO.

4. MODEL OF NO PRODUCTION

This section presents a model of the chemistry and fluid mechanics which occur within the LABCEDE chamber leading to NO absorption. This model, together with the data presented in the previous sections, sets bounds on the total branching of atomic nitrogen formed in the initial ionization.

In order to model the electron beam induced chemistry, an estimate must be first made on the total amount of irradiation by the electron beam. Since the absorption measurements are integrals through the electron beam excited cloud, some averaging is naturally present in the measurements. Nonlinear chemistry, therefore, such as the effects of dissociative recombination, could introduce errors in taking the averaged approach.

4.1 Ionization by Electron Beam

The ion pair production rate, as a function of distance away from the electron gun aperture is given by the formula;⁽⁴⁾

$$\frac{d(i.p.)}{dt} = \frac{I (\rho^{-1} dE/dX) \rho}{2eW\pi r_{1/2}^2} \quad (13)$$

where I is the beam current, ρ is the gas density, e is the electron charge, W is the energy required to create an ion pair, 34.6 eV in nitrogen,⁽¹⁰⁾ $r_{1/2}$ is the beam radius encompassing half the beam current, and $\rho^{-1} dE/dX$ is the local energy deposition rate, a function of the distance from the electron gun.⁽⁴⁾

The electron beam emerging from the gun is spread due both to collisions with the N_2 and from space charge effects. Using the spread

10. G. N. Whyte, Radiation Research, 18, 255 (1963).

measured by Center,⁽¹¹⁾ where the beam current was low enough to have no space charge effects, the beam radius an axial distance of 8 cm from the gun aperture is given by the thick target limit formula;

$$\theta = \tan^{-1}(r_{1/2}/L) \simeq \frac{2.7 \times 10^{-9}(NL)^{1/2}}{V(1-10^{-3}V)} \quad (14)$$

where N is the number density of Nitrogen, L is the distance from the gun, and V is the electron energy in kV. Thus, $r_{1/2} = 2.35$ cm for $L = 8$ cm., and 3.83 cm at 11 cm., respectively. Substituting $r_{1/2}$ into Equation (13) gives approximately 9.48×10^{15} i.p. $\text{cm}^{-3} \text{ s}^{-1} \text{ ma}^{-1}$ for the axial distance of 8 cm. One half of all the gun energy is assumed to be contained in a cylinder of radius 2.35 cm. We assume that the remaining half of the current is uniformly distributed over the remaining path between the mirrors. Thus, the column ion density is 5.5×10^{16} i.p. $\text{cm}^{-2} \text{ s}^{-1} \text{ ma}^{-1}$.

The 1 m.a. current in LARCEDE provides some space charge spreading which tends to broaden the beam somewhat near the gun. Its effect would be to cause an effective L of somewhat larger than the physical distance L . This effect is still small, however, compared to the spreading due to electron scatter.

The distribution of electron deposition outside the beam core has been measured by Cohn and Caledonia.⁽¹²⁾ They scale their measurements to a practical range given by the relation

$$R = 2.60 V^{7/4} \rho \text{ cm.} \quad (15)$$

11. R. E. Center, "Plural and Multiple Scattering of Fast Electrons in Gases," Phys. Fluids, 13, 3 (1970)
12. A. Cohn and G. E. Caledonia, "Spatial Distribution of the Fluorescent Radiation Emission Caused by an Electron Beam," J. Appl. Phys., 41, 9 (1970).

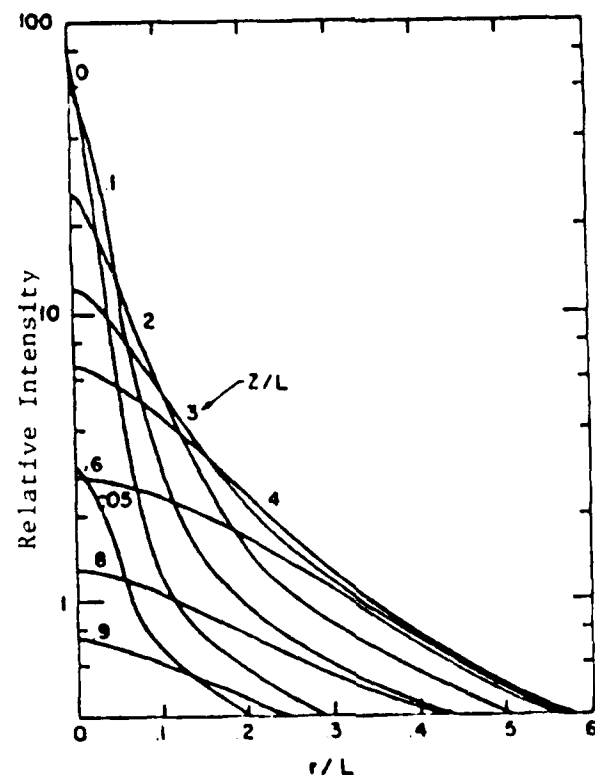


Figure 10. Normalized Point Intensity Profile Versus r/L for Given Z/L From Cohn and Caledonia. (12)

where p is the density in Torr, and V is the beam energy in kV. For a 35 kV beam, the practical range R is 26.2 cm. Thus, $L/R = 0.305$. Figure 10 shows their measurements of relative energy deposition rate at this and other axial stations.

Once the ionization takes place, chemistry between the beam created species occurs in the region where the energy is deposited until convective motion or diffusion spreads out the new species. The time scale for diffusion at 50 torr through the volume inscribed by the 2.35 cm radius is on the order of 0.25 seconds. The flow time out of the the beam irradiated region is on the order of 6 seconds.

4.2 Effects of Diffusion and Flow

The steady state measurements of NO are along the line of sight of the laser beam traversing the LARCEDE chamber. Diffusion of NO from the formation volume consisting of the beam irradiated region defines the NO concentration at the edges of the tank. The diffusion coefficients for NO and N diffusing through 50 torr of N_2 is 3.8 and 4.9 cm^2s^{-1} , respectively.⁽¹³⁾ Since the majority of the NO formation chemistry has time scales on the order of milliseconds, most of the atomic nitrogen has been removed by reaction before it has a chance to diffuse or flow out of the 2.35 cm radius cloud. Even if not all of the atomic nitrogen formed in this core region has reacted with O_2 , the excess atoms would quickly find NO molecules and react with before migrating to the walls. The only important diffusion time scale is that for NO formed in the central core by reactions of N and O_2 diffusing from this central core during the observation time. Hence, steady state measurements of NO are measures of NO formed primarily in the central core and later spreading to other parts of the chamber. As the NO is removed from the central core, it both moves downstream towards the electron gun aperture and across the irradiated region towards the pumping port. Some of the NO also diffuses across the chamber, staying within the line of sight of the absorption path, while the rest diffuses, or is otherwise transported out of the absorption path.

The time taken for the NO to disappear from the absorption field of view was measured by simply following the absorption signal with time after electron beam shut-off. Since the time required for all of the relevant chemistry to take place happens in a few milliseconds, the NO absorption signal seen after that time is due to NO formed upstream of the absorption region and either flowing or diffusing into the volume. Since fresh gas is pumped into the chamber at a known rate, the volume of the interaction region upstream of the absorption path is measured. For the majority of the experiments, the flow rate of fresh gas into the chamber was adjusted to 3.81 stand l/min. This rate, together with the chamber pressure and

13 T. R. Marrero and E. A. Mason, "Gaseous Diffusion Coefficients," J. Phys. Chem. Ref. Data, 1, 1 (1972).

the measure of the refill time provides a volume of approximately $4.92 \times 10^3 \text{ cm}^3$ of beam excited gas upstream of the absorption region. Using the very crude assumption of plug flow through the chamber, this volume flow rate corresponds to a 3 cm s^{-1} velocity.

The effect of diffusion on the spread of NO within the tank can best be assessed by looking at the an initial distribution of NO which is proportional to the electron dosing geometry and following the diffusion independent of the flow. If we assume that the initial distribution of NO after formation is in the form of a cylindrically symmetric cloud of radius given in Equation (14), whose distribution is a Gaussian in which the beam intensity drops to 1/2 of the centerline value at a distance r_G from the center. The effects of diffusion are approximated by the an expanding cylinder of NO by solving the axi-symmetric relation;

$$\frac{\partial^2 [\text{NO}]}{\partial r^2} + \frac{1}{r} \frac{\partial [\text{NO}]}{\partial r} = \frac{1}{D} \frac{\partial [\text{NO}]}{\partial t} \quad (16)$$

where the initial condition is

$$[\text{NO}](r,0) = [\text{NO}]_0(0) \exp - (\ln 2 \ r^2 / r_G^2) \quad (17)$$

where $[\text{NO}]_0(0)$ represents the centerline concentration of NO at zero time. Since $[\text{NO}]$ is considered not to be destroyed after the first few milliseconds, the centerline concentration decrease with time is a function only of diffusion and motion. The time dependent absorption signal measures the path integral of the NO density;

$$\frac{I}{I_0} = \exp - 2\sigma \int_{-a}^a [\text{NO}](r,t) dr \quad (18)$$

where σ is the absorption cross section, $-a$ and a are the radial distances from the axis to the window and mirror, respectively. The effect of diffusion on the integrated path is thus

$$\frac{dI}{dt} = I(t=0) (1 + Dt/r_G^2)^{-1/2} \quad (19)$$

where the diffusion coefficient for NO into N_2 is $3.8 \text{ cm}^2\text{s}^{-1}$, and the initial radius of the cloud, r_G , is 2.35 cm. In the absence of flow, diffusion would change the measured density at the central core by a factor of 2 after 6 seconds, comparable to the flow time. This would correspond to a central core becoming a factor of $\sqrt{2}$ broader. The measured column density would change from 5.5×10^{16} to $3.28 \times 10^{16} \text{ cm}^{-2}$, or decrease by 40%.

In order to take into account the effects of flow and diffusion a simplified picture of bulk transport is used. The $1/e$ disappearance time as measured in Figure 7 was used to provide a unimolecular disappearance rate for all beam created species. These rates are also equivalent to how radiative decay is treated in the model. N_2 and O_2 , introduced through bottled gas, were assumed to change only due to reaction, as their replenishment rate was assumed equal to the removal rate.

Since the chemistry was treated by assuming a "top hat" profile with a core region defined by Equation (14), and remaining ionization equally spread over the remainder of the chamber, it is somewhat of an underestimate of the total column density. Diffusion out of this "top hat" was assumed to be completely lost, also underestimating the total column. However, these effects are canceled by using the observed change in column as the time scale for loss of species from the central core.

4.3 Chemistry in the LABCEDE Chamber

Once the total ionization rate has been established, the chemistry can be studied by modeling all of the kinetic processes which may contribute to the formation of NO. This chemistry was modeled by using a modified version of the Sandia Laboratories CHEMKIN code.⁽¹⁴⁾ The reaction rates used in this code are a compilation from many sources. Those not referenced are from the DNA Handbook.⁽¹⁵⁾ The formation of NO was found highly

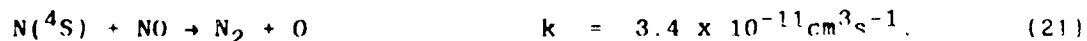
14 R. J. Kee, J. A. Miller and T. H. Jefferson, "CHEMKIN: A General Purpose, Problem Independent, Transportable, Fortran Chemical Kinetics Code Package," Sandia Laboratories Rpt. No. SAND80 8003 (1980)

15 M. H. Bortner and T. Baurer, "Reaction Rate Handbook Second Edition," Defense Nuclear Agency Rpt. No. DNA 1948H (March 1972).

dependent on the branching ratio in the atomic nitrogen formation. NO is primarily produced by the reaction of $N(^2D)$ with O_2 ; (16)



and destroyed by reaction with ground state $N(^4S)$; (17)

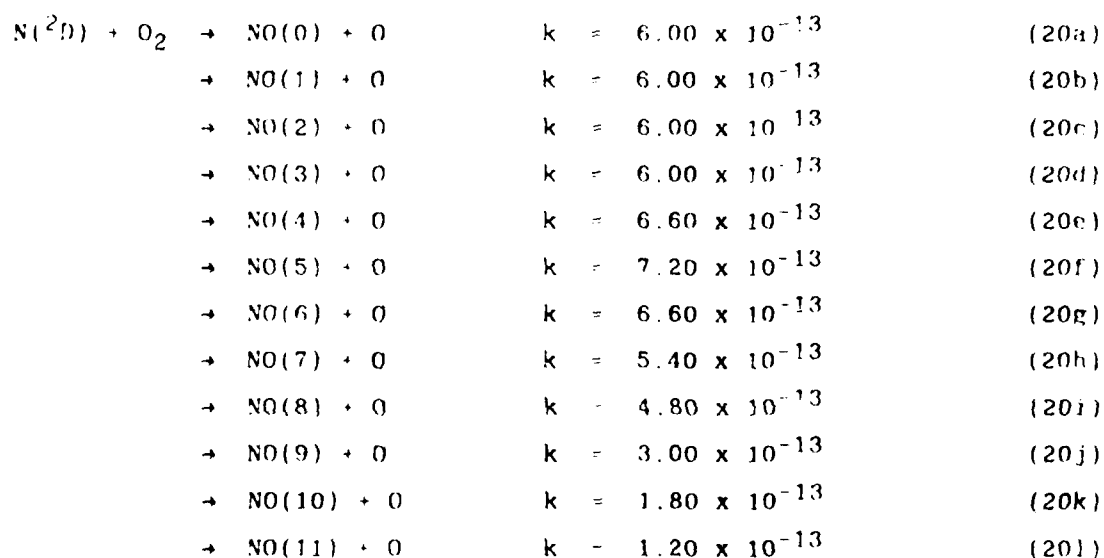


The observed NO concentrations are therefore strong functions of the relative populations of these two electronic states. Nitrogen atoms are produced in three ways: through direct dissociation of N_2 by the primary electrons produced in the electron beam, through recombination reactions of the primary ionic products with secondary electrons, and by charge transfer reactions of the primary ionic products followed by recombination reactions. Nitrogen atoms are also subject to chemical reaction with other species to compete with Reactions R(20) and R(21) in the production and destruction of NO.

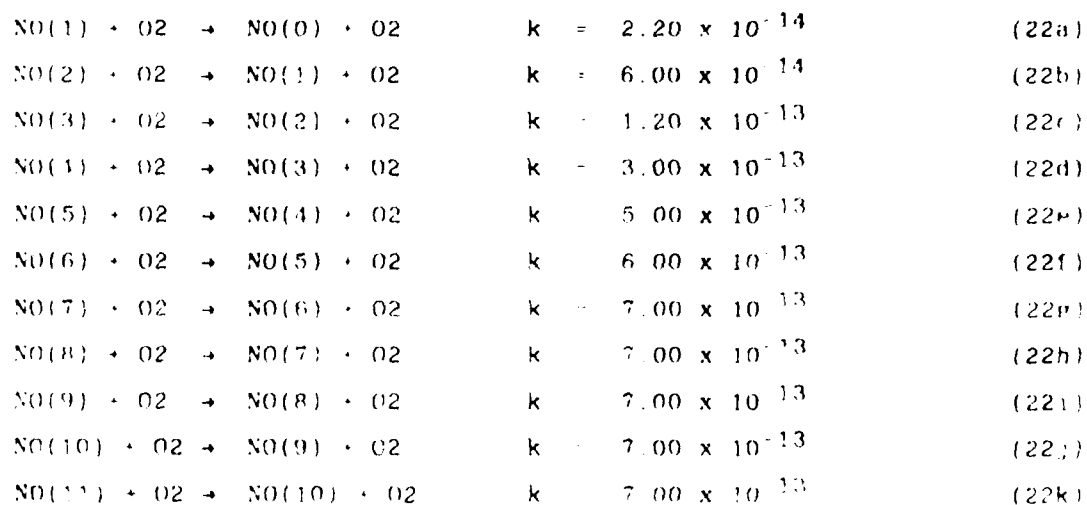
The measured concentration in LABCEDE is the actual population difference between the population of a single vibration-rotation level of NO in the ground vibrational level compared to the corresponding population in the ($v = 1$) level of that transition. The production of NO ground state population on the time scale of the electron beam pulse is dominated by the formation of vibrationally excited NO in Reaction R(20), and subsequent vibrational relaxation of NO to $v = 0$ through collisions with O_2 and N_2 , as well as radiative decay. The removal of NO on this time scale is dominated by reaction with beam created $N(^4S)$ via Reaction R(21). These effects were modeled based on the results presented by Green et al. (5) for $v \geq 1$

16. M. R. Torr, R. G. Burnside, P. B. Hays, A. I. Steward, D. G. Torr and J. C. G. Walker, "Metastable 2D Atomic Nitrogen in the Mid Latitude Nocturnal Ionosphere," *J. Geophys. Res.*, **81**, 4 (1976).
17. W. B. DeMore, J. J. Margitan, M. J. Molina, R. T. Watson, D. M. Golden, R. F. Hampson, M. J. Kurylo, C. J. Howard and A. R. Ravishankara, "Chemical Kinetics and Photochemical Data for Use in Stratospheric Modeling," NASA, Jet Propulsion Laboratory, Pasadena, CA, JPL Publication 85-37 (July 1985.)

and varying the branching ratio into NO ($v = 0$). Two cases were tried: one of the $v = 0$ equal to the rate for the first three excited levels, and a second using a factor of three higher than that for the first three vibrational levels. In order to follow the $v = 0$ vibrational level of NO, the nascent distribution of NO was simulated by dividing Reaction 20 into individual rates corresponding to their partitioning into different vibrational levels. Thus, in the first case Reaction R(20) becomes:



The vibrationally hot NO can be quenched into the ground state by O_2 . Using the same branching technique:



Similarly, the upper levels can emit radiation, and thus cascade down the vibrational ladder. The sum of radiative removal and bimolecular removal by N_2 we represented by the effective unimolecular rates;

$NO(1) \rightarrow NO(0)$	$k = 1.1 \times 10^{-3}$	(23a)
$NO(2) \rightarrow NO(1)$	$k = 2.0 \times 10^{-3}$	(23b)
$NO(3) \rightarrow NO(2)$	$k = 2.9 \times 10^{-3}$	(23c)
$NO(4) \rightarrow NO(3)$	$k = 3.7 \times 10^{-3}$	(23d)
$NO(5) \rightarrow NO(4)$	$k = 4.3 \times 10^{-3}$	(23e)
$NO(6) \rightarrow NO(5)$	$k = 4.9 \times 10^{-3}$	(23f)
$NO(7) \rightarrow NO(6)$	$k = 5.4 \times 10^{-3}$	(23g)
$NO(8) \rightarrow NO(7)$	$k = 5.8 \times 10^{-3}$	(23h)
$NO(9) \rightarrow NO(8)$	$k = 6.2 \times 10^{-3}$	(23i)
$NO(10) \rightarrow NO(9)$	$k = 6.6 \times 10^{-3}$	(23j)
$NO(11) \rightarrow NO(10)$	$k = 7.0 \times 10^{-3}$	(23k)

Cascading from the high v states by $\Delta v = 2$ is comparable to that for $\Delta v = 1$.⁽³⁾ However, these were neglected, as the quenching by O_2 for the range of conditions used in the experiment always dominated the radiative cascading. The time variation in the absorption signal disappears very rapidly once the electrons were turned off. Thus, in steady state, with duty cycles of less than 1/3, and repetition rates on the order of 100 s^{-1} , almost all of the NO is in the ground state. The production of atomic nitrogen in the electron beam excited region, then, controls the measured steady state signals.

Production of Atomic Nitrogen

The ionization of N_2 , O_2 and NO within the chamber produce molecular as well as atomic ions. Their relative concentrations are modeled by the following branching ratios:

$EP + N_2 \rightarrow N_2^+ ES + EP$	$.8 \Phi_{N_2}/IP$	(14)	(24)
$EP + N_2 \rightarrow 2N + EP$	$.6 \Phi_{N_2}/IP$	(15)	(25)
$EP + N_2 \rightarrow 2 N^+ + ES + EP$	$.1 \Phi_{N_2}/IP$	(14)	(26)
$EP + N_2 \rightarrow N_2(A) + EP$	$.4 \Phi_{N_2}/IP$	(15)	(27)

$EP + NO \rightarrow NO^+ + ES + EP$	$1.2\phi_{NO}/IP$	(14)	(28)
$EP + NO \rightarrow N(^4S) + O^+ + ES + EP$	$.5\phi_{NO}/IP$	(15)	(29)
$EP + NO \rightarrow N^+ + O + ES + EP$	$.5\phi_{NO}/IP$	(14)	(30)
$EP + O_2 \rightarrow O_2^+ + ES + EP$	$.95\phi_{O_2}/IP$	(14)	(31)
$EP + O_2 \rightarrow O + O + EP$	$8\phi_{O_2}/IP$	(15)	(32)
$EP + O_2 \rightarrow 2O^+ + EP$	$.05\phi_{O_2}/IP$	(14)	(33)

Where ϕ_M is the mixing ratio of species M, and /IP represents per ion pair produced. Here, we have combined the direct dissociation with the dissociative ionization such that the atomic neutral in Reaction R(26) would be included in Reaction R(25), and the neutral in Reaction R(33) is included in Reaction R(32). The relative ionization cross sections from Kieffer and Dunn⁽¹⁸⁾ were used to obtain the relative ionization rates. Note that the total ion concentration does not add up to exactly 1.00. This is not a severe problem as long as NO and O₂ are minor constituents. Care was taken to adjust these ratios when their concentrations became comparable to that of N₂. A total of 1.2 nitrogen atoms per ion pair are produced by the Reaction R(25).⁽¹⁹⁾ These are divided between ground state N(⁴S), and excited state atoms, which we have assumed to be exclusively N(²D).⁽²⁰⁾ This is equivalent to assuming that all of the N(²P) formed is quenched to N(²D) before reacting. The total NO produced was found to be a very strong function of the branching ratio N(²D)/N(⁴S). Simulations were made by varying this branching ratio in the percentages 50/50, 55/45, and 60/40.

From the above set of reactions, N₂⁺ is seen to be the principal ionic species produced. It is removed by the following reactions:

18. L. J. Kieffer and G. H. Dunn, "Electron Impact Ionization Cross-Section Data for Atoms, Atomic Ions, and Diatomic Molecules: I. Experimental Data," Rev. Mod. Phys., **38**, 1 (1966).
19. R. S. Stolarski and A. E. S. Green, "Calculations of Auroral Intensities from Electron Impact," J. Geophys. Res., **72** 3967 (1967).
20. D. F. Strobel, E. S. Oran, and P. D. Feldman, "The Aeronomy of Odd Nitrogen in the Thermosphere 2. Twilight Emissions," J. Geophys. Res., **81**, 3745 (1976).



where all reaction rates are in units of cm^3s^{-1} , the formation of $\text{N}(^2\text{D})$ from Reaction R(34) has a reported branching of 54%.⁽¹⁵⁾ This reaction is only of minor importance to the experimental conditions present in LABCEDE, however, as charge exchange and ion exchange dominate it even when only moderate quantities of NO or O_2 are present. The O^+ formed in Reaction R(38) also quickly cascades to ions with the lowest ionization energy:



where the three body Reaction R(40) is in units of cm^6s^{-1} and is comparable to two body rates 2×10^{18} larger. In the limit of high O_2 concentration ($\text{O}_2 > 10^{15} \text{ cm}^{-3}$), Reaction R(39) dominates Reaction R(40) and no N atoms are produced from O^+ . The O_2^+ ions recombine with secondary electrons:



or by reaction with neutral O_2 and N_2 to form O_4^+ which then dissociatively recombines with secondary electrons:



At low concentrations of NO, the above reactions are much faster than the charge transfer to NO: (21)



The dissociative recombination Reactions R(42) and R(46) do not form any atomic nitrogen. However, as NO builds up in the chamber, Reactions R(47) and R(48) become more and more important, until the primary positive ion is NO^+ .

In contrast to N_2^+ , N^+ ions formed in the primary ionization, which comprises of 1/4 of all N_2 ionization events, (22) do lead to N atom formation. N^+ is deactivated either by the channel leading to N_3^+ :



followed by transfer to O_2 .



or by reaction with O_2 : (23)



21. C. D. Sutherland and J. Zinn, "Chemistry Computations for Irradiated Hot Air," Los Alamos Scientific Laboratory, Los Alamos, NM, Rpt. No. LA-6055-MS (1975).
22. R. R. O'Neil, E. T. P. Lee, and E. R. Huppi, "Auroral $\text{O}(^1\text{S})$ Production and Loss Processes: Ground-Based Measurements of the Artificial Auroral Experiment Precede," J. Geophys. Res., **84**, 823 (1979).
23. M. A. Smith, V. M. Bierbaum, and S. R. Leone, "Infrared Chemiluminescence from Vibrationally Excited NO^+ : Product Branching in the $\text{N}^+ + \text{O}_2$ Ion-Molecule Reaction," Chem. Phys. Lett., **94**, 398 (1983).



Reactions R(52) through R(54) become comparable to Reactions R(44) through R(50) when the O_2 concentration gets above 2 torr.

As NO concentration increases, the minor channel exists for reaction with NO directly:



Each of the above channels leads to NO^+ formation. The NO^+ ion is stable with respect to charge exchange and is deactivated by recombination to yield N atoms: (24)



where the branching ratio of N into $\text{N}(^2\text{D})$ was measured to be $76 \pm 6\%$. (25) Thus the reactions of N^+ with N_2 and O_2 leads to an excess of $\text{N}(^2\text{D})$ atoms over $\text{N}(^4\text{S})$ atoms of the order of 0.1-0.15 per ion pair for $[\text{O}_2] > 10^{16} \text{ cm}^{-3}$. At these high O_2 densities, a new set of reactions, those in the formation of negative ions also become important. Their rates are:



and



These reactions, in turn neutralize the NO^+ ion directly into NO:

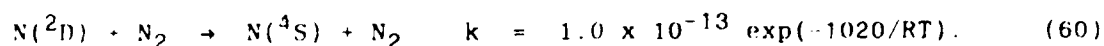


24. C. Huang, M. A. Biondi, and R. Johnsen, "Variation of Electron NO^+ -ion Recombination Coefficient with Electron Temperature," Phys. Rev. A, **11**, 901 (1985).
25. D. Kley, G. M. Lawrence, and E. J. Stone, "The Yield of $\text{N}(^2\text{D})$ Atoms in the Dissociative Recombination of NO^+ ," J. Chem. Phys., **66**, 4157 (1977).

Thus, NO^+ formed through charge exchange quickly return to NO, while ion exchange reactions which create NO^+ increase the NO concentration. Dissociative recombination of NO^+ tends to use up some of the NO created through charge exchange but adds a similar portion through ion exchange.

Destruction of Atomic Nitrogen

In addition to Reaction R(20), $\text{N}(^2\text{D})$ can be physically quenched by the reaction: (26)



This reaction is particularly important when the O_2 concentration is less than 0.3% of the N_2 concentration, corresponding to an $[\text{O}_2] < 5 \times 10^{15} \text{ cm}^{-3}$ for our operating conditions. For O_2 concentrations much less than this value, quenching of $\text{N}(^2\text{D})$ is very rapid compared to chemical reactions, and all chemical reactions of N atoms occur from the ground $\text{N}(^4\text{S})$ state. Therefore in the limit of $[\text{O}_2] \ll .2 \text{ torr}$, any NO originally present within the chamber would be removed by the sum of $\text{N}(^2\text{D})$ and $\text{N}(^4\text{S})$ formed by the electron beam irradiation.

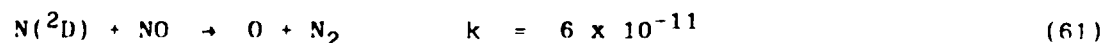
At higher O_2 concentrations, an appreciable fraction of the chemical reactions involve higher excited states of nitrogen atom. The $\text{N}(^2\text{D})$ atoms react with O_2 to form NO, while the ground state $\text{N}(^4\text{S})$ atoms react with the large pool of ground state NO to remove NO. Since both reactions occur very rapidly even compared to the electron beam operating time, only the difference in the production and removal rates can be observed by monitoring the ground state of NO. This is in marked contrast to what is observed in emission.

In the limit of very large O_2 concentrations, physical quenching of $\text{N}(^2\text{D})$ by N_2 is unimportant, and the steady state NO concentration approaches a limit determined by the difference in population between the $\text{N}(^2\text{D})$ and $\text{N}(^4\text{S})$ states produced each time the electron beam is pulsed. For

26. T. G. Slanger and G. Black, "Quenching of $\text{N}(^2\text{D})$ by N_2 and H_2O ," J. Chem. Phys., **64**, 44 (1976).

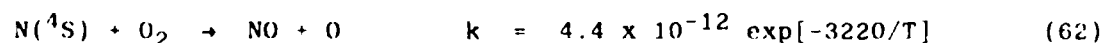
example for $O_2 > 15$ torr, physical quenching accounts for 3% of the $N(^2D)$ removal, and thus the net change in NO concentration is equal the the difference in population between the two atomic states minus 0.03 times the total $N(^2D)$ production.

Even if no $N(^4S)$ is formed by direct dissociation, the total NO within the chamber is limited by the reaction: (21)



which limits the total NO concentration within the chamber to one tenth of the O_2 concentration. We note that this concentration can never be achieved because of other, competing reactions.

Similarly if no $N(^2D)$ is formed, the $N(^4S)$ can also react with O_2 to form some NO: (27,28)

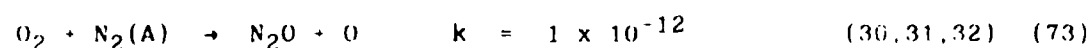
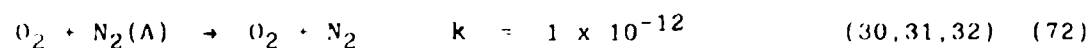
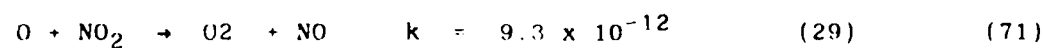
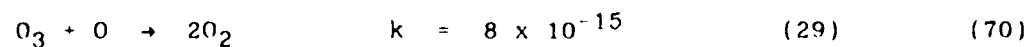
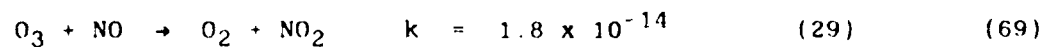
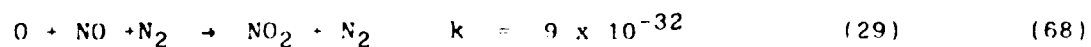
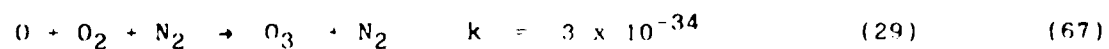
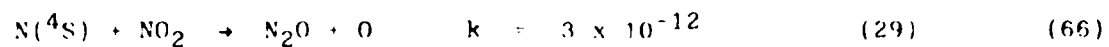


This establishes a minimum NO population in the chamber when there is O_2 present in the chamber and no $N(^2D)$ is formed to $[NO]/[O_2] = 3 \times 10^{-6}$.

The following reactions in the model establish the balance between the odd oxygen species, O, and O_3 , also formed within the LARCEDE chamber. They influence the total NO production and destruction only in second order:

<u>Reaction</u>	<u>Rate</u>	<u>Reference(s)</u>
$N(^2D) + O \rightarrow N(^4S) + O$	$k = 1 \times 10^{-12}$	(5) (63)
$N(^4S) + O + N_2 \rightarrow NO + N_2$	$k = 1 \times 10^{-32}$	(5) (64)
$N(^4S) + O_3 \rightarrow NO + O_3$	$k < 1 \times 10^{-15}$	(29) (65)

27. A. Rahbee and J. J. Gibson, "Rate Constants for Formation of NO in Vibrational Levels $v=2$ Through 7 from the Reaction $N(^4S) + O_2 \rightarrow NO^+ + O$," J. Chem. Phys., **74**, 5143 (1981).
28. R. R. Herm, B. J. Sullivan, and M. E. Whitson, "Nitric Oxide Vibrational Excitation from the $N(^4S)+O_2$ Reaction," J. Chem. Phys., **79**, 2221 (1983).



While Reactions R(63) through R(73) were not major contributors in the production of NO, vibrational or electronic excitation in the reaction channels may change their contribution.

5. SIMULATION RESULTS AND DISCUSSION

The computer simulations were designed to replicate experimental conditions shown in Figure 5. The experimental conditions were: $p_{\text{NO}} = 50$ torr, beam current 1 ma, beam voltage 35 kV, and the beam is on for 2.7 ms in each 10 ms period. The effects of diffusion and flow were taken into account by assuming that all of the beam formed species had a unimolecular decay time of $1/5.4$ seconds. We assume that the ion pair production rate is 10^{16} ion pairs per second, evenly distributed in a conical volume defined by the half radius for IP production calculated of $r_{1/2} = 2.35$ cm. In order to compare this model to experimental values, we convert concentrations to column densities of NO in a line of sight through the center of the reaction area. This line of sight is assumed to be $L = 5.5$ cm, where L is defined by dividing the mean ionization rate in the central core by the resulting column density in Subsection 4.1.

5.1 Simulations of NO Formation

A modified version of CHEMKIN is used to calculate the time dependent concentrations of all the chemical species listed in Section 4. The steady state concentrations of many species were established within one beam pulse, while others, which did not quite reach steady state, would require the full diffusion and flow time to come into steady state. Thus, since each pulse of the electron beam would produce a certain excess of NO, the total NO concentration would reach steady state only after the excess is

29. F. Westley, "Tables of Experimental Rate Constants for Chemical Reactions Occurring in Combustion (1971-1977)," National Bureau of Standards, Washington, DC, Rpt. No. NBSIR 81-2254 (April 1981).
30. M. P. Iannuzzi and F. Kaufman, "Rate Constants for the Reaction of $\text{N}_2(\text{A}^3\Sigma_u^+)$, $v = 0, 1$, and 2 with O_2 ," J. Phys. Chem., **85**, 2163 (1981).
31. L. G. Piper, G. E. Caledonia, and J. P. Kennealy, "Rate Constants for Deactivation of $\text{N}_2(\text{A})V^1 = 0, 1$ by O_2 ," J. Chem. Phys., **74**, 2808 (1981).
32. E. C. Zipf, Nature, **287**, 523 (1980).

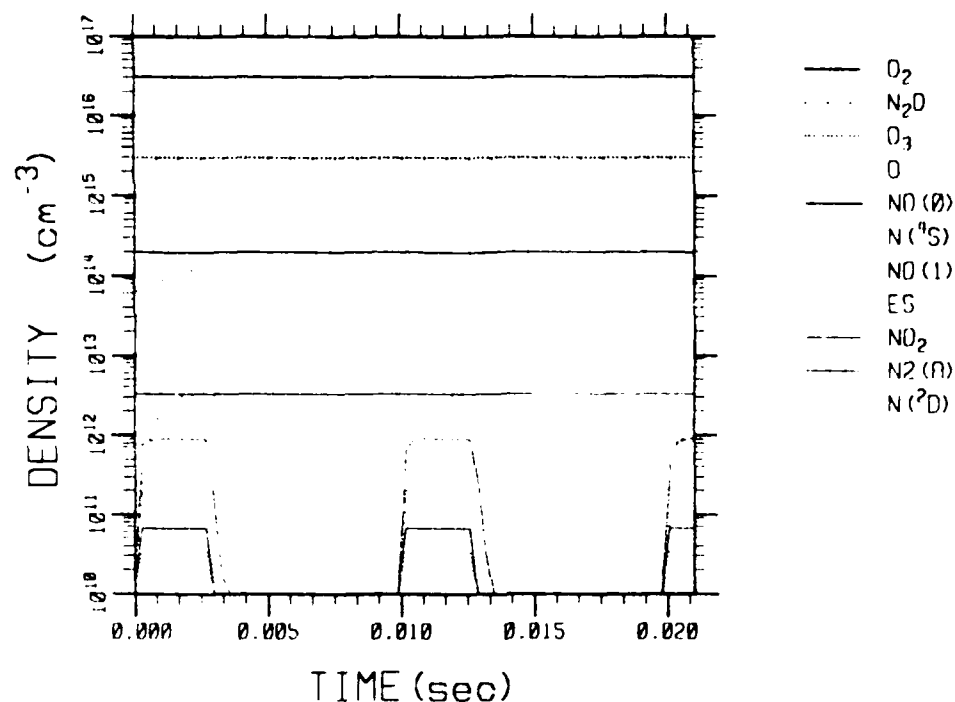


Figure 11. Simulated Concentrations of Beam Coated Species after Steady State has been Established. Electron Beam Current of 1 mA, Voltage 35 kv Irradiating 49 torr N_2 and 1 torr O_2 . Beam on for 2.7 ms Followed by 7.3 ms off. Electron Dissociation of N_2 is Assumed to be $\eta = .60$.

balanced by the flow time. In order to conserve computer time, quasi-steady concentrations were extrapolated from short computer runs, then substituted into the code as initial concentrations so as to obtain steady state populations of all species. Steady state was confirmed when the concentration for each reagent species was the same over two repetitions of the electron beam pulse.

The net amount of NO formed per electron beam pulse was found to be a very sensitive function of the ratio of $N(^2D)/N(^4S)$ produced during the primary ionization in Reaction R(25). We thus define a ratio $\eta = N(^2D)/[N(^4S) + N(^2D)]$. Figure 11 shows the predicted concentrations of minor species after steady state has been established for $\eta = .60$ and one torr of O_2 . Note that concentrations of both O_3 and N_2O rise to 1/10 that of O_2 .

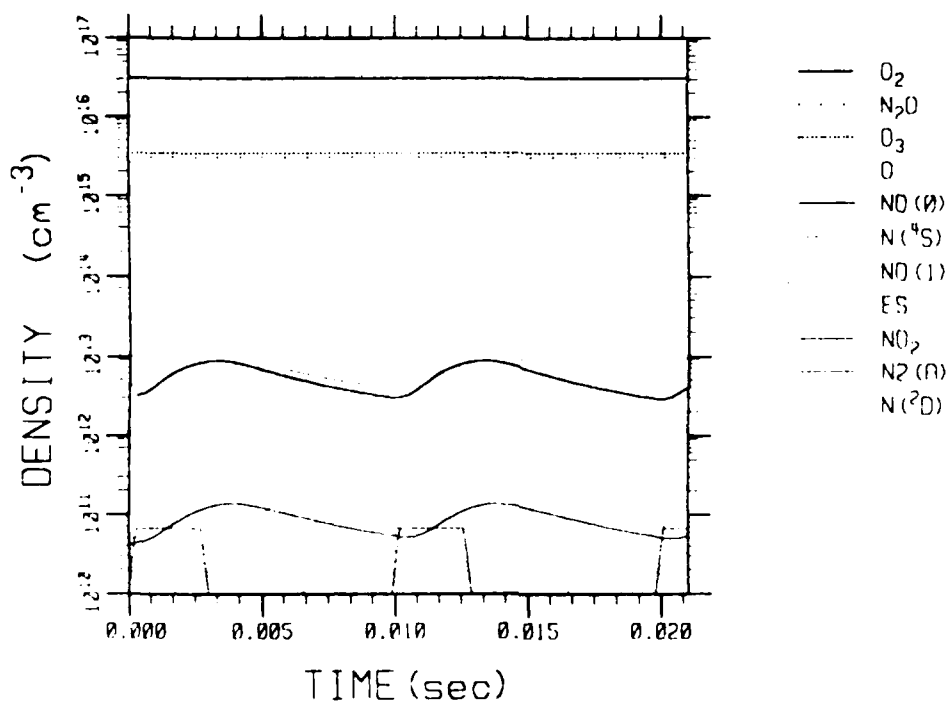


Figure 12. Same as Figure 11 Except $\eta = .50$.

while the NO concentration is a factor of 15 lower. The creation of $v = 0$ NO via Reaction R(20a) was assumed to be equal to Reaction R(20b) in this figure. Changes by a factor of 3 in Reaction R(20a) would increase the $v = 0$ population by less than 2% while decreasing Reaction R(20b) by a factor of 2. The measurement of the steady state NO($v = 0$) therefore does not appear to be sensitive to the $v = 0$ branching given in Reaction R(20a). Simulation of the same conditions as in Figure 11, except that $\eta = .50$ is presented in Figure 12. While a substantial amount of NO builds up when $\eta = .60$, virtually no NO build up is seen when $\eta = .50$. The variation of NO ($v = 0$) and N(4S) with electron beam operation is seen to vary by a factor of 3 from beam on to beam off. This is because of the very low residual NO predicted to be left in the chamber between electron beam pulses.

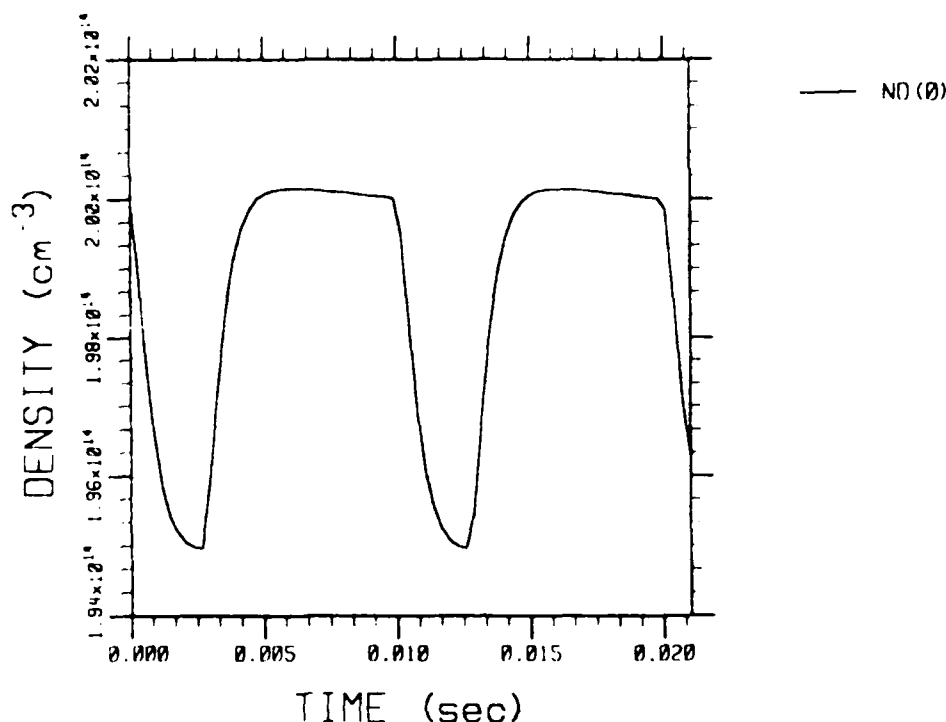


Figure 13. Change in NO ($v = 0$) Concentration with Time Displayed with Expanded Density Scale of Figure 10.

In all cases where an appreciable steady state concentration of NO is formed, the majority of the beam created species such as N atoms, ions, and secondary electrons reach steady state rapidly when the beam is turned on, and are removed rapidly when the beam is turned off. The species NO, NO₂, O₃, O and N₂O remain when the beam is off. Of these only the concentration of O atoms changes appreciably on the time scale between electron beam pulses. Thus the rate of any individual reaction can be readily approximated based on steady state concentrations of reactants, with the single exception of O atom.

During the course of the electron beam pulse, the NO ground state population decreases by $5 \times 10^{12} \text{ cm}^{-3}$ or 0.2 NO per ion pair formed. This is shown in Figure 13. The density scale in this plot has been expanded to show the transient NO on top of the steady state population. During the

beam pulse. Reaction R(20) produces while Reaction R(21) removes NO. Since the majority of NO in the $v = 0$ level is present before the electron beam pulse, Reaction R(21) removes more $v = 0$ than Reaction R(20) produces. The population in the vibrationless state decreases sharply during the beam pulse, and then increases as the vibrationally excited NO is relaxed into the vibrationless level. Changing the internal branching ratio for production of $v = 0$ by a factor of 3 has virtually no effect on the magnitude of the decrease. A net decrease of NO from flow is superimposed on these two processes to give the slight negative slope to the NO concentration when the beam is off. Vibrationally hot NO is also removed by $N(^4S)$. However, the fraction of NO ($v \geq 1$) removed is much smaller than the fractional increase in the upper levels due to formation. The change in $NO(v = 0)$ is thus anticorrelated with the NO in the vibrationally hot levels.

The simulation chemistry is very different when the NO steady state concentration is insufficient to consume all the $N(^4S)$ during the electron beam pulse. This is the case when η is 0.50 as shown in Figure 14. Because the residual NO is less than that formed during the electron beam pulse, the $NO(v = 0)$ is correlated with the formation by Reaction R(20). In this case the populations of $N(^4S)$, NO and NO_2 become strongly time dependent. The NO concentration increases during the beam pulse, and decreases after termination of the electron beam due to reaction with $N(^4S)$. The variation in NO ground state concentration is 6×10^{12} , or the same order of magnitude per ion pair as for $\eta = 0.60$.

The steady state populations calculated for NO are plotted as a function of O_2 concentration in Figure 15 for $\eta = 0.50$, 0.55, and 0.60. Superimposed onto these curves are the measured NO concentrations from Figure 5. The pathlength in which the column density was converted to number density was chosen to be 6.6 cm. The calculated densities for $\eta = 0.55$ and 0.60 are in reasonable agreement with both the magnitude and curvature of the observed relationship of NO concentration to O_2 concentration for O_2 concentrations greater than 1 torr. The simulation based on $\eta = 0.5$ predicts an onset of observable NO at substantially higher

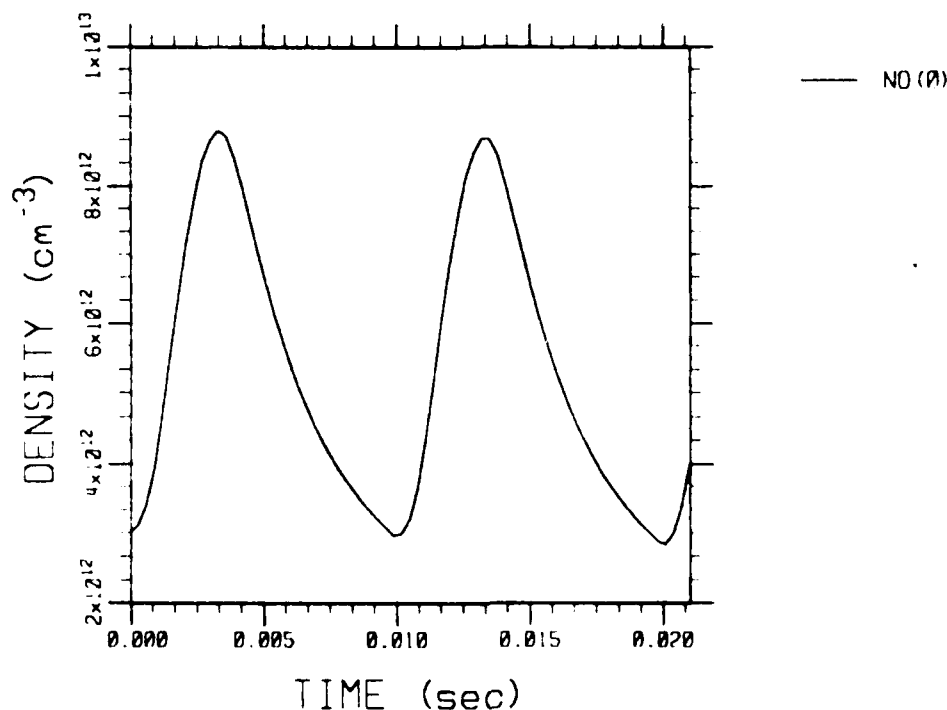


Figure 14. Change in NO ($v = 0$) Concentration with Time.
Expanded Scale from Figure 12.

O_2 pressures, and fails to display the observed leveling off of NO population at higher O_2 pressures. All simulations underestimate the concentration of NO at O_2 concentrations below 1 torr. This is due in part to the assumption made in Reaction R(50) that the product of recombination of N_3^+ is only $N(^4S)$.

The absolute magnitude of the calculated NO signal is largely dependent on the amount assumed for the electron beam irradiation width. These calculated signals are also somewhat influenced by other, minor, reactions. A full matrix using all of the reactions has not yet been carried out. Effects of diffusion out of the central volume would tend to dilute the NO in the central core, and thus, would mean that these calculations are a slight overestimate of the total concentrations.

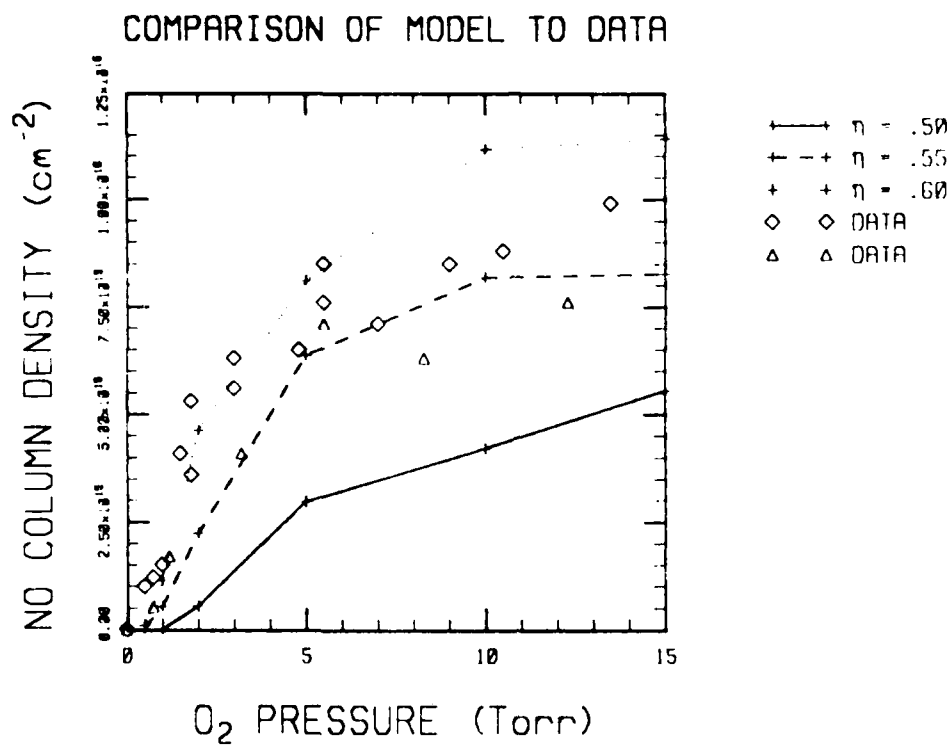


Figure 15. Comparison of NO Column Density Using $\eta = .50$, .55 and .60 to Data Points from Figure 5.

The change in $\text{NO}(v = 0)$ during the electron beam pulse gives the transient signal which we attempted to measure in LABCEDE. This signal was shown to be both the branching ratio η and the partial pressure of O_2 . The $\text{N}(^2\text{D})$ reacts totally with the O_2 just as the $\text{N}(^4\text{S})$ reacts totally with the NO. Since the total N produced per ion pair is a function mainly of the pressure, the net NO concentration reaches a steady state value. At high O_2 equal to the net excess of $\text{N}(^2\text{D})$ to $\text{N}(^4\text{S})$ made per pulse over the total number of pulses before the NO leaves the cell.

The simulations suggest that at least at low pressures the NO production and removal are dominated by the $\text{N}(^2\text{D})$ reaction. The measured values of NO can be explained by assuming that the excited state N atom production of $\sim .55$ at pressures of $< .7$ and higher show that the branching ratio η is $\sim .55$.

AD-A198 964

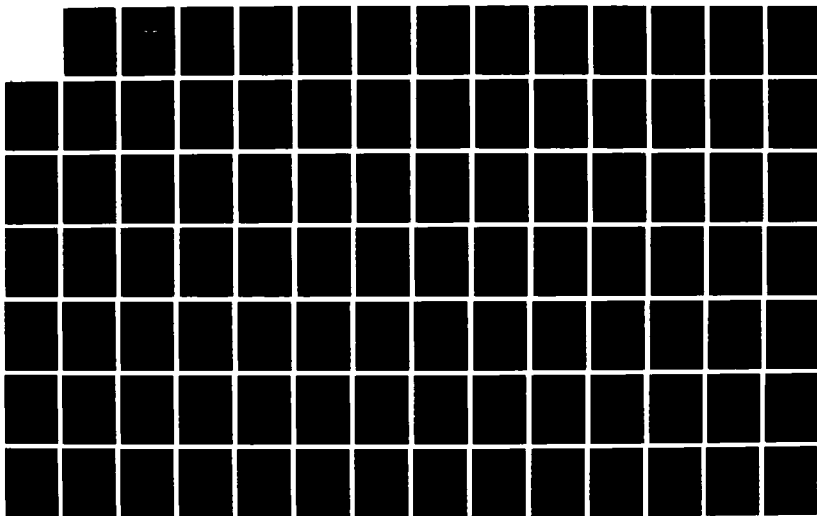
STUDY OF POLYATOMIC DYNAMICS IN THE ATMOSPHERE(U)
SPECTRAL SCIENCES INC BURLINGTON MA F BIEN ET AL
25 MAR 87 5551-TR-116 AFGL-TR-87-0223 F19628-84-C-0029

2/3

UNCLASSIFIED

F/G 4/1

NL





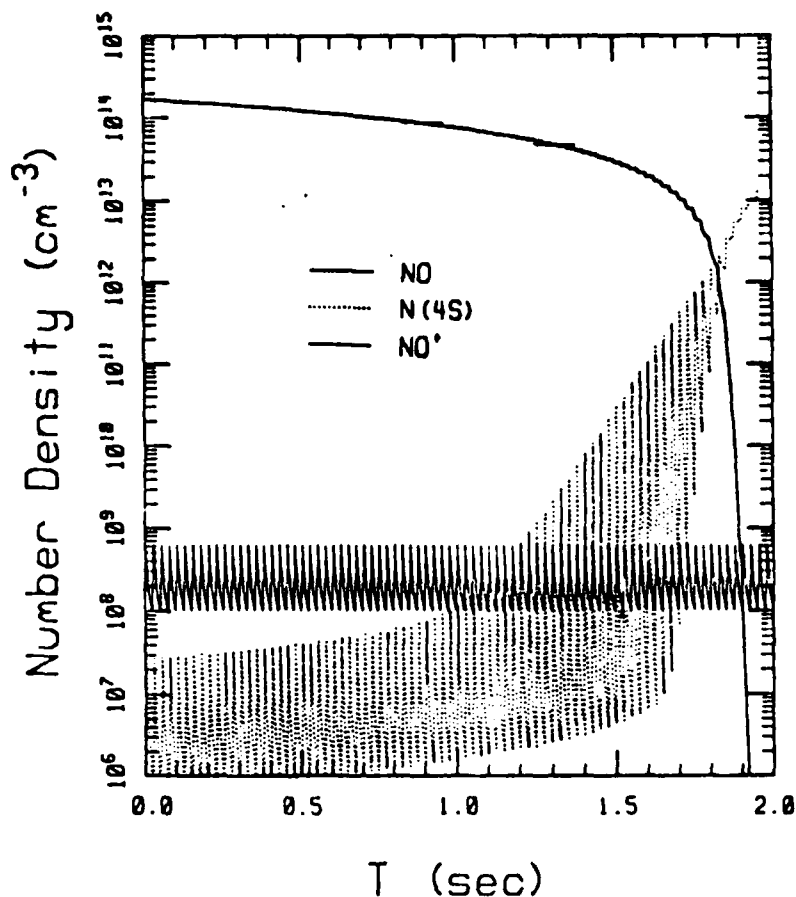


Figure 16. Simulation of the NO Morphology for a .5 mA Electron Beam Irradiating 5.5 m torr NO in 55 torr N₂.

linearly dependent on the excess N(²D). Possible effects of electron beam heating of the gas, as well as other possible mechanisms for NO production were also tested and are discussed below.

5.2 Simulations of NO Titration

When there is no O₂ in the chamber, all of the N(²D) is quenched to N(⁴S). Thus, even if we intentionally introduce some NO, it would be destroyed. This is shown by the titration experiment in Figure 8. The amount of NO destroyed is equal to the total N atom production plus the ion transfer from N₂⁺ and N⁺. Because the atomic nitrogen species stay around until they collide with an NO, N atom concentrations build slowly until they either disappear due to flow, or react with NO. The time history of this titration is shown in Figure 16. This titration is for the case of

0.5 ma electron beam into a chamber filled with 55 torr N_2 and 5.5 mtorr NO. The electron beam duty cycle was chosen to be 1.25 ms on and 23.5 ms off. The NO is seen to be completely titrated on a 1.9 s time scale. The $N(^4S)$ within the chamber was not allowed to flow out of the interaction region in this calculation. By adding flow to the depletion of beam excited species, a residue of NO is left within the chamber which depends on the electron beam current. Using this technique, it was found that there was approximately $2. \pm .2$ NO destroyed per ion pair produced.

5.3 Other Effects Not in the Model

Several effects which could contribute to NO formation which have not been included in the model are discussed below, and their relative contributions to the total NO production assessed. It is convenient to quantify their effects by putting their contributions in terms of NO/IP. For the sake of comparison, approximately 0.72 NO is formed per ion pair in the current model, and 0.48 is destroyed, leaving an excess of 0.24 NO/ion pair which builds up to a level until it can effectively compete with O_2 in the reaction set.

Heating Due To The Beam

The model of the NO formation within the chamber disregards the heating which takes place associated with the energy deposition into the chamber. Since about 1/2 of the 35 watts of beam power ends up as heat, the net increase in temperature is

$$\dot{Q} = 18 \text{ watts} = \dot{M} c_p \Delta T. \quad (74)$$

where \dot{M} is the mass flow-rate equal to 2.83×10^{-3} moles/sec, c_p is the heat capacity equal to $7/2 R$ where R is 8.3166 Joules/mole-K. Thus, if the beam was on continuously, and no heat was transferred to the walls, the mean gas temperature could rise as much as 219 K. This heating would never be a problem at 1/20 duty cycle, but could cause a mean temperature rise of 73 K for the duty cycle of 1/3 as used in Figure 5 and the model simulations.

The heating of the gas is not uniform, however, and the majority of the energy is deposited in the central core whose radius is given by Equation (14). The first order correction to the uniform temperature model is thus one of solving the heat transfer equation for a cylinder of N_2 . The heat transfer rate in a purely static chamber is

$$\dot{Q} = \frac{2\pi kL(\Delta T)}{\ln(r/r_{1/2})} \quad (75)$$

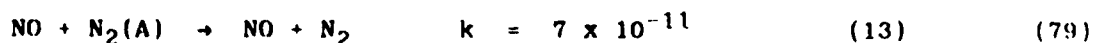
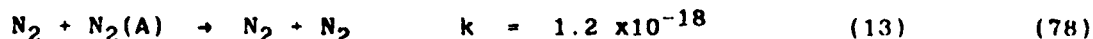
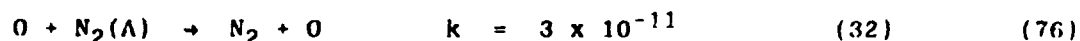
where k is the thermal conductivity of N_2 , equal to 2.62×10^{-4} w/cm²K, (33) at 300 K and increases with $T^{1/2}$. The maximum temperature gradient which can be supported by 50 torr of N_2 becomes 14 K for 1/20 duty cycle and 75 K for 1/3 duty cycle. Thus, at the 1/3 duty cycle, the temperature in the center of the chamber can be as much as 100 K higher than the room temperature.

A rise in temperature of 100 K would change the chemistry mainly in Reaction R(57). Here, the very large exponential term would increase this rate by a factor of 4. This reaction still produces only a small fraction of all of the NO produced, however.

Nitrogen Triplet State Chemistry

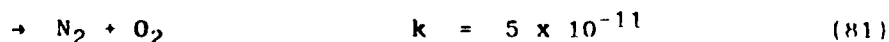
$N_2(A)$ state is expected to be a primary product of electron bombardment of N_2 . (34) It is extremely stable with respect to radiative relaxation and collisional quenching with N_2 . In our simulation we assumed that it was quenched primarily by reaction with O_2 . At low O_2 concentrations, it will also react with O, NO, and possibly O_3 . (35)

33. E. R. G. Eckert and R. M. Drake, Heat and Mass Transfer, McGraw-Hill Book Company, Inc., New York, NY (1959).
34. W. L. Borst and M. Imami, "Production of Secondary Electrons in Nitrogen by Fast Electrons and Simultaneous Excitation of N_2 Bands," J. Appl. Phys., **44**, 3 (1973).
35. L. G. Piper, G. E. Caledonia, and J. P. Kennealy, "Rate Constants for Deactivation of $N_2(A^3\Sigma(.))_u^+$, $v^1 = 0, 1$ by O," J. Chem. Phys., **75**, 6 (1981).



At low O_2 concentrations the O atom concentration can approach within two orders of magnitude of the O_2 concentration in the chamber. As O atoms are 15 times more effective in quenching $N_2(A)$ than O_2 atoms, roughly 10% of the $N_2(A)$ will react with O atoms. If the reaction proceeded primarily by R(77) to form NO this would lead to an additional production of NO of 0.04/IP. This reaction would in turn add somewhat to NO production when 0.1 to 1 torr O_2 is present in the chamber, while not materially affect the higher O_2 results.

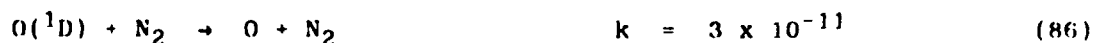
NO can also be produced indirectly from $N_2(A)$ by reactions of the N_2O made in the reaction of $N_2(A)$ with O_2 , R(73). If the branching ratio for N_2O is of the order of 50% as reported by Zipf,⁽³⁰⁾ then steady state N_2O populations approach 3×10^{15} in the reaction chamber. N_2O reacts only with excited state N and O atoms,⁽³⁶⁾ and perhaps O_3^* .⁽³⁷⁾



36. N. Goldstein, G. D. Greenblatt, and J. R. Weisenfeld, "Observation by Laser Ionization Spectroscopy of Vibrationally Excited Nitric Oxide Following $O(^1D_2) + N_2O \rightarrow 2NO$," Chem. Phys. Lett., 96, 4 (1983).

37. J. F. Steinfield, S. M. Adler-Golden, and J. W. Gallagher, "Critical Survey of Data on the Spectroscopy and Kinetics of Ozone in the Upper Atmosphere," Submitted to J. Phys. Chem. Ref. Data (1987).

The reaction of $O(^1D)$ with N_2O is slightly faster than the quenching rate of $O(^1D)$ by N_2 or O_2 :⁽²⁴⁾



Therefore roughly 5×10^{-3} NO are formed per $O(^1D)$. $O(^1D)$ is formed primarily from the recombination reaction of O_2^+ , R(42), to produce at most one $O(^1D)$ /IP. Therefore the rate of NO production by this channel can be no more than 5×10^{-3} /IP.

Excited Ozone

Recent evidence supplied by Locker et al.⁽³⁸⁾ indicates that approximately half the ozone formed in the reaction of O and O_2 , Reaction R(67), is formed in a metastable state, O_3^* . O atoms are formed in many reactions including the electron bombardment of O_2 , the reactions of the ions N^+ and N_3^+ with O_2 , and the recombination reaction of O_2 are secondary electrons. These lead to a O atom production rate between .5/IP and 2/IP and a minimum O_3^* production rate of .2/IP. There are several possible reactions of O_3^* which may lead to substantial NO production. In contrast to all previously discussed sources of NO these sources are relatively insensitive to the concentration of $[O_2]$, and therefore may be important in establishing the NO steady state population at low O_2 concentrations. O_3^* is relaxed slowly by N_2 on a millisecond time scale:



Therefore, O_3^* will have a characteristic lifetime of the order of 0.5 ms and the population of O_3^* will follow the population of O with a proportionality:

38. J. R. Locker, J. A. Joens, and E. J. Bair, "Metastable Intermediate in the Formation of Ozone by Recombination," Submitted to J. Chem. Phys. (1987).

$$[O_3^*]/[O] = 2 k_{66}/k_{88} [O_2] = 6 \times 10^{-19} [O_2] \quad (89)$$

When $[O_2]$ is less than 10^{17} cm^{-3} , O atom concentrations are substantial, and O_3^* populations will be of the order of 10^{12} cm^{-3} . This is sufficiently large for O_3^* to compete with NO for $N(^4S)$ atoms.



If the reaction proceeds with a near gas kinetic rate, it could consume as much as $0.3 N(^4S)/IP$, producing an equivalent amount of NO.

O_3^* may also react with N_2O to form some odd nitrogen species which equilibrates with NO. Since there are no major competing reactions for the depletion of N_2O , such a reaction would completely deplete all the N_2O if it proceeded with a rate constant of the order of $10^{-12} \text{ cm}^{-1} \text{ s}^{-1}$. Therefore if $N_2(A)$ does indeed react with O_2 to form $2NO$ with .5 branching ratio, and if O_3^* reacts with N_2O , the result is a net production of $0.4 NO/IP$.

Translationally Excited Atomic Nitrogen

Solomon⁽³⁹⁾ has suggested that translationally excited $N(^4S)$ atoms can be responsible for a substantial amount of NO production in the upper atmosphere. The reaction of $N(^4S)$ with O_2 has a 0.3 eV activation energy. It has been suggested that the preexponential term at high temperatures is 5 times greater than that at low temperatures,⁽⁴⁰⁾ i.e., $2 \times 10^{-11} \text{ cm}^3 \text{ s}^{-1}$. Therefore the reaction should proceed with a cross section between .03 - .1 gas kinetic. Most of the $N(^4S)$ atoms are produced in Reaction R(25) with approximately 5 eV of translational energy. Therefore it will take several collisions for the translational energy to be reduced to below the activation energy of the reaction. An upper limit

39. S. Solomon, "The Possible Effects of Translationally Excited Nitrogen Atoms on Lower Thermospheric Odd Nitrogen," Planet. Space Sci., 31, 1 (1983).

for the number of collisions required to relax the hot atoms can be established assuming totally elastic collisions with N_2 . Following Solomon, the energy of the atom after n collisions can be expressed as:

$$E_n = E_0 e^{-kn} \quad k = \frac{1 - (1-\gamma)(1-\ln(1-\gamma))}{\diamond} \quad (91)$$

$$\gamma = \frac{4M_1M_2}{(M_1+M_2)^2} \quad (92)$$

This establishes an upper limit of five collisions to relax the atoms to 0.3ev, and an upper limit on the fraction of hot $N(^4S)$ atoms which react with O_2 as $0.3[O_2]/[N_2]$. this effect is then insignificant at low O_2 concentrations. At $[O_2] = 10$ torr, it is equivalent to a change in the excited state N atom population of no more than 3%.

Vibrationally Excited O_2

Vibrationally excited O_2 can be produced directly by the recombination of O_4^+ , or by e-v transfer from $N_2(A)$ and electronically excited state O_2 . These reactions result in the vibrational excitation of at least 1 O_2 molecule per ion pair. O_2 can also be vibrationally excited by v-v transfer from N_2 , or from t-v transfer from hot atoms. Each of these processes can result in the excitation of multiple quanta of vibration in O_2 . V-v transfer among the various constituents is very rapid but since O_2 has the lowest vibrational quanta of the major species, relaxation of O_2 $v = 1$ is very slow.

If the rate of relaxation by N_2 is as low as 10^{-13} , perhaps as much as $0.1/EP$ O_2^* can be built up during the course of electron beam irradiation. O_2 $v = 1$ has enough energy to overcome the activation barrier to reaction with $N(^4S)$, and therefore may react with $N(^4S)$ with nearly the same rate as NO .

40. W. E. Wilson, J. Chem. Phys., **46**, 2017 (1967).

If the above two statements are true, then O_2^* will remove $0.1 N(^4S)/IP$, and form an equivalent amount of NO. This would vary linearly with O_2 concentration.

$O_2(^1\Delta)$

$O_2(^1\Delta)$ is stable with respect to all major species in the reaction chamber except N atoms on a one second time scale. It reacts with $N(^4S)$ an order of magnitude more slowly than O atoms and four orders of magnitude more slowly than with NO:



Therefore it will not seriously effect the NO production unless somehow all the O_2 is converted to $O_2(^1\Delta)$. This would require a production rate of the $\gg 1/IP$.

Other Excited O_2 Species

There is recent evidence that O_2 is formed in the 4-5 eV states, $A^3\Sigma_u^+$, $A'^3\Delta_u$, and $c^1\Sigma_u^-$, when excited by the electron beam.⁽⁴¹⁾ These levels could lead to formation of NO through $N(^4S)$. Since both O_2^* and $N(^4S)$ are formed in concentrations of one per ion pair, This channel could explain some of the apparent excess of $N(^2D)$ needed to explain the observations. Unfortunately, very little information is available on the formation or quenching of these O_2 states.

41. T. Slanger and V. Degen, "The Rotationally-Resolved Oxygen Afterglow, 373-474 nm," Planet. Space Sci., 34, 10 (1986).

6. SUMMARY AND CONCLUSIONS

Nitric Oxide ($v = 0$) formation from electron irradiation of N_2 with trace quantities of O_2 has been measured in absorption. Both the steady state concentration and the transient change of NO were measured using a pulsed electron beam. The results of these measurements were modeled using an extensive computer model based on the CHEMKIN code. The steady state concentration of NO was found to be a very sensitive function of the ratio of $N(^2D)$ to $N(^4S)$ formed by direct electron dissociation. Measured data fit a ratio of 55/45 to 60/40, not inconsistent with findings by Zipf and McLaughlin⁽⁴²⁾ and those used in models by Rees and Romick.⁽⁴³⁾ Other reactions which may affect this ratio have been assessed.

No transient NO build-up was measured in LABCEDE, placing the upper limit of $4 \times 10^{13} \text{ cm}^{-2}$ on the transient column density. The limit on the detection sensitivity was found to be due to the frequency jitter of the laser line across the absorption peak of the NO. This jitter limited the detection of transients to the larger of 5% of the total absorption signal, or 0.08% of the total laser intensity.

The transient NO signal was also modeled. These models of the NO signals during beam irradiation showed a net loss of $v = 0$ during electron beam irradiation due to $N(^4S)$ formation by the electron beam. The net

42. E. C. Zipf and R. W. McLaughlin, "On the Dissociation of Nitrogen by Electron Impact and by E.U.V. Photo-Absorption," Planet. Space Sci., **26**, 449 (1978).
43. M. H. Rees and G. J. Romick, "Atomic Nitrogen in Aurora: Production, Chemistry, and Optical Emissions," J. Geophys. Res., **90**, 9871 (1985).

transient signal was found to be equal to a change of $2 \times 10^{12} \text{ cm}^{-3}$ averaged over 5.5 cm. This signal would be a factor of 2 below the transient detection limit established in the experiment.

Other sources of NO which could account for the observations, but were not included within the model have been discussed. The most likely sources which would help explain the results are the formation of O_2^* and O_3^* . These processes would either enhance the $\text{N}(^2\text{D})$ populations, as is the case of O_2^* , or depress the $\text{N}(^4\text{S})$ population as in the case of O_3^* . As yet, there is insufficient evidence to either support or dismiss either process.

7. REFERENCES

1. W. P. Reidy, T. C. Degges, A. G. Hurd, A. T. Stair, Jr., and J. C. Ulwick, "Auroral Nitric Oxide Concentration and Infrared Emission," J. Geophys. Res., **87**, 3591 (1982).
2. G. E. Caledonia and J. P. Kennealy, "No Infrared Radiation in the Upper Atmosphere," Planet. Space Sci., **30**, 1043 (1982).
3. B. D. Green, G. E. Caledonia, and R. E. Murphy, "A Determination of the Nitric Oxide Einstein Coefficient Ratios," J. Quant. Spectrosc. Radiat. Transfer, **26**, 215 (1981).
4. B. D. Green, G. E. Caledonia, L. G. Piper, J. S. Goela, A. Fairbairn, and R. E. Murphy, "LARCEDE Studies," Air Force Geophysics Laboratory Rpt. No. AFGL-TR-82-0060 (September 1981). ADA114389
5. B. D. Green, G. E. Caledonia, R. E. Murphy, and F. X. Robert, "The Vibrational Relaxation of NO($v=1-7$) by O₂," J. Chem. Phys., **76**, 2441 (1982).
6. B. D. Green, L. G. Piper, G. E. Caledonia, P. F. Lewis, H. C. Murphy, and W. J. Marinelli, "Fluorescence from Electron Irradiated Gases in Refurbished Labcede," Air Force Geophysics Laboratory Rpt. No. AFGL-TR-84-0218 (September 1985). ADA161674
7. C. Amiot, R. Bacis, and G. Guelachvili, "Infrared Study of the X²II_v - O, 1, 2 Levels of ¹⁴N¹⁶O. Preliminary Results on the $v = 0, 1$ Levels of ¹⁴N¹⁷O, ¹⁴N¹⁸O, and ¹⁵N¹⁶O," Can. J. Phys., **56**, 251 (1978).
8. P. K. Falcone, R. K. Hanson, and C. H. Kruger, "Tunable Diode Laser Measurements of the Band Strength and Collision Halfwidths of Nitric Oxide," J. Quant. Spectrosc. Radiat. Transfer, **29**, 205 (1983).
9. A. S. Pine and K. W. Nill, "Molecular-Beam Tunable-Diode-Laser Sub-Doppler Spectroscopy of A-Doubling in Nitric Oxide," J. Mol. Spec., **74**, 43 (1979).
10. G. N. Whyte, Radiation Research, **18**, 255 (1963).
11. R. E. Center, "Plural and Multiple Scattering of Fast Electrons in Gases," Phys. Fluids, **13**, 3 (1970).
12. A. Cohn and G. E. Caledonia, "Spatial Distribution of the Fluorescent Radiation Emission Caused by an Electron Beam," J. Appl. Phys., **41**, 9 (1970).
13. T. R. Marrero and E. A. Mason, "Gaseous Diffusion Coefficients," J. Phys. Chem. Ref. Data, **1**, 1 (1972).

14. R. J. Kee, J. A. Miller, and T. H. Jefferson, "CHEMKIN: A General-Purpose, Problem-Independent, Transportable, Fortran Chemical Kinetics Code Package," Sandia Laboratories Rpt. No. SAND80 8003 (1980).
15. M. H. Bortner and T. Baurer, "Reaction Rate Handbook Second Edition," Defense Nuclear Agency Rpt. No. DNA 1948H (March 1972).
16. M. R. Torr, R. G. Burnside, P. B. Hays, A. I. Steward, D. G. Torr, and J. C. G. Walker, "Metastable 2D Atomic Nitrogen in the Mid-Latitude Nocturnal Ionosphere," J. Geophys. Res., **81**, 1 (1976).
17. W. B. DeMore, J. J. Margitan, M. J. Molina, R. T. Watson, D. M. Golden, R. F. Hampson, M. J. Kurylo, C. J. Howard, and A. R. Ravishankara, "Chemical Kinetics and Photochemical Data for Use in Stratospheric Modeling," NASA, Jet Propulsion Laboratory, Pasadena, CA, JPL Publication 85-37 (July 1985.)
18. L. J. Kieffer and G. H. Dunn, "Electron Impact Ionization Cross Section Data for Atoms, Atomic Ions, and Diatomic Molecules: I. Experimental Data," Rev. Mod. Phys., **38**, 1 (1966).
19. R. S. Stolarski and A. E. S. Green, "Calculations of Auroral Intensities from Electron Impact," J. Geophys. Res., **72** 3967 (1967).
20. D. F. Strobel, E. S. Oran, and P. D. Feldman, "The Aeronomy of Odd Nitrogen in the Thermosphere 2. Twilight Emissions," J. Geophys. Res., **81**, 3745 (1976).
21. C. D. Sutherland and J. Zinn, "Chemistry Computations for Irradiated Hot Air," Los Alamos Scientific Laboratory, Los Alamos, NM, Rpt. No. LA-6055-MS (1975).
22. R. R. O'Neil, E. T. P. Lee, and E. R. Huppi, "Auroral $O(^1S)$ Production and Loss Processes: Ground Based Measurements of the Artificial Auroral Experiment Precede," J. Geophys. Res., **84**, 823 (1979).
23. M. A. Smith, V. M. Bierbaum, and S. R. Leone, "Infrared Chemiluminescence from Vibrationally Excited NO^+ : Product Branching in the $N^+ - O_2$ Ion-Molecule Reaction," Chem. Phys. Lett., **94**, 398 (1983).
24. C. Huang, M. A. Biondi, and R. Johnsen, "Variation of Electron- NO^+ ion Recombination Coefficient with Electron Temperature," Phys. Rev. A, **11**, 901 (1985).
25. D. Kley, G. M. Lawrence, and E. J. Stone, "The Yield of $N(^2D)$ Atoms in the Dissociative Recombination of NO^+ ," J. Chem. Phys., **66**, 4157 (1977).

26. T. G. Slanger and G. Black, "Quenching of $N(^2D)$ by N_2 and H_2O ," J. Chem. Phys., 64, 44 (1976).
27. A. Rahbee and J. J. Gibson, "Rate Constants for Formation of NO in Vibrational Levels $v=2$ Through 7 from the Reaction $N(^4S) + O_2 \rightarrow NO^+ + O$," J. Chem. Phys., 74, 5143 (1981).
28. R. R. Herm, B. J. Sullivan, and M. E. Whitson, "Nitric Oxide Vibrational Excitation from the $N(^4S)+_2$ Reaction," J. Chem. Phys., 79, 2221 (1983).
29. F. Westley, "Tables of Experimental Rate Constants for Chemical Reactions Occurring in Combustion (1971-1977)," National Bureau of Standards, Washington, DC, Rpt. No. NBSIR 81-2254 (April 1981).
30. M. P. Iannuzzi and F. Kaufman, "Rate Constants for the Reaction of $N_2(A^3\Sigma_u^+, v = 0, 1, \text{ and } 2)$ with O_2 ," J. Phys. Chem., 85, 2163 (1981).
31. L. G. Piper, G. E. Caledonia, and J. P. Kennealy, "Rate Constants for Deactivation of $N_2(A)V^1 = 0, 1$ by O_2 ," J. Chem. Phys., 74, 2888 (1981).
32. E. C. Zipf, Nature, 287, 523 (1980).
33. E. R. G. Eckert and R. M. Drake, Heat and Mass Transfer, McGraw-Hill Book Company, Inc., New York, NY (1959).
34. W. L. Borst and M. Imami, "Production of Secondary Electrons in Nitrogen by Fast Electrons and Simultaneous Excitation of N_2 Bands," J. Appl. Phys., 44, 3 (1973).
35. L. G. Piper, G. E. Caledonia, and J. P. Kennealy, "Rate Constants for Deactivation of $N_2(A^3\Sigma_u^+, V^1 = 0, 1)$ by O_2 ," J. Chem. Phys., 75, 6 (1981).
36. N. Goldstein, G. D. Greenblatt, and J. R. Weisenfeld, "Observation by Laser Ionization Spectroscopy of Vibrationally Excited Nitric Oxide Following $O(^1D_2) + N_2O \rightarrow 2NO$," Chem. Phys. Lett., 96, 4 (1983).
37. J. F. Steinfield, S. M. Adler-Golden, and J. W. Gallagher, "Critical Survey of Data on the Spectroscopy and Kinetics of Ozone in the Upper Atmosphere," Submitted to J. Phys. Chem. Ref. Data (1987).
38. J. R. Locker, J. A. Joens, and E. J. Bair, "Metastable Intermediate in the Formation of Ozone by Recombination," Submitted to J. Chem. Phys. (1987).
39. S. Solomon, "The Possible Effects of Translationally Excited Nitrogen Atoms on Lower Thermospheric Odd Nitrogen," Planet. Space Sci., 31, 1 (1983).

40. W. E. Wilson, J. Chem. Phys., 46, 2017 (1967).
41. T. Slinger and V. Degen, "The Rotationally-Resolved Oxygen Afterglow, 373-474 nm," Planet. Space Sci., 34, 10 (1986).
42. E. C. Zipf and R. W. McLaughlin, "On the Dissociation of Nitrogen by Electron Impact and by E.U.V. Photo-Absorption," Planet. Space Sci., 26, 449 (1978).
43. M. H. Rees and G. J. Romick, "Atomic Nitrogen in Aurora: Production, Chemistry, and Optical Emissions," J. Geophys. Res., 90, 9871 (1985).

APPENDIX A

FORMULAS FOR TRANSFORMING FROM INTERNAL
COORDINATES TO ECKART FRAME COORDINATES
OF A SYMMETRIC TRIATOMIC MOLECULE

FORMULAS FOR TRANSFORMING FROM INTERNAL COORDINATES TO ECKART FRAME COORDINATES OF A SYMMETRIC TRIATOMIC MOLECULE

Steven M. ADLER-GOLDEN

Spectral Sciences, Inc., 111 South Bedford St., Burlington, Massachusetts 01803, USA

and

Grady D. CARNEY

Department of Chemistry, Allegheny College, Meadville, Pennsylvania 16335, USA

Received 6 October 1984

Analytical formulas are presented for transforming from internal coordinates (r_1, r_2, θ) of a symmetric triatomic molecule to a set of coordinates which satisfy the Eckart conditions. An expression is also given for the angle β by which the instantaneous angle bisector is rotated in the Eckart frame.

Molecular properties which depend on the instantaneous nuclear geometry, such as the potential energy and dipole moment, may be expressed in any of several coordinate systems. Internal coordinates, consisting of bond lengths and internal angles, are both convenient and physically informative, and they are coordinates typically used in *ab initio* electronic structure calculations. Internal coordinates do not explicitly define the molecule's orientation in space, however. For this purpose one utilizes the Eckart [1] reference frame, in which for a specific geometry defined as the equilibrium there is no net translation or rotation of the molecule.

The Eckart frame is highly useful in spectral analysis for several reasons. In the Eckart frame one can construct a set of orthonormal coordinates, such as the conventional normal coordinates as well as symmetry [2] and "t" [3] coordinates, in which the vibrational Hamiltonian is conveniently written. For example, an *ab initio* potential energy surface calculated on a grid of internal coordinate geometries can be transformed to normal coordinate space to generate normal coordinate force constants; then, standard methods can be used to calculate vibrational energy levels. This transformation is avoided when an internal coordinate formulation of the vibrational Hamiltonian

is used, as in the case of a triatomic molecule where the exact Hamiltonian has been given [4,5]. However, even with the latter Hamiltonian, knowledge of the Eckart frame is still required for the calculation of vector properties such as dipole moment matrix elements, since these properties depend on the molecule's orientation. In particular, it has been shown [6-8] that for the accurate calculation of infrared intensities the dipole moment must be expressed in terms of spatial components which are fixed in the Eckart frame. To define these components we need to know the geometrical relationship between the Eckart frame and the internal coordinate reference frame. In a triatomic molecule the key parameter is β , the instantaneous angle of rotation of the valence angle bisector [6-8]. In a symmetric triatomic β is non-zero at asymmetric geometries.

The transformation from internal coordinates to Eckart frame coordinates and the calculation of β have been previously described by Ernler and Krohn [8] for a general triatomic molecule. They developed an iterative algorithm for solving a set of simultaneous, non-linear equations derived from the Eckart conditions, and they used this algorithm to generate normal coordinate expansions of the dipole moment and potential energy surfaces for the water molecule from

0 009-2614/85/\$ 03.30 © Elsevier Science Publishers B.V.
(North-Holland Physics Publishing Division)

The U.S. Government is authorized to reproduce and sell this report. Permission for further reproduction by others must be obtained from the copyright owner.

a grid of *ab initio* data points. Other computer programs are available for generating normal coordinate expansions of molecular properties for larger polyatomics [9,10], but they do not rely on a point-by-point transformation from internal to normal coordinates.

The purpose of this Letter is to point out that in the case of symmetric triatomic molecules the internal to Eckart coordinate transformation and calculation of β reduce to very simple, analytical results, which to our knowledge have not appeared in the literature. While the restriction to symmetric molecules makes the formulas presented here less versatile than the Emler and Krohn method, a number of important molecules fall into this category, including the atmospheric species H_2O , O_3 , CO_2 , and NO_2 . These formulas can serve as a double check on alternative, more general methods, and they may also be useful for developing new analytical relationships between spectroscopic parameters.

Our coordinate definitions are shown in fig. 1. The equilibrium geometry is defined by the bond length r_e and half-angle α , while the instantaneous geometry is defined by r_1, r_2 , and internal angle θ . The Cartesian x and y unit vectors in the Eckart frame are defined as the equilibrium angle bisector \hat{i} and a vector \hat{j} perpendicular to \hat{i} . The as yet unknown angle between r_1 and \hat{i} is denoted ϕ . The components of r_1 and r_2 along \hat{i} and \hat{j} are then given by

$$r_{1x} = r_1 \cos \phi, \quad (1a)$$

$$r_{2x} = r_2 \cos (\theta - \phi), \quad (1b)$$

$$r_{1y} = r_1 \sin \phi, \quad (1c)$$

$$r_{2y} = r_2 \sin (\theta - \phi). \quad (1d)$$

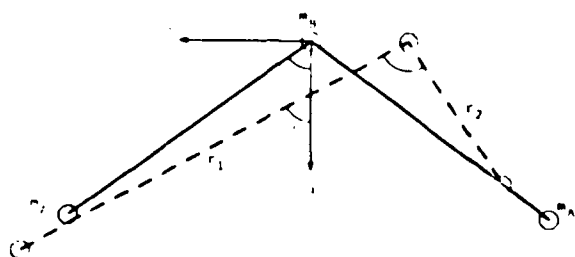


Fig. 1. Schematic diagram of equilibrium (—) and instantaneous (---) molecular geometry.

To derive an expression for the angle ϕ we examine the asymmetric stretching normal coordinate q_3 , which is identical to the symmetry coordinate S_3 given in fig. 55 of Herzberg [2]. We obtain

$$r_{1x} - r_{2x} = 2S_3 \cos \alpha, \quad (2a)$$

$$r_{1y} - r_{2y} = 2pS_3 \sin \alpha, \quad (2b)$$

where $p = 1 + 2m_A/m_B$. Inserting eqs. (1a)–(1d) into eqs. (2a) and (2b) and making use of trigonometric identities, the resulting two equations may be solved simultaneously, yielding

$$\tan \phi = \frac{p(r_1 - r_2 \cos \theta) \tan \alpha + r_2 \sin \theta}{pr_2 \sin \theta \tan \alpha + r_1 + r_2 \cos \theta}. \quad (3a)$$

In the above derivation we have implicitly assumed a bent molecule. The procedure for a linear molecule is the same if it is understood that the Eckart reference frame is chosen to pass through the molecular plane during vibrational motion. The result is

$$\tan \phi = (r_1 - r_2 \cos \theta)/r_2 \sin \theta, \quad (3b)$$

which is the $\alpha = \frac{1}{2}\pi$ limit of eq. (3a).

Having solved for ϕ , we may readily transform to the symmetry coordinates, which are Eckart frame coordinates. From eq. (2b) we have

$$S_3 = (r_{1y} - r_{2y})/2p \sin \alpha, \quad (4)$$

Finally, the definitions of S_1 and S_2 yield

$$S_1 = r_e \sin \alpha - \frac{1}{2}(r_{1y} + r_{2y}), \quad (5)$$

$$S_2 = r_e \cos \alpha/p - (r_{1x} + r_{2x})/2p. \quad (6)$$

In the linear molecule limit, the symmetry coordinates become equivalent to those shown in fig. 25 of Herzberg [2].

Having obtained the symmetry coordinates, transformation to any other set of Eckart orthonormal coordinates is straightforward, since they are linearly related. In particular, the method for transforming from symmetry to normal coordinates may be found in Herzberg [2]. For a linear molecule the symmetry and normal coordinates are identical.

As discussed elsewhere [6–8], the orientation of the Eckart frame relative to the instantaneous geometry enters into the calculation of dipole moment matrix elements. Here, the parameter of interest is the angle

of rotation β between the unit vector \hat{i} and the instantaneous angle bisector \hat{i}_{VAB} . The dipole moment components (μ_{xVAB}, μ_{yVAB}) in the $\hat{i}_{VAB}, \hat{j}_{VAB}$ frame are used to generate the dipole moment components (μ_x, μ_y) in the \hat{i}, \hat{j} (Eckart) frame via the transformation

$$\begin{pmatrix} \mu_x \\ \mu_y \end{pmatrix} = \begin{pmatrix} \cos \beta & -\sin \beta \\ \sin \beta & \cos \beta \end{pmatrix} \begin{pmatrix} \mu_{xVAB} \\ \mu_{yVAB} \end{pmatrix}. \quad (7)$$

From fig. 1,

$$\beta = \phi - \frac{1}{2}\theta. \quad (8)$$

Application of the formulas presented here will be illustrated in a forthcoming publication on ozone vibrational intensities [11].

We gratefully acknowledge the support of the Air Force Geophysics Laboratory, Hanscom AFB, MA, under Contract Nos. F19628-81-C-0140 and F19628-83-C-0056, and also thank Dr. W.C. Ermler and Dr. B.J. Krohn for their helpful comments.

References

- [1] C. Eckart, Phys. Rev. 47 (1935) 552.
- [2] G. Herzberg, Molecular spectra and molecular structure, Vol. 2. Infrared and Raman spectra of polyatomic molecules (Van Nostrand, Princeton, 1945).
- [3] G.D. Carney, S.R. Langhoff and L.A. Curtiss, J. Chem. Phys. 66 (1977) 3724.
- [4] D. Cropek and G.D. Carney, J. Chem. Phys. 80 (1984) 4280.
- [5] S. Carter and N.C. Handy, Mol. Phys. 47 (1982) 1455.
- [6] G.D. Carney, L.L. Sprandel and C.W. Kern, Advan. Chem. Phys. 37 (1978) 305.
- [7] G.D. Carney, S. Giorgianni and K.N. Rao, J. Mol. Spectry. 80 (1980) 158.
- [8] W.C. Ermler and B.J. Krohn, J. Chem. Phys. 67 (1977) 1360.
- [9] B.J. Krohn and J. Overend, J. Phys. Chem. 88 (1984) 564.
- [10] L.H. Harding and W.C. Ermler, J. Comput. Chem., to be published.
- [11] S.M. Adler-Golden, S.R. Langhoff, C.W. Bauschlicher Jr. and G.D. Carney, to be published.

APPENDIX B

THEORETICAL CALCULATION OF OZONE
VIBRATIONAL INFRARED INTENSITIES

Theoretical calculation of ozone vibrational infrared intensities

Steven M. Adler-Golden

Spectral Sciences, Inc., Burlington, Massachusetts 01803

Stephen R. Langhoff and Charles W. Bauschlicher, Jr.

NASA/Ames Research Center, Moffett Field, California 94035

Grady D. Carney

Department of Chemistry, Allegheny College, Meadville, Pennsylvania 16335

(Received 28 January 1985; accepted 25 March 1985)

An *ab initio* dipole moment function for ozone has been computed using the CASSCF (complete active space self-consistent field) method, and forms the basis for a calculation of ozone infrared band intensities. Vibrational wave functions were generated using the variational method with potential energy surfaces derived from experimental force constants. Computed values of the permanent dipole moment, dipole moment derivatives, and infrared band strengths are all found to be in remarkably good agreement with experiment. Intensities are predicted for hot bands for which experimental values are unavailable, and implications for atmospheric ozone spectroscopy are discussed. As the dipole moment matrix element signs are now established for nearly all of the observed bands, further refinement of the dipole moment function is possible.

I. INTRODUCTION

As the ozone molecule is one of the most important species in the earth's atmosphere, its spectral properties have been the subject of intensive study. Of particular interest is its infrared spectrum, which is prominent in long path absorption, and which has also been seen in emission in the upper atmosphere. Recently, new attention has focused on the properties of ozone's excited vibrational levels, motivated in large measure by the observation of atmospheric emission in the $10\ \mu$ (ν_3) band resulting from the $O + O_2 \rightarrow O_3$ recombination process.¹ Further studies have been conducted by Rawlins *et al.*^{2,3} at the Air Force Geophysics Laboratory's COCHISE facility, which provides a low pressure, cryogenic environment for the observation of infrared chemiluminescence. These experiments have identified ozone $10\ \mu$ chemiluminescence from vibrational levels containing as many as five stretching quanta. This hot band emission, which is red shifted from the ν_3 fundamental, may provide a significant source of infrared background radiation in the upper atmosphere. Some ozone hot bands also appear in atmospheric absorption spectra, and need to be taken into account in applications such as the detection of trace gases.

As the bulk of our knowledge of ozone infrared properties is derived from ambient temperature absorption experiments, which observe mainly transitions from the ground vibrational state, considerably less is known about hot band properties. To better understand ozone infrared spectroscopy, and, in particular, to permit vibrational level populations to be derived from hot band spectra, we have undertaken the theoretical calculation of ozone pure vibrational intensities. The intensities may be expressed either in terms of the Einstein A coefficient,

$$A/s^{-1} = 2.026 \times 10^{-6} (\tilde{\nu}/\text{cm}^{-1})^3 (R/ea_0)^2 \quad (1)$$

or in terms of the band strength S ,

$$S/\text{atm}^{-1}\text{cm}^{-2}\text{at } 298\text{ K} = 66.15 (\tilde{\nu}/\text{cm}^{-1}) (R/ea_0)^2, \quad (2)$$

where $\tilde{\nu}$ is the wave number of the band origin and R is the

dipole moment matrix element in atomic units ($1ea_0 = 2.541\ 77\text{ D}$). The results presented in this paper are based on a new *ab initio* dipole moment function which was generated using the CASSCF (complete active space self-consistent field) method, and which constitutes a great improvement over previous calculations. For the potential energy function a polynomial expansion derived from experimental force constants was used. The vibrational analysis was carried out using the variational method to generate accurate vibrational wave functions. With this approach we have obtained remarkably good agreement with fundamental, overtone, and combination band intensities observed in infrared absorption from the ground vibrational state. We feel that the calculated hot band intensities are comparably reliable, and will be valuable for the modeling of atmospheric and laboratory spectra. Moreover, since ambiguities in the signs of the dipole moment matrix elements have now been resolved, the dipole moment can be further refined using the experimental band strengths.

II. AB INITIO DIPOLE MOMENT AND POTENTIAL ENERGY SURFACES FOR OZONE

The dipole moment and potential energy surfaces were calculated using two different Cartesian basis sets. For generating the global surfaces a standard double-zeta plus polarization (DZP) basis was used which consisted of the (9s5p) set of Huzinaga⁴ contracted to [4s2p] according to Dunning,⁵ augmented with a d function with an orbital exponent of 0.85. In addition, to study the sensitivity of the dipole moment and its first derivatives to basis set quality, calculations were performed at points near the equilibrium geometry using a (11s6p2d) [6s3p2d] triple-zeta plus double polarization (TZ2P) basis. The 6s3p basis consisted of the [61111/411] contraction of van Duijneveldt,⁶ and was augmented with two d functions ($\alpha = 0.85$ and 0.20).

In C_{2v} symmetry the ground state of ozone can be written as

$$1a_1^2 \dots 6a_1^2 1b_1^2 1b_2^2 \dots 4b_2^2 1a_2^2 \quad ({}^1A_1). \quad (3)$$

It is well known that the Hartree-Fock (HF) level provides a rather poor description of the biradical character of the 1A_1 ground state. The first qualitatively correct description of the bonding is given by the two-configuration generalized valence bond (GVB) wave function, which can be written in C_{2v} symmetry as⁷

$$1a_1^2 \dots 6a_1^2 1b_1^2 1b_2^2 \dots 4b_2^2 [c_1(1a_2^2) - c_2(2b_1^2)]. \quad (4)$$

The description of the wave function can be further improved with more elaborate GVB wave functions constructed with correlating configurations involving both the σ and π electrons. We have also considered all single- and double-excitation configuration-interaction [CI(SD)] wave functions from both the HF and GVB (two-configuration) references with a variety of molecular orbital bases. Finally, we have considered complete active space self-consistent field (CASSCF)^{8,9} wave functions in which the 12 1s and 2s electrons were inactive (doubly occupied) and the 12 O(2p) electrons were active.

In Table I we have summarized the effects of electron correlation on the dipole moment of ozone near the equilibrium geometry using both the DZP and TZ2P basis sets. At nearly all levels of correlation the TZ2P basis gives a slightly smaller magnitude for the dipole moment, owing to the somewhat more diffuse nature of the wave functions when the diffuse d function is included. Once the basis sets reach DZP quality, the magnitude of the dipole moment is significantly overestimated at the HF level, but significantly underestimated at the GVB level, mainly through changes in the doubly occupied orbitals. As more configurations are added to the GVB, the dipole moment increases in magnitude, and the occupied orbitals more closely resemble those

obtained from HF. These same trends can be seen in the CI(SD) results as well. All singles and doubles from the HF configuration, although better than HF, still results in a dipole moment that is larger in magnitude than experiment. Similarly, the two-reference CI(SD) dipole moment (using GVB orbitals), although significantly better than GVB, is still too small. The two-reference CI(SD) result is further improved upon a natural orbital iteration. Also, from Table I one can see that the dipole moment is significantly better when a mixed orbital set is used (HF occupied orbitals combined with GVB 2b₁ and virtual orbitals). These results suggest the need for a balanced treatment of both the correlation and orbital optimization, such as in the CASSCF approach. The CASSCF wave functions produce dipole moments in quantitative accord with experiment, differing only by about 0.02 D between the two bases. This good agreement suggests that the CASSCF wave function provides a balanced description of the charge distribution in ozone, as has been the case in previous POLCI treatments.¹⁰

In Table II we compare the dipole moment first derivatives computed with both the DZP and TZ2P basis sets at the CASSCF level with those obtained from experimental infrared intensity data.¹¹ (The dipole moment vector components are given as $\mu_{x_{VAB}}$ and $\mu_{y_{VAB}}$, where the x_{VAB} axis is defined as the valence angle bisector, and the y_{VAB} axis is perpendicular to x_{VAB} and directed towards the r_1 side of the molecule; this is consistent with Fig. 1 of Ref. 12.) The derivatives are found to be in far better agreement with experiment than previous HF and selected CI(SD) results.¹³ The derivatives using the TZ2P basis are in particularly good agreement with experiment, suggesting that a diffuse d function is required for very quantitative results.

The goal of the present study was to construct a global dipole moment surface for ozone that extended to large enough displacements to allow the determination of overtone, combination and hot band intensities. The CASSCF method was selected not only because of its quantitative description of the dipole moment and its first derivatives, but

TABLE I. Basis set and correlation effects on the dipole moment of ozone.

Description of method	Dipole moment/D	
	DZP ^a	TZ2P ^a
HF	-0.830	-0.766
GVB	-0.127	-0.141
GVB + $\pi^2 \rightarrow \sigma^2 (1b_1^2 \rightarrow 2b_1^2)$		-0.203
GVB + $\pi^2 \rightarrow \sigma^2$	-0.238 ^b	
GVB + $\pi^2 \rightarrow \sigma^2 + \sigma^2 \rightarrow \sigma^2$	-0.317 ^b	
CI (SD) from HF reference	-0.709	-0.668
CI (SD) from two-references (GVB) using GVB orbitals	-0.356	-0.339
CI (SD) from two-references (GVB) using natural orbitals from previous CI		-0.402
CI (SD) from two-reference (GVB) using HF occupied orbitals and GVB virtual orbitals		-0.534
CASSCF with 1s, 2s orbitals inactive, 2p orbitals active	-0.557	-0.536
Experimental	-0.532 ± 0.002 ^c	

^a Calculated at $r = 1.278$ Å, $\theta = 116.8^\circ$; see the text for description of the basis sets. The positive direction is taken as the valence angle bisector vector.

^b Carried out in C_v symmetry to allow the orbitals to localize, thus minimizing the number of configurations included. Note that the overall wave function has C_{2v} symmetry even though the individual orbitals do not.

^c Absolute value measured in Ref. 15.

TABLE II. Ozone dipole moment first derivatives using CASSCF wave functions. Units are D, Å, and rad.

Derivative ^a	DZP ^b	TZ2P ^b	Expt. ^c
$\frac{\partial \mu_{x_{VAB}}}{\partial r}$	0.87	0.78	0.76
$\frac{\partial \mu_{y_{VAB}}}{\partial \theta}$	0.95	0.83	0.74
$\frac{\partial \mu_{r_{VAB}}}{\partial r}$	-2.41	-2.45	-2.60

^a The derivatives are the coefficients in the Taylor expansions

$$\mu_{x_{VAB}} = \mu_0 + \frac{\partial \mu_{x_{VAB}}}{\partial r} (\Delta r_1 + \Delta r_2) + \frac{\partial \mu_{x_{VAB}}}{\partial \theta} \Delta \theta$$

and

$$\mu_{r_{VAB}} = \frac{\partial \mu_{r_{VAB}}}{\partial r} (\Delta r_1 - \Delta r_2)$$

^b Evaluated at $r = 1.278$ Å, $\theta = 116.8^\circ$.

^c From Ref. 11, obtained by fitting the dipole moment to infrared intensity data, and evaluated at the experimental equilibrium geometry, $r = 1.272$ Å, $\theta = 116.8^\circ$.

also because the method uses a fixed configuration list, and is therefore capable of high precision, especially when quadratic convergence is employed. All calculations were carried out in C_s symmetry to ensure that no discontinuities arose upon asymmetric bond stretches. In C_s symmetry using the DZP basis the CASSCF included 1292 CSFs, which includes all possible arrangements of the 12 valence $O(2p)$ electrons in nine active $2p$ orbitals. The CASSCF energy and dipole moment were evaluated at over 200 geometries which thoroughly covered the range of vibrational energies from 0 to 1 eV for bond lengths of up to 1.754 Å. As will be shown in Sec. V, the good agreement between the experimental and calculated band strengths suggests that this *ab initio* dipole moment function is reasonably accurate over the range of geometries probed by the vibrational states considered.

Near the equilibrium geometry the shape of the CASSCF potential energy surface is quite accurate. We have obtained values for the equilibrium bond length and internal angle and internal coordinate force constants by performing least squares polynomial fits to the grid of potential energy values. The calculated equilibrium bond length r_e is 1.2956 Å, which is only slightly longer than the experimental value^{14,15} of 1.2717 Å, while the equilibrium angle θ_e is 116.5°, essentially identical to the experimental value of 116.8°. Another measure of the accuracy of the potential surface is provided by the force constants, which are the coefficients K_{ijk} in the Dunham expansion

$$V = r_e^3 \sum_{ijk} K_{ijk} (x_1^i + x_2^i)(x_1 x_2)^j x_3^k / (1 + \delta_{0i}), \quad (5)$$

where $x_1 = \Delta r_1/r_e$, $x_2 = \Delta r_2/r_e$, $x_3 = \Delta\theta$ (Δr_i and $\Delta\theta$ denote displacements relative to equilibrium); $\delta_{0i} = 1$ when $i = 0$ and $\delta_{0i} = 0$ otherwise. To facilitate comparison with experimental force constants we took r_e in the above expression as 1.2717 Å, while the Δr_i were taken relative to the calculated equilibrium distance of 1.2956 Å. This effectively shifts the CASSCF surface to match the experimental equilibrium distance. We derived force constants from two separate fits to test for stability. The quadratic and cubic force constants were found to be stable, and appear in Table III. They agree very well with experimental values derived from rotation-vibration spectral analysis.^{16,17}

TABLE III. Quadratic and cubic force constants of the DZP CASSCF potential energy surface for ozone (10^{-12} erg/Å²).

<i>i</i>	<i>j</i>	<i>k</i>	Fit 1 ^a	Fit 2 ^b	Experimental ^c
0	1	0	17.1	17.1	16.02
0	1	1	-15.4	-11.9	-13.0
0	0	2	6.30	6.29	6.5
0	0	3	-3.68	-3.60	-3.9
1	1	0	-9.13	-11.2	-16.8
1	0	1	3.61	3.64	4.02
1	0	2	-15.1	-14.4	-15.4
2	0	0	27.4	27.9	30.815
2	0	1	-6.37	-8.74	-15.8
3	0	0	-116.9	-118.4	-116.4

^aSixth degree Dunham polynomial, 50 terms, $\sigma = 0.0060 \times 10^{-12}$ erg

^bFifth degree Dunham polynomial, 34 terms, $\sigma = 0.0075 \times 10^{-12}$ erg

^cFrom Ref. 16.

As a further test of the CASSCF potential energy surface, we calculated the frequencies of the lowest few vibrational levels using the variational procedure described in Sec. IV; the results are presented in Table IV. Agreement with the experimental values is within 2% to 11%, which is consistent with the small error in the quadratic force constants.

Although the CASSCF calculation is size consistent, the computed binding energy is only about 0.5 eV, compared to the experimental value of 1.1 eV,¹⁸ owing to the fact that the calculation recovers only a portion of the extra molecular correlation energy. The surface is thus not globally accurate, and would not be appropriate for studying the dissociative pathways of ozone. The dipole moment surface should be less sensitive to the missing correlation energy and should therefore be more globally accurate. In fact, we feel that extending the dipole moment surface to the TZ2P CASSCF level would be more accurate and precise than extending the DZP CASSCF with a CI(SD) from the important references in the CASSCF. It would be difficult to extend to the CI(SD) level in a precise way because there are many important references that change with geometry in the CASSCF wave functions.

Given the limitations of the CASSCF potential energy surface, especially at large vibrational amplitudes, we next consider alternative potential surfaces which are more suitable for the calculation of ozone infrared intensities.

III. IMPROVED OZONE POTENTIAL ENERGY SURFACES

A. Available potential energy surfaces

A number of potential energy surfaces for ozone derived from observed spectra have appeared in the literature. One class of surfaces is in a functional form due to Sorbie and Murrell^{19,20} which insures proper dissociation to products. The most recent of these surfaces, that of Carter *et al.*,²¹ reproduces the observed band frequencies reasonably well, but contains cubic and quartic force constants which differ considerably from the experimental ones. This is of particular concern in the case of the cubic force constants, whose experimental values should be very reliable as they derive from rotational constants measured from high resolution spectra.

An alternative approach which incorporates the experi-

TABLE IV. Vibrational energy levels of the DZP CASSCF potential energy surface for ozone (cm^{-1}).

ν_1	ν_2	ν_3	Calculated ^a	Experimental (Ref. 16)
0	1	0	684	701
0	0	1	928	1042
1	0	0	1050	1103
0	2	0	1364	1399
0	1	1	1589	1727
1	1	0	1721	1795
1	0	1	1911	2111

^aSixth degree Dunham polynomial, 147 basis functions per vibrational symmetry.

mental force constants is to use a potential function consisting of a polynomial in suitable expansion variables such as the Simons-Parr-Finlan^{22,23} (SPF) variables $\Delta r_1/r$, $\Delta r_2/r$, and $\Delta\theta$. The force constants C_{ijk} associated with this new set of variables are defined in a way such that when the Taylor expansion (5) in the Dunham variables x_i is taken, the coefficients K_{ijk} are exactly the experimental force constants. Carney *et al.*²³ have applied this method to water and ozone, obtaining improved band centers by using SPF variables instead of Dunham variables. The optimum ozone results were, however, obtained by using a potential energy function which is a linear combination of the two expansions.

While an SPF or other expansion variable potential energy function cannot exhibit proper long range behavior at all geometries, it can do a reasonably good job at modest bending angles.²² Moreover, its polynomial form is highly efficient for our variational program, as it avoids the need for a three-dimensional integration to evaluate potential energy matrix elements. Thus, for both the sake of accuracy and efficiency, we used an expansion variable polynomial as our potential energy function in the following calculations. However, to study higher-lying vibrational states a more realistic potential energy surface will be required.

B. Choice of expansion variables

Calculations were performed using three different expansion variable potential energy surfaces. The force constants were taken as the experimental values from Barbe *et al.*¹⁶ The first surface was the Dunham expansion, which as discussed in Sec. IV was used mainly as a test of our variational algorithm, since it gives rather poor agreement with experimental energy levels. Next, we used the SPF variables and obtained improved results similar to those given previously.²³ Finally, hoping to further improve upon the calculated energy levels, we tried the set of expansion variables given by

$$y_1 = \frac{1 - \exp(-\alpha \Delta r_1)}{\alpha r_1}, \quad (6)$$

$$y_2 = \frac{1 - \exp(-\alpha \Delta r_2)}{\alpha r_2}, \quad (7)$$

$$y_3 = \Delta\theta, \quad (8)$$

which are the expansion variables appropriate for treating the bond stretches as Morse-like oscillators.^{24,25} We shall refer to the potential surface based on the variables (6)–(8) as the MPMO potential, since it is a multidimensional generalization of the potential function which Refs. 24 and 25 call the perturbed Morse oscillator (PMO). The algebra for generating the MPMO force constants from Dunham force constants is given in Appendix A. We performed calculations with two different α values, 2.5 and 2.7192 Å⁻¹. The former value is appropriate for the oxygen molecule, while the latter was chosen to give a zero quartic expansion coefficient C_{400} and a nearly zero cubic coefficient C_{300} (see Appendix A). The calculated vibrational energy levels differed by at most 2 cm⁻¹ for the two different values of α .

A comparison of experimental and calculated vibrational energy levels using the MPMO potential function ap-

TABLE V. Vibrational energy levels of ozone (cm⁻¹) relative to the ground state (0 0 0).

State	v_1	v_2	v_3	Exptl. ^a	MPMO ^b	Carter <i>et al.</i>
2A	0	1	0	700.9	700.5(0.1)	701
1B	0	0	1	1042.1	1042.4(0.0)	1043
3A	1	0	0	1103.1	1101.1(0.1)	1103
4A	0	2	0	1399.3	1397.4(0.1)	...
2B	0	1	1	1726.5	1724.7(0.0)	1730
5A	1	1	0	1795.3	1792.2(0.2)	1790
6A	0	0	2	2058.0	2059.8(0.6)	2061
7A	0	3	0	...	2088.5(1.1)	...
3B	1	0	1	2110.8	2108.6(0.2)	2112
8A	2	0	0	2201.3	2196.6(0.3)	2201
4B	0	2	1	2409.5	2401.6(0.2)	2409
9A	1	2	0	...	2482.3(1.5)	...
10A	0	1	2	2725.6	2724.9(1.7)	2736
5B	1	1	1	2785.2	2781.5(0.5)	2786
12A	2	1	0	...	2874.5(1.4)	...
6B	0	0	3	3046.0	3050.9(1.1)	3054
7B	0	3	1	...	3071.1(1.4)	...
8B	2	0	1	3185.7	3183.0(0.6)	3207
15A	3	0	0	...	3282.8(1.5)	...

^a Band origins from Ref. 16, except for the (0 2 0) state from Ref. 26.

^b $\alpha = 2.7192$ Å⁻¹, 224 basis functions per vibrational symmetry. Number in parentheses is the change in energy when using 147 functions per vibrational symmetry. The zero point energy is 1454.9 cm⁻¹.

^c Reference 21.

pears in Table V. The good agreement is comparable to that obtained with either the Carter *et al.* function²¹ or the optimal Dunham-SPF function of Carney *et al.*,²³ and superior to that obtained with the pure SPF function. We have included several additional levels not reported in Refs. 21 or 23 which were well converged in our calculation.

At this point it is worthwhile to briefly discuss the variational vibrational analysis method used to generate the energy levels in Tables IV and V and the infrared intensities to be presented in Sec. V.

IV. VIBRATIONAL ANALYSIS METHOD

An overview of our procedure for generating vibrational energies and intensities is provided by the Fig. 1 flow chart. Force constants appropriate to the chosen set of expansion variables (Dunham, SPF, or MPMO) were generated from either experimental Dunham force constants or by least squares fitting the grid of *ab initio* points. Next, the force constants were input into our variational vibrational state program, which is based on the Carney-Cropek algorithm.²⁷ This algorithm solves the exact pure vibrational Hamiltonian in internal coordinates, generating energy levels and wave functions, and is described in detail elsewhere.²⁸ The basis functions are products of one-dimensional radial and angular wave functions. Although ideally suited for molecules such as water which have predominantly local-mode vibrational motion, this variational program also works quite well for ozone. With the Dunham expansion potential surface, ten quadrature points per vibrational coordinate, and a total of 448 basis functions (224 per vibrational symmetry) we achieved 0.3 cm⁻¹ or better energy level agreement with a converged 1140-function calculation which used the Watson Hamiltonian in "r" coordinates.²¹

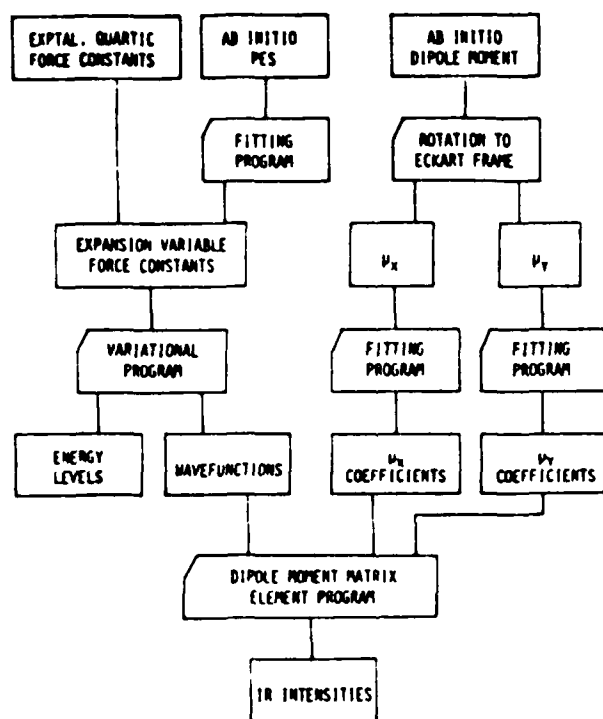


FIG. 1. Vibrational analysis flow chart.

(An error in an earlier program version was primarily responsible for the poorer agreement in Ref. 27.) Also computed are the matrix elements of the first through sixth powers of the expansion variables, evaluated in the basis set of one-dimensional functions. These matrix elements were used together with the full vibrational wave functions in the calculation of the dipole moment matrix elements.

The next step is to generate an expansion variable polynomial expression for the dipole moment function. As discussed elsewhere^{11,12,29,30} it is necessary to transform from the valence angle bisector (VAB) reference frame used in the *ab initio* calculation to the Eckart frame; this transformation involves a rotation in the plane of the molecule by a small angle β . The case of symmetric triatomic molecules, such as the principal isotope of ozone, is discussed in further detail by Adler-Golden and Carney,¹² who present an analytical formula for β . This transformation was applied at each *ab initio* geometry, yielding the values of μ_x and μ_y , the Eckart frame analogs of the VAB dipole components defined in Sec. II. The resulting grids of μ_x and μ_y values were each least squares fitted to an expansion variable polynomial of the appropriate symmetry. The expansion coefficients obtained using MPMO variables are given in Table VI. The dipole function has been shifted to account for the difference between the CASSCF and experimental equilibrium geometries; as shown in Sec. VI, this gives improved agreement with the experimental permanent dipole moment. Since μ_x and μ_y are, respectively, even and odd upon interchange of r_1 and r_2 , the μ_x function is in the same form as Eq. (5) and Appendix A potential functions, while for μ_y , the plus sign in the numerator is changed to a minus sign. Finally, the dipole moment polynomial, the one-dimensional matrix elements, and the vibrational wave functions were combined to yield

TABLE VI Coefficients of the dipole moment expansion in MPMO variables, $\alpha = 2.7192 \text{ \AA}^{-1}$; units are $e a_0 \text{ \AA}$, and $\text{rad. } \mu_x$ has the same functional form as the potential V in Appendix A. For μ_y , the plus sign is changed to a minus sign.

i	j	k	$C_{\mu_x}(\mu_x)$	$C_{\mu_y}(\mu_y)$
0	0	0	-0.129 280	
0	1	0	1.618 824	
0	2	0	73.329 074	
0	3	0	2038.330 737	
0	0	1	0.222 561	
0	1	1	-1.694 511	
0	2	1	-60.239 628	
0	0	2	0.051 054	
0	1	2	-6.189 115	
0	2	2	60.192 979	
0	0	3	-0.011 992	
0	1	3	5.451 635	
0	0	4	0.073 791	
0	1	4	9.835 044	
0	0	5	-0.793 267	
0	0	6	0.731 255	
1	0	0	0.269 474	-0.764 747
1	1	0	1.153 712	7.355 033
1	2	0	-38.709 046	113.705 808
1	0	1	-0.332 911	-0.174 804
1	1	1	-0.143 461	21.900 499
1	2	1	588.775 938	625.090 694
1	0	2	-0.206 479	0.588 447
1	1	2	7.152 872	6.540 124
1	0	3	-0.015 209	-1.421 678
1	1	3	-25.820 810	67.313 793
1	0	4	0.851 250	-0.097 543
1	0	5	-0.303 191	1.706 157
2	0	0	-0.261 773	0.894 413
2	1	0	-65.590 140	12.641 198
2	2	0	-1443.695 438	561.993 531
2	0	1	-0.551 988	0.994 855
2	1	1	67.665 722	-29.843 219
2	0	2	0.157 490	1.580 799
2	1	2	181.952 908	144.223 878
2	0	3	-2.478 166	-2.531 431
2	0	4	-1.986 866	-3.578 547
3	0	0	-1.068 208	-0.139 399
3	1	0	-89.134 210	-180.674 123
3	0	1	-7.747 853	11.880 138
3	1	1	-43.679 204	-352.908 770
3	0	2	1.140 281	-6.552 610
3	0	3	28.356 612	42.887 331
4	0	0	4.689 580	-5.934 924
4	1	0	438.770 088	2.294 425
4	0	1	-2.780 916	14.829 801
4	0	2	21.503 060	-45.486 291
5	0	0	37.969 141	30.593 030
5	0	1	40.015 850	272.205 108
6	0	0	133.329 614	292.803 732

the dipole moment matrix elements R . R is calculated somewhat differently for each combination of vibrational symmetries A and B :

$$R_{AB} = \langle A | \mu_y | B \rangle, \quad (9a)$$

$$R_{AA} = \langle A | \mu_x | A \rangle, \quad (9b)$$

$$R_{BB} = \langle B | \mu_x | B \rangle. \quad (9c)$$

The $|A\rangle$ and $|B\rangle$ wave functions have, respectively, even and odd values of the asymmetric stretching quantum number ν_3 .

It should be noted that β and hence the orientations of

TABLE VII. Dipole moment matrix elements ($e a_0$) connecting the *A* and *B* vibrational states.

	(001)	(011)	(101)	(021)	(111)	(003)	(031)
(000)	-0.068 12	0.003 30	-0.015 34	0.000 43	0.001 66	0.003 85	-0.000 24
(010)	-0.006 55	-0.067 52	-0.002 58	-0.005 40	-0.014 92	0.001 80	-0.001 08
(100)	-0.011 21	-0.002 39	0.065 50	-0.000 46	-0.002 62	-0.007 86	0.000 91
(020)	0.000 24	0.009 86	-0.000 15	-0.066 82	0.003 92	-0.000 72	-0.007 47
(110)	-0.004 24	-0.011 45	0.006 77	0.003 46	0.064 95	-0.001 77	0.001 04
(002)	0.093 28	0.009 48	-0.018 43	0.000 00	-0.007 17	-0.108 02	0.003 39
(030)	-0.001 30	-0.000 67	0.000 65	0.012 82	0.000 48	-0.001 34	-0.066 03
(200)	0.023 10	0.000 62	0.012 49	-0.000 03	0.002 52	0.001 71	-0.000 39
(120)	-0.000 11	0.007 01	-0.000 23	-0.012 00	-0.010 42	0.000 06	0.004 37
(012)	-0.004 73	0.092 65	-0.003 82	-0.014 07	-0.018 50	-0.011 40	0.000 65
(040)	0.000 11	-0.001 55	0.000 24	0.001 19	0.001 25	-0.000 50	-0.015 72
(210)	0.000 49	0.021 40	0.004 97	-0.000 74	0.013 06	0.000 25	0.000 19
(102)	-0.020 59	-0.003 36	-0.087 66	-0.000 15	-0.010 38	-0.026 78	0.002 05
	(201)	(121)	(013)	(041)	(211)	(103)	
(000)	0.001 06	-0.000 26	0.000 53	-0.000 07	-0.000 34	-0.001 27	
(010)	-0.000 30	0.002 55	-0.003 51	0.000 34	0.001 09	-0.000 71	
(100)	-0.020 11	0.000 64	-0.001 02	0.000 23	0.001 73	0.004 40	
(020)	0.000 16	0.014 78	0.002 78	-0.002 00	0.000 42	0.000 15	
(110)	-0.003 61	-0.004 51	0.006 73	-0.001 71	-0.020 04	0.001 99	
(002)	0.036 80	0.000 21	-0.005 93	0.000 27	0.000 69	0.024 48	
(030)	-0.001 09	-0.005 14	-0.001 44	-0.009 58	-0.000 02	-0.000 55	
(200)	0.067 16	-0.000 60	-0.000 36	0.000 07	-0.001 86	-0.005 50	
(120)	-0.000 19	-0.064 43	-0.002 37	0.001 86	0.005 72	-0.000 34	
(012)	0.001 50	-0.011 39	0.107 64	-0.005 24	0.033 93	0.003 94	
(040)	-0.000 10	0.000 99	0.002 44	0.065 11	-0.001 65	-0.000 18	
(210)	0.006 81	0.003 68	-0.001 17	0.000 56	0.066 05	-0.002 33	
(102)	-0.017 54	-0.000 54	0.006 09	-0.000 81	-0.009 09	-0.099 97	

the Eckart frame *x* and *y* axes are dependent on the relative atomic masses. Therefore, slightly different dipole moment components would be obtained with different partially substituted isotopes. All calculations reported here pertain to the principal ozone isotope (mass of each O = 15.9997 amu). Another caveat is that our matrix element signs are specific to the phases of our numerical wave functions, a fact which must be considered when comparing the current results to calculations which employ a different phase convention.

V. RESULTS

Results for the dipole moment matrix elements connecting the first 13 vibrational states of each symmetry are presented in Tables VII through IX. For these calculations the $\alpha = 2.7192 \text{ \AA}^{-1}$ MPMO potential energy surface was used with 224 basis functions of each symmetry. The dipole moment function was the sixth degree polynomial fit given in Table VI. The matrix elements are well converged with

TABLE VIII. Dipole moment matrix elements ($e a_0$) connecting the *A* vibrational states.

	(000)	(010)	(100)	(020)	(110)	(002)	(030)
(000)	-0.213 76						
(010)	0.023 49	-0.210 23					
(100)	0.006 57	0.000 18	-0.208 99				
(020)	0.000 86	-0.033 23	-0.001 03	-0.206 63			
(110)	-0.002 81	0.005 48	0.022 56	-0.000 55	-0.205 49		
(002)	0.004 31	0.000 88	0.000 75	-0.000 90	0.000 55	-0.213 48	
(030)	0.000 05	-0.001 75	0.000 03	-0.040 66	0.001 82	0.000 18	-0.202 86
(200)	0.002 33	0.000 15	0.010 52	0.000 92	0.000 34	-0.002 01	0.000 18
(120)	-0.000 03	0.003 93	0.000 85	0.004 27	-0.031 82	0.000 54	-0.001 09
(012)	-0.000 71	0.004 11	0.000 95	-0.001 35	0.001 60	0.022 77	0.001 18
(040)	0.000 04	0.000 20	-0.000 72	0.002 90	0.000 03	0.000 24	0.046 85
(210)	0.000 04	0.002 28	-0.004 01	-0.000 24	0.009 16	-0.000 15	-0.002 04
(102)	-0.000 83	-0.000 26	0.003 49	0.000 03	0.000 67	0.004 94	-0.000 08
	(200)	(120)	(012)	(040)	(210)	(102)	
(200)	-0.204 92						
(120)	-0.001 40	-0.201 92					
(012)	0.000 93	-0.000 78	-0.209 43				
(040)	0.000 09	-0.002 70	0.000 30	-0.198 63			
(210)	0.021 71	-0.000 69	-0.001 71	0.000 32	-0.201 25		
(102)	0.001 43	-0.000 11	-0.000 10	0.000 01	0.000 68	-0.208 58	

TABLE IX. Dipole moment matrix elements (ea_0) connecting the B vibrational states.

	(001)	(011)	(101)	(021)	(111)	(003)	(031)
(001)	-0.214 81						
(011)	0.023 15	-0.211 02					
(101)	-0.005 73	-0.000 03	-0.210 30				
(021)	0.001 04	-0.032 71	0.001 07	-0.207 15			
(111)	0.003 16	-0.004 50	0.022 08	0.000 35	-0.206 51		
(003)	0.005 66	0.001 20	-0.000 41	-0.002 27	-0.000 69	-0.210 57	
(031)	-0.000 07	-0.002 13	-0.000 04	-0.039 91	-0.001 86	0.000 37	-0.203 11
(201)	-0.004 24	-0.000 44	0.009 83	-0.001 11	0.000 32	0.002 32	-0.000 23
(121)	-0.000 13	0.004 45	-0.001 11	0.003 12	0.031 08	0.000 98	-0.000 89
(013)	0.001 09	-0.005 36	0.001 74	0.001 74	0.001 92	-0.022 36	-0.003 19
(041)	-0.000 10	-0.000 05	-0.000 38	-0.003 49	-0.000 08	-0.000 48	-0.045 82
(211)	0.000 08	-0.004 02	-0.004 20	0.000 70	0.008 45	0.000 38	0.002 31
(103)	0.001 10	-0.000 32	-0.004 19	0.000 08	-0.001 05	0.004 33	-0.000 24
	(201)	(121)	(013)	(041)	(211)	(103)	
(201)	-0.207 14						
(121)	0.001 29	-0.202 62					
(013)	0.001 61	0.000 93	-0.206 29				
(041)	-0.000 07	0.002 72	0.000 67	-0.198 63			
(211)	0.021 30	0.000 61	-0.001 97	0.000 36	-0.203 00		
(103)	-0.001 96	-0.000 29	0.000 21	-0.000 01	-0.000 77	-0.205 27	

respect to the choice of potential energy surface, degree of the dipole moment polynomial, and number of basis functions. With a smaller basis set (147 functions), only a few of the matrix elements involving the higher-lying states change appreciably. In particular, the changes are small enough that the allowed $10\mu v_1$ transitions are not appreciably affected. The use of SPF rather than MPMO expansion variables had an even smaller effect, as did the use of a fifth rather than a sixth degree dipole moment fit.

We conclude that the dipole moment matrix elements in Tables VII through IX do not significantly reflect either approximations in the vibrational wave functions or the manner in which the dipole moment function is fit, except possibly where forbidden transitions between high energy levels are involved. Thus, by comparing calculated infrared intensities [using Eq. (2)] with experimental values a direct test of the quality of the *ab initio* dipole moment is afforded.

VI. COMPARISON WITH EXPERIMENTAL VIBRATIONAL INTENSITIES

A. Survey of experimental data

A large amount of infrared absorption data exists for ozone, including many high resolution spectra which have been analyzed in detail. References 31 and 32 by Rothman *et al.* describe the AFGL atmospheric line parameter compilation, and provide a comprehensive survey of ozone spectra. To derive pure vibrational intensities from this data, care must be taken to account for the influence of Coriolis coupling, which mixes the rotational manifolds of adjacent bands. Where available, we have used deperturbed dipole moment matrix elements derived from rotation-vibration analyses. Another complication is the presence of hot bands arising primarily from the (0 1 0) state population, about 3% at room temperature. Table X lists the values which we have selected as the experimental pure vibrational band strengths. Rationales for choosing these values are presented below.

1. v_1 and v_3

We used the combined v_1 and v_3 band strength of $379.5 \text{ atm}^{-1} \text{ cm}^{-2}$ from Secroun *et al.*³³ and the dipole moment ratio R_3/R_1 of 9.4 ± 1 from Flaud *et al.*³⁴ The hot bands are included in the total band strength, and we assume that they contribute the same as the cold bands relative to their population. Therefore, no further correction is required to obtain the pure vibrational band strengths. We chose error bars of 5% for v_3 and 25% for v_1 , which are probably generous in view of the excellent measurement precision reported in Ref. 33.

2. $v_1 + v_3$, $2v_3$, and $2v_1$

Flaud *et al.*³⁵ report dipole moment matrix element absolute values of 0.0383, 0.0082, and 0.0019 D for these respective bands based on a rotation-vibration intensity analysis. The band strengths are therefore given by Eq. (2) after converting from Debye to ea_0 . Error bars were not reported,

TABLE X. Experimental and calculated pure vibrational band strengths ($\text{atm}^{-1} \text{ cm}^{-2}$ at 298 K).

Band	Experimental ^a	Calculated
v_3	17.4 ± 1.7	25.6
v_1	375 ± 19	320.0
v_1	4.5 ± 1.1	3.15
$2v_3$...	0.07
$v_2 + v_1$	1.47 ± 0.15	1.24
$v_1 + v_2$	0.59 ± 0.12	0.94
$2v_1$	1.42 ± 0.28	2.53
$v_1 + v_3$	31.7 ± 3.2	32.9
$2v_1$	0.08 ± 0.02	0.79
$v_1 + v_2 + v_3$	0.81 ± 0.08	0.51
$3v_1$	3.0 ± 0.3	2.99
$2v_1 + v_3$	0.33 ± 0.07	0.24

^a See the text for derivation of these values.

^b Not observed.

however. We have assumed uncertainties of 10%, 20%, and 30% for the respective band strengths.

3. $\nu_1 + \nu_2 + \nu_3$

We used the band strength reported by Darbe *et al.*³⁶ of $0.78 \text{ atm}^{-1} \text{ cm}^{-2}$ which excludes hot bands, and renormalized by dividing by the room temperature Boltzmann population of the ground state. We chose 10% error bars.

4. ν_2

We used the band strength [including the (0 1 0) hot band] of $18 \text{ atm}^{-1} \text{ cm}^{-2}$ from the low resolution study by McCaa and Shaw³⁷ and corrected for the factor of 2 greater intensity of the hot band as suggested by Goldman *et al.*³⁸ We chose 10% error bars.

5. $\nu_1 + \nu_2$, $\nu_2 + \nu_3$, $3\nu_3$, and $2\nu_1 + \nu_3$

We used the band strengths from McCaa and Shaw,³⁷ which are not corrected for Coriolis effects. For reasons discussed above in the case of the ν_1 and ν_3 bands, no further adjustment to account for hot bands is required. We chose 10% error bars for $\nu_2 + \nu_3$ and $3\nu_3$ and 20% error bars for the other two bands since they are much weaker and hence more susceptible to Coriolis effects.

6. $2\nu_2$

The observation of this band by McCaa and Shaw³⁷ has not been duplicated in subsequent studies, and has been ascribed to an impurity.¹⁶ Thus, we conclude that the $2\nu_2$ band strength is less than the typical instrumental sensitivity in these studies, which is on the order of $0.1 \text{ atm}^{-1} \text{ cm}^{-2}$.

7. Permanent dipole moment

The permanent dipole moment has been measured accurately by microwave spectroscopy, and has the absolute value $0.5324 \pm 0.0024 \text{ D}$ ($0.210 \pm 0.001 \text{ ea.}$).¹⁵

B. Comparison of experiment and theory

The calculated band strengths, derived from the dipole matrix elements in Tables VII through IX, are compared with the experimental values in Table X. The agreement is remarkably good for an *ab initio* calculation, especially considering that the values span three orders of magnitude. The only severe disagreement occurs for the $2\nu_1$ band, which according to Ref. 35 derives virtually all of its intensity in the room temperature spectrum via Coriolis coupling with the $\nu_1 + \nu_3$ band. It is particularly significant that even the weak transitions are well described since they are sensitive to the detailed shape of the dipole moment function and serve as a measure of the extent of deviation from harmonic oscillator selection rules. The deviation from harmonic behavior is not large, as evidenced by both the small size of the matrix elements for forbidden transitions and the fact that the harmonic scaling rule $R^2 \sim \nu$ is obeyed reasonably well for most of the $\Delta\nu = -1$ transitions. This is consistent with the small size of the high-order terms in the normal coordinate polynomial expansion (Appendix B).

The permanent dipole moment is given by the diagonal matrix elements in Tables VIII and IX. For the ground vibrational state the calculated value is -0.543 D , in excellent agreement with the experimental absolute value of $0.5324 \pm 0.0024 \text{ D}$. This calculated value differs from (and is superior to) the value given in Table II mainly because as mentioned in Sec. IV the dipole function has been shifted to account for the difference between the *ab initio* and experimental equilibrium geometries. A slight dependence of the permanent dipole on vibrational excitation is predicted.

We believe that the CASSCF dipole moment function is sufficiently reliable that most of the Table VII through IX matrix elements are of comparable accuracy to those of the corresponding cold bands in Table X, especially for the well-converged states listed in Table V. Moreover, for the strongly allowed $10\mu\nu_3$ bands we expect an accuracy of several percent in the band strengths relative to the (0 0 1) fundamental. This very good relative accuracy is expected in view of the approximately harmonic behavior described above.

VII. DISCUSSION

The calculated dipole moment matrix elements will be very useful for the analysis of ozone $10\mu\nu_3$ emission spectra which have been observed in the atmosphere and in the laboratory. According to recent observations in the COCHISE experiment³ the most heavily populated levels in ozone formed from recombination are the states (0 0 N), $N = 1$ through 5, and (1 0 N), $N = 1$ through 4. In Table VII the relevant ν_3 matrix elements are given for N of up to 3. It is found that the harmonic scaling mentioned above, used previously² to analyze the COCHISE data, is approximately obeyed for both (0 0 N) and (1 0 N) states. It also holds reasonably for levels containing additional excitation in the bending mode. Thus, more accurate relative values derived from Table VII matrix elements will not have a large impact on the analysis of ν_3 hot band emission.

As for the radiative properties of ozone vibrational levels which are higher in energy than those studied here, it seems unlikely that any drastic change in this roughly harmonic behavior will occur until both the level density and mode coupling are sufficient to set up accidental resonances. A region of extensive resonances, which might appropriately be termed "quantum chaos,"³⁹ seems to occur in ozone at very high vibrational energies, judging from the appearance of dense line clusters in the resonance Raman spectrum.⁴⁰ In order for theory to reliably address questions about the properties of these very high-lying levels both a larger vibrational basis set and a more accurate potential energy function would be required.

Concerning atmospheric absorption spectra of ozone, the current calculation may suggest improved intensity values for a number of hot bands, particularly for forbidden transitions where harmonic or separable mode approximations may break down. Predicted intensities for the stronger hot bands are given in Table XI using the calculated dipole moment matrix elements. Accurate experimental values for these bands have not to our knowledge been published. In general, the predictions agree roughly with expectations. However, there is one surprising result: a heretofore unob-

TABLE XI. Calculated strengths of selected hot bands, Boltzmann factor not included.

Transition	$\tilde{\nu}/\text{cm}^{-1}$ ^a	$S/\text{atm}^{-1}\text{cm}^{-2}$ at 298 K
$2\nu_2-\nu_2$	698.4	51.0
$\nu_2 + \nu_3-\nu_3$	684.4	24.3
$\nu_2 + \nu_1-\nu_1$	692.2	23.3
$\nu_2 + \nu_3-\nu_2$	1025.6	309.3
$2\nu_3-\nu_3$	1015.9	584.7
$\nu_1 + \nu_3-\nu_1$	1007.7	286.0
$\nu_1 + \nu_2-\nu_2$	1094.4	2.2
$\nu_1 + \nu_3-\nu_3$	1068.7	2.3
$2\nu_1-\nu_1$	1098.2	8.0
$\nu_1 + \nu_2 + \nu_3-\nu_3$	2084.3	30.7
$\nu_1 + 2\nu_3-\nu_3$	2042.0	57.3
$2\nu_1 + \nu_3-\nu_1$	2082.6	55.7
$2\nu_1-\nu_3$	1159.2	40.9

^a From Refs. 16 and 26.

served hot band, the forbidden transition (0 0 1)–(2 0 0) at 1159 cm^{-1} , is predicted to have a remarkably large band strength of about $40\text{ atm}^{-1}\text{ cm}^{-2}$ ($0.27\text{ atm}^{-1}\text{ cm}^{-2}$ using a 298 K Boltzmann factor). Indeed, this band is strong enough to be included in the AFGL atmospheric absorption line atlas.³² This surprisingly large intensity is caused by borrowing from the strong (0 0 1)–(0 0 2) transition via Darling–Dennison resonance.^{16,41} Presumably the reason why the 1159 cm^{-1} band has not yet been observed is that it lies within the wings of the stronger ν_1 and ν_3 bands. However, it might show up in high resolution spectra. A detailed re-examination of high resolution spectra in this region would be very desirable.

An important benefit of the quantitative agreement which we have obtained between experimental and calculated band strengths is that the signs of the dipole moment matrix elements have now been established for these bands. With the sign ambiguities removed it should be possible to refine the ozone dipole moment function to give essentially perfect agreement with experimental dipole moment matrix elements; this in turn would yield even more accurate band strength predictions. Unfortunately, there are a number of different ways in which the dipole moment can be adjusted, and it is not clear to us which way is best. Not only are there many more expansion coefficients necessary for an accurate fit than there are available band strengths, there are also different expansions possible depending on the choice of variables. However, if additional experimental intensity data become available, or if appropriate theoretical constraints on the functional form of the dipole moment could be applied, refinement of the dipole moment function for ozone could be accomplished with greater confidence.

ACKNOWLEDGMENTS

We wish to thank a number of people whose assistance proved invaluable to this project: Dr. R. A. Armstrong and Dr. W. A. M. Blumberg of the Air Force Geophysics Laboratory, Hanscom AFB, D. Cropek of the University of Illinois, and Dr. W. T. Rawlins of Physical Sciences Inc. This work was supported by the Air Force Geophysics Laboratory under Contract Nos. F19628-81-C-0140 and F-19628-83-C-0056.

APPENDIX A: THE MPMO POTENTIAL ENERGY FUNCTION

The MPMO potential energy function is written

$$V = r_e^2 \sum_{ijk} C_{ijk} (y_1^i + y_2^j)(y_1 y_2)^k y_3^l / (1 + \delta_{0l}),$$

where the y_i are defined in Eqs. (6)–(8). The C_{ijk} are related to the Dunham coefficients K_{ijk} as follows:

$$C_{200} = K_{200}, \quad C_{010} = K_{010},$$

$$C_{101} = K_{101}, \quad C_{002} = K_{002},$$

$$C_{300} = K_{300} + \gamma K_{200},$$

$$C_{110} = K_{110} + \frac{1}{2}\gamma K_{010},$$

$$C_{201} = K_{201} + \frac{1}{2}\gamma K_{101},$$

$$C_{011} = K_{011}, \quad C_{102} = K_{102}, \quad C_{003} = K_{003},$$

$$C_{400} = K_{400} - \frac{1}{2}\gamma^2 C_{200} + \frac{1}{2}\gamma C_{300},$$

$$C_{210} = K_{210} + \gamma C_{110} - \frac{1}{2}\gamma^2 C_{010},$$

$$C_{020} = K_{020} - \frac{1}{2}\gamma^2 C_{010} + \gamma C_{110},$$

$$C_{301} = K_{301} - \frac{1}{2}\gamma^2 C_{101} + \gamma C_{201},$$

$$C_{111} = K_{111} + \frac{1}{2}\gamma C_{011},$$

$$C_{202} = K_{202} + \frac{1}{2}\gamma C_{102},$$

$$C_{012} = K_{012}, \quad C_{103} = K_{103}, \quad C_{004} = K_{004},$$

where $\gamma = ar_e$.

APPENDIX B: NORMAL COORDINATE REPRESENTATION OF THE OZONE CASSCF DIPOLE MOMENT FUNCTION

For the benefit of workers who employ normal coordinate methods we have fit the CASSCF dipole moment components to polynomials in the dimensionless normal coordinates q_i pertaining to O^{16}_3 ozone. The polynomials are

$$\mu_{x,y} = \sum_{ijk} \mu_{ijk} q_1^i q_2^j q_3^k, \quad (\text{B1})$$

where $i + j + k \leq 6$; k is even for μ_x and odd for μ_y . In our sign convention positive q_3 corresponds to positive Δr_1 and negative Δr_2 . The fit was performed by first transforming each *ab initio* geometry to symmetry coordinates S_i (using the equations in Ref. 12) and then linearly transforming to the q_i using the quadratic force constants of Ref. 16; next, the dipole moment components μ_x and μ_y were least squares fit to the function (B1). The following coefficients μ_{ijk} were obtained:

μ_x/ea_0				μ_y/ea_0			
<i>i</i>	<i>j</i>	<i>k</i>	μ_{yx}	<i>i</i>	<i>j</i>	<i>k</i>	μ_{yx}
0	0	0	-0.207 730	0	0	1	-0.095 921
0	0	2	-0.005 741	0	0	3	-0.001 492
0	0	4	0.000 294	0	0	5	0.000 024
0	0	6	-0.000 003				
0	1	0	0.032 824	0	1	1	-0.000 263
0	1	2	0.000 124	0	1	3	-0.000 168
0	1	4	-0.000 034	0	1	5	0.000 002
0	2	0	0.000 392	0	2	1	0.000 695
0	2	2	0.000 053	0	2	3	0.000 030
0	2	4	0.000 001				
0	3	0	-0.000 152	0	3	1	-0.000 038
0	3	2	-0.000 004	0	3	3	0.000 001
0	4	0	0.000 004	0	4	1	0.000 004
0	4	2	-0.000 001				
0	5	0	-0.000 001	0	5	1	-0.000 001
0	6	0	0.000 000				
1	0	0	0.009 154	1	0	1	0.018 339
1	0	2	0.000 046	1	0	3	0.000 429
1	0	4	-0.000 015	1	0	5	-0.000 005
1	1	0	-0.004 120	1	1	1	-0.001 264
1	1	2	-0.000 114	1	1	3	0.000 083
1	1	4	0.000 007				
1	2	0	0.000 035	1	2	1	-0.000 012
1	2	2	0.000 031	1	2	3	-0.000 012
1	3	0	-0.000 006	1	3	1	-0.000 003
1	3	2	0.000 000				
1	4	0	0.000 009	1	4	1	0.000 000
1	5	0	-0.000 001				
2	0	0	0.002 701	2	0	1	-0.000 534
2	0	2	0.000 005	2	0	3	-0.000 051
2	0	4	-0.000 001				
2	1	0	0.000 048	2	1	1	0.000 098
2	1	2	0.000 053	2	1	3	-0.000 008
2	2	0	-0.000 085	2	2	1	-0.000 021
2	2	2	-0.000 012				
2	3	0	-0.000 012	2	3	1	0.000 003
2	4	0	0.000 003				
3	0	0	-0.000 065	3	0	1	-0.000 132
3	0	2	0.000 036	3	0	3	0.000 004
3	1	0	-0.000 029	3	1	1	-0.000 008
3	1	2	-0.000 007				
3	2	0	0.000 003	3	2	1	0.000 005
3	3	0	0.000 002				
4	0	0	-0.000 064	4	0	1	0.000 008
4	0	2	-0.000 003				
4	1	0	-0.000 010	4	1	1	0.000 002
4	2	0	0.000 005				
5	0	0	-0.000 002	5	0	1	0.000 000
5	1	0	0.000 002				
6	0	0	0.000 001				

As mentioned in Sec. IV, the partitioning of μ into these specific x and y components pertains only to the fully substituted ozone isotopes as a consequence of the mass dependence of the x and y axes in the Eckart frame.

- ¹T. C. Degges, A. T. Stair, Jr., R. M. Nadile, and E. R. Hegblom, EOS Trans. AGU 60, 338 (1979).
- ²W. T. Rawlins, G. E. Caledonia, and J. P. Kennealy, J. Geophys. Res. 86, 5247 (1981).
- ³W. T. Rawlins, H. C. Murphy, G. E. Caledonia, J. P. Kennealy, F. X. Robert, A. Cormann, and R. A. Armstrong, Appl. Opt. 23, 3316 (1984).
- ⁴S. Huzinaga, J. Chem. Phys. 42, 1293 (1965).
- ⁵T. H. Dunning, Jr., J. Chem. Phys. 53, 2823 (1970).
- ⁶F. B. van Duijneveldt, IBM Research Report RJ 945, 1971.
- ⁷P. J. Hay and T. H. Dunning, Jr., J. Chem. Phys. 67, 2290 (1977).
- ⁸B. O. Roos, Int. J. Quantum Chem. Quantum Chem. Symp. 14, 175 (1980).
- ⁹P. E. M. Siegbahn, J. Amlof, A. Heiberg, and B. O. Roos, J. Chem. Phys. 74, 2384 (1981).
- ¹⁰P. J. Hay, T. H. Dunning, Jr., and W. A. Goddard III, J. Chem. Phys. 62, 3912 (1975).
- ¹¹G. D. Carney, S. Giorgianni, and K. N. Rao, J. Mol. Spectrosc. 80, 158 (1980).
- ¹²S. M. Adler-Golden and G. D. Carney, Chem. Phys. Lett. 113, 582 (1985).
- ¹³L. A. Curtiss, S. R. Langhoff, and G. D. Carney, J. Chem. Phys. 71, 5016 (1979).
- ¹⁴T. Tanaka and Y. Morino, J. Mol. Spectrosc. 33, 538 (1970).
- ¹⁵M. Lichtenstein, J. J. Gallagher, and S. A. Clough, J. Mol. Spectrosc. 40, 10 (1971).
- ¹⁶A. Barbe, C. Secroun, and P. Jouve, J. Mol. Spectrosc. 49, 171 (1974).
- ¹⁷P. Hennig and G. Strey, Z. Naturforsch. Teil A 31, 244 (1976).
- ¹⁸C. W. Wilson, Jr. and D. G. Hopper, J. Chem. Phys. 74, 595 (1981).
- ¹⁹K. S. Sorbie and J. N. Murrell, Mol. Phys. 29, 1387 (1975).
- ²⁰J. N. Murrell, K. S. Sorbie, and A. J. C. Varandas, Mol. Phys. 32, 1359 (1976).
- ²¹S. Carter, I. M. Mills, J. N. Murrell, and A. J. C. Varandas, Mol. Phys. 11, 1 (1982).
- ²²G. Simons, J. Chem. Phys. 61, 369 (1974).
- ²³G. D. Carney, L. A. Curtiss, and S. R. Langhoff, J. Mol. Spectrosc. 61, 371 (1976).
- ²⁴I. I. Tugov and V. P. Chernyavsky, J. Mol. Spectrosc. 99, 302 (1983).
- ²⁵J. N. Huffaker, J. Chem. Phys. 64, 3175 (1976).
- ²⁶V. M. Devi, S. P. Reddy, K. N. Rao, J. M. Flaud, and C. Camy-Peyret, J. Mol. Spectrosc. 77, 156 (1979).
- ²⁷D. Cropek and G. D. Carney, J. Chem. Phys. 80, 4280 (1984).
- ²⁸G. D. Carney, Thesis, Allegheny College, PA, 1983; D. Cropek, Thesis, Allegheny College, PA 1983.
- ²⁹G. D. Carney, L. L. Sprandel, and C. W. Kern, Adv. Chem. Phys. 37, 305 (1978).
- ³⁰W. C. Ermler and B. J. Krohn, J. Chem. Phys. 67, 1360 (1977).
- ³¹L. S. Rothman, Appl. Opt. 20, 791 (1981).
- ³²L. S. Rothman, R. R. Gamache, A. Barbe, A. Goldman, J. R. Gillis, L. R. Brown, R. A. Toth, J. M. Flaud, and C. Camy-Peyret, Appl. Opt. 22, 2247 (1983).
- ³³C. Secroun, A. Barbe, P. Jouve, P. Arcas, and E. Arie, J. Mol. Spectrosc. 85, 8 (1981).
- ³⁴J. M. Flaud, C. Camy-Peyret, and L. S. Rothman, Appl. Opt. 19, 655 (1980).
- ³⁵J. M. Flaud, C. Camy-Peyret, A. Barbe, C. Secroun, and P. Jouve, J. Mol. Spectrosc. 80, 185 (1980).
- ³⁶A. Barbe, C. Secroun, A. Goldman, and J. R. Gillis, J. Mol. Spectrosc. 100, 377 (1983).
- ³⁷D. J. McCaa and J. H. Shaw, J. Mol. Spectrosc. 25, 374 (1968).
- ³⁸A. Goldman, J. R. Gillis, D. G. Murray, A. Barbe, and C. Secroun, J. Mol. Spectrosc. 96, 279 (1982).
- ³⁹D. W. Noid, M. L. Koszykowski, and R. A. Marcus, Annu. Rev. Phys. Chem. 32, 267 (1981).
- ⁴⁰D. G. Imre, J. L. Kinsey, R. W. Field, and D. H. Katayama, J. Phys. Chem. 86, 2564 (1982).
- ⁴¹B. T. Darling and D. M. Dennison, Phys. Rev. 57, 128 (1940).

APPENDIX C

A COMPARISON OF FORCE FIELDS AND
CALCULATION METHODS FOR VIBRATION
INTERVALS OF ISOTOPIC H_3^+ MOLECULES

A comparison of force fields and calculation methods for vibration intervals of isotopic H_3^+ molecules

Grady D. Carney

New York Institute of Technology, Center for Natural Sciences, New York, New York 10023

Steven M. Adler-Golden

Spectral Sciences, Inc., Burlington, Massachusetts 01803

David C. Lesseski

Department of Chemistry, Allegheny College, Meadville, Pennsylvania 16335

(Received 26 August 1985; accepted 22 November 1985)

This paper reports (a) improved values for low-lying vibration intervals of H_3^+ , H_2D^+ , D_2H^+ , and D_3^+ calculated using the variational method and Simons-Parr-Finlan representations of the Carney-Porter and Dykstra-Swope *ab initio* H_3^+ potential energy surfaces, (b) quartic normal coordinate force fields for isotopic H_3^+ molecules, (c) comparisons of variational and second-order perturbation theory, and (d) convergence properties of the Lai-Hagstrom internal coordinate vibrational Hamiltonian. Standard deviations between experimental and *ab initio* fundamental vibration intervals of H_3^+ , H_2D^+ , D_2H^+ , and D_3^+ for these potential surfaces are 6.9 (Carney-Porter) and 1.2 cm^{-1} (Dykstra-Swope). The standard deviations between perturbation theory and exact variational fundamentals are 5 and 10 cm^{-1} for the respective surfaces. The internal coordinate Hamiltonian is found to be less efficient than the previously employed "t" coordinate Hamiltonian for these molecules, except in the case of H_2D^+ .

I. INTRODUCTION

The H_3^+ molecular ion and its isotopic species, which have the simplest electronic structure of any known polyatomic molecule, have attracted considerable experimental and theoretical interest. Their vibration-rotation spectra have been studied extensively in the laboratory¹⁻⁶ and are important in astrophysics.⁷ Their simple electronic structure makes it possible to calculate a very accurate ground electronic state potential energy surface (PES). When combined with a variational vibrational energy calculation method, the PES yields excellent *ab initio* predictions of vibration-rotation energies. One of the first accurate PES's was calculated by Carney and Porter,⁸ who used it to derive vibrational intervals, rotational constants, vibrational transition intensities, and vibration-rotation energies.⁹ The heteronuclear isotopes were handled using Carney, Langhoff, and Curtiss¹⁰ "t" coordinate method, which provided a generalization of the Carney-Porter formalism. Details of early studies in variational vibrational energy methods may be found in the review by Carney, Sprandel, and Kern.¹¹

Several new developments have motivated us to reexamine the isotopic H_3^+ vibration spectra. Recent experiments have provided new spectroscopic data for several of the fundamental frequencies of isotopic H_3^+ molecules. Oka¹ has reported ν_2 of H_3^+ , Lubic and Amato² have reported ν_1 of D_2H^+ , Amato and Watson³ have reported ν_1 of H_2D^+ , and Foster *et al.*⁴ have reported ν_2 of D_3^+ , and ν_2 and ν_3 of H_2D^+ and D_2H^+ . Experiments of Shy *et al.*⁵ have also provided very accurate infrared spectroscopic data for the H_2D^+ , D_2H^+ , and D_3^+ molecules, while Warner *et al.*⁶ have reported submillimeter spectroscopic data for the H_2D^+ molecule.

Recent theoretical developments¹²⁻¹⁷ include further progress in vibrational energy calculation methods as well as improved potential energy surfaces. Variational vibrational energy calculations have been carried out^{16,17} using much larger basis sets than in the earlier work, and suggest that the original Carney-Porter vibration energies were not completely converged. In addition, new vibrational Hamiltonians based on nonrectilinear coordinates have been developed, providing additional flexibility in basis set selection. These include the Lai-Hagstrom¹¹ and Carter-Handy¹² internal coordinate Hamiltonians and the Tennyson-Sutcliffe¹³ Hamiltonian in close-coupling coordinates. Finally, better converged PES's have been reported, such as that of Dykstra and Swope.¹⁴ Prior to Martire and Burton's recent work¹⁷ the Dykstra-Swope surface had not been utilized for vibrational level calculations. Although agreement between theory and experiment is already good, more accurate estimates of vibration intervals may be useful to experimentalists as they learn more about these interesting molecules.

In this paper we compare different PES's and calculation methods for H_3^+ isotope vibration intervals. Calculations were performed using the Carney-Cropek internal coordinate variational algorithm¹⁵ and are compared with both the "t" coordinate calculations^{9,10} and second-order perturbation theory based on normal coordinates. In addition, results using the Carney-Porter⁸ PES are compared with those using a new fit to the Dykstra-Swope PES, and both are compared with experimental data. From these comparisons the current study is able to separately assess the PES and vibrational energy calculation accuracy. By using a Simons-Parr-Finlan^{18,19} fit to the Dykstra-Swope PES and large vibrational basis sets we have obtained significantly

improved vibrational interval predictions. Agreement of our calculation with the experimental fundamental frequencies is better than two wave numbers.

II. CALCULATION OVERVIEW

This section briefly describes the key ingredients in our calculation, the Dykstra-Swope PES and the variational and perturbation theory vibrational methods.

A. The Dykstra-Swope potential energy surface

Dykstra and Swope¹⁴ used a large electronic basis set, 63 contracted Cartesians, and determined grid-point energies within the Born-Oppenheimer approximation by means of a self-consistent-electron-pair (SCEP) technique which, for two-electron systems, is equivalent to a full CI method. Their potential energy surface contains 68 geometries with some energies lying as much as 20 000 wave numbers above the PES minimum. Dykstra and Swope suggested that their H_3^+ surface should be capable of producing vibration intervals accurate to within two wave numbers. However, they did not report a fitting function, so we had to develop one prior to calculating vibration intervals with their PES. Retaining two wave number accuracy in the vibration energy calculation requires a suitable fitting function, such as a Simons-Parr-Finlan^{18,19} (SPF) polynomial or some alternative scheme which is capable of the highest accuracy possible with the fewest adjustable parameters.

B. Vibration energy calculations

It is desirable to try more than one variational vibrational method since different methods will differ in their efficiency for a given molecule. In addition, the complexity of computer codes makes it very helpful to use two or more independent algorithms for a given potential energy surface as a double check. Finally, perturbation theory should be examined to determine whether it is sufficiently accurate for the molecule being studied.

The original variational method for H_3^+ isotopes is that of Carney, Langhoff, and Curtiss,¹⁰ which develops the vibrational Hamiltonian operator in rectilinear symmetry coordinates t_i ($i = 1-3$), which are closely related to normal coordinates Q_i ($i = 1-3$). The vibrational basis functions are defined analytically in terms of either harmonic or Morse oscillators.

The method employed in the current calculations is the Carney-Cropek algorithm,¹⁵ used by Adler-Golden *et al.*²⁰ It employs the Lai-Hagstrom Hamiltonian,¹¹ which develops the vibrational Hamiltonian operator in internal coordinates consisting of two bond lengths and the central angle. Vibration basis functions are defined numerically using the Numerov-Cooley²¹ finite-difference technique.

To test the accuracy and convergence properties of the Carney-Cropek internal coordinate method we performed calculations on the Carney-Porter fifth-degree SPF PES, for which vibration energies have been previously obtained. These calculations examine convergence in vibration energy as a function of the number and type of vibrational configu-

ration basis functions employed.

As an alternative to variational theory, we also determine intervals using second-order perturbation theory (PT) with the Carney-Porter and Dykstra-Swope PES's rewritten as quartic force fields defined in dimensionless normal coordinates.

III. COMPUTATIONAL DETAILS

This section describes computational details for (A) determining an accurate SPF model potential energy function for Dykstra and Swope's *ab initio* H_3^+ PES, (B) determining accurate quartic normal force fields in dimensionless normal coordinates, (C) determining appropriate vibrational basis sets and calculating vibration energies using variational theory, and (D) using second-order perturbation theory to calculate vibration energies.

A. Fitting the H_3^+ potential surface

The procedure for obtaining SPF expansion coefficients for the Dykstra-Swope PES is as follows. First, the internal coordinates used by Dykstra and Swope, namely, displacement coordinates in cylindrical polar form, S , R , and ϕ , are transformed into the rectilinear symmetry coordinates S_1 , S_2 , S_3 for each grid point geometry. The appropriate equations are

$$S_1 = bS; \quad b = 3^{1/2},$$

$$S_2 = bR \cos \phi,$$

and

$$S_3 = bR \sin \phi.$$

Next, the three internuclear distances R_i ($i = 1, 2, 3$) are calculated:

$$R_1 = [R_{eq}^2 + S_1^2 + S_2^2 + S_3^2 + R_{eq}(2S_1 - S_2 - bS_3) - S_1(bS_3 + S_2)]^{1/2},$$

$$R_2 = [R_{eq}^2 + S_1^2 + S_2^2 + S_3^2 + R_{eq}(2S_1 - S_2 + bS_3) + S_1(bS_3 - S_2)]^{1/2},$$

and

$$R_3 = [(R_{eq} + S_1 + S_2 + S_3)^2 + S_3^2]^{1/2}.$$

The SPF internal coordinates ρ_i ($i = 1, 2, 3$) $= (R_i - R_{eq})/R_i$ are then calculated and used to evaluate the SPF algebraic polynomial functions P_i ($i = 1-21$) defined in Table I. These polynomial functions are symmetrized to maintain the threefold permutational symmetry of the molecular force field with respect to the three internuclear distances R_i ($i = 1-3$).

Standard regression analysis is used to find the SPF expansion coefficients. Preliminary calculations were made using only the grid point geometries and energies tabulated for the isosceles structures, and expansion coefficients for a

TABLE I. Expansion coefficients for SPF fits of H₃⁺ potential energy surfaces.

Term Number <i>n</i>	Expansion coefficients <i>C_n</i>		Polynomial function <i>P_n</i>
	I (Dykstra-Swope) ^a	II (Carney-Porter) ^b	
1	0.246 305 26	0.244 944	$\rho_1^2 + \rho_2^2 + \rho_3^2$
2	-0.040 552 42	-0.036 801	$\rho_1 \rho_2 + \rho_1 \rho_3 + \rho_2 \rho_3$
3	0.071 947 44	0.078 313	$\rho_1^3 + \rho_2^3 + \rho_3^3$
4	-0.037 907 14	-0.042 076	$\rho_1^2(\rho_1 + \rho_2) + \rho_1^2(\rho_1 + \rho_3) + \rho_2^2(\rho_1 + \rho_2)$
5	0.177 756 21	0.217 788	$\rho_1 \rho_2 \rho_3$
6	-0.027 142 27	0.011 167	$\rho_1^4 + \rho_2^4 + \rho_3^4$
7	-0.049 498 64	-0.061 533	$\rho_1^3(\rho_1 + \rho_2) + \rho_1^3(\rho_1 + \rho_3) + \rho_2^3(\rho_1 + \rho_2)$
8	-0.020 040 15	-0.037 214	$\rho_1^2 \rho_2^2 + \rho_1^2 \rho_2^2 + \rho_2^2 \rho_3^2$
9	0.141 689 61	0.086 770	$\rho_1 \rho_2 \rho_3(\rho_1 + \rho_2 + \rho_3)$
10	-0.040 368 80	-0.003 403	$\rho_1^5 + \rho_2^5 + \rho_3^5$
11	0.033 825 17	-0.038 229	$\rho_1(\rho_1^2 + \rho_2^2) + \rho_2(\rho_1^2 + \rho_2^2) + \rho_3(\rho_1^2 + \rho_2^2)$
12	-0.045 716 12	-0.046 858	$\rho_1^3(\rho_1^2 + \rho_2^2) + \rho_2^3(\rho_1^2 + \rho_2^2) + \rho_3^3(\rho_1^2 + \rho_2^2)$
13	0.120 555 35	-0.018 078	$\rho_1 \rho_2 \rho_3(\rho_1^2 + \rho_2^2 + \rho_3^2)$
14	-0.042 737 25	0.064 343	$\rho_1 \rho_2 \rho_3(\rho_1 \rho_2 + \rho_1 \rho_3 + \rho_2 \rho_3)$
15	-0.011 830 68		$\rho_1^6 + \rho_2^6 + \rho_3^6$
16	0.113 473 39		$\rho_1^5 \rho_2 + \rho_1^5 \rho_3 + \rho_2^5 \rho_3$
17	0.536 618 54		$\rho_1^4 \rho_2^2 + \rho_1^4 \rho_3^2$
18	0.003 164 49		$\rho_1^3(\rho_1 + \rho_2) + \rho_1^3(\rho_1 + \rho_3) + \rho_2^3(\rho_1 + \rho_2)$
19	-0.019 564 78		$\rho_1^2(\rho_1^2 + \rho_2^2) + \rho_2^2(\rho_1^2 + \rho_2^2) + \rho_3^2(\rho_1^2 + \rho_2^2)$
20	-0.253 447 45		$\rho_1 \rho_2 \rho_3(\rho_1^2 + \rho_2^2 + \rho_3^2)$
21	0.031 806 87		$\rho_1 \rho_2 \rho_3[\rho_1^2(\rho_1 + \rho_2) + \rho_2^2(\rho_1 + \rho_3) + \rho_3^2(\rho_1 + \rho_2)]$

^a $R_{\text{eq}} = 1.6504$ bohr, and coefficients are in a.u.^b $R_{\text{eq}} = 1.6574$ bohr.

fifth-degree potential function were obtained. Then the geometries and energies for the asymmetric structures were combined with the data for the isosceles structures and a second set of SPF expansion coefficients were obtained. These two sets of coefficients were virtually identical, demonstrating the balanced accuracy obtained in these two PES regions by Dykstra and Swope's SCEP method. Finally, for improved accuracy a set of six-degree SPF coefficients was generated.

In our attempts to obtain the best SPF representation of the PES we discovered that a small group of grid points were limiting the precision in the expansion coefficients, and that a more precise set of coefficients could be obtained if an energy-based criterion were used to select the geometries before doing the regression analysis. A set of sixth-degree expansion coefficients was obtained by requiring predicted and known grid point energies to agree to within a prechosen energy threshold or tolerance, dE ; values of 6.6 and 2.2 wave numbers were used for dE .

B. Calculating the quartic normal force fields

This section describes the calculation of quartic normal force fields from the Carney-Porter and Dykstra-Swope SPF fits for the isotopic H₃⁺ molecules.²² Normal force fields are defined as expansions in normal coordinates Q_k ($k = 1-3$) rather than in SPF internal coordinates. The initial step in this calculation involves numerically evaluating the matrix

$$f = [f_{i,j} = d^2V/dt_i dt_j]$$

of second derivatives of the potential function V with respect to the three independent rectilinear vibrational coordinates t_i ($i = 1-3$) introduced by Carney, Langhoff, and Curtiss.¹⁰ This gives

$$V(t_1, t_2, t_3) = 1/2(f_{1,1}t_1^2 + f_{2,2}t_2^2 + f_{3,3}t_3^2) + (f_{1,2}t_1t_2 + f_{1,3}t_1t_3 + f_{2,3}t_2t_3 + \dots).$$

The second step involves finding the normal coordinates as linear combinations of the t_i coordinates,

$$t_i = L_{i,1}Q_1 + L_{i,2}Q_2 + L_{i,3}Q_3.$$

This calculation determines harmonic vibration frequencies, ω_k , and coefficients, $L_{i,k}$, which are the solutions of a 3×3 eigenvalue-eigenvector matrix equation involving the reduced mass μ and quadratic force constant matrix f ,

$$fL = LG,$$

where

$$G = 4\pi^2\mu[\omega_j^2\delta_{i,j}].$$

The properties of the L matrix allow the Q_k to be written as

$$Q_k = L_{1,k}t_1 + L_{2,k}t_2 + L_{3,k}t_3.$$

The third step involves numerically calculating third and fourth mixed and pure partial derivatives of the potential function with respect to the normal coordinates. From these derivatives values of the cubic, K_{ijk} , and quartic, K_{ijkl} , force constants are determined, and the quartic potential is set up using a restricted summation convention:

$$V(Q_1, Q_2, Q_3) = 2\pi^2\mu \sum \omega_i^2 Q_i^2 + \sum \sum \sum K_{i,j,k} Q_i Q_j Q_k \\ + \sum \sum \sum \sum K_{i,j,k,l} Q_i Q_j Q_k Q_l$$

A second method for calculating $K_{i,j,k}$ and $K_{i,j,k,l}$ utilized regression analysis and fifth-degree expansions in the normal coordinates Q_k ; the two sets of force constants were found to agree excellently.

The next step introduces dimensionless normal coordinates q_k as

$$q_k = (4\pi^2\omega_k \mu c/h)^{1/2} Q_k$$

and sets up the quartic force field as

$$V(q_1, q_2, q_3) = 1/2 \sum v_i q_i^2 + \sum \sum \sum k_{i,j,k} q_i q_j q_k \\ + \sum \sum \sum \sum k_{i,j,k,l} q_i q_j q_k q_l$$

using cubic, k_{ijk} and quartic, k_{ijkl} , force constants, a restricted summation convention, and $\omega_k = v_k c$; v is in units of wave numbers. A second method for calculating $k_{i,j,k}$ and $k_{i,j,k,l}$ utilized regression analysis and fifth-degree expansions in the dimensionless normal coordinates q_k ; the two sets of force constants were found to agree excellently.

C. Selecting vibration basis sets for the variational calculation

From initial calculations it quickly became evident that the internal coordinate Carney-Cropek method is very inefficient for converging the vibrational levels of the H₂⁺ isotopes; extremely large basis sets and multidimensional numerical quadrature grids for matrix element evaluation were required. Computer time was further increased as different basis sets with different distributions of vibrational quanta were tried. To keep the calculation tractable an effective basis function selection strategy was required.

The strategy we developed is similar to one often employed in electronic structure calculations, in which the wave function coefficients are examined to determine which basis functions have the largest contributions to the eigenstates of interest. In our case the eigenstates of interest were the ten lowest states, i.e., the one- and two-quantum states,

which we wished to converge to within one and five wave numbers, respectively. The figure of merit in assigning a relative importance to each basis function was chosen as the weight, W , of that function in the Hilbert space of the ten lowest calculated eigenstates.

$$W = \sum_{i=1}^{10} \langle b | Y_i \rangle \langle Y_i | b \rangle,$$

where $|Y_i\rangle$ is the i th vibrational eigenstate and $|b\rangle$ is the basis function.

In setting up a subsequent trial diagonalization in which the basis set was enlarged, the limits on the numbers of vibrational quanta were chosen so that previously included basis functions having small values of W were dropped from the new basis set. After several such iterations we returned some of the previously dropped basis functions to test their effect on convergence.

It was found that by selecting only the basis functions having $W > 10^{-5}$ reasonably good convergence was obtained, although additional functions continued to improve the energies slightly. Adding extra bending quanta (as many as 25 quanta) to this "core" basis had a much more pronounced effect upon convergence than did adding extra stretching quanta, even though in all cases the new functions had $W < 10^{-5}$. This result is not surprising, since a perturbation theory analysis indicates that the energy improvement upon adding a given basis function is proportional not only to its weight, but also to its energy relative to that of the eigenstates of interest.

In our final calculations we included all basis functions having $n_1 < 5$, $n_2 < 5$, and $n_1 + n_2 < 7$, where n_1 and n_2 are the bond-stretch (radial coordinate) quantum numbers, while the limit, N , on the angle-bend (angular coordinate) quantum number n_3 was chosen as 25 for H₂⁺ and D₂H⁺ and 22 for H₂D⁺ and D₃⁺. The smaller N required for D₃⁺ and H₂D⁺ reflects the reduced vibrational momentum coupling due to heavier masses and a more favorable mass ratio in these respective molecules. With the basis sets described above the Hamiltonian matrix factors into A and B submatrices of dimension 442 and 338, respectively, for H₂⁺ and D₂H⁺, and dimension 391 and 229, respectively, for H₂D⁺ and D₃⁺. The number of quadrature points was 19 in the radial coordinates, and $N + 1$ in the angular coordinate.

TABLE II. Second-order perturbation theory formulas for vibration energies of bent XY₂ molecules.*

XY ₂ vibration energy formula	
$E(n_1, n_2, n_3) = \sum_{i=1}^3 \omega_i (n_i + \frac{1}{2}) + \sum_{i,j} X_{ij} (n_i + \frac{1}{2})(n_j + \frac{1}{2})$	
X ₂ vibration energy formula	
$E(n_1, n_2, l) = \omega_1 (n_1 + \frac{1}{2}) + \omega_2 (n_2 + \frac{1}{2}) \\ + X_{11} (n_1 + \frac{1}{2})^2 + X_{12} (n_1 + \frac{1}{2})(n_2 + \frac{1}{2}) + X_{22} (n_2 + \frac{1}{2})^2 + g_{12} l^2$	

* Reference 23. n_i ($i = 1-3$) are the normal mode quantum numbers for the XY₂ molecule, while the l quantum number and n_2 quantum numbers are for the axial molecule X₂.

TABLE III. Formulas for anharmonic vibrational term coefficients of bent XY₂ molecules, from Ref. 23.*

XY ₂ molecule	
$x_{11} = \frac{1}{2} k_{1111} - \frac{15k_{111}^2}{4\omega_1} - \frac{k_{111}^2 (8\omega_1^2 - 3\omega_2^2)}{4\omega_2 (4\omega_1^2 - \omega_2^2)}$	
$x_{22} = \frac{1}{2} k_{2222} - \frac{15k_{222}^2}{4\omega_2} - \frac{k_{222}^2 (8\omega_2^2 - 3\omega_1^2)}{4\omega_1 (4\omega_2^2 - \omega_1^2)}$	
$x_{33} = \frac{1}{2} k_{3333} - \frac{k_{111}^2}{4\omega_1} - \frac{(8\omega_1^2 - 3\omega_2^2)}{(4\omega_2^2 - \omega_1^2)} - \frac{k_{222}^2 (8\omega_2^2 - 3\omega_1^2)}{4\omega_2 (4\omega_1^2 - \omega_2^2)}$	
$x_{12} = k_{1122} - \frac{3k_{111}k_{222}}{\omega_1} - \frac{3k_{222}k_{111}}{\omega_2} - \frac{2k_{111}^2\omega_1}{(4\omega_1^2 - \omega_2^2)} - \frac{2k_{222}^2\omega_2}{(4\omega_2^2 - \omega_1^2)}$	
$x_{13} = k_{1133} - \frac{3k_{111}k_{333}}{\omega_1} - \frac{k_{222}k_{333}}{\omega_2} - \frac{2k_{111}^2\omega_1}{(4\omega_1^2 - \omega_2^2)} + C_e \xi_{13}^2 \left(\frac{\omega_1}{\omega_2} + \frac{\omega_2}{\omega_1} \right)$	
$x_{23} = k_{2233} - \frac{k_{333}k_{222}}{\omega_1} - \frac{3k_{222}k_{333}}{\omega_2} - \frac{2k_{222}^2\omega_2}{(4\omega_2^2 - \omega_1^2)} + C_e \xi_{23}^2 \left(\frac{\omega_2}{\omega_1} + \frac{\omega_1}{\omega_2} \right)$	
X ₂ axial molecule	
$x_{11} = \frac{1}{2} k_{1111} - \frac{15}{4} \frac{k_{111}^2}{\omega_1}$	
$x_{22} = \frac{1}{2} k_{2222} - \frac{15}{4} \frac{k_{222}^2}{\omega_2} - \frac{k_{222}^2 (8\omega_2^2 - 3\omega_1^2)}{4\omega_1 (4\omega_2^2 - \omega_1^2)}$	
$x_{12} = k_{1122} - \frac{3}{\omega_1} k_{111}k_{222} - \frac{2\omega_2 k_{222}^2}{(4\omega_2^2 - \omega_1^2)}$	
$g_{22} = C_e - \frac{1}{2} k_{2222} - \frac{\omega_1 k_{222}^2}{4(4\omega_2^2 - \omega_1^2)} + \frac{21}{4\omega_2} k_{222}^2$	

* The equilibrium rotation constant C_e is for rotational motion about an axis perpendicular to the plane of the molecule, and ξ_{23} is the Coriolis coupling constant.

D. Second-order perturbation theory

Standard methods for calculating vibration energies of polyatomic molecules use second-order perturbation theory and molecular force fields developed as quartic polynomial expansions in dimensionless normal coordinates.²³ The vibration energy is given by this theory as an expansion in the vibration quantum numbers as shown in Table II for the axial and nonaxial isotopic H₂⁺ molecules. The quantities ω_i and $x_{k,j}$, respectively the harmonic and anharmonic coefficients in the energy expansion, are dependent upon the quadratic, cubic, and quartic force constants in the quartic normal force fields as shown in Table III.

IV. RESULTS AND DISCUSSION

In the following Secs. IV A–IV C we discuss the SPF and normal coordinate potential functions, variational convergence properties, and variationally and perturbationally calculated vibration intervals. The *ab initio* vibration intervals are compared to observed excitation energies and to results obtained by other authors.

A convenient and concise way to compare two sets (A) and (B) of N corresponding vibration intervals $E(A)_i$ and $E(B)_i$, $i = 1-N$, is to calculate a standard deviation in excitation energy E_{sd} , as

$$E_{sd} = \left\{ N^{-1} \sum [E(A)_i - E(B)_i]^2 \right\}^{1/2}.$$

A. Potential energy functions

1. The SPF fit to Dykstra and Swope's H₂⁺ PES

An energy acceptance criterion of $dE = 6.6$ wave numbers deleted four geometries from the input set of 68, and subsequent sixth degree regression analysis gave the SPF expansion coefficients quoted in Table I with an average energy error of 1.2 wave numbers. Reducing dE to 2.2 wave numbers deleted six additional geometries and reduced the average energy error to 0.71 wave numbers. However, deletion of as many as ten geometries from the data set seemed to us to be excessive, so we decided to use the Table I coefficients in our final vibration energy calculations. Identification numbers (as found in Table I of Dykstra and Swope's paper) for the four deleted geometries are 56, 63, 65, and 66. These geometries all have negative S and large positive R as polar displacement coordinate values.

An examination of the deleted geometries was made using the Carney–Porter SPF expansion coefficients given in Table I. Note that the Dykstra–Swope and Carney–Porter SPF fits have slightly different equilibrium internuclear dis-

TABLE IV. Quartic normal force fields derived from the Carney-Porter PES.

Force constants (cm ⁻¹)	H ₂ ⁺	H ₂ D ⁺	D ₂ H ⁺	H ₂ ⁺	
ω_1	3452.63	3244.03	2939.51	2442.38	
ω_2	2746.10	2386.85	2083.05	1942.58	
ω_3	2746.10	2507.04	2242.64	1942.58	
k_{1111}	-325.36	-341.42	-279.16	-193.58	
k_{1222}	-195.88	24.54	-241.01	-116.54	
k_{1112}	0.00	-212.52	38.44	0.00	
k_{1122}	-664.45	-577.68	-145.76	-395.33	
k_{1133}	-664.45	-339.40	-647.17	-395.33	
k_{2233}	587.63	642.18	217.97	349.62	
k_{11111}	37.80	52.22	31.52	18.92	
k_{22222}	13.51	-7.88	37.58	6.76	
k_{13333}	13.51	22.03	-5.23	6.76	
k_{11112}	0.03	91.56	7.52	0.02	
k_{11222}	137.15	2.17	61.88	68.63	
k_{11222}	163.40	165.58	-29.43	81.77	
k_{11222}	163.40	-11.70	220.69	81.77	
k_{12222}	27.02	94.09	-29.59	13.52	
k_{12222}	-412.82	-346.04	-159.25	-206.58	
Force constants (cm ⁻¹)	H ₂ T ⁺	D ₂ T ⁺	T ₂ H ⁺	T ₂ D ⁺	T ₂ ⁺
ω_1	3206.03	2331.79	2800.48	2189.24	1995.83
ω_2	2205.33	1795.29	1726.28	1670.01	1587.41
ω_3	2422.25	1831.86	2047.83	1713.99	1587.41
k_{1111}	-358.85	-193.78	-261.30	-173.64	-142.00
k_{1222}	59.19	-20.52	-188.53	-155.86	-86.09
k_{1112}	-214.22	-95.32	-13.08	43.73	0.0
k_{1122}	-485.37	-389.60	-37.07	-186.97	-292.03
k_{1133}	-253.41	-262.76	-585.07	-404.63	-292.03
k_{2233}	614.90	385.09	136.17	197.17	258.26
k_{11111}	61.01	21.80	26.46	17.24	12.63
k_{12222}	-5.99	-3.39	28.90	18.61	4.51
k_{13333}	24.00	9.79	-12.93	0.80	4.51
k_{11112}	99.47	34.16	24.49	-6.27	0.01
k_{11222}	-21.44	21.36	24.81	53.51	45.83
k_{11222}	127.31	97.31	-34.30	4.81	54.60
k_{11222}	-50.60	19.24	208.41	109.13	54.60
k_{12222}	94.06	40.77	-22.59	-12.63	9.03
k_{12222}	-306.65	-191.77	-105.03	-120.10	-137.95

TABLE V. Quartic normal force fields derived from the Dykstra-Swope PES.

Force constants (cm ⁻¹)	H ₂ ⁺	H ₂ D ⁺	D ₂ H ⁺	D ₂ ⁺
ω_1	3447.29	3243.87	2940.74	2438.60
ω_2	2774.63	2408.03	2100.56	1962.76
ω_3	2774.63	2533.09	2265.94	1962.76
k_{1111}	-336.51	-354.22	-286.63	-200.21
k_{2222}	-206.31	27.39	-250.00	-122.75
k_{1112}	0.0	-214.50	22.93	0.0
k_{1122}	-672.19	-586.57	-132.12	-399.93
k_{1133}	-672.19	-326.07	-666.30	-399.93
k_{2233}	618.94	673.61	227.59	368.25
k_{11111}	47.60	58.26	34.34	23.82
k_{22222}	13.40	-9.16	37.73	6.70
k_{13333}	13.40	22.57	-5.96	6.70
k_{11112}	0.02	77.90	23.60	0.01
k_{11222}	138.63	1.93	56.52	69.37
k_{11222}	148.78	163.44	-29.48	74.45
k_{11333}	148.78	-29.06	215.96	74.45
k_{22333}	26.80	96.74	-32.47	13.41
k_{12233}	-415.97	-339.19	-161.95	-208.16

Force constants (cm ⁻¹)	H ₂ T ⁺	D ₂ T ⁺	T ₂ H ⁺	T ₂ D ⁺	T ₂ ⁺
ω_1	3208.34	2329.91	2804.62	2187.87	1992.74
ω_2	2223.21	1812.59	1738.95	1685.81	1603.90
ω_3	2447.42	1850.89	2069.10	1713.81	1603.90
k_{1111}	-371.76	-200.95	-266.48	-179.34	-147.90
k_{2222}	62.26	-20.13	-194.04	-163.38	-90.68
k_{1112}	-234.12	-97.17	-30.47	38.64	0.0
k_{1122}	-492.38	-396.66	-27.76	-179.52	-295.43
k_{1133}	-238.26	-257.57	-603.22	-415.64	-295.43
k_{2233}	642.76	405.34	143.37	205.90	272.03
k_{11111}	65.47	25.62	27.25	20.08	15.91
k_{22222}	-7.04	-4.09	28.59	19.03	4.48
k_{13333}	24.76	9.95	-13.87	0.54	4.48
k_{11112}	85.27	28.70	37.66	1.05	0.01
k_{11222}	-22.03	21.64	21.73	51.04	46.32
k_{11222}	128.29	94.46	-29.10	0.42	49.72
k_{11333}	-66.64	10.27	205.07	105.82	49.72
k_{22333}	95.44	42.35	-24.49	-14.34	8.95
k_{12233}	-298.57	-189.94	-109.24	-121.26	-139.00

tances. For geometry number 56, the Carney-Porter fit gives an energy of 0.040 a.u. relative to the potential minimum and the Dykstra-Swope fit gives 0.039 a.u. However, the relative energy value reported by Dykstra and Swope for this geometry is 0.105 a.u. According to Martire and Burton¹⁷ this value is in error. The other three deleted geometries had predicted relative energies which were quite close to the values given by the Carney-Porter PES as well as those of Dykstra and Swope. Thus, the Table I SPF fit is seen to provide a very accurate representation of Dykstra and Swope's PES over the entire range of geometries encompassed by their calculation.

2. Quartic normal force fields

The ω_k , k_{ijk} , and k_{ijkl} , which define the quartic normal force fields, are presented in Tables IV and V, respectively.

for the Carney-Porter and Dykstra-Swope PES's. Force constants for tritiated isotopes are also given in these tables. These force fields should be helpful for calculating such spectroscopic parameters as the anharmonic rotation constants and centrifugal distortion constants.

B. Variational results

1. Convergence properties of internal and *t* coordinate Hamiltonians

As mentioned in Sec. III C our energy level convergence and basis set selection study utilized the Carney-Porter SPF PES, for which results may be compared with previous stud-

TABLE VI. Zero-point and one-quantum excitation energies for isotopic H_3^+ molecules (cm^{-1}).

Vibration methods	Variational r coordinate	Variational internal coordinate	PT	Variational internal coordinate	PT
Potential surface	Carney and Porter	Fifth degree SPF	Carney-Porter force field	Dykstra and quartic normal degree SPF	Dykstra-Swope sixth force field
H_3^+ molecule					
E_0	4345.3	4345.1	4304.1	4363.5	4312.6
ω_2	2516	2516	2509	2522	2512
ω_1	3185	3185	3179	3180	3163
D_3^+ molecule					
E_0	3099.8	3099.8	3079.5	3114.6	3089.2
ω_2	1826	1826	1824	1835	1832
ω_1	2307	2307	2306	2303	2296
D_2H^+ molecule					
E_0	3547.5	3547.5	3548.7	3563.9	3562.9
ω_2	1961	1961	1959	1969	1966
ω_3	2072	2073	2067	2080	2069
ω_1	2742	2743	2739	2739	2731
H_2D^+ molecule					
E_0	3963.0	3962.8	3952.6	3980.5	3965.8
ω_2	2203	2201	2196	2207	2199
ω_3	2328	2327	2324	2336	2330
ω_1	3000	2999	2993	2994	2979

ies. The vibration energies obtained are shown in Tables VI and VII; experimental values are quoted in Table VIII. We estimate that for H_2D^+ and D_3^+ the two-quantum levels are converged to within several wave numbers while the fundamentals are converged to better than 1 wave number. For H_3^+ the convergence error is somewhat greater, perhaps as large as five wave numbers for the two-quantum levels, and for D_2H^+ the error is even larger. For every molecule studied except D_2H^+ the energies are better converged than the values obtained in Carney and Porter's r coordinate calculations on the same PES with a smaller basis set.

Our rough convergence estimates are based on the stability of the energies when the basis set is expanded or contracted and on the magnitude of the splittings of the degenerate states of H_3^+ and D_3^+ . These estimates are also reinforced by the discussion of Burton *et al.*,¹⁷ who estimated the convergence error for H_3^+ and D_3^+ arising from the use of a 220 term basis set which corresponds closely to Carney and Porter's.

From the above discussion it is evident that H_3^+ is more difficult to converge with internal coordinate basis functions than are D_3^+ and H_2D^+ , and that D_2H^+ is the most difficult of all. This conclusion is verified by examining the basis function weights, W . From Table IX it is seen that for every weight category the number of basis functions required increases in the order D_3^+ , H_2D^+ , H_3^+ , and D_2H^+ . A similar

pattern is seen in the number of bending quanta required, shown in Table IX. On the other hand, it is not clear whether these molecules differ significantly in the number of stretching quanta required for convergence, as in all cases this number is small.

The very large number of basis functions required for convergence in the current study is a reflection of the limitations of internal coordinate-separable basis functions for this class of molecules. Still, the internal coordinate approach may be competitive in efficiency with the r coordinate method in the case H_2D^+ .

2. Improved vibration intervals

Comparisons of the experimental and theoretical fundamental excitation energies of the isotopic H_3^+ molecules are given in Table VIII using the Dykstra-Swope SPF PES and the vibration basis sets which were found to be most satisfactory for the Carney-Porter PES. The superb agreement between theoretical and experimental fundamental vibration frequencies, $E_{\text{ex}} = 1.2$ wave numbers, confirms the accuracy claim made by Dykstra and Swope about their PES. Since the Carney-Porter PES gives an E_{ex} of 6.9 wave numbers, the Dykstra-Swope PES is clearly more accurate than Carney and Porter's.

TABLE VII. Two-quantum excitation energies for isotopic H₃⁺ molecules (cm⁻¹).

Vibration methods	Variational coordinate	Variational internal coordinate	PT	Variational internal coordinate	PT
Potential surface	Carney and Porter fifth degree SPF	Carney and Porter fifth degree SPF	Carney-Porter quartic normal force field	Dykstra and Swope sixth degree SPF	Dykstra-Swope quartic normal force field
$n_1, n_2, \pm l$	H ₃ ⁺ molecule				
0,2,0	4799	4795	4733	4785	4710
0,2,2	5000	4997	5003	5002	5010
1,1,1	5568	5560	5532	5554	5495
2,0,0	6268	6262	6243	6269	6223
$n_1, n_2, \pm l$	D ₃ ⁺ molecule				
0,2,0	3528	3526	3505	3532	3505
0,2,2	3639	3638	3640	3653	3556
1,1,1	4062	4061	4051	4060	4038
2,0,0	4561	4560	4553	4560	4541
n_1, n_2, n_3	H ₂ D ⁺ molecule				
0,2,0	4314	4292	4309	4290	4307
0,0,2	4605	4594	4545	4607	4545
0,1,1	4490	4464	4456	4468	4456
1,1,0	5067	5051	5042	5041	5018
1,0,1	5246	5241	5223	5245	5205
2,0,0	5888	5882	5856	5880	5825
n_1, n_2, n_3	D ₂ H ⁺ molecule				
0,2,0	3819	3817	3817	3820	3817
0,0,2	4041	4044	4009	4049	4001
0,1,1	4046	4048	4046	4065	4062
1,1,0	4644	4644	4629	4653	4629
1,0,1	4688	4695	4683	4684	4656
2,0,0	5391	5395	5374	5394	5357

Vibration intervals calculated variationally by Tennyson and Sutcliffe¹⁶ for H₃⁺ and H₂D⁺ with Schinke *et al.*²⁴ PES, and those obtained for H₃⁺ and D₃⁺ by Burton *et al.*¹⁷ were generated using accurate PES's and high quality vibrational basis sets, and also give small E_{ad} 's for theory vs experiment [22 (Tennyson-Sutcliffe) and 9 (Burton) wave numbers]. We believe that the differences between their calculated vibration intervals and those of the present study are

TABLE VIII. Theoretical and experimental vibration intervals for isotopic H₃⁺ molecules (cm⁻¹).

Molecule	Excitation	Variational Dykstra-Swope sixth-degree SPF	Experimental Refs. 1-4
H ₃ ⁺	ν_R	2522	2521.6
H ₂ D ⁺	ν_1	2994	2992.5
	ν_2	2207	2205.9
	ν_3	2336	2335.4
D ₂ H ⁺	ν_1	2739	2737.0
	ν_2	1969	1968.1
	ν_3	2080	2078.4
D ₃ ⁺	ν_R	1835	1835.7

TABLE IX. Convergence properties of the internal coordinate vibration wave functions.

Weight W	H ₃ ⁺	D ₃ ⁺	H ₂ D ⁺	D ₂ H ⁺
Number of basis functions of a given weight, W , in the subspace of the ten lowest vibrational states.				
$W > 10^{-2}$	51	42	44	56
$10^{-2} > W > 10^{-3}$	89	65	70	92
$10^{-3} > W > 10^{-4}$	124	109	109	130
Maximum number of bending quanta for basis functions of a given weight				
$W > 10^{-2}$	6	5	5	6
$W > 10^{-3}$	12	8	10	12
$W > 10^{-4}$	16	14	14	16
Maximum number of stretching quanta per bond for basis functions of a given weight				
$W > 10^{-2}$	3	3	3	3
$W > 10^{-3}$	4	4	4	5
$W > 10^{-4}$	5	5	5	5

TABLE X. Anharmonic vibration term coefficients calculated from the Carney-Porter quartic normal force fields for isotopic H₃⁺ molecules (cm⁻¹).

X ₃ molecule	x ₁₁	x ₂₂	x ₃₃	x ₁₂	x ₁₃	x ₂₃
H ₃ ⁺	-58.08	-75.33	-157.00			67.50
D ₃ ⁺	-29.06	-37.69	-78.56			33.78
T ₃ ⁺	-19.41	-25.17	-52.46			22.56

XY ₂ molecule	x ₁₁	x ₂₂	x ₃₃	x ₁₂	x ₁₃	x ₂₃
H ₂ D ⁺	-64.93	-42.13	-51.67	-147.60	-94.36	-64.66
D ₂ H ⁺	-52.27	-50.15	-62.30	-68.55	-122.70	20.29
H ₂ T ⁺	-70.50	-31.04	-44.20	-139.16	-84.11	-71.14
T ₂ H ⁺	-51.59	-34.04	-58.76	-50.69	-100.49	19.86
D ₂ T ⁺	-29.89	-26.66	-29.70	-78.20	-55.74	-25.92
T ₂ D ⁺	-26.22	-31.68	-33.19	-46.42	-70.48	7.77

due mainly to small differences in the PES's used. More recently Martire and Burton¹⁷ fitted Dykstra and Swope's PES and also obtained an improved fit to their own *ab initio* PES. E_{ad} values, 6 and 3 cm⁻¹, are obtained for H₃⁺ and D₃⁺, respectively, when their fit and our fit to the Dykstra-Swope PES are compared. E_{ad} values, 5 and 7 cm⁻¹, are obtained for H₃⁺ and D₃⁺, respectively when their improved fit to their own PES and our fit to the Dykstra-Swope PES are compared. Again, the differences in vibration intervals are probably due mainly to the PES fits used.

As for the zero-point vibration energies of H₃⁺ and H₂D⁺, quantities which are important in determining the equilibrium constant for the isotopic exchange reaction, all of the above studies are in excellent agreement with each other, the differences not exceeding 1.2 wave numbers.

On the other hand, the present Carney-Porter and Dykstra-Swope vibration intervals for several two-quantum excitations in H₃⁺ differ from the earlier values reported by Burton *et al.* and by Tennyson and Sutcliffe by considerable amounts. These differences are greater than our vibrational convergence errors, as seen from the D₃⁺ results, which are well converged in the present study.

More recently, Meyer and Botschwina²⁵ have calculated an H₃⁺ *ab initio* PES using a 10s,4p,2d electronic orbital basis set which they fitted to a function expressed in curvilinear

symmetry coordinates, and determined the vibrational frequencies and zero-point energies for isotopic H₃⁺ molecules using 504 vibrational basis functions. Comparing their results for H₃⁺, H₂D⁺, D₂H⁺, and D₃⁺ to the present improved vibrational intervals derived from the Dykstra-Swope PES for one- and two-quantum excitations, that is, using the two sets of 30 transitions, gives an E_{ad} of 5.9 wave numbers. Comparing the fundamentals of the four isotopic molecules for the Dykstra-Swope PES against those for the Meyer-Botschwina PES gives an E_{ad} of only 2.4 wave numbers. These small differences in the E_{ad} 's indicate that the two potential functions are nearly equivalent. Comparing Meyer and Botschwina's results for the fundamentals to the experimental data in Table VIII gives an E_{ad} of 1.8 wave numbers. Thus, the Dykstra-Swope and Meyer-Botschwina PES's both give superb agreement with experiment.

C. Perturbation theory results

The calculated anharmonic coefficients x_{ij} are given in Tables X and XI. Vibrational intervals given by second-order perturbation theory (PT) are presented in Tables VI and VII along with the accurate variational results. Including all 30 one- and two-quantum excitation intervals the E_{ad} value for variational vs PT methods is 20 wave numbers for the Carney-Porter PES, and 31 wave numbers for the Dykstra-

TABLE XI. Anharmonic vibrational term coefficients calculated from the Dykstra-Swope quartic normal force fields for isotopic H₃⁺ molecules (cm⁻¹).

X ₃ molecule	x ₁₁	x ₂₂	x ₃₃	x ₁₂	x ₁₃	x ₂₃
H ₃ ⁺	-51.78	-82.37	-180.66			75.18
D ₃ ⁺	-25.91	-41.22	-90.40			37.62
T ₃ ⁺	-17.30	-27.53	-60.37			25.12

XY ₂ molecule	x ₁₁	x ₂₂	x ₃₃	x ₁₂	x ₁₃	x ₂₃
H ₂ D ⁺	-66.45	-45.93	-57.30	-160.38	-103.68	-73.30
D ₂ H ⁺	-52.12	-57.14	-68.92	-67.49	-143.90	26.52
H ₂ T ⁺	-74.82	-34.36	-49.22	-146.65	-91.18	-80.56
T ₂ H ⁺	-54.32	-38.31	-63.40	-48.03	-116.76	22.39
D ₂ T ⁺	-28.94	-28.85	-32.82	-87.75	-62.28	-29.15
T ₂ D ⁺	-25.41	-35.52	-36.19	-49.40	-81.88	9.97

Swope PES. If only the fundamental excitations are considered, the E_{ad} 's are reduced to five and ten wave numbers for the respective PES's. For both PES's rather large differences are found in the variational and PT derived zero-point vibration energies.

These comparisons of variational results with PT demonstrate that second-order PT has limited accuracy with these light molecules. Of course, for some purposes an accuracy of 10–30 wave numbers in the vibration energy calculation might be acceptable, and then the convenience of PT would offset the improved accuracy with the variational method. For example, when Polak's²⁶ diatomics-in-molecules PES for H_2^+ is used the fundamental excitation energies are $\nu_E = 2255$ and $\nu_A = 3315$ wave numbers for H_2^+ , and $\nu_E = 1627$ and $\nu_A = 2391$ wave numbers for D_2^+ .²⁷ Comparing these four DIM vibrational intervals to those obtained from the Dykstra-Swope PES gives $E_{ad} = 187$ wave numbers.

V. CONCLUSIONS

A sixth-degree Simons-Parr-Finlan polynomial expansion is found to give a very precise fit to the Dykstra-Swope *ab initio* potential energy surface for H_2^+ , the average error being only 1.2 wave numbers. Using this potential function and the variational method, fundamental vibration intervals are obtained which agree with experimental values to within an average of 1.2 wave numbers. This level of agreement is comparable to recent results obtained by Meyer and Botschwina. With the Carney-Porter fifth degree SPF surface the average agreement with experiment is 6.9 wave numbers.

The r coordinate vibrational Hamiltonian is found to give a much more compact wave function expansion for the isotopic H_2^+ molecules compared to the internal coordinate Lai-Hagstrom Hamiltonian used in the current Carney-Cropek variational method. The possible exception is H_2D^+ , for which the two Hamiltonians may be comparably efficient. Very careful basis set selection is required to converge the Carney-Cropek algorithm for isotopic H_2^+ molecules.

The standard second-order perturbation theory approach is found to give an accuracy of about five-ten wave numbers for the fundamental vibration intervals and about 20–30 wave numbers for the two-quantum intervals. Thus, perturbation theory is suitable for these light molecules only when highly accurate vibrational energies are not required.

ACKNOWLEDGMENTS

The authors gratefully acknowledge W. Meyer and P. Botschwina, and B. Martire and P. G. Burton for providing us with their unpublished results for the isotopic H_2^+ molecules, and members of the Allegheny College Computer

Center, especially Jeff Gleason, Pete Gifford, Mary Jane Lombardi, and Rich Metzger. S.M.A.-G. gratefully acknowledges the support of the Air Force Geophysics Laboratory, Hanscom AFB, MA, under Contract No. F19628-83-C-0056.

¹T. Oka, *Phys. Rev. Lett.* **45**, 531 (1980).

²K. G. Lubic and T. Amano, *Can. J. Phys.* **62**, 1886 (1984).

³T. Amano and J. K. G. Watson, *J. Chem. Phys.* **81**, 2869 (1984).

⁴S. C. Foster, A. R. W. McKellar, and J. K. G. Watson, Paper TE10, 40th Symposium on Molecular Spectroscopy, Ohio State University, Columbus, Ohio, June 1985.

⁵J. T. Shy, J. W. Farley, W. E. Lamb, Jr., and W. H. Wing, *Phys. Rev. Lett.* **45**, 535 (1980); J. T. Why, J. W. Farley, and W. H. Wing, *Phys. Rev. A* **24**, 1146 (1980).

⁶H. E. Warner, W. T. Conner, R. H. Petrmichl, and R. C. Woods, *J. Chem. Phys.* **81**, 2514 (1984).

⁷E. Herbst and W. Klemperer, *Phys. Today* **20**, 32 (1976); T. Oka, in *Molecular Spectroscopy, Structure and Chemistry*, edited by T. A. Miller and V. E. Bondybey (North-Holland, Amsterdam, 1983).

⁸G. D. Carney and R. N. Porter, *J. Chem. Phys.* **60**, 4251 (1974); **65**, 3547 (1976).

⁹G. D. Carney and R. N. Porter, *Chem. Phys. Lett.* **50**, 327 (1977); G. D. Carney, *Mol. Phys.* **39**, 923 (1980); G. D. Carney and R. N. Porter, *Phys. Rev. Lett.* **45**, 537 (1980); G. D. Carney, *Chem. Phys.* **54**, 103 (1980); *Chem. Phys. Lett.* **78**, 200 (1981); *Can. J. Phys.* **62**, 1871 (1984).

¹⁰G. D. Carney, S. R. Langhoff, and L. A. Curtiss, *J. Chem. Phys.* **66**, 3724 (1977).

¹¹G. D. Carney, L. L. Sprandel, and C. W. Kern, *Adv. Chem. Phys.* **37**, 305 (1978).

¹²J. Carter and N. Handy, *Mol. Phys.* **47**, 1445 (1982).

¹³J. Tennyson and B. T. Sutcliffe, *J. Chem. Phys.* **77**, 4061 (1982).

¹⁴C. E. Dykstra and W. C. Swope, *J. Chem. Phys.* **70**, 1 (1979); C. E. Dykstra, A. S. Gaylord, W. D. Gwinn, W. C. Swope, and H. F. Schaefer, *J. Chem. Phys.* **68**, 3951 (1978).

¹⁵D. Cropek and G. D. Carney, *J. Chem. Phys.* **80**, 4280 (1984); *Adv. Comput. Methods. Part. Diff. Eqs.* **5**, 534 (1984); D. Cropek, Dept. of Chemistry and Computer Science, Senior thesis project, Allegheny College, Meadville, PA, 1983.

¹⁶J. Tennyson and B. T. Sutcliffe, *Mol. Phys.* **51**, 887 (1984).

¹⁷P. G. Burton, E. Von Nagy-Felsobuki, G. Doherty, and M. Hamilton, *Chem. Phys.* **83**, 83 (1984); P. G. Burton, E. Von Nagy-Felsobuki, and G. Doherty, *Chem. Phys. Lett.* **104**, 323 (1984); B. Martire and P. G. Burton, *Chem. Phys. Lett.* **121**, 479 (1985).

¹⁸G. Simons, R. G. Parr, and J. M. Finlan, *J. Chem. Phys.* **59**, 3229 (1973).

¹⁹G. D. Carney, L. A. Curtiss, and S. R. Langhoff, *J. Mol. Spectrosc.* **61**, 371 (1976); G. D. Carney, *Mol. Phys.* **37**, 659 (1979).

²⁰S. M. Adler-Golden, S. R. Langhoff, C. W. Bauschlicher, Jr., and G. D. Carney, *Chem. Phys.* **83**, 255 (1985).

²¹B. Numerov, *Publ. Obs. Cent. Astrophys. Russ.* **2**, 188 (1933); J. W. Cooley, *Math. Comput.* **XV**, 363 (1961); J. M. Blatt, *J. Comp. Phys.* **1**, 382 (1967).

²²D. C. Leseski, Dept. of Chemistry, Senior thesis project, Allegheny College, Meadville, PA, 1985.

²³(a) Y. Morino, Y. Kikuchi, S. Saito, and E. Hirota, *J. Mol. Spectrosc.* **13**, 95 (1964); (b) Y. Morino, K. Kuchitsu, and S. Yamamoto, *Spectrochim. Acta Part A* **24**, 335 (1968); (c) I. M. Mills, in *Molecular Spectroscopy: Modern Research*, edited by K. N. Rao and C. W. Mathews (Academic, New York, 1972).

²⁴R. Schinke, M. Dupuis, and W. A. Lester, Jr., *J. Chem. Phys.* **72**, 3909 (1980).

²⁵W. Meyer and P. Botschwina (private communication, 1985).

²⁶R. Polak, *Chem. Phys.* **16**, 353 (1976).

²⁷G. D. Carney and G. Schatz (unpublished, 1984).

APPENDIX D

THE NO + O AND NO + O₃ REACTIONS:

I. ANALYSIS OF NO₂ VIBRATIONAL
CHEMILUMINESCENCE

THE NO + O AND NO + O₃ REACTIONS:

I. ANALYSIS OF NO₂ VIBRATIONAL CHEMILUMINESCENCE

Steven M. Adler-Golden
Spectral Sciences, Inc.
111 So. Bedford Street
Burlington, MA 01803

July 1986

THE NO + O AND NO + O₃ REACTIONS: I. ANALYSIS OF NO₂ VIBRATIONAL CHEMILUMINESCENCE

Steven M. Adler-Golden

Spectral Sciences, Inc., 111 So. Bedford St., Burlington, MA 01803

Low resolution NO₂ $\nu_1+\nu_3$ and ν_3 chemiluminescence spectra from the NO + O and NO + O₃ reactions are simulated with a stepladder kinetic/spectroscopic model. The model uses simple parameterizations of radiative and collisional processes and assumes equipartition of electronic and vibrational energy. Good agreement is obtained with measurements of the $\nu_1+\nu_3$ band shape and absolute intensity.

I. INTRODUCTION

Among the best-known chemiluminescent reactions are the reactions of nitric oxide (NO) with atomic oxygen (O) and ozone (O₃), producing excited nitrogen dioxide (NO₂). Visible and near-IR emission results from electronically excited NO₂ (NO₂^{*}), and appears as an essentially continuous spectrum.^{1,2} At longer IR wavelengths, NO₂ vibrational bands are observed.³⁻⁶

An understanding of NO₂ chemiluminescence is especially important in view of its potential as a source of atmospheric background radiation,⁷ particularly in disturbed atmospheres.^{8,9} Indeed, measurement of the NO₂ airglow can yield information on atmospheric composition. Visible airglow measurements have been used to extract approximate NO densities in the 100 - 110 km altitude range.⁹ NO₂ chemiluminescence may also be an important source of radiation in the glow surrounding orbiting spacecraft, such as the Space Shuttle.¹⁰

Although detailed study of the NO₂ chemiluminescence has focused mainly on the visible region, the IR region is also important. Substantial NO₂ vibrational chemiluminescence might occur in disturbed atmospheres and in spacecraft glows.¹¹ Of particular interest are the 3.5 - 3.7 μ $\nu_1+\nu_3$ combination band, which lies in an atmospheric window, and the strong ν_3 fundamental at 6.3 μ .

Experimental data on NO_2 vibrational chemiluminescence is rather limited. Following initial observations of IR band emission,^{3,4,6} the quenching kinetics of the $\nu_1+\nu_3$ band were studied by Golde and Kaufman,⁵ who extracted effective vibrational deactivation rate constants by monitoring the emission intensity as a function of gas composition. More recently, Hui and Cool¹² observed time-resolved $\nu_1+\nu_3$ emission from the $\text{O}_3 + \text{NO}$ reaction following CO_2 laser excitation of the ozone, and derived deactivation rate constants in rough agreement with Golde and Kaufman's. However, neither study attempted to explain the band shape or absolute intensity, or to provide an interpretation of the rate constants in terms of energy loss. Very little information is available on emission from other bands, including ν_3 . Furthermore, to our knowledge the only spectrum available at low pressures (below the 0.2 - 2 torr range studied in Refs. 4 - 6 and 12) is a single measurement of $\text{NO} + \text{O}_3$ $\nu_1+\nu_3$ emission in 20 mtorr NO by Clough and Thrush.³

This paper presents a model for the room temperature, low resolution ν_3 and $\nu_1+\nu_3$ emission spectra from both the $\text{NO} + \text{O}$ and $\text{NO} + \text{O}_3$ reactions, applicable to a wide range of pressures and gas mixtures. Comparison with the rather limited experimental data demonstrates better than factor-of-2 absolute intensity accuracy and better than 2% wavelength accuracy for these bands.

II. KINETIC MODEL DESCRIPTION

A. Overview

Despite intensive research, our understanding of NO_2 chemiluminescence is quite limited. Much of the blame is due to the complexity of NO_2 's kinetics and spectroscopy. The state specification of excited NO_2 is uncertain due to strong mixing between the ground and one or more excited electronic states,¹³⁻¹⁶ causing remarkable congestion and irregularity in the visible spectrum.¹⁷⁻²⁰ The kinetics of excited NO_2 are complicated not only by the lack of state specification, but also by the variety of pathways for creation and destruction, which include chemical reaction, vibrational relaxation, and visible and IR radiation.

In the face of these complexities, several workers²¹⁻²⁴ have adopted a greatly simplified approach, in which state specification is reduced to a single parameter, E , the sum of the vibrational and electronic energy. (Rotational energy is assumed to be equilibrated with the translational temperature and is ignored.) In this model the kinetic entities are not individual eigenstates, but instead are evenly spaced "energy levels" which form a stepladder. Each level is intended to represent an ensemble of eigenstates having E close to $E(i)$, the energy of level i . All kinetic and spectroscopic properties of excited NO_2 therefore depend on E alone. The kinetics of the energy level stepladder are easily solved; in the steady-state approximation a small set of simultaneous linear equations is obtained. The stepladder model has been highly valuable for analyzing NO_2 visible chemiluminescence and fluorescence.²¹⁻²⁴

The current study develops a stepladder model capable of predicting the low resolution NO_2 ν_3 and $\nu_1 + \nu_3$ band spectra in the $\text{NO} + \text{O}$ and $\text{NO} + \text{O}_3$ reactions. Development of such a model requires careful parameterization of the energy dependence of vibrational and radiative relaxation rates, which span 3 orders of magnitude over the full range of E . Even with the drastic simplification that the stepladder model affords, there is insufficient direct experimental data to fully specify these rates. Our approach is to use the available data to define semi-empirical functions which describe NO_2 's kinetics and spectroscopy for all E .

At high pressures (>1 torr) the model's components are the collisional formation and removal rates and the vibrational emission rates for each band. For the $\text{NO} + \text{O}$ reaction the formation kinetics are well known.^{14,22} For the $\text{NO} + \text{O}_3$ reaction an initial state distribution is inferred from results of trajectory calculations.^{25,26} Collisional relaxation by O_2 , NO and N_2 is modeled by combining results from the laser studies of Donnelly et al.²³ and Hui and Cool¹² with the $\nu_1 + \nu_3$ band measurements of Golde et al.^{4,5} The IR band emission rate is modeled assuming vibrational energy equipartition and harmonic oscillator scaling for the dipole moment matrix elements. Validation of the model at high pressures (ca. 1 torr) is provided by comparison with experimental^{4,5} IR band shapes and absolute intensities.

For modeling low pressures radiative relaxation must be included; this is accomplished using a semi-empirical continuum function derived elsewhere (Ref. 27, hereafter denoted Paper II). The resulting complete chemiluminescence model can be used to predict infrared band spectra over a wide range of laboratory conditions. It also generates predictions of continuum emission; details are given in Paper II.

B. Mechanisms of NO₂ Formation and Relaxation

The basic mechanism of the NO + O reaction is well established.^{14,21,22} The formation of stable NO₂ molecules from this reaction requires the removal of excess energy from the O-NO collision complex, which may be accomplished either by radiation or by collision with a third body, denoted M. At pressures below a few millitorr radiation provides the dominant formation and relaxation pathway, made possible by the presence of one or more low-lying excited electronic states.^{15,16} At intermediate pressures the O-NO complex is stabilized via collisions with the bath gas, and a partially relaxed distribution of excited states is established, which can further relax or radiate. In this pressure region the NO₂ formation rate is trimolecular. At pressures above ~1 torr a limiting distribution of emitting states is reached, and the rate constant for chemiluminescence is bimolecular.

The NO + O₃ reaction yields stable NO₂ directly, primarily in the ground electronic state.^{2,3} A small fraction of the reaction yields NO₂^{*}, which emits IR-visible continuum. It has been conjectured that the NO₂^{*} results from a second, excited electronic reaction channel (see discussions in Refs. 25, 26, and 28); however, Paper II provides a different interpretation. According to trajectory calculations on the ground potential energy surface (particularly the recent study by Viswanathan and Raff²⁶) the reaction energy is partitioned nearly statistically among the available vibrational, rotational, and translational degrees of freedom (see the following subsection).

Relaxation of excited NO₂ proceeds both radiatively and collisionally, with rates which decrease steadily towards lower energy.^{22,23,29,30} Near the dissociation limit, vibrational relaxation is nearly gas kinetic, and the average radiative lifetime is about 50 μsec.^{22,23} Below the origin of

the 2B_2 state (around $10,000\text{ cm}^{-1}$) the only radiative relaxation mechanism is vibrational band emission, a much slower process. The vibrational relaxation rate also decreases markedly below the 2B_2 origin, where it is typically ~ 0.01 gas kinetic or less.⁵ In the $O + NO$ system, reaction of NO_2 with atomic oxygen can be an important removal process for these low energy states.^{4,5}

C. Kinetic Model Assumptions

As mentioned in Sec. IIA, the fundamental assumption of the current as well as previous²¹⁻²⁴ models is that a given quantity of NO_2 vibrational plus electronic energy E is distributed statistically among all degrees of freedom. This assumption of energy equipartition can be rationalized in several ways. One can invoke vibronic mixing between the ground and excited electronic states.¹³⁻²⁰ Perhaps a better argument, which would apply even below the excited electronic origin, is that collisional scrambling will rapidly equilibrate nearby energy levels, especially at the pressures considered here. This scrambling should be very fast (\sim gas kinetic) since the density of states exceeds $1/kT$ at most energies of interest. The rapidity of this process is consistent with the observation of fast collisional relaxation following laser excitation of NO_2 , giving rise to a pseudo-continuous spectrum.²³

At energies well below the excited electronic origin, intramode vibrational relaxation may exceed intermode scrambling, and vibrational energy equipartition may not, in general, hold. However, we note that these low energy states are formed with a scrambled vibrational energy distribution, either via cascade from higher-lying states (in the $NO + O$ reaction) or else via a direct, statistical mechanism (in the $NO + O_3$ reaction). Unless the vibrational relaxation process is highly mode-specific, approximate equipartition will probably be maintained.

Since a state-specific description of NO_2 is abandoned, exact values of the energy levels are irrelevant. In the interest of mathematical simplicity the energy is discretized to form a stepladder of evenly spaced levels.²¹⁻²⁴ For the current model a spacing of 1000 cm^{-1} has been arbitrarily chosen, a convenient number which is consistent with the energy "resolution" desired, and which is also the rough size of a vibrational

quantum. The energy of level i is therefore given by $E(i) = 1000(i-1)$. Provided that the rate constants are properly adjusted to take the 1000 cm^{-1} spacing into account, the stepladder approach should yield a faithful account of excited NO_2 kinetics. Thus, rate constants for vibrational energy relaxation from level i to level $i-1$ are to be understood as rate constants for 1000 cm^{-1} energy loss, rather than as the actual removal rate of a molecular state. Finally, collisional relaxation is assumed to proceed solely from level i to level $i-1$, i.e., via single-quantum steps.

The stepladder scheme allows the steady-state kinetics to be described via a system of linear equations for the level populations $\text{NO}_2(i)$,

$$\begin{aligned} d\text{NO}_2(i)/dt = 0 = & \sum_j \text{NO}_2(j) \left\{ \sum_M k_M(j,i)[M] + r(j,i) \right\} \\ & + f_R(i)[\text{NO}][\text{R}] - \text{NO}_2(i) \left\{ \sum_j \sum_M k_M(i,j)[M] + \sum_j r(i,j) + x(i)[\text{O}] \right\} \quad (1) \end{aligned}$$

where $k_M(i,j)$ is the second-order rate constant for transfer from level i to level j via collision partner M , $r(i,j)$ is the (first-order) rate constant for radiative transfer, $f_R(i)$ is the second-order rate constant for formation of level i via chemical reaction (R denotes the reagent, O or O_3) and $x(i)$ is the second order rate constant for reactive removal of level i by atomic oxygen. By neglecting up-pumping (processes for which $i < j$) the solutions to Eq. (1) are obtained by starting with the topmost $\text{NO}_2(i)$ level and working downward. Up-pumping occurs via excitation by the bath gas thermal energy, and may be neglected when $\text{NO}_2(i)/\text{NO}_2(i-1) \gg \exp(-1000/kT)$. Under most conditions in the current study, processes such as relaxation, reaction, or diffusion ensure that this inequality is satisfied; therefore, up-pumping has been omitted from the current model.

In the case of the $\text{NO} + \text{O}$ reaction the kinetics are simplified in several ways. The topmost level is the activated complex, taken as $i = 27$, which is the only level for which $f_0(i)$ is nonzero. Secondly, at the high total pressures (several torr) at which the key IR band measurements^{4,5} were made, radiative relaxation makes a negligible contribution to the kinetics, which means that one can treat the continuum emission as a problem entirely separate from the IR spectrum. The neglect of radiative relaxation and the assumption of single-quantum deactivation imply that the

net formation rate of each $\text{NO}_2(i)$ state equals the known 3-body $\text{NO} + \text{O} + \text{M}$ formation rate. At lower total pressures the radiative rate constants $r(i,j)$ must be included, and the formation kinetics become more complex. At these pressures one must be able to model the continuum emission in order to calculate not only the visible spectrum, but the IR band spectrum as well.

In the case of the $\text{NO} + \text{O}_3$ reaction, collisional relaxation again dominates radiative relaxation at the pressures (0.2 - 2 torr) of typical experiments.^{3-6,12} A complicating feature of this reaction is that the nascent state distribution $f_{\text{O}_3}(i)$ is an important model input. A good starting point for $f_{\text{O}_3}(i)$ is the "prior"³¹ vibrational probability distribution $dP(E)/dE$, which assumes statistical deposition of the reaction energy in the $\text{NO}_2 + \text{O}_2$ products. Using the rigid rotor-harmonic oscillator (RRHO) approximation, and assuming formation of ground electronic products only, it may be shown that

$$dP(E)/dE = 105(E+E_0)^2(E_T-E)^4/(E_T+E_0)^7 \quad (2)$$

where E_T is the total available reaction energy and E_0 is the NO_2 vibrational zero point energy. E_T is taken as 18600 cm^{-1} , calculated from the sum of the reaction exoergicity, the reactant thermal energy, and the activation energy (see Paper II).

The distribution of reaction energy predicted by the statistical RRHO model is 3/8 (0.38) in NO_2 vibration, 3/16 (0.19) in NO_2 rotation, 1/8 (0.13) in O_2 vibration, and 1/8 (0.13) in O_2 rotation. These values compare favorably with those obtained from Viswanathan and Raff's trajectory calculations²⁶ (0.39 - 0.45, 0.13 - 0.20, 0.02 - 0.06, and 0.06 - 0.11, respectively) on several quite different model potential energy surfaces. Similar results were also obtained by Chapman.²⁵ The relative insensitivity of these values to the potential surface increases our confidence that Eq. (2) is a good approximation to the actual nascent distribution.

III. SPECTROSCOPIC MODEL

A. IR Band Emission

IR bands of NO_2 formed from the $\text{O} + \text{NO}$ reaction were first observed by Stair and Kennealy,⁶ who assigned the band near 6.3μ as the ν_3 transition. Later work by Golde et al.^{4,5} assigned the 3.7μ broad band as $\nu_1 + \nu_3$ hot band emission from high vibrational levels. Similar emission was observed by Clough and Thrush³ from the $\text{NO} + \text{O}_3$ reaction. The ν_3 and $\nu_1 + \nu_3$ bands are the strongest vibrational transitions of NO_2 , with Einstein A coefficients of about 110 and 13 sec^{-1} , respectively, for the transitions $(0\ 0\ 1) - (0\ 0\ 0)$ and $(1\ 0\ 1) - (0\ 0\ 0)$.³²⁻³⁴ The aim of this section is to develop approximate spectral components for these two bands for each stepladder level $\text{NO}_2(i)$.

The first step involved calculating NO_2 vibrational energy levels using published anharmonic constants,³⁵ the calculation being performed for levels as high as $16500\ \text{cm}^{-1}$. While an extrapolation to such high energies is ordinarily quite hazardous, it is probably satisfactory for the present approximate, low resolution model. Furthermore, we shall see that the levels which contribute most strongly to the spectrum have energies below $10,000\ \text{cm}^{-1}$. Next, the computed levels were binned at $1000\ \text{cm}^{-1}$ energy intervals to correspond to levels $i = 1 - 16$ of the stepladder model. The spectrum of each stepladder level was then calculated by assigning each transition an Einstein coefficient given by

$$A_3 = 110\nu_3(\nu/\nu_{001})^3\ \text{sec}^{-1} \quad (\nu_3\ \text{band}) \quad (3)$$

or

$$A_{13} = 13\nu_1\nu_3(\nu/\nu_{101})^3\ \text{sec}^{-1} \quad (\nu_1 + \nu_3\ \text{band}) \quad (4)$$

These formulas use the known Einstein coefficients of the cold bands and assume harmonic oscillator scaling for the dipole moment matrix elements. Finally, the resolution of each stepladder level spectrum was degraded by binning the individual transitions to the nearest 0.1 or $0.2\ \mu$ (for the combination and fundamental bands, respectively), and smoothing slightly.

Resulting stepladder spectral components are shown in Figs. 1 and 2. The spectral components of levels differing by several thousand cm^{-1} are seen to be well separated from each other, surprisingly so considering that each component contains contributions from individual vibrational levels having a very wide range of quantum numbers. The NO_2 IR band emission spectrum can therefore serve as a low resolution map of the vibrational energy distribution.

Although these spectral components should be reasonably accurate for low energies, as the energy is increased it is expected that the harmonic oscillator scalings will break down. In ozone, for example, significant weakening of the harmonic dipole moment scaling sets in about half way towards dissociation.³⁶ Bearing this effect in mind, we chose the smaller of the experimental band strength values³²⁻³⁴ for the Einstein coefficient calculation (Eq. (4)).

At low pressures, radiative relaxation must be included as a pathway for energy loss via the term $r(i,j)$ in Eq. (1), given by

$$r(i,j) = r_3(i,j) + r_{13}(i,j) + r_c(i,j) \quad (5)$$

where the first two terms refer to radiative relaxation via ν_3 and $\nu_1 + \nu_3$, and the last term refers to relaxation via continuum emission. To calculate the contribution from the IR bands we start from the spectral components shown in Figs. 1 and 2. We define a set of effective IR radiative rate constants as the areas under the curves; these are reasonably well approximated by the formulas

$$r_3(E) = 110C_3E/(3\nu_3) \text{ sec}^{-1} \quad (6a)$$

$$r_{13}(E) = 13C_{13}(E - 725\text{cm}^{-1})^2/(12\nu_1\nu_3) \text{ sec}^{-1} \quad (6b)$$

where the factors C_3 and C_{13} are corrections for the red shift with increasing energy, approximated by

$$C_3 = [1 - 0.014(i-3)]^3 \quad (7)$$

$$C_{13} = [1 - 0.014(i-4)]^3 \quad (8)$$

Eqs. (6a) and (6b) represent "average" Einstein coefficients for energy E. To convert the $r(E)$'s to $r(i,j)$'s appropriate to our stepladder model, ν_3 is rounded to 2000 cm^{-1} , while $\nu_1 + \nu_3$ is rounded to 3000 cm^{-1} . The final results are

$$r_3(i,i-2) = r_3(E)\nu_3/(2000\text{cm}^{-1}) \quad (9)$$

$$r_{13}(i,i-3) = r_{13}(E)(\nu_1 + \nu_3)/(3000\text{cm}^{-1}) \quad (10)$$

B. Continuum Emission

At low total pressures NO_2 continuum emission needs to be considered even when modeling only the infrared bands, since below -1 torr it provides an important mechanism for energy loss. In the present study the rate constant for continuum emission was represented by the expression

$$r_c(i,j) = \frac{5 \times 10^{-7} [E(i) - 9000 - 3.4 \times 10^{-5} (\nu - 4000)^2]^{5/2} \nu^3}{(E(i) - 9000)^3 \{1 + 1.4 [(E(i) + 1800)/(E(i) - 8200)]^2\}} \text{ sec}^{-1} \quad (11)$$

where $\nu = E(i) - E(j)$ in cm^{-1} . This formula is derived and discussed in Paper II, where it is found to give very good agreement with measured continuum emission spectra and lifetimes.

IV. RATE CONSTANTS

In this section the rate constants for deactivation, $k_M(i,j)$, formation, $f_R(i)$, and reaction, $\kappa(i)$, are developed. The collision partners considered here are O_2 , N_2 , NO , NO_2 , O_3 , and O . Since IR band shape and intensity modeling requires good rate constant accuracy over a wide range of excitation energy, use is made of experimental data at several energies. Interpolation between the data is accomplished using simple functional fits.

A. Vibrational Deactivation

Vibrational deactivation rate constants have been measured at high excitation energies via laser-induced visible fluorescence,²³ and, at lower excitation energies (6000 - 9000 cm⁻¹) via IR chemiluminescence.^{5,12} To define $k_M(i,j)$ over the entire energy range a simple parameterization of the experimental data is desired. If as a rough approximation we assume that the deactivation rate is proportional to the density of states, and that the rate differs in the ground and excited (²B₂) electronic states, then

$$k_M(i,i-1) = C_M^0 \rho^0 + C_M^* \rho^* \quad (12)$$

where C_M^0 and C_M^* are empirical constants and ρ^0 and ρ^* are respectively the ground and ²B₂ vibration-rotation state densities. In the semiclassical RRHO approximation the state densities are proportional to $(E + E_0 - E_e)^2$, where E_0 is the vibrational zero point energy and E_e is the excitation energy of the electronic origin. The ²B₂ origin is taken as 10,000 cm⁻¹, and the zero point energy is taken as 1800 cm⁻¹ in both states. This leads to

$$k_M(i,i-1) = a_M(E+1800\text{cm}^{-1})^2, \quad E \leq 8200 \text{ cm}^{-1} \quad (13a)$$

$$= a_M(E+1800\text{cm}^{-1})^2 + b_M(E-8200\text{cm}^{-1})^2,$$

$$25,000 \geq E > 8200 \text{ cm}^{-1}, \quad (13b)$$

where the empirical constants are now a_M and b_M . These equations apply only to the bound NO₂ levels; the kinetics of the NO + O activated complex are more accurately treated as described in Section IV.C.

The a_M and b_M values derived for the collision partners considered are listed in Table I. Details of their derivation are given below for specific collision partners. The general procedure was to select $k_M(i,i-1)$ values at two energies, 18800 cm⁻¹ (corresponding to Donnelly's 532 nm LIF study²³) and 6000 cm⁻¹ (corresponding to the peak of the NO + O₃ IR emission³⁻⁵) from which a_M and b_M are uniquely determined. For reasons

given in Paper II we assumed a mean vibrational energy loss of 1500 cm^{-1} per deactivation event at 18800 cm^{-1} . (Donnelly's own modeling suggested an energy loss value of roughly 1000 cm^{-1}).²³ $k_M(i,i-1)$, which pertains to the loss of 1000 cm^{-1} , is then obtained from Donnelly's measured deactivation rate constant k_C by multiplying by 1.5. The value of $k_M(i,i-1)$ at 6000 cm^{-1} has been derived from effective v_1+v_3 deactivation rate constants, denoted k_{M13} , measured by Hui and Cool¹² and Golde and Kaufman,⁵ as discussed below.

1. NO and NO₂

Donnelly et al.²³ measured a vibrational deactivation rate constant k_C of $1.2 \times 10^{-10} \text{ cm}^3 \text{ molec}^{-1} \text{ sec}^{-1}$ for collisions with NO₂ at $E = 18800 \text{ cm}^{-1}$. As discussed above, this value is multiplied by 1.5 to yield $k_{\text{NO}_2}(i,i-1)$. Based on relative continuum quenching measurements by Clough and Thrush,² $k_{\text{NO}}(i,i-1)$ is taken as 0.7 of $k_{\text{NO}_2}(i,i-1)$.

From measurements of NO + O₃ laser-induced chemiluminescence the rate constant for v_1+v_3 band deactivation, k_{NO}^{13} , was found to be 1.8×10^{-12} by Hui and Cool.¹² However, Golde and Kaufman's data⁵ suggest that this value is somewhat low. The low value may have been due to an electronics rise time in Hui and Cool's apparatus, which we believe could have caused a ~40% error. Accordingly, we have increased Hui and Cool's value by 40%. To obtain $k_{\text{NO}_2}^{13}$ at 6000 cm^{-1} we multiplied the result by $1/0.7 = 1.4$, by analogy with the continuum quenching. Golde and Kaufman's data⁵ also support this NO₂/NO IR band deactivation ratio.

Next, to convert from k_M^{13} to $k_M(i,i-1)$ we use the relationship

$$k_M(i,i-1) = k_M^{13} / (1000 \text{ cm}^{-1} (1/I) dI/dE) \quad (14)$$

where $(1/I)dI/dE$ is the fractional loss of combination band intensity I per unit energy loss, evaluated at the energy E corresponding to the peak of the emission band. Because of the v_1v_3 scaling of the combination band Einstein coefficients, I has an energy squared dependence; thus, $(1/I)dI/dE = 2/E$, and $k_M(i,i-1) = k_M^{13} E / (2000 \text{ cm}^{-1})$. Since E is taken as 6000 cm^{-1} , corresponding to the peak of the NO + O₃ emission at 3.6μ , $k_M(i,i-1) = k_M(7.6) = 3k_M^{13}$.

2. O_2 , N_2 , and O_3

For O_2 and N_2 , Donnelly's k_C values are about $5 \times 10^{-11} \text{ cm}^3 \text{ molec}^{-1} \text{ sec}^{-1}$. For O_2 , $k_{O_2}^{13} = 5.1 \times 10^{-13}$ as measured by Hui and Cool. $k_{N_2}^{13}$ is 0.4 of $k_{O_2}^{13}$, according to Golde and Kaufman.⁵ The corresponding $k_M(i,i-1)$ values and the constants a_M and b_M were then derived in exactly the same manner as for NO and NO_2 .

For O_3 there are no accurate deactivation measurements. Golde and Kaufman suggest that its rate constant is close to that of O_2 , so for the present we have set them exactly equal. Fortunately, the exact value of the rate constant for O_3 is unimportant, since O_3 is always a minor constituent.

3. O Atoms

In the absence of data on NO_2 vibrational deactivation by O atoms this rate constant was set equal to the NO rate constant. Since the O atom proportion is low under most experimental conditions, its contribution to the total deactivation rate is usually small. However, for accurate modeling of NO_2 chemiluminescence in the upper atmosphere a better estimate may be needed.

4. Discussion

The relaxation rate constants $k_M(i,i-1)$ given by Eq. (13) are plotted in Fig. 3 for O_2 , N_2 and NO. (The NO_2 rate constant is 1.4 times the NO rate constant). The general correctness of the shapes of these curves is supported by the reasonably good agreement with the NO_2 self-quenching measurements of Donnelly and Kaufman²³ down to around 12000 cm^{-1} . The kinks at 9000 cm^{-1} are caused by the onset of excited state character. It is likely that the portion of these curves near the kinks are the least accurate, given possible shortcomings of Eq. (13) and the lack of data in this energy region. Indeed, since the justification for Eq. (13) is somewhat questionable, we were concerned that the shapes of these curves may be somewhat arbitrary. To get a feel for the accuracy of Eq. (13), several alternative functions for $k_M(i,i-1)$ were tried, including a power

law ($k \sim E^N$) expression for $E > 10,000 \text{ cm}^{-1}$, and an SSH ($k \sim E$) expression for $E < 10,000 \text{ cm}^{-1}$. The results almost always agreed with Eq. (13) to within a factor of 2 or better. Perhaps a more convincing case to be made for Eq. (13) is that it yields IR band spectra (and continuum spectra in Paper II) in very good agreement with experiment.

B. Chemical Reaction with O Atoms

A major pathway for removal of low energy NO_2 population in the $\text{NO} + \text{O}$ system is reaction with atomic oxygen. For the ground vibrational level the rate constant is $9.3 \times 10^{-12} \text{ cm}^3 \text{ molec}^{-1} \text{ sec}^{-1}$ at room temperature,³⁷ and the temperature dependence is found to be negligible. The negligible temperature effect suggests little dependence on internal energy. Thus, in initial calculations the ground vibrational state rate constant was used as the value $x(i)$ (see Eq. (1)) for all NO_2 energies.

On the other hand, if Hui and Cool's value for deactivation of $\text{NO} + \text{O } \nu_1 + \nu_3$ emission by O_2 , $5.1 \times 10^{-13} \text{ cm}^3 \text{ molec}^{-1} \text{ sec}^{-1}$, is accurate, the 30:1 rate constant ratio measured by Golde and Kaufman for O versus O_2 deactivation implies an $\text{NO}_2 + \text{O}$ rate constant about 50% higher ($1.5 \times 10^{-11} \text{ cm}^3 \text{ molec}^{-1} \text{ sec}^{-1}$) at $E \sim 9000 \text{ cm}^{-1}$ (corresponding to the peak of the $\text{NO} + \text{O}$ emission). In our final calculations this increased rate constant was incorporated via a simple linear fit,

$$x(i) = 9.3 \times 10^{-12} [1 + 6 \times 10^{-5} E(i)] \quad (15)$$

An alternative possibility is that the apparent vibrational enhancement of the removal rate by O atoms reflects vibrational deactivation rather than chemical reaction.

C. Kinetics of NO_2 Formation

1. The $\text{NO} + \text{O}$ Reaction

At total pressures above ~ 1 torr the rate of formation of the activated complex, $f_0(27)[\text{NO}][\text{O}]$, equals the 3 body NO_2 formation rate $k_{3M}[\text{NO}][\text{O}][\text{M}]$. Values of k_{3M} consistent with the latest measurements^{37,38} are $7.0 \times 10^{-32} \text{ cm}^6 \text{ molec}^{-2} \text{ sec}^{-1}$, $1.0 \times 10^{-31} \text{ cm}^6 \text{ molec}^{-2} \text{ sec}^{-1}$, and $1.4 \times$

$10^{-31} \text{ cm}^6 \text{ molec}^{-2} \text{ sec}^{-1}$ at room temperature for $M = \text{O}_2$, N_2 , and NO , respectively.

At lower pressures one must include the radiative contribution to $f_0(27)$, given by a bimolecular rate constant, k_2 . As discussed by Becker et al.,²² k_2 and k_{3M} are related to the rate constants for formation, relaxation, dissociation and radiation of the activated complex. Denoting the (unimolecular) dissociation rate constant of the complex as k_{-1} , the bimolecular relaxation constant as $k_M(27,26)$, and the formation rate constant as k_1 , we have $k_{3M} = k_1 k_M(27,26)/k_{-1}$. Denoting the complex radiation rate as $k_r = 1/\tau$, where τ is the continuum radiative lifetime, we have $k_2 = k_1 k_r/k_{-1}$. Thus, $k_M(27,26)$ is given by $k_{3M}/(k_2 \tau)$, where $\tau = 50 \text{ } \mu\text{sec}$ ^{21-23,27} and $k_2 = 4.2 \times 10^{-18} \text{ cm}^3 \text{ molec}^{-1} \text{ sec}^{-1}$.²² Finally, using the value $k_1 = 3 \times 10^{-11} \text{ cm}^3 \text{ molec}^{-1} \text{ sec}^{-1}$,³⁹ one obtains $k_{-1} = 1.4 \times 10^{11} \text{ sec}^{-1}$.

2. The $\text{NO} + \text{O}_3$ Reaction

As mentioned previously, the $\text{NO} + \text{O}_3$ formation rate constants $f_{\text{O}_3}(i)$ were scaled to the statistical RRHO probability, dP/dE . The $f_{\text{O}_3}(i)$ sum was normalized to the net rate constant, $1.8 \times 10^{-14} \text{ cm}^3 \text{ molec}^{-1} \text{ sec}^{-1}$ at room temperature.²⁸ No provision was explicitly made for formation of electronically excited NO_2 , NO_2^* . Given the state-mixing assumption incorporated in the current model, all states formed with $E \geq -10,000 \text{ cm}^{-1}$ emit in the continuum, and are therefore implicitly classified as NO_2^* . Further discussion of NO_2^* is reserved for Paper II.

V. RESULTS AND DISCUSSION

A. Population Distributions

The level populations, $\text{NO}_2(i)$, are found by solving Eqs. (1). Typical experimental gas mixtures (mostly O_2 or N_2 , with small amounts of NO and either O or O_3) have similar deactivation rates for mid- to high-energy NO_2 levels, so the bulk of the NO_2 population distribution is not very

sensitive to the exact composition. The continuum chemiluminescence arises mainly from these mid- to high-energy levels, and therefore tends to be insensitive to composition for a given reaction.

At low NO_2 energy the deactivation rates vary considerably with collision partner, so the populations (and IR band emissions) depend strongly on the gas composition. Furthermore, in the $\text{NO} + \text{O}$ system the $\text{NO}_2(i)$ populations are affected by the reaction with atomic oxygen. This is shown in Fig. 4, which displays calculated energy level distributions arising from the $\text{NO} + \text{O}$ reaction using two different atomic oxygen pressures (0.09 and 0.009 torr) with 2.3 torr of O_2 . At the higher O atom concentration low energy levels are removed and the energy distribution is "hotter".

B. $\text{NO} + \text{O}$ IR Band Emission

1. Experimental Data

Several $\nu_1 + \nu_3$ band emission spectra from the $\text{O} + \text{NO}$ reaction appear in the papers by Golde et al.^{4,5} Fig. 2 of Ref. 4 displays two low resolution spectra taken with 2.3 torr O_2 , a much lower pressure (probably ca. 0.03 torr) of NO , and two different (but, unfortunately, unspecified) O atom concentrations, reported to be in a 10:1 ratio. The spectra are given in arbitrary units after dividing by $[\text{O}][\text{NO}]$. Also shown in the figure is a portion of the continuum. The accompanying Fig. 3 shows the continuum labeled with absolute units ($\text{cm}^3 \text{ molec}^{-1} \text{ sec}^{-1} \mu^{-1}$). Thus, by combining Figs. 2 and 3 of Ref. 4 the $\nu_1 + \nu_3$ emission intensity can be placed on an absolute basis. The only unknowns are the absolute O atom concentrations. These may be inferred approximately from the ratio of intensities, -0.5:1, in going from high to low atomic oxygen, combined with the 30:1 ratio of rate constants for quenching by O and O_2 , respectively.⁵ The low and high O atom concentrations are deduced to be 0.009 ± 0.001 torr and 0.09 ± 0.01 torr, respectively, corresponding (not accidentally) to our Fig. 4.

In addition to the spectra in Fig. 2, Ref. 4, a more detailed, but relative, spectrum taken under high O conditions (0.1 torr) is shown in Fig. 1 of Ref. 5. Scaling that spectrum according to Fig. 2, Ref. 4 yields the absolute high O spectrum shown in our Fig. 5.

2. Model Calculations

$\nu_1 + \nu_3$ spectra calculated using the Fig. 4 populations and the Fig. 2 components are shown in Fig. 5. The agreement between calculation and experiment for the high O case is remarkably good. The small discrepancy near 3.4μ may be due to a small contribution from the continuum in the experimental spectrum. The calculated low O spectrum appears to agree equally well with the experimental spectrum in Fig. 2, Ref. 4, although the small size of the published figure makes the comparison more difficult.

The calculated ν_3 spectrum is shown in Fig. 6. Unfortunately, there is no reliable experimental data for this band to our knowledge. As with the combination band, there is a strong red shift compared to the "cold" spectrum. Due to the lack of experimental data on vibrational relaxation of levels having $E < -5000 \text{ cm}^{-1}$, the blue end of the ν_3 spectrum is probably the least reliable. This problem is much less important with the combination band, whose intensity falls off more rapidly towards low energy.

3. Sources of Error

The remarkable agreement between the calculated and experimental NO + O $\nu_1 + \nu_3$ spectrum may be somewhat fortuitous, since the differences are smaller than the combination of experimental error and uncertainty in the model. The O₂ vibrational deactivation rate constant in the important 7000 - 11000 cm^{-1} energy region may be uncertain by up to ~50% due to experimental error in Hui and Cool's measurement and, perhaps more importantly, from possible error in our method of extrapolation (via Eq. (13)) from $E = 6000 \text{ cm}^{-1}$ to higher energy. The 3-body formation rate constant for NO₂ in O₂ may have an experimental error of up to 20%. Finally, the Einstein coefficients are probably accurate to only ~25%.

The experimental $\nu_1 + \nu_3$ spectrum of Golde et al.⁸ was stated to have an absolute calibration uncertainty of up to 30%. Recent evidence suggests that the uncertainty may be greater than this. An absolute measurement of the visible and near-IR O + NO continuum by Sutoh et al.,⁴⁰ which agrees very well with previous results in the visible region,¹ is about a factor of 2 smaller than Golde's at 1.3μ where the two studies overlap. The

continuum shape has also been remeasured by Bradburn et al.,⁴¹ who find excellent agreement with Sutoh. If the discrepancy at 1.3 μ also holds for the $\nu_1+\nu_3$ band one would conclude that Golde's measurements (as well as our model) overestimate the true band intensity by a factor of 2. On the other hand, if the discrepancy pertains only to the continuum, Golde's band intensities would presumably be accurate to within the stated 30%.

C. NO + O₃ IR Band Emission

1. Experimental Data

The $\nu_1+\nu_3$ spectrum arising from the NO + O₃ reaction is shown in the papers by Golde and Kaufman⁵ and Clough and Thrush³ in relative units. It is similar in shape to the NO + O spectrum but peaks somewhat bluer, at around 3.6 μ . Band intensities were reported as a ratio of the total continuum emission; these ratios are 0.7 in 20 mtorr of NO with trace O₃³ and 5.3 ± 1 in 0.2 torr of Ar with trace O₃ and NO.⁵ The ratios may be converted to absolute $\nu_1+\nu_3$ intensities using the known continuum intensity I, given by²

$$I = I_0[\text{NO}][\text{O}_3]/([M] + P_{1/2}) \quad (16)$$

where I_0 and $P_{1/2}$ are respectively the intensity factor and half-quenching pressure for buffer gas M. The $\nu_1+\nu_3$ band intensity I_v may be written

$$I_v = k_v[\text{NO}][\text{O}_3] \quad (17)$$

where k_v is constant for a specific buffer gas and pressure. Using appropriate values for I_0 and $P_{1/2}$ (from Ref. 2 and Paper II) and the observed I_v/I ratios, k_v is calculated to be 1.5×10^{-16} cm³ molec⁻¹ sec⁻¹ for 20 mtorr NO and 3.1×10^{-16} cm³ molec⁻¹ sec⁻¹ for 0.2 torr Ar.

The ν_3 band has not been studied in detail, although Clough and Thrush³ report that it is roughly 8 times more intense than the $\nu_1+\nu_3$ band in 20 mtorr NO.

2. Model Calculation

$\nu_1 + \nu_3$ intensity calculations were performed for the above two experimental conditions. Since Ar was not one of the quencher gases included in the current model, the 0.2 torr Ar was modeled using 0.1 torr N_2 , based on the 2:1 ratio of N_2 /Ar quenching rates.⁵ The k_q values were found to be 1.6×10^{-16} and 3.4×10^{-16} $\text{cm}^3 \text{ molec}^{-1} \text{ sec}^{-1}$ for the 20 mtorr NO and 0.2 torr Ar conditions, respectively, in remarkable agreement with the experimental values in the previous section.

A second set of calculations was performed which assumed that vibrational emission is quenched with unit efficiency at the vessel walls. This was done by introducing first-order removal rate constants of 450 and 600 sec^{-1} for the 20 mtorr NO and 0.2 torr Ar conditions, respectively, based on estimated diffusion coefficients and the known vessel diameters. This resulted in k_q values of 1.3×10^{-16} and 1.8×10^{-16} $\text{cm}^3 \text{ molec}^{-1} \text{ sec}^{-1}$, respectively. While the latter intensity seems a bit too low, better agreement with experiment would be achieved by normalizing the $\nu_1 + \nu_3$ Einstein coefficients to the band strength measurement of Shafer and Young,³⁴ which is 25% higher than what the model currently assumes (see Sec. III).

The calculated ratio of ν_3 to $\nu_1 + \nu_3$ intensity is 16 in the first calculation (no wall quenching) and 13 in the second (with wall quenching) for the 20 mtorr NO condition. Using the Shafer and Young $\nu_1 + \nu_3$ band intensity, the ratios drop to 12 and 10, respectively. The latter values agree especially well with the measured value of 8.

The shapes of experimental⁵ and calculated $\nu_1 + \nu_3$ spectra are compared in Fig. 7. The agreement is fairly good, although somewhat inferior to the NO + O spectrum; the calculated spectrum is too blue, especially when wall quenching is omitted. This discrepancy probably contributes to the overestimation of the ν_3 to $\nu_1 + \nu_3$ intensity ratio.

3. Sources of Error

The probable errors in the NO + O₃ IR band calculation are similar to those in the NO + O calculation. An additional source of uncertainty arises from the initial state distribution, which is based on a statistical

RRHO parameterization of classical trajectory calculations, and is therefore somewhat speculative. Furthermore, comparison of calculation and experiment is complicated by the lack of information on vibrational quenching at the vessel walls. Given these uncertainties, the model's performance is quite good. Further experimental work to clarify the NO_2 initial state distribution and vibrational quenching properties would be very helpful.

VI. IR EMISSION AT LOW PRESSURES

Little experimental information is available on NO_2 IR emission at low pressures (below ~ 0.1 torr). The ν_3 and $\nu_1 + \nu_3$ band intensities were calculated with the current model from 2 mtorr to 1 torr, assuming trace reagents in O_2 and N_2 buffer gases. The $\nu_1 + \nu_3$ intensity (photons/ $\text{cm}^3\text{-sec}$) was converted to a second-order rate constant by dividing by $[\text{NO}][\text{O}]$ for the $\text{NO} + \text{O}$ reaction (see Fig. 8) and $[\text{NO}][\text{O}_3]$ for the $\text{NO} + \text{O}_3$ reaction (see Fig. 9). The calculated $\nu_3/(\nu_1 + \nu_3)$ intensity ratio is 10 - 11 for the $\text{NO} + \text{O}$ reaction and 15 - 16 for the $\text{NO} + \text{O}_3$ reaction over this pressure range.

We now consider the question of the pressure range over which the calculation can be trusted. The model's key assumption is equipartition of vibrational and electronic energy, which, although not directly proved, has led to reasonable agreement with experimental results at pressures of 20 mtorr and above. At these pressures energy loss is governed mainly by collisional processes. At lower pressures radiation provides an increasingly important relaxation pathway. To the extent that radiative relaxation is vibrational-mode-specific, and occurs faster than mode-scrambling processes, the current model would need revision. For the continuum radiation, mode-specificity is probably an unimportant factor due to the extensive collision-free mixing of the electronic states, and the fact that electronic transitions conserve kinetic energy. However, after the continuum emission is complete, the remaining vibrational energy (about $5000 - 6000 \text{ cm}^{-1}$, divided roughly equally among the three vibrational modes) radiates in a very mode-specific way, i.e., via the strong ν_3 band. Whereas the current model predicts that at the lowest pressures nearly all of this vibrational energy is radiated in ν_3 , it may be more realistic to assume that the ν_3 mode is capable of radiating little more than the 1/3 of

this energy which it initially possesses, while the remaining 2/3 is mainly quenched or radiated in ν_1 and ν_2 bands. Thus, to predict NO_2 IR emission at the low pressures typical of the upper atmosphere it would be best to use a model which treats each vibrational mode separately.

VII. SUMMARY

A kinetic/spectroscopic model has been derived for NO_2 vibrational band emission in the $\text{NO} + \text{O}$ and $\text{NO} + \text{O}_3$ reactions at room temperature. The ν_3 and $\nu_1 + \nu_3$ IR band spectra were calculated, and the latter spectrum was found to agree remarkably well with experimental data. The agreement supports the essential validity of the model's assumptions, in particular, equipartition of energy among vibrational and electronic degrees of freedom. The calculated vibrational energy distributions will be useful for predicting the NO_2 continuum emission as well (see Paper II). Finally, this model can serve as a starting point for calculations applicable to a wider range of conditions, such as those found in the upper atmosphere.

ACKNOWLEDGEMENTS

I wish to thank Dr. W. A. M. Blumberg and Dr. R. Sharma of the Air Force Geophysics Laboratory (AFGL) for stimulating discussions and for encouragement of this project, Dr. A. Berk (Spectral Sciences, Inc.) and Prof. M. Golde for their critical comments, and Dr. G. R. Bradburn and Dr. H. V. Lilenfeld for communicating their unpublished results. This work was supported by AFGL under Contract No. F19628-83-C-0056.

REFERENCES

1. A. Fontijn, C. B. Meyer, and H. I. Schiff, J. Chem. Phys. 40, 64 (1964).
2. P. N. Clough and B. A. Thrush, Trans. Faraday Soc. 63, 124 (1967).
3. P. N. Clough and B. A. Thrush, Trans. Faraday Soc. 65, 23 (1969).
4. M. F. Golde, A. E. Roche, and F. Kaufman, J. Chem. Phys. 59, 3953 (1973).

5. M. F. Golde and F. Kaufman, Chem. Phys. Lett. 29, 480 (1974).
6. A. T. Stair, Jr., and J. P. Kennealy, J. Chem. Phys. 64, 124 (1964).
7. D. J. Baker and R. O. Waddoups, J. Geophys. Res. 72, 4881 (1967).
8. A. T. Stair, Jr., and H. P. Gauvin, in Aurora and Airglow, edited by B. M. McCormac, Reinhold, NY, p. 365-390 (1967).
9. W. E. Sharp, J. Geophys. Res. 83, 4373 (1978); Planet. Space Sci. 32, 257 (1984).
10. G. R. Swenson, S. B. Mende, and K. S. Clifton, Geophys. Res. Lett. 12, 97 (1985).
11. I. L. Kofsky and J. L. Barrett, submitted to Journal of Spacecraft and Rockets.
12. K. K. Hui and T. A. Cool, J. Chem. Phys. 68, 1022 (1978).
13. A. E. Douglas, J. Chem. Phys. 45, 1007 (1966).
14. F. Kaufman, in Chemiluminescence and Bioluminescence, edited by M. J. Cormier, D. M. Hercules, and J. Lee (Plenum, New York, 1973), pp. 83-101.
15. G. D. Gillispie, A. U. Khan, A. C. Wahl, R. P. Hosteny, and M. Krauss, J. Chem. Phys. 63, 3425 (1975).
16. C. F. Jackels and E. R. Davidson, J. Chem. Phys. 65, 2941 (1976); 64, 2908 (1976).
17. R. E. Smalley, L. Wharton, and D. H. Levy, J. Chem. Phys. 63, 4977 (1975).
18. J. C. D. Brand, W. H. Chan, and J. L. Hardwick, J. Mol. Spectrosc. 56, 309 (1975).
19. D. K. Hsu, D. L. Monts, and R. N. Zare, Spectral Atlas of Nitrogen Dioxide (Academic Press, New York, 1978).
20. E. Haller, H. Koppel, and L. S. Cederbaum, J. Mol. Spectrosc. 111, 377 (1985).
21. L. F. Keyser, S. Z. Levine, and F. Kaufman, J. Chem. Phys. 54, 355 (1971).
22. K. H. Becker, W. Groth, and D. Thran, Chem. Phys. Lett. 15, 215 (1972).

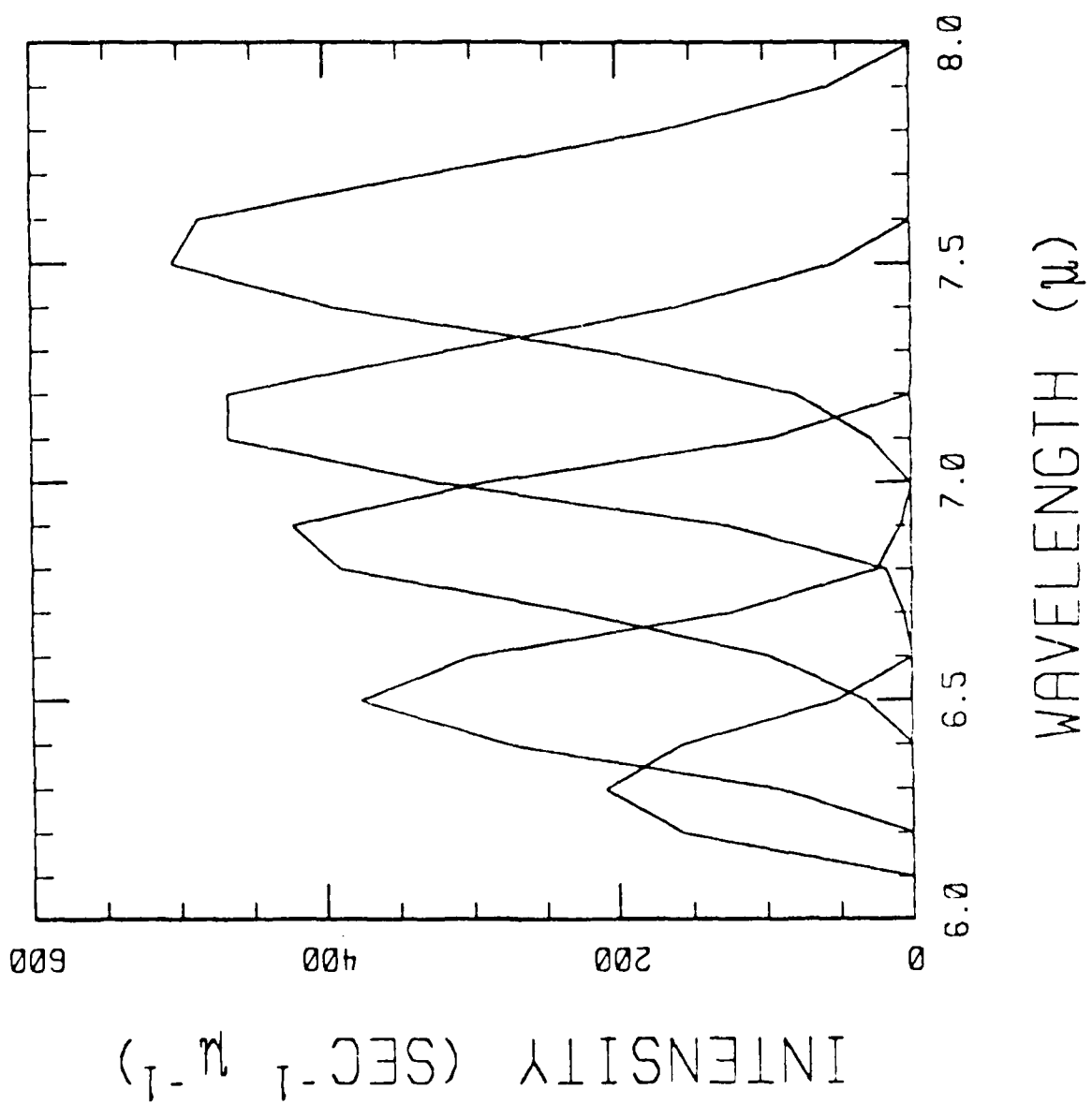
23. V. M. Donnelly, D. G. Keil, and F. Kaufman, J. Chem. Phys. 71, 659 (1979).
24. J. Y. Tsao, T. R. Simpson, N. Bloembergen, and I. Burak, J. Chem. Phys. 77, 1274 (1982).
25. S. Chapman, J. Chem. Phys. 74, 1001 (1981).
26. R. Viswanathan and L. M. Raff, J. Phys. Chem. 87, 3251 (1983).
27. S. M. Adler-Golden, accompanying paper.
28. J. V. Michael, J. E. Allen, Jr., and W. D. Brobst, J. Phys. Chem. 85, 4109 (1981).
29. V. M. Donnelly and F. Kaufman, J. Chem. Phys. 66, 4100 (1977).
30. V. M. Donnelly and F. Kaufman, J. Chem. Phys. 69, 1456 (1978).
31. R. B. Bernstein and R. D. Levine, Adv. At. Mol. Phys. 11, 215 (1975).
32. A. Guttman, J. Quant. Spectrosc. Radiat. Transfer 2, 1 (1962).
33. A. Goldman, F. S. Bonomo, W. J. Williams and D. G. Murcray, J. Quant. Spectrosc. Radiat. Transfer 15, 107 (1975).
34. J. H. Shafer and C. Young, App. Opt. 15, 2551 (1976).
35. K. Abe, J. Mol. Spectrosc. 48, 395 (1973).
36. S. M. Adler-Golden, S. R. Langhoff, C. W. Bauschlicher, Jr., and G. D. Carney, J. Chem. Phys. 83, 255 (1985).
37. R. F. Hampson, "Chemical Kinetic and Photochemical Data Sheets for Atmospheric Reactions", U. S. Dept. of Transportation, Report No. FAA-EE-80-17 (1980).
38. M. Schieferstein, K. Kohse-Hoinghaus, and F. Stuhl, Ber. Bunsenges. Phys. Chem. 87, 361 (1983).
39. H. Hippler, C. Schippert, and J. Troe, Int. J. Chem. Kinet., Symp. No. 1, 27 (1975).
40. M. Sutoh, Y. Morioka, and M. Nakamura, J. Chem. Phys. 72, 21 (1980).
41. G. R. Bradburn, H. V. Lilenfeld, and R. P. Neisler (McDonnell Douglas Research Laboratories), work in progress.

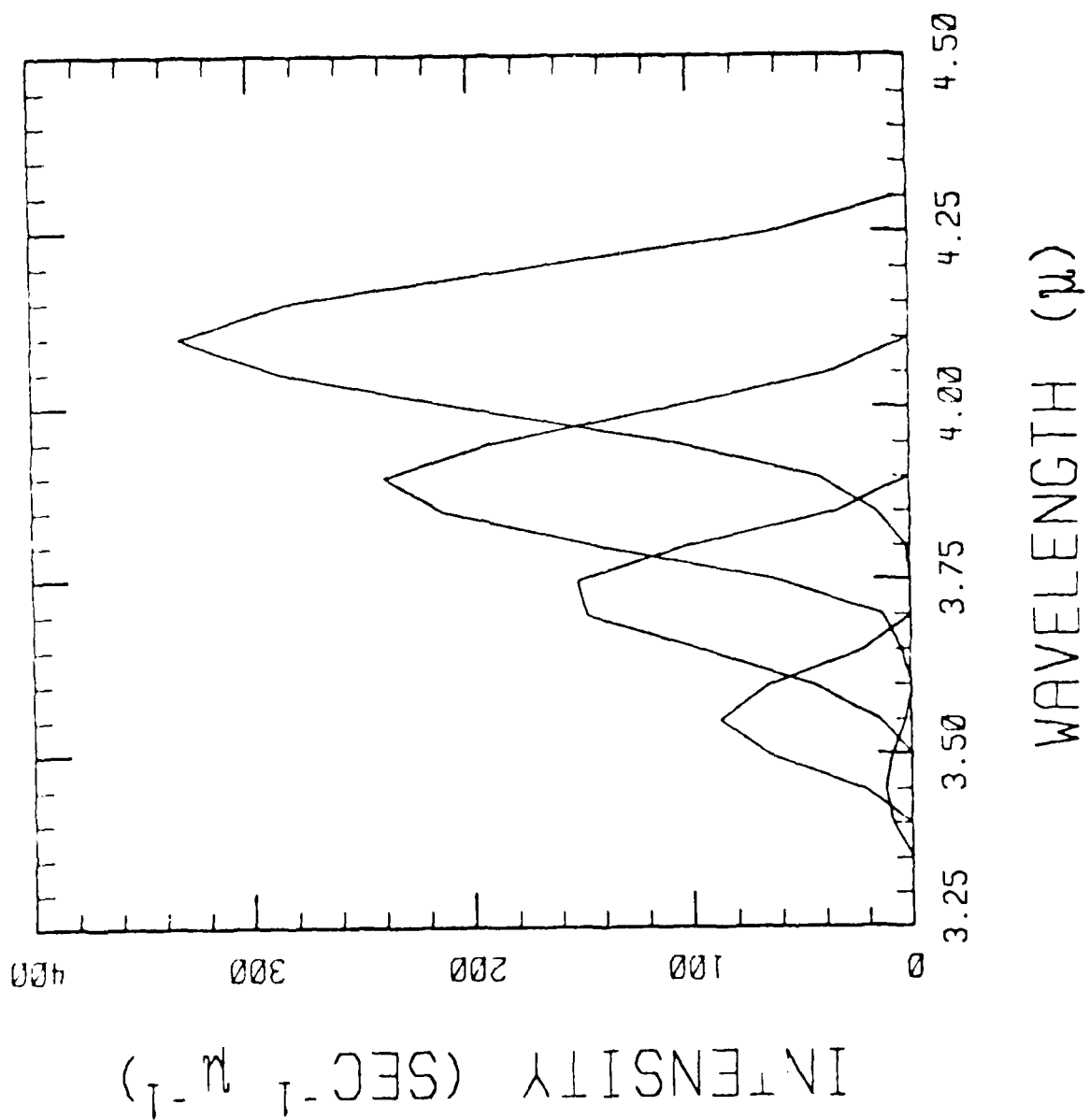
FIGURE CAPTIONS

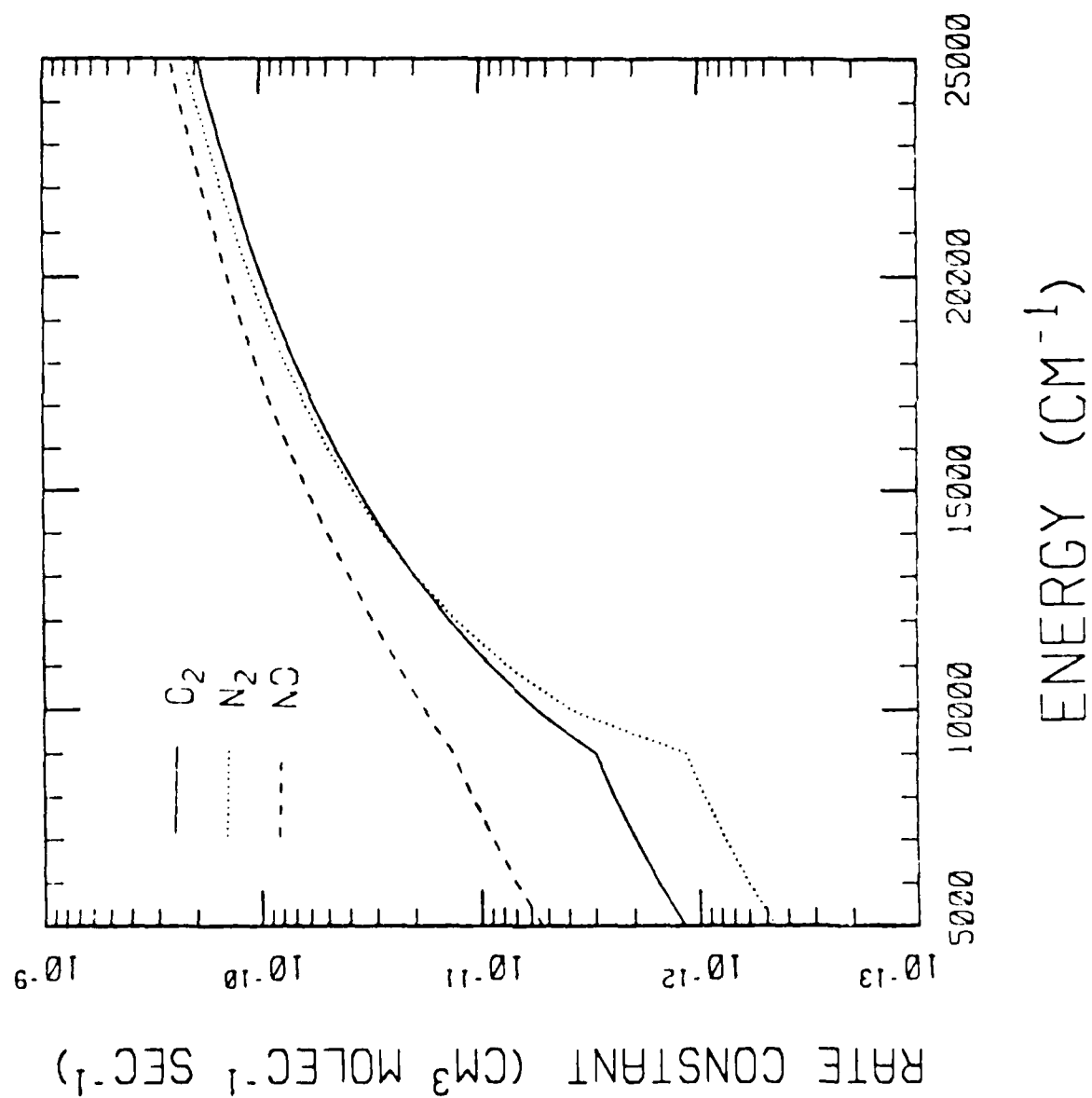
- Figure 1. Model NO_2 ν_3 band spectral components for different excitation energies, E. From left to right, E = 3000, 6000, 9000, 12000, and 15000 cm^{-1} .
- Figure 2. Model NO_2 $\nu_1+\nu_3$ band spectral components for different excitation energies, E. From left to right, E = 3000, 6000, 9000, 12000, and 15000 cm^{-1} .
- Figure 3. Model rate constants for NO_2 vibrational deactivation (per 1000 cm^{-1} removed).
- Figure 4. Calculated NO_2 population distributions for a mixture of 2.3 torr O_2 , 0.03 torr NO, and two different atomic oxygen concentrations: 0.09 torr (high O) and 0.009 torr (low O).
- Figure 5. Calculated and experimental (see text) NO + O $\nu_1+\nu_3$ spectrum for the conditions of Fig. 4.
- Figure 6. Calculated NO + O ν_3 spectrum for the conditions of Fig. 4.
- Figure 7. Calculated and experimental (Ref. 5) NO + O_3 $\nu_1+\nu_3$ spectrum for a mixture of 0.24 torr Ar, 0.013 torr NO, and 0.040 torr O_3 . The experimental spectrum was scaled to match the calculation.
- Figure 8. Calculated second order rate constant for $\nu_1+\nu_3$ emission from the NO + O reaction in O_2 and N_2 buffer gases.
- Figure 9. Calculated second order rate constant for $\nu_1+\nu_3$ emission from the NO + O_3 reaction in O_2 and N_2 buffer gases.

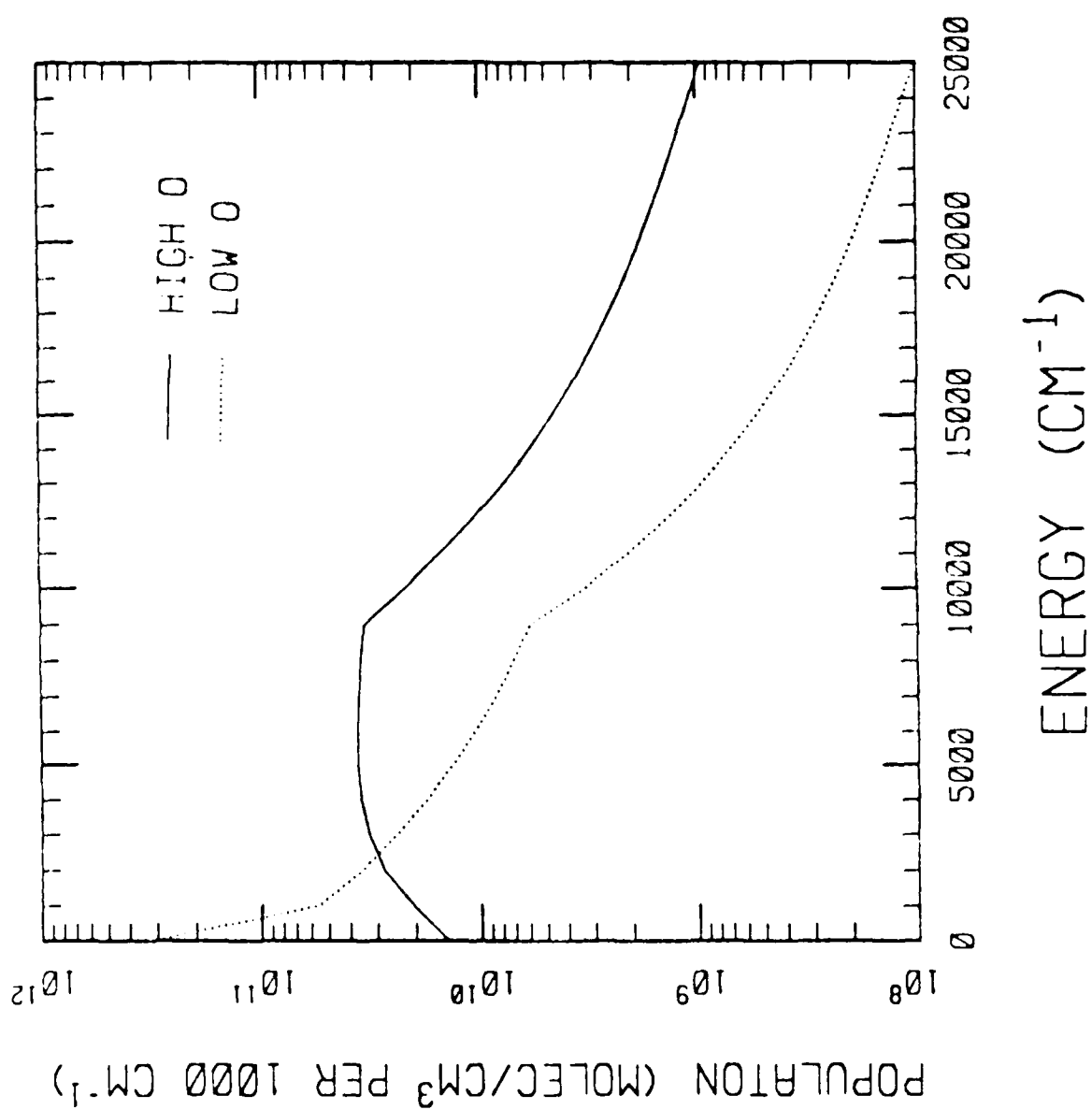
TABLE I. VIBRATIONAL DEACTIVATION PARAMETERS FOR EQS. (13a) AND (13b).
($\text{cm}^5 \text{ molec}^{-1} \text{ sec}^{-1}$)

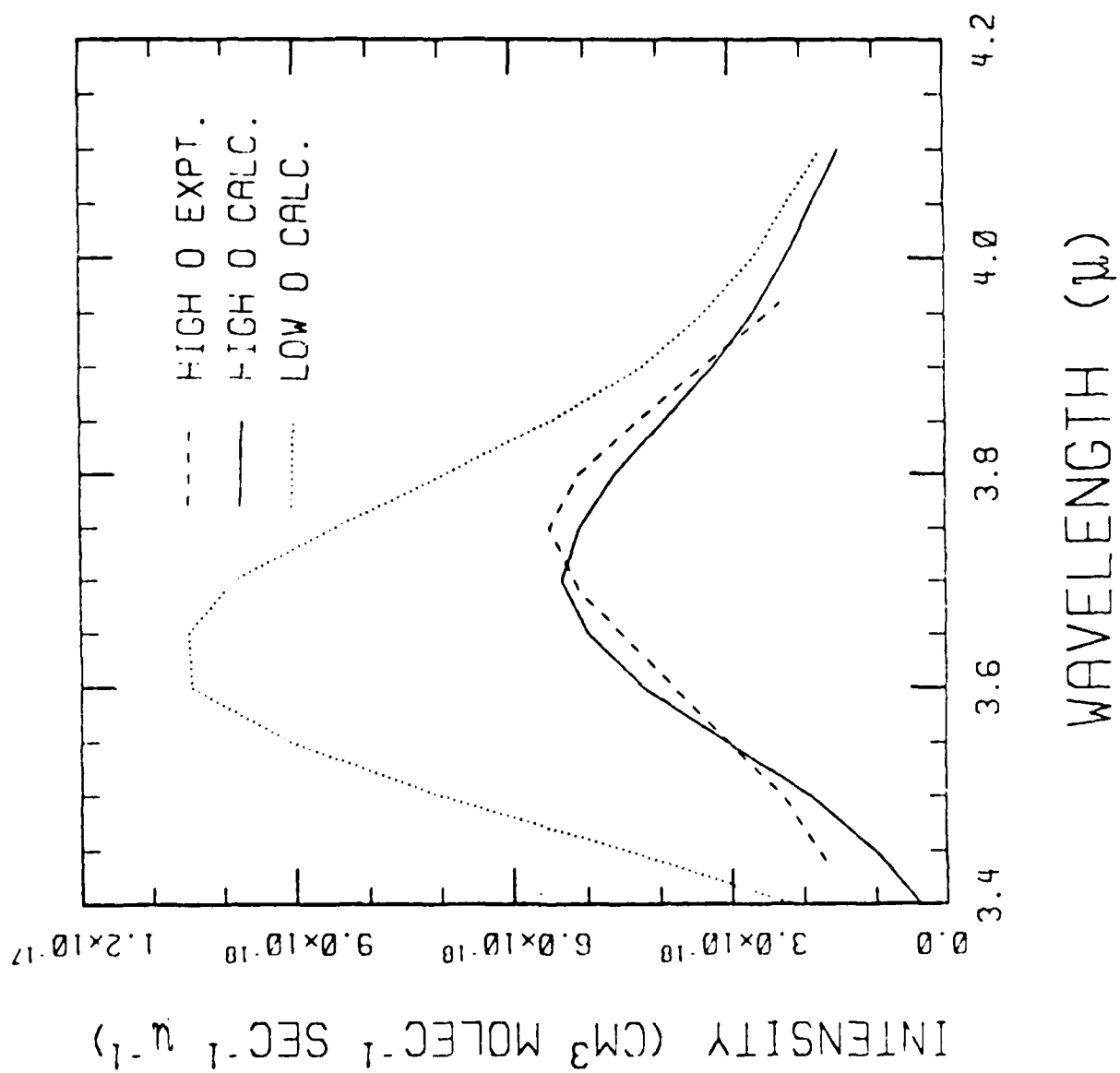
<u>Species</u>	<u>a_M</u>	<u>b_M</u>
NO	1.2×10^{-19}	6.3×10^{-19}
NO ₂	1.6×10^{-19}	9.0×10^{-19}
O ₂	2.6×10^{-20}	6.3×10^{-19}
N ₂	1.0×10^{-20}	7.6×10^{-19}

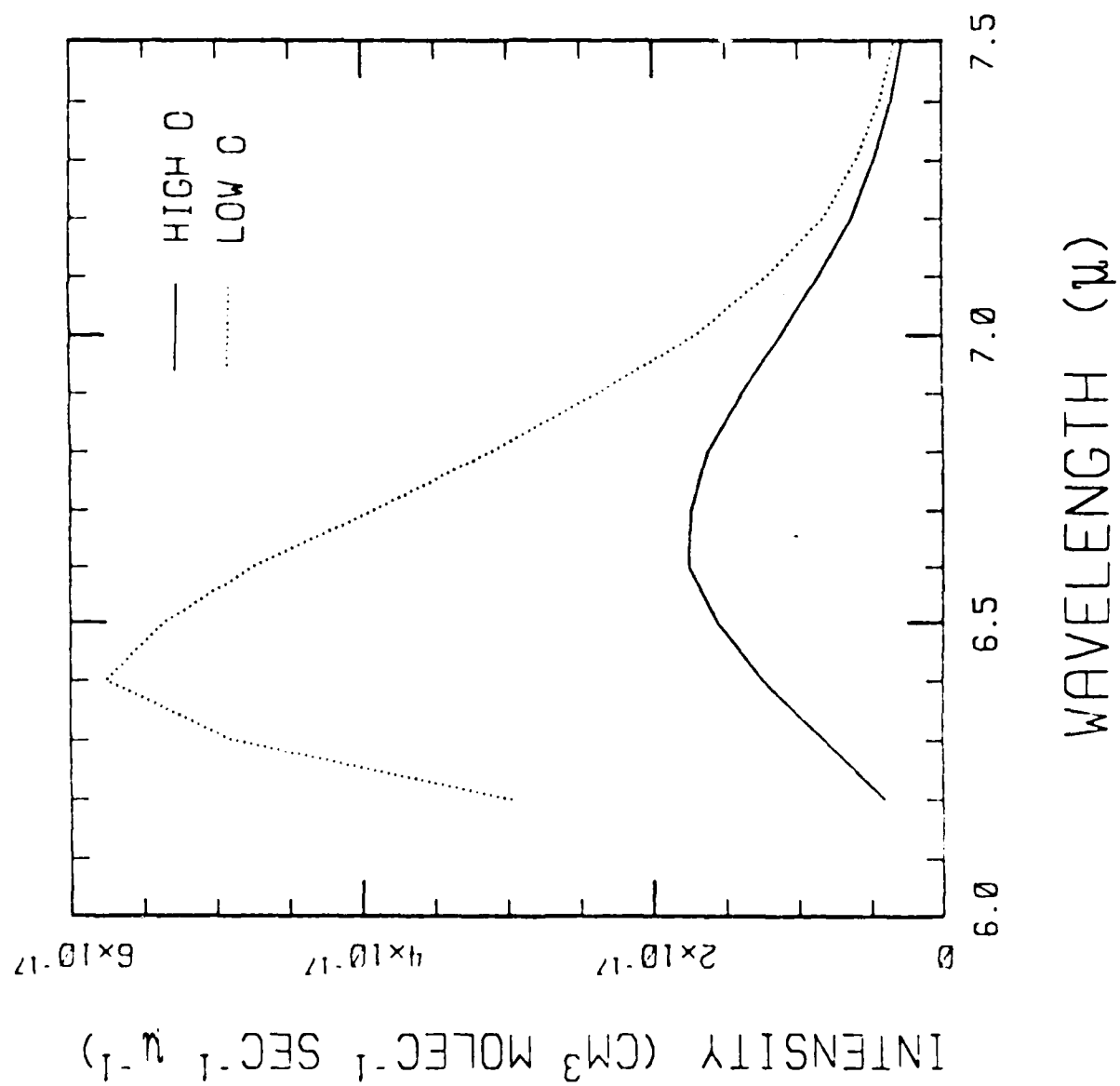


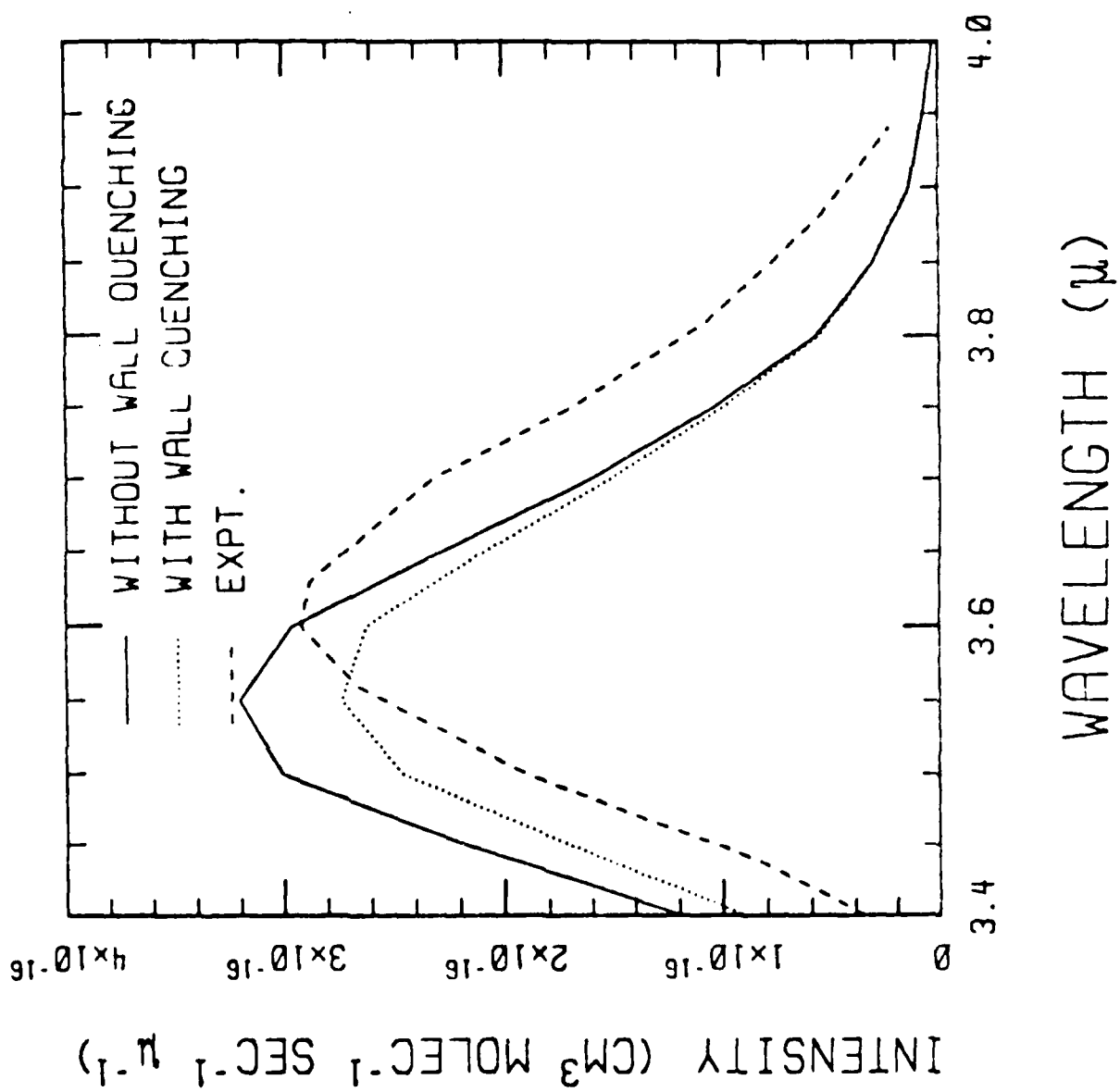


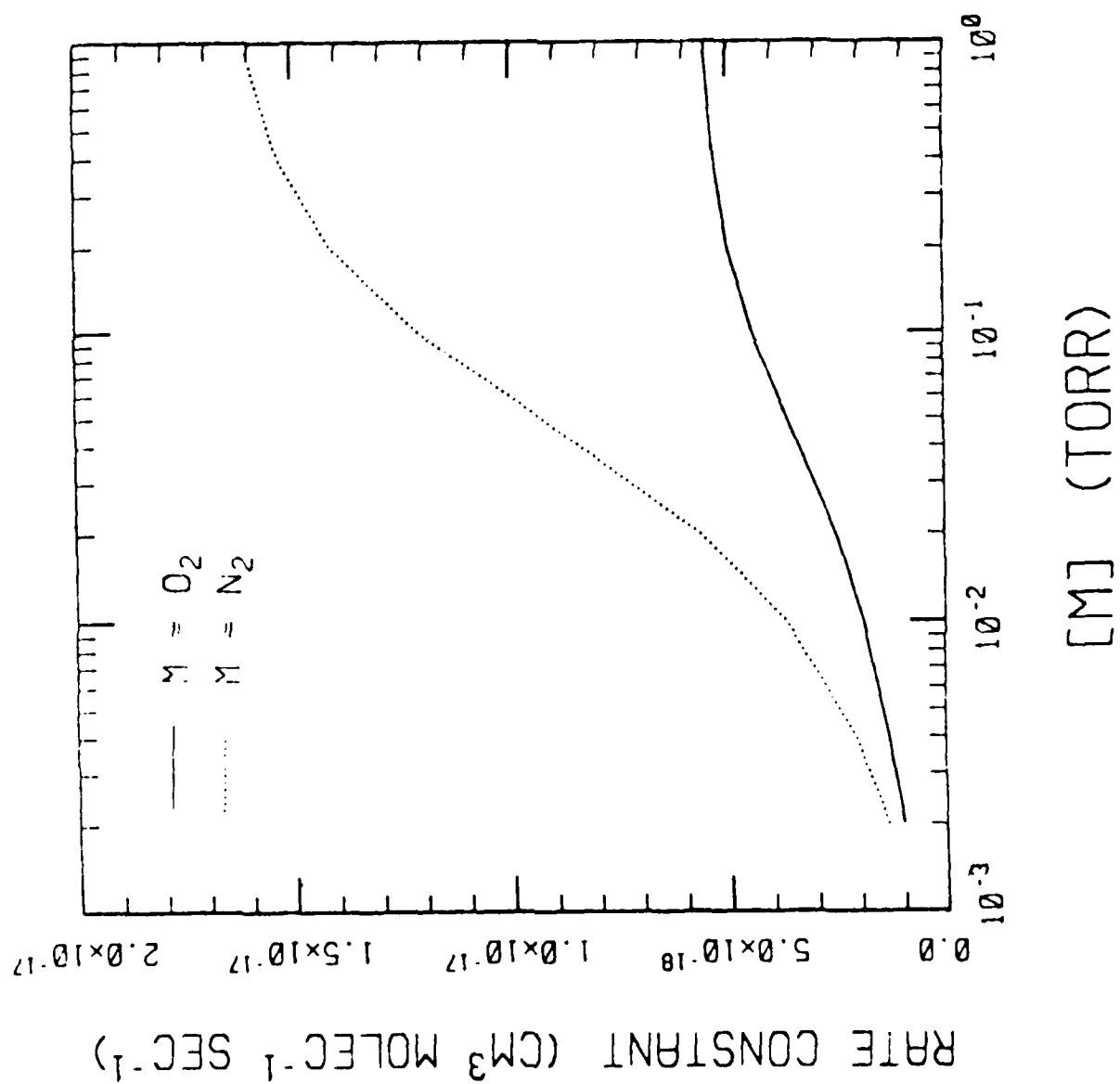


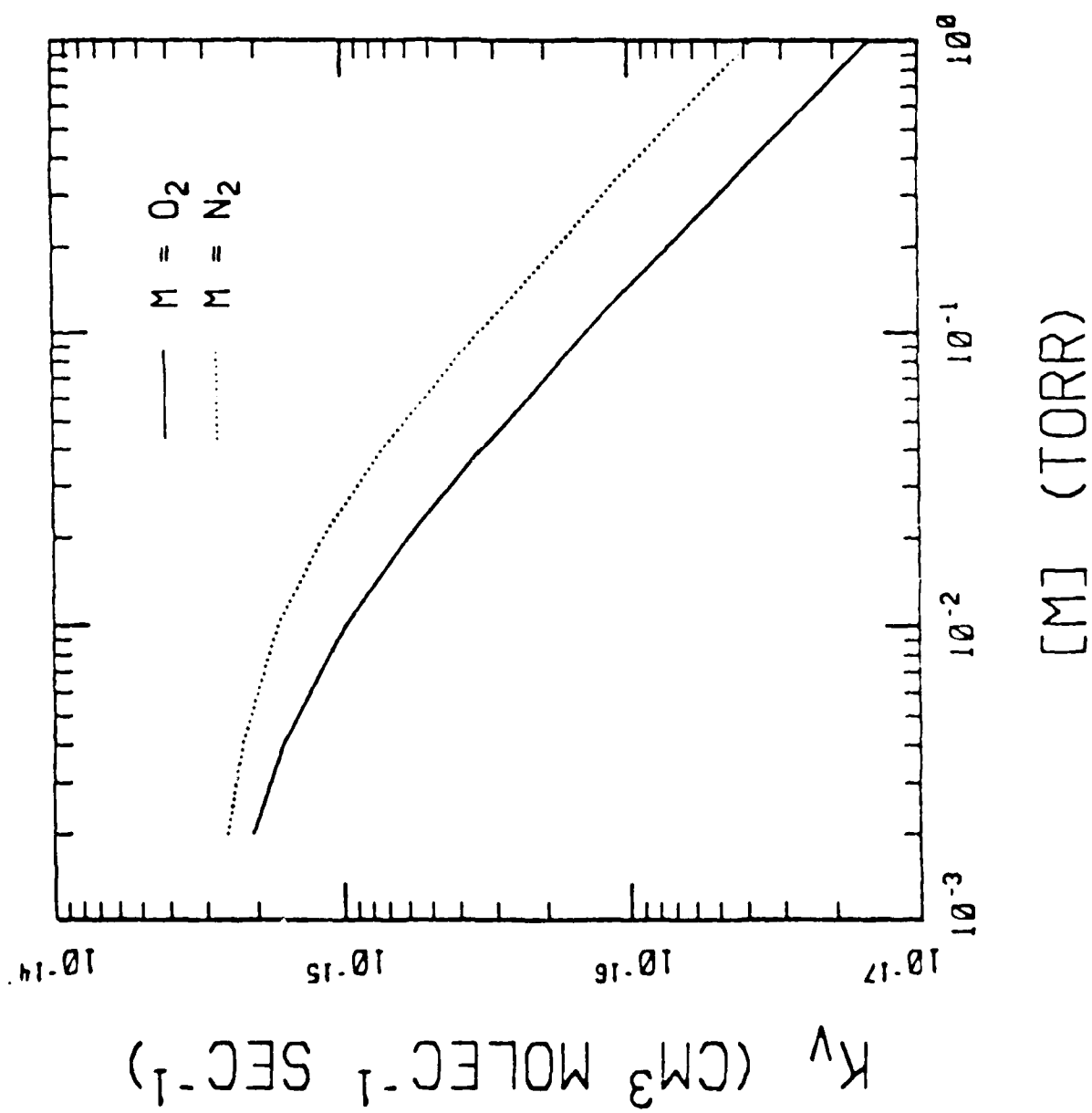












APPENDIX E

THE NO + O AND NO + O₃ REACTIONS:

II. ANALYSIS OF NO₂ CONTINUUM
CHEMILUMINESCENCE

THE NO + O AND NO + O₃ REACTIONS:

II. ANALYSIS OF NO₂ CONTINUUM CHEMILUMINESCENCE

Steven M. Adler-Golden
Spectral Sciences, Inc.
111 So. Bedford Street
Burlington, MA 01803

July 1986

THE NO + O AND NO + O₃ REACTIONS: II. ANALYSIS OF NO₂ CONTINUUM CHEMILUMINESCENCE

Adler-Golden, Steven M.

Spectral Sciences, Inc., 111 So. Bedford Street, Burlington, MA 01803

The NO₂^{*} continuum chemiluminescence from the NO + O and NO + O₃ reactions is simulated using the model presented in the accompanying paper. The model's accuracy is supported by the good agreement between calculated and experimental NO + O continuum spectra. A calculation of NO + O₃ chemiluminescence assuming reaction on the ground electronic potential energy surface alone is found to give surprising agreement with experimental data on the continuum shape, absolute intensity, half-quenching pressure, and activation energy. This finding contradicts the popular hypothesis that NO₂^{*} is formed in the NO + O₃ reaction via an excited electronic channel.

I. INTRODUCTION

The NO₂^{*} visible/near-IR "continuum" emission has been the subject of numerous experimental and theoretical studies due to its usefulness in the laboratory as well as its importance as a source of atmospheric radiation. Considerable progress has been made through the years in understanding excitation mechanisms, kinetics and spectroscopy of NO₂^{*}. Without attempting a complete literature survey, we note several important papers which discuss NO₂^{*} chemiluminescence (from the NO + O reaction, Refs. 1-4, and the NO + O₃ reaction, Refs. 5-9), NO₂^{*} kinetics (Refs. 10, 11), NO₂^{*} spectroscopy (Refs. 12-15), and NO₂ electronic structure (Refs. 16-19).

The NO + O → NO₂^{*} chemiluminescence has previously been modeled with reasonable success in the visible region using a simple vibrational level stepladder scheme.^{2,20} In the accompanying paper²¹ (Paper I) an improved and extended stepladder model was developed for predicting NO₂ IR band chemiluminescence from that reaction as well as the NO + O₃ reaction. The model, which assumes complete vibrational and electronic energy mixing, yields good agreement with observed vibrational band shapes and factor-of-2 or better agreement in absolute intensity.

In Paper I the NO_2^* continuum emission was not discussed, although it was included as a relaxation mechanism. An expression representing the continuum spectrum was given without proof. The purpose of the present paper is to derive the continuum expression, and to further validate the model as a whole (and, in particular, the assumed NO_2 nascent distribution from the $\text{NO} + \text{O}_3$ reaction) by comparing the calculated continuum spectrum with experimental measurements.

A brief derivation of the continuum model is given in Sec. II. In Sec. III $\text{NO} + \text{O}$ continuum chemiluminescence is modeled over a wide range of pressures (mtorr and above) and wavelengths ($0.4\text{--}3.0\ \mu$). Good agreement is obtained with experimental measurements of the spectrum in both low and high pressure limits. Having demonstrated the reasonableness of the continuum model, we turn to the $\text{NO} + \text{O}_3$ reaction in Sec. IV. Continuum chemiluminescence from this reaction is calculated assuming (as in Paper I) reaction on the ground electronic potential energy surface alone.

As it has been generally believed that NO_2^* is formed in the $\text{NO} + \text{O}_3$ reaction via a separate, excited electronic channel,⁵⁻⁹ the calculation was not expected to replicate the experimental measurements. To our surprise, remarkably good agreement was found. The calculation even explains the conflict between two experimental studies (Clough and Thrush⁶ and Schurath, Lippmann and Jesser⁹) of the chemiluminescence. It is concluded that reaction on the ground electronic potential energy surface provides the dominant, if not the sole, source of NO_2^* .

Although this paper deals only with chemiluminescence, the continuum model may also be applied to NO_2^* emission excited by optical^{10,11} or thermal²² means.

II. DESCRIPTION OF THE MODEL

A. Background

Details of the model, except those dealing with the continuum spectrum, are discussed in Paper I. The NO_2 "states" consist of a stepladder of levels, $\text{NO}_2(i)$, $i = 1\text{--}27$, at $1000\ \text{cm}^{-1}$ energy intervals, each level representing the set of actual states whose electronic plus

vibrational energy rounds to $E = 1000(i-1)$. Rotational energy is assumed to be equilibrated with the translational temperature. Associated with each level are (1) second-order rate constants for collisional transfer from level i to level j , $k(i,j)$, for removal via chemical reaction with O atoms, $x(i)$, and for formation via chemical reaction, $f(i)$, and (2) first order rate constants for radiation from level i to level j , $r(i,j)$, and for quenching at the vessel wall, k_w . In the case of the $\text{NO} + \text{O}$ reaction, NO_2 formation occurs via an activated complex, taken as level $i = 27$, which subsequently relaxes to form stable NO_2 levels ($i = 1-26$). In the case of the $\text{NO} + \text{O}_3$ reaction, stable NO_2 is formed directly; the nascent distribution $f(i)$ is taken as a statistical RRHO vibrational distribution.

Explicit expressions for the room temperature rate constants are given in Paper I, where a variety of collision partners (N_2 , O_2 , NO , NO_2 , O_3 , O) were considered. In the steady state the model yields simultaneous, linear equations which are solved for the $\text{NO}_2(i)$ number densities. The $\text{NO}_2(i)$ densities are combined with spectral functions, corresponding to $r(i,j)$, to yield the continuum and IR band spectra.

The radiative rate constants are given by

$$r(i,j) = r_3(i,j) + r_{13}(i,j) + r_c(i,j), \quad (1)$$

where r_3 and r_{13} are the ν_3 and $\nu_1+\nu_3$ infrared band contributions and r_c is the continuum contribution. Expressions for the first two terms were derived in Paper I. The continuum contribution may be written as

$$r_c(i,j) = I_\nu(E)(1000 \text{ cm}^{-1}), \quad (2)$$

where $I_\nu(E)$ is the absolute rate constant for continuum emission per frequency interval (in units of sec^{-1} per cm^{-1}) associated with excitation energy E , and $\nu = E(i)-E(j)$ in cm^{-1} . A suitable formula for $I_\nu(E)$ is derived below.

B. Continuum Spectral Model

Previous models^{2,11,20} employed a smooth, empirical spectral function which was shifted on the frequency scale in accordance with the excitation energy; i.e., a 1000 cm^{-1} energy loss was assumed to shift the entire

spectrum by 1000 cm^{-1} to the red. Such an approach is not theoretically rigorous, and is expected to work poorly at low excitation energies and long wavelengths. Here, an improved spectral model is developed based on Franck-Condon arguments. It is assumed that the continuum emission arises from the 2B_2 state, whose energy levels are completely mixed with those of the 2A_1 ground state.

First, I_ν is written in the Condon approximation as the product of a squared overlap integral S^2 (whose meaning will be clarified below), a ν^3 factor, a factor X denoting fractional excited state character, and a multiplicative constant C :

$$I_\nu(E) = C\nu^3 S^2(E, \nu) X(E). \quad (3)$$

Since S^2 is unit normalized in wavenumber ν , integrating Eq. (3) over ν yields the relationship between the continuum lifetime τ_c and the average value of ν^3 ,

$$1/\tau_c(E) = C\langle \nu^3 \rangle X(E) \quad (4)$$

C may be determined from the strength of the absorption spectrum. According to Donnelly and Kaufman's analysis,²³ a Born-Oppenheimer ($X = 1$) lifetime τ_{BO} of 1.5×10^{-6} sec corresponds to $\langle \nu^3 \rangle = (15400 \text{ cm}^{-1})^3$, yielding $C = 1.8 \times 10^{-7} \text{ cm}^3/\text{sec}$.

An approximate expression for X is

$$X(E) = \frac{1}{1 + R(E + E_0)^2 / (E + E_0 - E_e)^2}, \quad (5)$$

where E_e is the 2B_2 electronic origin, E_0 is the vibrational zero point energy, and R is the ratio of rotational state densities in the ground and excited electronic states. Eq. (5) was derived using semiclassical rigid rotor-harmonic oscillator (RRHO) densities of states with equal vibrational frequencies in the two electronic states. For a rigid rotor the rotational density of states scales with the rotational constant B as $B^{-3/2}$. Using experimental and theoretical B values (0.434 cm^{-1} for 2A_1 ,²⁴ 0.548 cm^{-1} for 2B_2 ¹⁷), $R = 1.4$. As in Paper I, approximate values for the remaining parameters are $E_0 = 1800 \text{ cm}^{-1}$ and $E_e = 10,000 \text{ cm}^{-1}$.

The next step is the determination of a suitable expression for the continuum Franck-Condon integral, S^2 . The emitting "level" is actually a statistical mixture of individual states with energy E , whose vibrational progressions superimpose to give the appearance of a continuous spectrum. Thus, we define S^2 as the Franck-Condon integral averaged over the emitting states. Since our aim is to reproduce the smooth continuum envelope, without worrying about the contributions of individual bands, a rather crude model for S^2 will suffice.

We note that the ${}^2B_2 - {}^2A_1$ spectrum is dominated by progressions in a single normal mode, the bending coordinate q_2 .^{11,17} The S^2 envelope may therefore be approximated with displaced harmonic oscillators in a single active mode, with the remaining modes inactive. Using a linear approximation to the difference potential along q_2 , the 2A_1 and 2B_2 oscillator frequencies are taken as equal. Next, the average over all 3 vibrational modes is performed. This averaging should enable a classical treatment to reasonably approximate the quantum mechanical solution, since it removes the classical singularities at the vibrational turning points (see Eq. (A3) in Appendix A). The classical approach has the advantages of yielding a smooth spectrum and a simple, analytical formula. As shown in Appendix A, the classical, mode-averaged S^2 is given by

$$S^2(E, \nu) = 48\alpha^{1/2} [E + E_0 - E_e - \alpha(\Delta\nu)^2]^{5/2} / [15\pi(E + E_0 - E_e)^3], \quad (6)$$

where $\Delta\nu = \nu - \nu_0$, ν_0 is the wavenumber of the Franck-Condon maximum, and α is a parameter related to the relative displacement between the two oscillators.

The above expression should work quite well for the visible portion of the continuum. However, in the near IR this simple model may break down, since some emission in this region can arise from vertical transitions in the vicinity of the avoided crossing with the ground state. (For details of NO_2 potential energy surfaces see Refs. 16-19). From the diabatic point of view, a portion of the 2B_2 state lies slightly below the ground (2A_1) state; therefore, emission can also occur via ${}^2A_1 \rightarrow {}^2B_2$. This component, which should be most important in the near IR, would need to be added to the above expression. Alternatively, in the adiabatic description, the upper state origin E_0 is interpreted as the adiabatic minimum, i.e., the

apex of the conical intersection which comprises the crossing region. In this case one regards the potential surfaces as highly anharmonic, and therefore not very amenable to the above simple treatment.

While ultimately one should aim for a theory which accounts for these effects, for the present they are circumvented by treating Eq. (6) empirically, fixing its parameters in accordance with observed spectra.

For high excitation energies and short wavelengths the spectrum is not very sensitive to the values of ν_0 and E_e , but it is quite sensitive to the value of α , which determines the breadth of the spectrum. The spectrum arising from energies near the excited state origin E_e is much more sensitive to ν_0 and E_e . The value $\nu_0 = 4000 \text{ cm}^{-1}$ was chosen, based on the observed $\text{NO} + \text{O}_3$ chemiluminescence spectrum,⁶ since this spectrum arises mainly from low-lying energy levels. We have set $E_e - E_0 = 9000 \text{ cm}^{-1}$, which is close to the value, 8200 cm^{-1} , predicted using the estimate $E_e = 10,000 \text{ cm}^{-1}$. (The difference was mainly for convenience and should not be considered significant.) Finally, the value $\alpha = 3.4 \times 10^{-5} \text{ cm}$ was chosen to give the correct peak wavelength in simulated $\text{NO} + \text{O}$ and laser-induced fluorescence¹¹ spectra.

The continuum lifetimes (Eq. (4)) calculated with the above parameter values showed the proper dependence on excitation energy E when compared with experiment,^{10,11} but were consistently about a factor of 2 too short. The model was therefore corrected empirically by multiplying the right hand side of Eq. (3) by a "fudge factor." Considering the approximations used in the model (the Condon approximation, harmonic 1-dimensional potentials, RRHO state densities, classical mechanics), this lifetime discrepancy is understandable. Taking the "fudge factor" as exactly 0.5 leads to lifetimes (shown in Fig. 1) which are a compromise between two sets of experimental data (τ_{0L} and (τ_{0L}) in Ref. 10) believed to represent upper and lower limits. It should be cautioned that since the lifetime data extend down to only $E \sim 15000 \text{ cm}^{-1}$, at lower energies we are forced to be totally at the mercy of the model's extrapolation ability.

The continuum spectrum $I_\nu(E)$ is plotted in Fig. 2 for excitation energies $E = 13000, 16000, 19000, 22000$, and 25000 cm^{-1} . Inspection of Fig. 2 reveals that the dependence of the spectrum on excitation energy is described fairly well by a simple frequency shift only near the blue end of the spectrum. Since the spectrum gets narrower at lower excitation energy,

the shift of the peak is considerably less than the change in excitation energy (about 2/3 as great). This phenomenon is a general feature of electronic spectra and not simply an artifact of the model.

The 2:3 ratio of spectral shift to excitation energy affects the interpretation of NO_2^* relaxation, since previous studies^{2,11,20} assumed a 1:1 ratio. The consensus of those studies was that NO_2^* loses about 1000 cm^{-1} per deactivating collision; the current model implies that the correct value is closer to 1500 cm^{-1} , as assumed in Paper I. Further confirmation of this value is provided by the calculation of the $\text{NO} + \text{O}$ continuum spectrum, as discussed in Sec. III.

In the following sections, we compare model calculations using $I_v(E)$ with experimental measurements of the NO_2 continuum.

III. $\text{NO} + \text{O}$ CONTINUUM EMISSION

A. The High Pressure Limit

At high pressures (above ~1 torr) a limiting NO_2 energy level distribution is achieved for a given buffer gas which depends solely on the vibrational relaxation kinetics. Assuming that the kinetic model (given in Paper I) is accurate, a comparison of calculated and observed spectra provides a direct test of the NO_2^* continuum model.

The calculated high pressure spectrum in O_2 buffer gas at room temperature is depicted in Fig. 3. Using N_2 buffer gas the results are essentially the same except for a slight increase in absolute intensity, which results from the larger 3-body formation rate assumed by the model (see Paper I). This increase is consistent with measurements by Becker, Groth and Thran² and Vanpee, Hill and Kineyko.²⁵ The experimental measurements in Fig. 3 are by Sutoh, Morioka and Nakamura⁴ in the visible and near IR, and Golde, Roche and Kaufman²⁶ in the IR.

A brief discussion of the experimental measurements is in order. Sutoh's spectrum agrees very well with the generally accepted work of Fontijn, Meyer and Schiff¹ except in the IR, where Fontijn's sensitivity dropped off. It is clear from Fig. 3 that Sutoh's and Golde's results are not very compatible, as they differ by a factor of 2 in the near IR. Sutoh

rationalized the difference by invoking the presence of ozone in Golde's flow system, leading to $\text{NO} + \text{O}_3$ emission, but this argument does not explain the magnitude of the discrepancy, and indeed Golde explicitly ruled out ozone as a significant source of emission. An attempt to settle the dispute using additional measurements proves only more frustrating; the work of Bradburn, Lilenfeld and Neisler²⁷ supports Sutoh's spectrum, while Vanpee's work supports Golde's. Of course, it must be borne in mind that the experimental conditions were different in different studies, both with respect to buffer gas (Sutoh worked mainly with N_2 , Golde and Bradburn used O_2 , Vanpee used both and had rather high NO concentrations) and temperature (Vanpee's measurements were mainly at 360 K). On the other hand, according to Vanpee none of these conditions significantly affect the spectral shape. Finally, one must consider the possibility of absolute calibration error in these measurements (about 30%^{4,26}).

The model calculation is found to agree extremely well with Sutoh's (and Fontijn's) spectrum in the visible and, interestingly, yields a compromise between Sutoh and Golde in the disputed near IR region which turns out to be very close to Vanpee's spectrum. Although the model calculation is not accurate enough to favor or disfavor a particular measurement, it can be said that the model agrees with available data to within experimental uncertainty at most wavelengths.

The good agreement in absolute chemiluminescence intensity as well as spectral shape indicates that the model $\text{NO}_2(i)$ relaxation rates are of the correct magnitude relative to the emission rates $1/\tau_c(i)$. These relaxation rate constants are actually per 1000 cm^{-1} energy loss, and, as explained in Paper I, were derived from experimental values¹¹ by multiplying by 1.5 in accordance with the energy loss estimate of 1500 cm^{-1} per deactivation event. Had the loss been taken as 1000 cm^{-1} the calculated spectral intensity would have been 50% higher, in poorer agreement with experiment.

B. The Low Pressure Limit

In the low pressure limit the $\text{NO} + \text{O}$ reaction proceeds by 2-body radiative recombination, and the spectrum arises mainly from the activated complex. An advantage of analyzing the low pressure spectrum is its

independence from collisional processes. A disadvantage is that, in the absence of collisions, energy mixing may be incomplete, which would make the continuum model inaccurate.

The calculated low pressure spectrum is shown in Fig. 4. The kinetic parameters governing the formation and decay of the activated complex, described in Paper I, determine the absolute intensity; the particular set of parameters used had been chosen to give an intensity close to Becker et al.'s measurement, $4.2 \times 10^{-18} \text{ cm}^3 \text{ molec}^{-1} \text{ sec}^{-1}$.² The "experimental" spectra were derived by combining the "fall-off ratios" measured by Becker et al. and Cody and Kaufman, tabulated in Ref. 3, with Sutoh's high pressure spectrum. The important comparison is the spectral shape, where the model is seen to agree quite well with the measurements, particularly Becker's. Assuming that the agreement is not accidental, energy mixing appears to be reasonably complete in the complex.

C. Conclusions

The good agreement between calculated and observed $\text{NO} + \text{O}$ chemiluminescence spectra bolsters confidence in both the continuum model, Eqs. (3)-(6), and the kinetic model developed in Paper I. The agreement is especially clear-cut in the visible region. Further refinement could be achieved with additional data on the continuum spectral shape and intensity, radiative lifetimes, and quenching rates, particularly in the IR where both model and observations are most uncertain.

IV. THE $\text{NO} + \text{O}_3$ REACTION

A. Background

NO_2 formed from the reaction of NO with O_3 emits continuum and IR band chemiluminescence which is qualitatively similar to that from the $\text{NO} + \text{O}$ reaction, although as a result of the reduced exoergicity the continuum is shifted to the red. Detailed gas phase measurements of the shape, absolute intensity, temperature dependence, and quenching kinetics of the chemiluminescence were performed by Thrush and co-workers^{5,6,28} in the

1960's. One of their key findings was that the NO_2^* continuum emission, which appeared to account for a small fraction of the NO_2 formed (about 0.06, using recent measurements of the total formation rate⁸), has a -1.8 kcal/mole higher activation energy than the total formation rate. This led to the hypothesis that NO_2^* and NO_2 are formed via separate reaction channels. More recent measurements by Michael, Allen and Brobst⁸ and Schurath, Lippmann and Jesser⁹ confirm a difference in activation energies, although the difference is found to be smaller than in the earlier work. Measurements in molecular beams²⁹ also tend to support the dual channel hypothesis; however, the correspondences between quantities measured in different studies is unclear.

The apparent complexity of the reaction mechanism is exacerbated by inconsistencies in the experimental data. For example, Clough and Thrush²⁸ observed that the near-IR continuum and IR band emission have the same activation energy, a surprising finding, since the IR band spectrum arises from the ground electronic NO_2 channel. The recent work of Schurath, Lippmann and Jesser⁹ appears to provide the answer, with the observation of different activation energies at different wavelengths. However, this raises the question of what is the "true" NO_2^* activation energy. In addition, Schurath et al. obtained half-quenching pressures and an NO_2^* quantum yield differing from those of Clough and Thrush⁶ by factors of 2 to 3, but did not provide a satisfactory explanation for these discrepancies.

In Paper I the IR band chemiluminescence from the $\text{NO} + \text{O}_3$ reaction was successfully modeled assuming NO_2 formation via the ground electronic channel alone, using results of classical trajectory calculations³⁰ to set up the nascent NO_2 distribution. The model's success with the $\text{NO} + \text{O}$ continuum (Sec. III) encouraged us to try a simulation of the $\text{NO} + \text{O}_3$ continuum as well.

If we truly believe the hypothesis of complete vibrational and electronic energy mixing (via either intramolecular or collisional processes), then all states having sufficient energy to emit in the continuum are classified as NO_2^* regardless of the channel by which they are formed. "Sufficient" energy means $E > 11000 \text{ cm}^{-1}$, for which the continuum emission rate $1/\tau_c$ equals or exceeds the total vibrational band emission rate. We may therefore estimate the contribution to NO_2^* from the ground electronic channel by integrating the nascent distribution ($dP(E)/dE$ in Paper I) above $E = 11000 \text{ cm}^{-1}$; this results in an NO_2^* quantum yield of

0.16. This estimate is larger than Clough and Thrush's experimental value of 0.06, but is quite close to the value 0.20 obtained by Schurath, Lippmann and Jesser. It is concluded that the ground electronic channel is capable of providing the full quantity of emission experimentally observed.

Further confirmation of the ground electronic mechanism as the source of NO_2^* is provided by computing such properties as the continuum spectral distribution, half-quenching pressures and activation energies. The detailed results are presented below.

B. Results

1. NO_2^* Spectrum

The $\text{NO} + \text{O}_3$ continuum spectrum was calculated for gas mixtures representative of Clough and Thrush's⁶ experimental conditions (mostly NO and O_2 at total pressures in the tens of mtorr); a typical result is depicted in Fig. 5.

The corresponding "experimental" spectrum is based on Clough and Thrush's relative intensity tabulation,³¹ which was converted to intensity per cm^{-1} and normalized to the observed integrated intensity I using the formula

$$I = I_0[\text{NO}][\text{O}_3]/([M] + P_{1/2}) \quad (7)$$

derived from Eq. (i) of Ref. 6. Here $[M]$ is the total pressure, $P_{1/2}$ is the half-quenching pressure for a specified gas composition, and $I_0 = k_{1a}P_{1/2}$, where k_{1a} is the rate constant for NO_2^* formation. Based on the absolute intensity and $P_{1/2}$ in NO and O_2 buffer gases, the experimental value of I_0 is 0.22 sec^{-1} for the Fig. 5 gas mixture. $P_{1/2}$ is estimated as 3 mtorr using the data in Table I, discussed below. Since $[M] = 48 \text{ mtorr} \gg P_{1/2}$, the absolute intensity in Fig. 5 essentially reflects the value of I_0 alone.

As seen in Fig. 5, the agreement between the calculated and observed spectra in both shape and absolute intensity is remarkable; it is undoubtedly somewhat fortuitous given the uncertainties in both spectra. The agreement certainly seems to confirm the conjecture that NO_2^* emissions results from the ground electronic channel.

2. NO_2^* Quenching Behavior and Quantum Yield

Playing Devil's advocate for a moment, one could argue that the agreement between the calculated and observed NO_2^* intensity is accidental: since $I_0 = k_{1a}P_{1/2}$, perhaps k_{1a} and $P_{1/2}$ are both coincidentally in error by large but canceling amounts. To test this possibility, the spectrum was calculated as a function of pressure, and $P_{1/2}$ was derived from a Stern-Volmer plot of the intensity at a selected wavelength.

The results are given in Table I. Although the relative half-quenching pressures for different buffer gases agree very well with Clough and Thrush's, they are smaller in absolute value by a factor of 2 to 3. However, the calculated values for N_2 and O_2 agree much better with the recent measurements of Schurath, Lippmann and Jesser.⁹

Since Clough and Thrush's experimental values were all derived relative to NO buffer gas, we decided to examine the NO measurements more closely. The NO Stern-Volmer plot was recalculated, this time including the effect of quenching at the vessel walls by introducing a removal rate constant, k_w . As in Paper I, k_w was taken as $(9 \text{ sec}^{-1})/([\text{NO}]/\text{torr})$ in Clough and Thrush's experiment.

The Stern-Volmer plots with and without wall quenching are shown in Fig. 6 for $\lambda = 700 \text{ nm}$. The model calculations, indicated by the squares and triangles, duplicate the NO pressures shown in Clough and Thrush's Fig. 3.⁶ Apparent half-quenching pressures were determined via linear least squares fits to the calculated points. It is observed that wall quenching introduces a barely noticeable curvature into the plot, but increases the linear fit's y-intercept (and therefore the apparent half-quenching pressure) by nearly a factor of 2. The apparent half-quenching pressure, 3.7 mtorr, is in fairly good agreement with Clough and Thrush's reported value of 5.2 mtorr. At longer wavelengths the wall quenching effect is even larger; an apparent value of 6.8 mtorr is obtained at 1.5μ , a threefold increase over the value obtained without wall quenching.

We conclude that the half-quenching pressures measured by Clough and Thrush are too large by factors of 2 to 3. Furthermore, presuming that the measured value of I_0 is correct, k_{1a} should actually be larger by the same factor--i.e., the NO_2^* quantum yield is in the range 0.12-0.18 rather than 0.06 as determined by Clough and Thrush.

The above analysis is fully consistent with the more recent measurements at several different wavelengths by Schurath, Lippmann and Jesser, who used a sufficiently large reaction vessel (radius - 400 cm) to eliminate wall quenching effects. In the visible region the agreement between the model and Schurath et al.'s half-quenching pressures is quite good; this is consistent with the model's reliability in this wavelength region demonstrated in the $\text{NO} + \text{O}$ calculations. In the near IR ($\sim 1.25 \mu$) the measurements disagree with the model by about a factor of 2, but this time the disagreement is in the opposite direction (the model predictions are too high). Because of this discrepancy in the near IR, Schurath's NO_2^* quantum yield value, 0.20, is higher than the model's result, which turns out to be 0.11. Both values are close to the range 0.12-0.18 estimated in the previous paragraph, as well as the value 0.16 estimated in Sec. IV.A.

The factor-of-2 disagreement with Schurath's results in the near IR is not surprising, given the large uncertainty in the model's assumed quenching and radiative rates for the states lying very near the excited electronic origin (around $10,000 \text{ cm}^{-1}$), which are responsible for emission in this wavelength region. The discrepancy is seen to be largest for N_2 buffer gas, traceable to an especially steep decline in the model quenching rate for N_2 as the electronic origin is approached (see Fig. 3 of Paper I).

3. NO_2^* Activation Energy

The original motivation behind the dual channel hypothesis for NO_2 formation was the difference in activation energies found for total NO_2 formation and NO_2^* emission, i.e., an enhancement of the NO_2^* quantum yield at high temperatures. Schurath et al. pointed out that much of this enhancement is due to a blue shift with increasing temperature, caused by increased reactant energy. One would actually expect some enhancement of NO_2^* at all wavelengths as the available energy increases, since emission even at long wavelengths occurs from the high-energy tail of the NO_2 vibrational distribution. We performed some model calculations to examine these effects by including temperature dependence in the average available reaction energy, E_T . E_T is used in calculating the NO_2 nascent distribution, as described in Paper I.

Assuming that translational, rotational, ozone vibrational, and NO spin-orbit energy are equally effective in promoting the reaction, the average available reaction energy is given by

$$E_T = \Delta E + 4RT + \langle E_v \rangle + \langle E_{SO} \rangle + E_a \quad (8)$$

(see Appendix B), where ΔE is the reaction exoergicity ($\sim 16700 \text{ cm}^{-1}$), R is the gas constant, $\langle E_v \rangle$ is the ozone thermal vibrational energy, $\langle E_{SO} \rangle$ is the NO thermal spin-orbit energy, and E_a is the reaction's activation energy. The second term assumes $3 \times 5 - 4$ (vibrational) $- 3$ (center-of-mass translational) = 8 translational/rotational degrees of freedom. For E_a we use the formula of Borders and Birks,³² $E_a = 1.52 \text{ kcal/mole} + 2.2RT$. The $\text{NO}_2^* - \text{NO}_2$ activation energy difference, denoted ΔE_a , is determined from an Arrhenius plot of the spectral intensity at a constant NO_2 formation rate. The model calculations were performed in the temperature range 300-400 K, corresponding to the experimental measurements.^{5,8,9}

The calculated values of ΔE_a as a function of wavelength are compared with the values obtained by Schurath et al., Michael et al.,⁸ and Clyne, Thrush and Wayne⁵ in Fig. 7. In the latter two experiments, which measured broadband emission collected by S-20 photomultiplier tubes, the average detected wavelength was approximately 750 nm. It is seen that the trend of increasing ΔE_a at shorter wavelengths is quantitatively reproduced by the calculation, although a discrepancy of about 0.6 kcal/mole remains between model and experiment. Thus, the current model, employing a single ground electronic reaction mechanism, is capable of explaining much, but not all, of the activation energy difference between NO_2 and NO_2^* .

C. Conclusions

The current model of the $\text{NO} + \text{O}_3$ reaction does a remarkably good job of explaining the observed gas phase NO_2^* chemiluminescence using a single ground electronic reaction channel, forming NO_2^* indirectly via collisional or intramolecular energy mixing, with little or no contribution from an excited electronic channel. The discrepancy, 0.6 kcal/mole, between the predicted and experimental $\text{NO}_2^* - \text{NO}_2$ activation energy difference is greater

than experimental errors. However, given the model uncertainties, this discrepancy would not seem to be by itself strong enough evidence to justify inclusion of a second channel.

On the other hand, additional evidence suggests at least two different reaction channels, as exemplified by molecular beam experiments³³ which observe a bimodal NO_2 angular distribution, as well as a bimodal distribution of emission as a function of NO orientation. Taken together, these findings suggest that both channels contribute to the chemiluminescence with roughly comparable NO_2^* quantum yields. A reasonable explanation of the molecular beam results is that two distinguishable channels indeed exist, but that both are associated with the ground electronic surface. Since an excited electronic channel would produce far more (and far bluer) NO_2^* emission than a ground electronic channel, the presence of the former in any significant quantity is unlikely, as it would destroy the good agreement between model and experimental spectral shapes and intensities obtained in this study.

A possible weakness in the model is the questionable validity of the vibrational and electronic energy mixing assumption in the region near the $^2\text{B}_2$ origin, which contributes most strongly to long wavelength NO + O_3 chemiluminescence. This problem would be exacerbated at very low pressures (below several mtorr), where collisions would be unavailable to promote mixing. Even as high as $E \sim 15000 \text{ cm}^{-1}$ mixing seems to be incomplete, judging from the scatter in measured continuum lifetimes.^{10,11} However, it is not clear whether incomplete mixing is to blame for the model's factor-of-2 discrepancies with Schurath et al. in the near IR, which could be virtually eliminated by small adjustments in the nascent distribution, the quenching rates and the continuum spectrum expression. Indeed, it is perhaps surprising that a model this crude works as well as it does.

V. SUMMARY

The NO_2 chemiluminescence model presented here and in Paper I has been used to analyze NO_2 chemiluminescence from the NO + O and NO + O_3 reactions over a wide range of experimental conditions. Theoretical considerations aside, the model's empirical success in simulating a large body of data (including continuum and IR band spectral shapes and intensities, quenching

parameters, radiative lifetimes, NO_2^* activation energies) is remarkable. The $\text{NO} + \text{O}_3$ calculation indicates a dominant role for the ground electronic reaction channel in yielding NO_2^* chemiluminescence. Clearly, additional experimental investigations would be very helpful to more accurately characterize the $\text{NO} + \text{O}$ and $\text{NO} + \text{O}_3$ spectral properties, particularly in the near IR where both the model and the existing data are most uncertain.

Although not reported here, preliminary simulations have also been carried out on NO_2^* laser-induced fluorescence and thermal emission spectra, with encouraging results.

ACKNOWLEDGEMENTS

I wish to thank Dr. W. A. M. Blumberg and Dr. R. Sharma of the Air Force Geophysics Laboratory (AFGL) for stimulating discussions and for encouragement of this project, Prof. M. Golde for helpful comments, and Dr. G. R. Bradburn and Dr. H. V. Lilenfeld for communicating their unpublished results. This work was supported by AFGL under Contract No. F19628 81-C-0029.

REFERENCES

1. A. Fontijn, C. B. Meyer, and H. I. Schiff, J. Chem. Phys. 40, 64 (1964).
2. K. H. Becker, W. Groth, and D. Thran, Chem. Phys. Lett. 15, 215 (1972).
3. F. Kaufman, in Chemiluminescence and Bioluminescence, edited by M. J. Cormier, D. M. Hercules, and J. Lee (Plenum, New York, 1973), pp. 83-101.
4. M. Sutoh, Y. Morioka, and M. Nakamura, J. Chem. Phys. 72, 21 (1980).
5. M. A. A. Clyne, B. A. Thrush, and R. P. Wayne, Trans. Faraday Soc. 60, 359 (1964).
6. P. N. Clough and B. A. Thrush, Trans. Faraday Soc. 63, 124 (1967).
7. K. K. Hui and T. A. Cool, J. Chem. Phys. 68, 1022 (1978).
8. J. V. Michael, J. E. Allen, Jr., and W. D. Brobst, J. Phys. Chem. 85, 4109 (1981).
9. U. Schurath, H. H. Lippmann, and B. Jesser, Ber. Bunsenges. Phys. Chem. 85, 807 (1981).
10. V. M. Donnelly and F. Kaufman, J. Chem. Phys. 69, 1456 (1978).
11. V. M. Donnelly, D. G. Keil, and F. Kaufman, J. Chem. Phys. 71, 659 (1979).
12. R. E. Smalley, L. Wharton, and D. H. Levy, J. Chem. Phys. 63, 4977 (1975).
13. J. C. D. Brand, W. H. Chan, and J. L. Hardwick, J. Mol. Spectrosc. 56, 309 (1975).

14. D. K. Hsu, D. L. Monts, and R. N. Zare, Spectral Atlas of Nitrogen Dioxide (Academic Press, New York, 1978).
15. E. Haller, H. Koppel., and L. S. Cederbaum, J. Mol. Spectrosc. 111, 377 (1985).
16. G. D. Gillispie, A. U. Khan, A. C. Wahl, R. P. Hosteny, and M. Krauss, J. Chem. Phys. 63, 3425 (1975).
17. G. D. Gillispie and A. U. Khan, J. Chem. Phys. 65, 1624 (1976).
18. C. F. Jackels and E. R. Davidson, J. Chem. Phys. 64, 2908 (1976).
19. C. F. Jackels and E. R. Davidson, J. Chem. Phys. 65, 2941 (1976).
20. L. F. Keyser, S. Z. Levine, and F. Kaufman, J. Chem. Phys. 54, 355 (1971).
21. S. M. Adler-Golden, accompanying paper.
22. D. E. Paulsen, W. F. Sheridan, and R. E. Huffman, J. Chem. Phys. 53, 647 (1970).
23. V. M. Donnelly and F. Kaufman, J. Chem. Phys. 66, 4100 (1977).
24. K. Abe, J. Mol. Spectrosc. 48, 395 (1973).
25. M. Vanpee, K. D. Hill, and W. A. Kineyko, AIAA Journal 9, 105 (1971).
26. M. F. Golde, A. E. Roche, and F. Kaufman, J. Chem. Phys. 59, 3953 (1973).
27. G. R. Bradburn, H. V. Lilenfeld, and R. P. Neisler (McDonnell Douglas Research Laboratories), work in progress.
28. P. N. Clough and B. A. Thrush, Trans. Faraday Soc. 65, 23 (1969).
29. For recent articles which review molecular beam work on the $\text{NO} + \text{O}_3$ reaction, see Viswanathan and Raff,³⁰ Michael et al.,⁸ van den Ende et al.,³³ and S. Chapman, J. Chem. Phys. 74, 1001 (1981).
30. R. Viswanathan and L. M. Raff, J. Phys. Chem. 87, 3251 (1983).
31. P. N. Clough and B. A. Thrush, Chem. Comm. 783 (1966).
32. R. A. Borders and J. W. Birks, J. Phys. Chem. 86, 3295 (1982).
33. D. van den Ende, S. Stolte, J. B. Cross, G. H. Kwei, and J. J. Valentini, J. Chem. Phys. 77, 2206 (1982).

AD-A190 964

STUDY OF POLYATOMIC DYNAMICS IN THE ATMOSPHERE(U)
SPECTRAL SCIENCES INC BURLINGTON MA F BIEN ET AL.
25 MAR 87 SSSI-TR-116 AFGL-TR-87-0223 F19620-84-C-0029

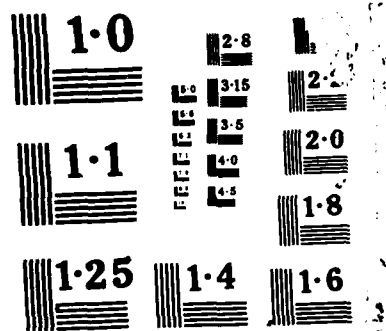
3/3

UNCLASSIFIED

F/G 4/1

NL





APPENDIX A: Derivation of the Continuum Franck-Condon Integral, Eq. (6).

Let q denote the active vibrational coordinate, V the upper state potential along q relative to $q = 0$, E_q the vibrational energy in mode q , and ΔV the difference potential along q . For fixed E_q the classical S^2 is given by

$$S^2(E_q, \Delta V) = N \frac{dP/dq}{d\Delta V/dq} \quad (A1)$$

where ΔV is equated with the transition energy ν . dP/dq is the probability density and N is a normalization constant such that

$$\int S^2(E_q, \Delta V) d\Delta V = 1 \quad (A2)$$

The probability density dP/dq is proportional to $(\text{velocity})^{-1}$, i.e., $(E_q - V)^{-1/2}$. In the approximation that ΔV is linear in q , the denominator of Eq. (A1) is constant. Integrating Eq. (A1) over all vibrational states of fixed total vibrational energy E_v yields

$$S^2(E_v, \Delta V) = N \int_V^{E_v} (E_q - V)^{-1/2} (E_v - E_q)^2 dE_q \quad (A3)$$

where the proportionality constants have been combined into N . The factor $(E_v - E_q)^2$ is proportional to the number of vibrational states in a 3-dimensional harmonic oscillator having energy E_q in one mode and a total energy of E_v .

In the harmonic approximation, $V \sim q^2$, and in the linear ΔV approximation, $q \sim \Delta V - \nu_0$, where ν_0 is a constant. Thus,

$$V = \alpha(\Delta V - \nu_0)^2 \quad (A4)$$

where α is a constant. Eq. (A3) then yields

$$S^2(E_V, \Delta V) = \frac{48}{15\pi} \alpha^{1/2} [E_V - \alpha(\Delta V - \nu_0)^2]^{5/2} / E_V^3 \quad (A5)$$

Eq. (6) results on substituting $E_V = E + E_0 - E_e$ and $\nu = \Delta V$.

APPENDIX B: Derivation of Eq. (8)

Let $k(E_r)$ be the $\text{NO} + \text{O}_3$ rate constant at reagent energy E_r ; then the net rate constant at temperature T is

$$k(T) = \frac{1}{Z} \int_0^{\infty} k(E_r) \rho(E_r) \exp(-\beta E_r) dE_r \quad (\text{B1})$$

where $\rho(E_r)$ is the reagent density of states, Z is the reagent partition function, $\int_0^{\infty} \rho(E_r) \exp(-\beta E_r) dE_r$, and $\beta = \frac{1}{kT}$ (k is the Boltzmann constant).

The average energy of the molecules which react is given by

$$\langle E \rangle = \frac{1}{Zk(T)} \int_0^{\infty} k(E_r) \rho(E_r) E_r \exp(-\beta E_r) dE_r \quad (\text{B2})$$

The activation energy is defined as

$$E_a = -\frac{1}{k(T)} \frac{dk(T)}{d\beta} \quad (\text{B3})$$

Substituting Eq. (B1) into Eq. (B3) leads to

$$\langle E \rangle = Z \frac{d(1/Z)}{d\beta} + E_a \quad (\text{B4})$$

The first term is the average reagent thermal energy, ϵ . The average energy available to the products is therefore

$$E_T = \Delta E + \langle E \rangle = \Delta E + \epsilon + E_a \quad (\text{B5})$$

where ΔE is the reaction exoergicity. Eq. (8) results from setting $\epsilon = 4RT + \langle E_v \rangle + \langle E_{so} \rangle$.

FIGURE CAPTIONS

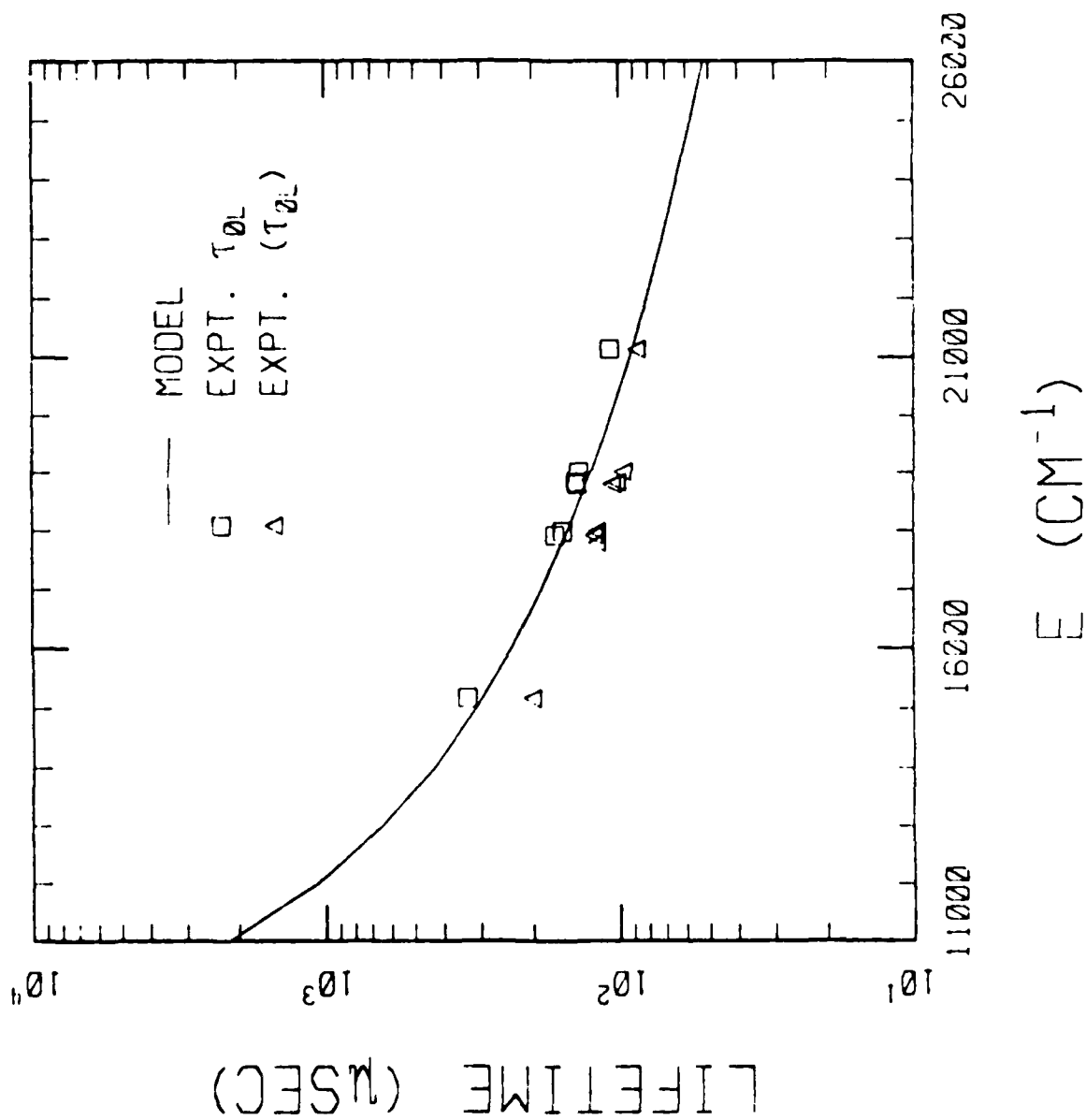
- Figure 1. Model and experimental¹⁰ continuum radiative lifetimes.
- Figure 2. The model continuum spectrum as a function of excitation energy. From bottom to top, $E = 13000, 16000, 19000, 22000,$ and 25000 cm^{-1} .
- Figure 3. The high pressure $\text{NO} + \text{O}$ continuum spectrum (O_2 buffer gas).
- Figure 4. The low pressure $\text{NO} + \text{O}$ continuum spectrum.
- Figure 5. The $\text{NO} + \text{O}_3$ continuum spectrum, $[\text{NO}] = 14 \text{ mtorr}$, $[\text{O}_2] = 28 \text{ mtorr}$, $[\text{O}_3] = 6 \text{ mtorr}$.
- Figure 6. Model Stern-Volmer plots of NO_2^* chemiluminescence quenching by NO , $\lambda = 700 \text{ nm}$, with (triangles) and without (squares) quenching at the vessel walls.
- Figure 7. The $\text{NO}_2^* - \text{NO}_2$ activation energy difference as a function of ν .

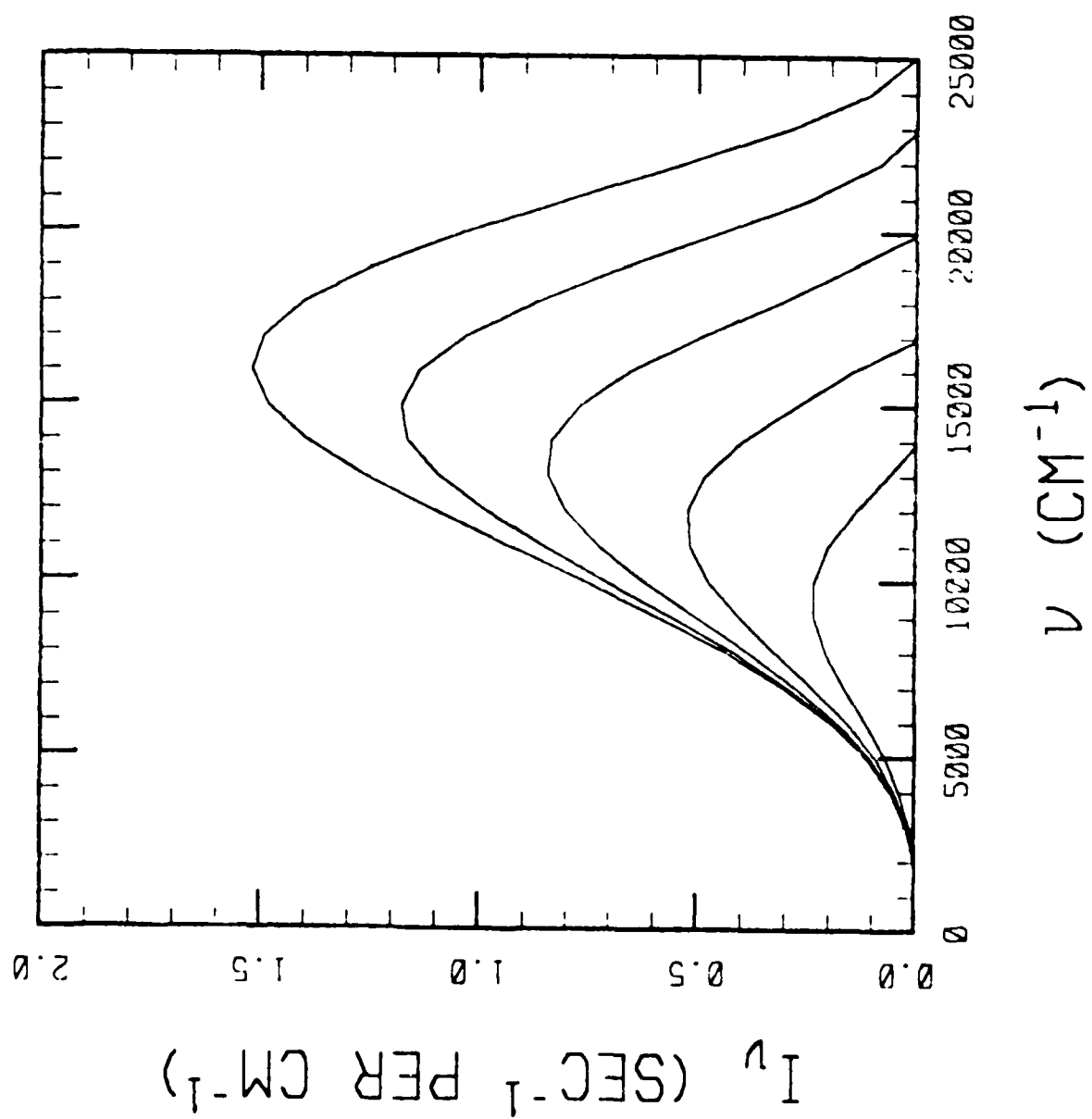
Table I. Half-quenching pressures
(mtorr) for NO + O₃ continuum emission.

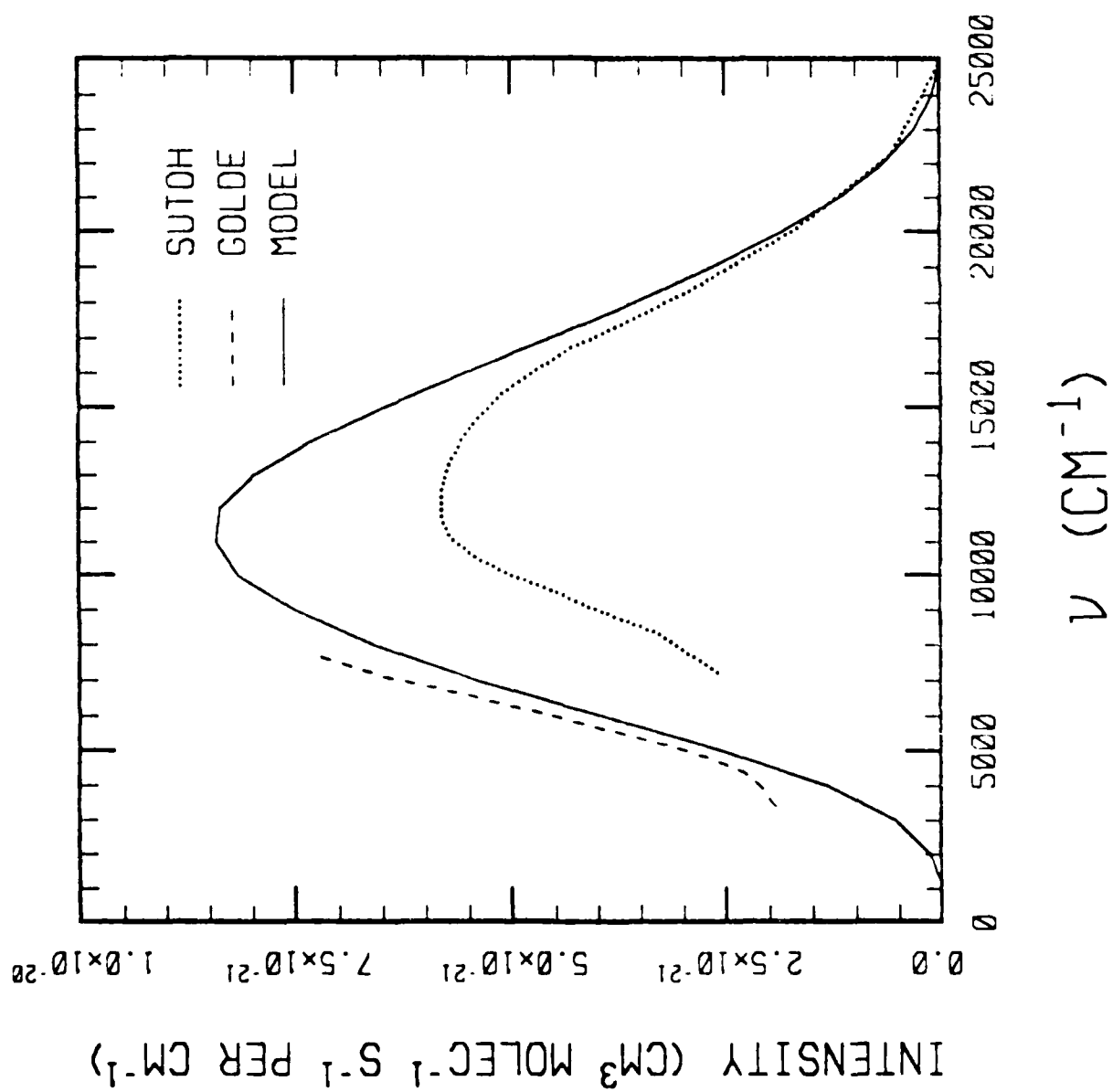
$\lambda =$	616 nm		1.27 μ		~750 nm Broad Band		Various ^b
<u>Quencher</u>	<u>Expt.^a</u>	<u>Calc.</u>	<u>Expt.^a</u>	<u>Calc.</u>	<u>Expt.^a</u>	<u>Calc.</u>	<u>Expt.^b</u>
NO		2.1		2.1		2.3	5.2 \pm 0.3
O ₂	4.6	3.3	2.4	4.8	4.1	4.7	8.3 \pm 0.5
N ₂	5.2	3.1	2.3	5.9	4.1	4.7	8.4 \pm 0.5

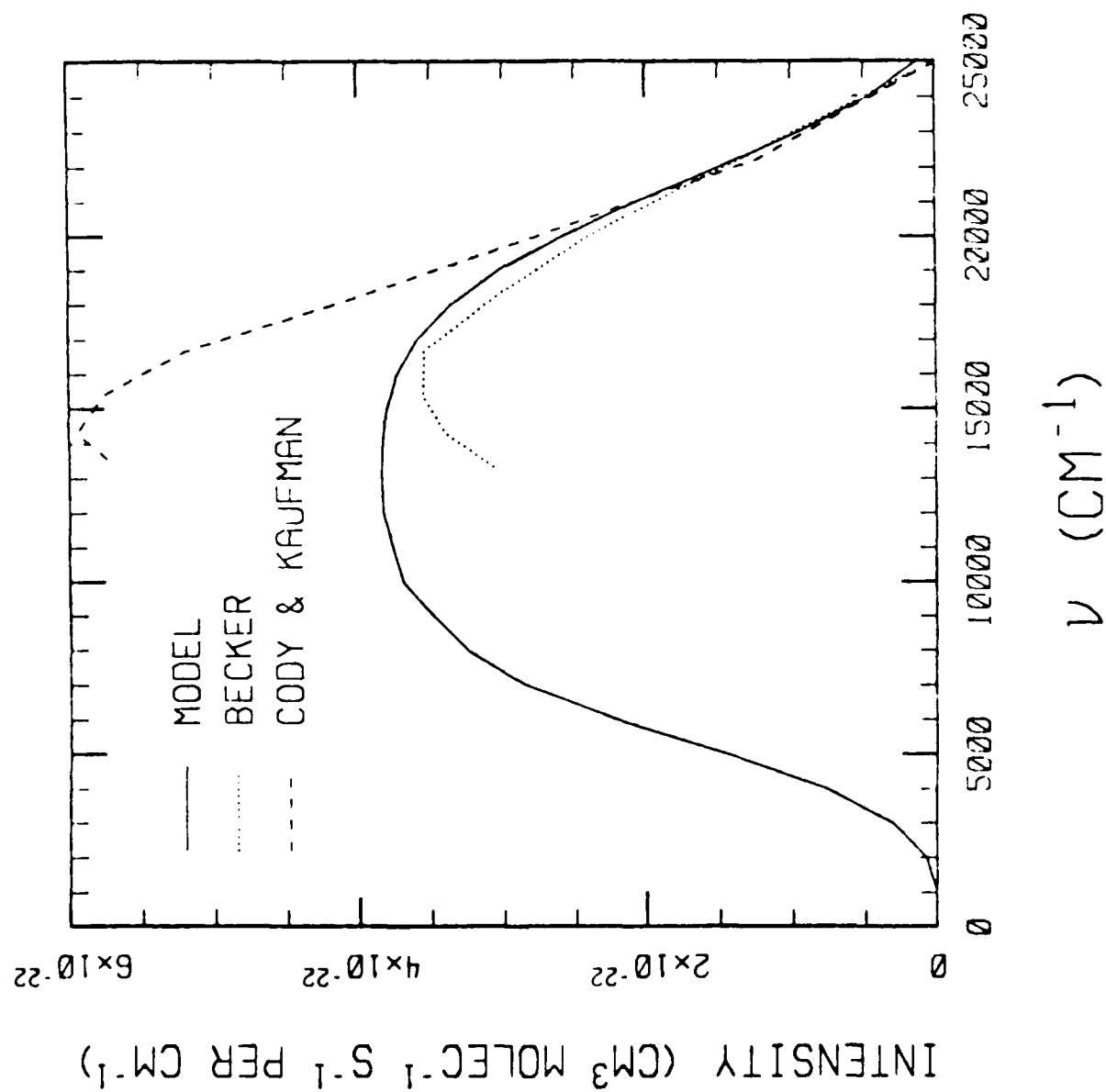
^aSchurath, Lippmann and Jesser. (9)

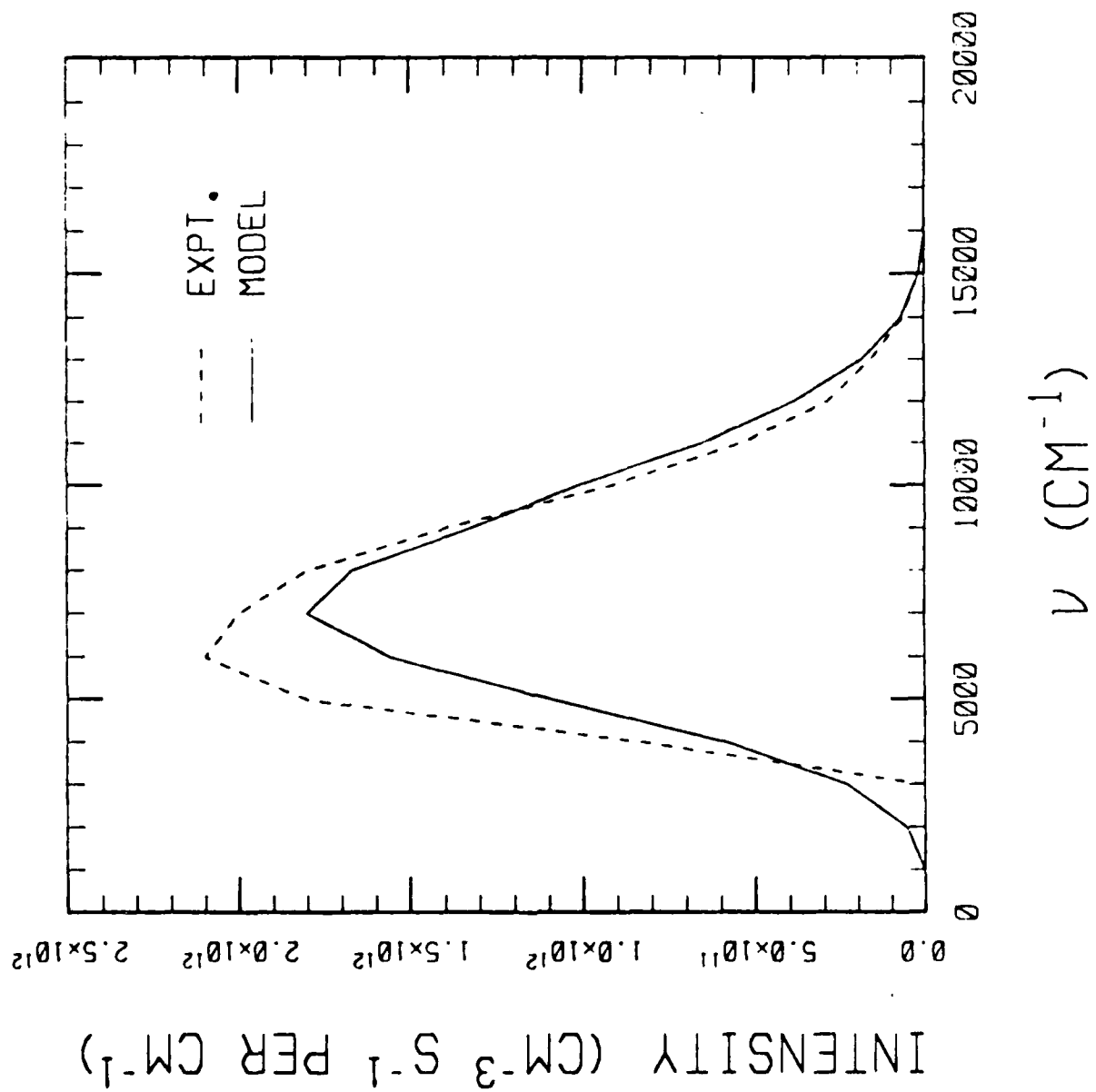
^bClough and Thrush, (6,28) reported to be independent of wavelength.

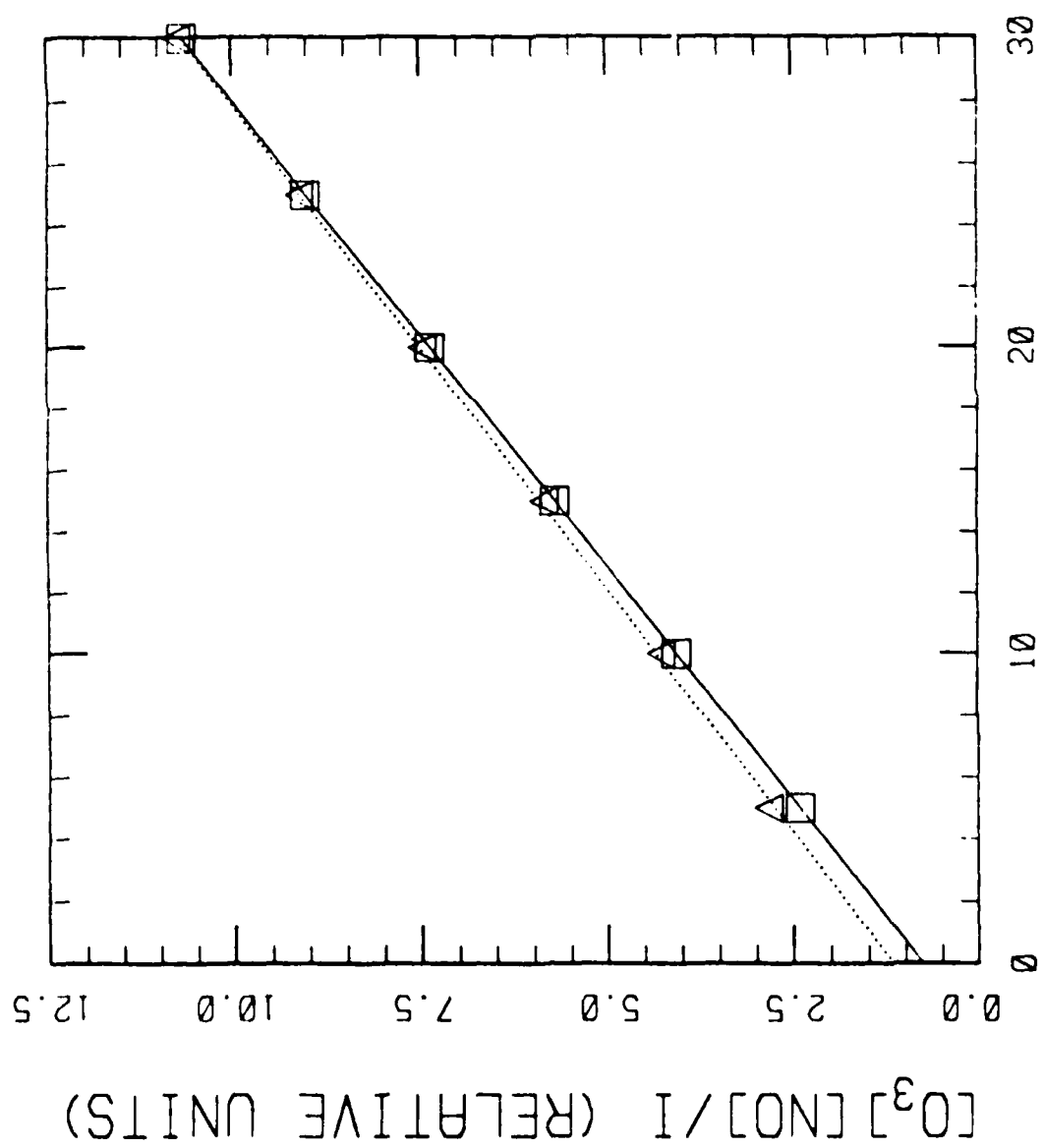




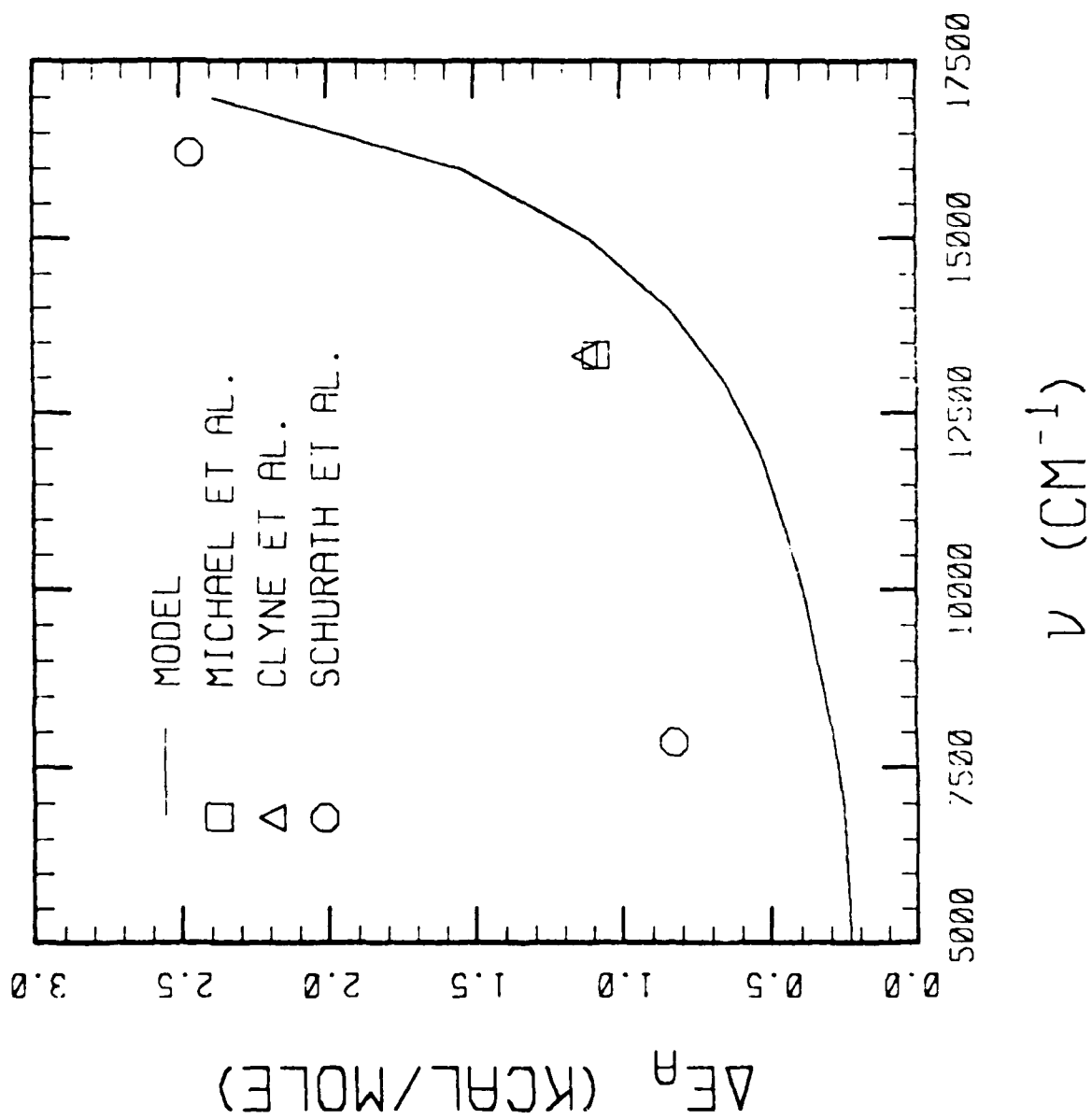








NO PRESSURE (MTORR)



END
DATE
FILMED
5-88
DTIC